SPH Simulations of Accretion Disks in Cataclysmic Variables

James Rhys Murray
B.Sc. (Hons)

Thesis submitted for the degree of
Doctor of Philosophy

Department of Mathematics
Monash University

August 1994

In loving memory of
Elizabeth Valerie Murray

3rd November 1939 - 23rd January 1994

Fear no more the heat o' the sun,
Nor the furious winter's rages;
Though thy worldly task hast done,
Home art gone, and ta'en thy wages:

William Shakespeare, *Cymbeline*

Statement

This thesis contains no material which has been accepted for any other degree or diploma in any university and, to the best of my knowledge, contains no material previously published or written by another person, except where otherwise stated in the text.

James Rhys Murray

Abstract

In this thesis a two dimensional Smoothed Particle Hydrodynamics code suitable for simulating the viscous evolution of geometrically thin disks is developed. The algorithm incorporates operator splitting, a technique which allows different physical processes in the disk to be treated separately, using numerical methods appropriate to them. Operator splitting in SPH is presented as a general technique with many applications. The code is tested against axisymmetric disk theory and a new class of axisymmetric disk solutions is found.

Simulations are described that verify the numerical results of Whitehurst (1988 a), and Hirose and Osaki (1990), that showed that accretion disks in binaries with a relatively low mass secondary are tidally unstable. The unstable disks precess with a period a few percent longer than the binary orbital period. The precession has been proposed as the cause of superhump in the SU UMa subclass of cataclysmic variables.

The condition that each element of the disk's surface radiates as a blackbody is incorporated into the SPH code. Simulations are compared with observations of OY Car in outburst and Z Cha in superoutburst. The tidally induced cyclic component of the energy dissipation in the disk simulation is compared with observed superhumps. This work is seen as a first step towards modelling disks that have more complicated energy transport physics.

Acknowledgements

Thanks to my supervisor Professor J. J. Monaghan, who always asked the difficult questions, but did not let me lose sight of the final goal.

There are many who provided friendship and support over the last few years. In particular my roommates Ernest Chow and Robin Humble have been great friends and colleagues.

I owe a debt of gratitude to my mother-in-law, Tina Hogeboom for her help when the crisis came. My father, James Murray, gave his emotional support when I needed it.

The greatest thanks of all go to my wife Karen Murray-Hogeboom.

This work was carried out with the support of an Australian Postgraduate Research Award.

Chapter 1.
Introduction

The Concise Oxford Dictionary defines accretion as "Growth by organic enlargement; growth of separate things into one; product of such growing ...". In an astrophysical sense, accretion is defined as the accumulation of mass onto a central object on a time scale that is long in comparison to the free fall time. Very rapid phenomena are referred to as collapse rather than accretion processes.

The source of the accreting matter may be, for example, a gas cloud or a mass losing star. The central object may be a small planetoid, a star, or even a black hole. Typically, the central object is very small relative to the system from which it accretes. Thus, rather than falling directly upon the central body, the accreting matter ends up in orbit around it.

The lowest energy state of a cloud of gas, rotating with a fixed angular momentum would have all the gas in circular orbits in a single plane. For this reason, disk structures are the most common starting point for accretion models.

In order for gas in the inner disk to be accreted, energy and angular momentum must be extracted from it. Thus a dissipative mechanism producing a shear viscosity is invoked. This mechanism would transfer angular momentum outwards through the disk whilst converting orbital energy to heat which is then radiated away. Thus accretion disks are luminous. Their brightness and the frequencies at which they radiate will depend upon the rate at which matter is accreted, and upon the compactness of the central object.

Accretion disks have been incorporated into models of a range of astrophysical phenomena; protostars, protoplanets, close binary systems such as cataclysmic variables and low mass X-ray binaries, and active galactic nuclei, to name a few. Observationally, the presence of disks in cataclysmic variables and low mass X-ray binaries has been well established. The case for disks in AGNs is not nearly so conclusive.

Cataclysmic variables (CVs) are close binary systems composed of a white dwarf, and a low mass companion on or near the main sequence. A general feature of CVs is that mass transfer is occurring from the companion star to the white dwarf, often via an accretion disk. Such a disk can dominate the optical light from the system. For this reason, and because the binary orbital motion (particularly in eclipsing systems) yields valuable spatial information about the disk, CVs are used as an observational test case of accretion disk theory.

Dwarf novae are a class of cataclysmic variables that exhibit periodic eruptions of $2-5$ magnitudes at semi regular intervals of weeks to months. Warner (1974) identified the accretion disk as the source of these 'outbursts'. Bath (1973) suggested that they were caused by 'mass transfer bursts' from the companion star. An alternative explanation put forward by Smak (1971) and Osaki (1974) was that outbursts were caused by an instability in the disk itself. Meyer and Meyer-Hofmeister (1981) identified a thermal instability that had the potential to do just as Smak and Osaki proposed. Since then, the thermal instability has been considered in great detail (see Cannizzo 1993 for a summary), and is the strongest contender to be the outburst mechanism. Attempts to model outburst (and accretion disk theory in general) have however been hampered by the lack of knowledge of the source of the viscous dissipation in the disk. Shakura and Sunyaev (1973) developed a parametrisation of the disk viscosity upon which most current disk theory is based. In fact what they did was to encapsulate our ignorance of the viscosity in one dimensionless parameter α, and then estimated a range of possible values for it.

However, Balbus and Hawley (1991) discovered that weakly magnetised disks are subject to a powerful shearing instability. They later (Hawley and Balbus 1992) found that the instability was capable of transporting angular momentum outwards through the disk. What is now known as the Balbus-Hawley instability has emerged as a very likely candidate to be the cause of a turbulent viscosity in accretion disks. But it is not the only possibility. Goodman (1993) found that tidally distorted disks suffered from a local three dimensional hydrodynamic instability that could also be the source of the dissipation. This instability however has been less well studied than even the Balbus-Hawley one.

The SU UMa subclass of dwarf novae exhibit, in addition to normal outbursts, a second type of eruptive behaviour. Superoutbursts are longer lasting and approximately one magnitude brighter than standard eruptions. During superoutburst a periodic phenomena known as superhump is observed. With a period a few percent longer than the rotation period of the binary, the total optical luminosity varies cyclically by up to $30 - 40\%$. Vogt (1983) postulated that the accretion disk was eccentric and precessed in the binary's reference frame. At the point where the gas stream from the companion star strikes the disk quite a large amount of energy is dissipated. This 'hot spot' is often observed in quiescent dwarf novae disks. Vogt suggested that as the disk precessed, the energy released at the hot spot varied, and that this was in fact the superhump variation.

Whitehurst (1988 a) used a particle scheme to conduct two dimensional simulations of accretion disks in cataclysmic variables. He found that when the mass ratio was small (i.e. when the companion star had a low mass relative to the white dwarf), the disk became tidally unstable. The disk would become eccentric and precess with a period a few percent longer than the binary's. Using a different particle method, Hirose and Osaki (1990) obtained similar results to Whitehurst. They showed with a first order analysis that the tidal resonance was a 3 : 1 resonance between orbits in the disk and the orbit of the binary itself. Further work by Lubow (1991 a) identified it as the 3 : 1 inner Lindblad resonance. It appeared that the superhump culprit had been apprehended red handed!

Horne (1985) developed a method of deconvolving photometric observations of eclipsing cataclysmic variables in order to obtain two dimensional maps of the accretion disk. O'Donoghue (1990) used the eclipse mapping technique to analyse the eclipsing SU UMa system Z Cha in superoutburst. He obtained two dimensional maps of the superhump source for four separate eclipses. In only one case did the source coincide with the hot spot. The other superhump maps showed a three source structure on the side of the disk lying between the two stars. He still felt the results were consistent with the eccentric precessing model for superhump. However these, and other observations (e.g. Naylor et al. 1987) which showed the superhump source to have a surface area of the same order as the entire disk, indicated that the superhump luminosity was more complicated than just a periodic brightening of the hot spot.

In this thesis we develop and test a two dimensional Smoothed Particle Hydrodynamics code specifically to examine geometrically thin disk problems. The code is used to verify the work of Whitehurst, and Hirose and Osaki, that showed accretion disks in low mass ratio binaries to be tidally unstable.The program is then adapted to incorporate the assumption that each element of the disk's surface radiates as a blackbody. This is seen as a first step towards incorporating more sophisticated energy transport physics into these simulations. Observations indicate that accretion disks of dwarf novae in outburst are in fact optically thick. Blackbody simulations are compared with observations of OY Car in outburst (largely by Rutten et al. 1992), and of Z Cha in superoutburst (Warner and O'Donoghue 1988, O'Donoghue 1990).

In Chapter 2 the theory of geometrically thin disks is reviewed. The derivation of Lynden-Bell and Pringle's (1974) time dependent disk solution is summarised, and the result is then extended to a disk with an initially Gaussian radial density profile. The steady state solution for axisymmetric Keplerian disks is outlined. Work on determining a suitable inner disk boundary condition for cataclysmic variables is reviewed. The possible nature of the source of viscous dissipation in disks is discussed. Finally, a first order picture of the radiative profile of an accretion disk is obtained.

In Chapter 3 cataclysmic variables are introduced in more detail. A phenomenological classification concentrating on non magnetic systems is given, and then key observations and typical values for system parameters are noted.

Chapter 4 is concerned with the numerical methods used in this thesis. The use of the SPH artificial viscosity term to model viscous shear is discussed and a theoretical estimate of the kinematic viscosity for disk problems is derived. Various methods for finding near neighbours are compared. In these simulations the viscous timescale is very long, and the gravitational timescale shows a wide variation over the computational domain. Two methods of improving the code's efficiency in such circumstances, multiple time stepping, and operator splitting, are discussed. In Chapter 5 the SPH code is tested against the axisymmetric disk solutions derived in Chapter 1.

Previous numerical studies of accretion disks in cataclysmic variables are reviewed in Chapter 6. Two simulations using an isothermal equation of state are discussed and compared in detail with the simulations of Whitehurst, and Hirose and Osaki. The incorporation of the 'blackbody' equation of state into the code is then discussed. Two blackbody simulations are then detailed. Comparisons are made with both isothermal simulation results and with observations.

In Chapter 7 the instability of a single ring of SPH particles is investigated. A linear analysis of the instability is presented and compared with numerical results. The results are summarised in Chapter 8.

Chapter 2.
The Theory of Thin Disks

2.1. Introduction

Current work on accretion disks has heavily relied upon the results of thin disk theory, developed in the early seventies by Shakura and Sunyaev (1973), Lynden-Bell and Pringle (1974), Lightman (1974 a) and others. Thin disk theory has been enormously successful in providing us with a first simple picture of accretion disks and their behaviour. With this in mind, this chapter summarises thin disk theory, highlighting the main assumptions and approximations. Key equations and results to be used in later chapters are derived here. The reader seeking a more comprehensive coverage of thin disk theory is referred to Pringle (1981) and Frank et al. .

The central assumption underlying thin disk theory is of course that the disk is geometrically thin. Specifically, at any radius r, the scale height of the disk $H(r) \ll r$. The assumption's basis is that gravity dominates pressure and viscous effects. In the next section we discuss this **thin disk approximation**, and its important consequence, that the radial and vertical structures of the disk are effectively decoupled. This enormously simplifies the task of modelling the disk. We then go on to develop the basic time dependent disk equations. The general time dependent solution is obtained and the evolution of a particular density distribution is outlined. The equations for stationary disks are obtained. We then discuss how viscous dissipation, critical to accretion disks, is treated with standard theory. Finally we examine the radiation expected from a disk. The decoupling of the radial and vertical disk structures make this relatively straightforward. We will look at the simplest case, where each element of the disk surface is assumed to radiate as a black body. This is used to determine the spectrum expected from disks around various astrophysical objects. The factors that determine an accretion disk's luminosity are discussed.

2.2. The Basic Equations

Consider a cylindrically symmetric gravitational potential $\Phi(r,z)$. The velocities of particles on circular orbits in this potential are given by

$$\frac{v_\phi^2}{r} = -\frac{\partial \Phi}{\partial r}. \tag{2.2.1}$$

If the potential is due to a point mass M,

$$\Phi(r,z) = -\frac{GM}{\sqrt{r^2+z^2}}, \tag{2.2.2}$$

where G is the gravitational constant. Circular orbits in this potential are said to be Keplerian and have velocity

$$v_\phi(r) = \sqrt{\frac{GM}{r}}, \tag{2.2.3}$$

where coordinates have been chosen so that the particle orbit lies in the $z=0$ plane.

Think now of a gaseous disk lying in the $z=0$ plane. Assume the pressure and viscous forces are small compared to the gravitational force in the plane. The disk can therefore be treated as geometrically thin. In this case the scale height of the disk at radius r, $H(r) \ll r$. With this assumption, motion in the z direction is neglected. The z component of the Navier-Stokes equation becomes an equation of hydrostatic support,

$$\frac{1}{\rho}\frac{\partial P}{\partial z} = \frac{\partial \Phi}{\partial z}, \tag{2.2.4}$$

where P is the gas pressure and ρ is the density. For the point mass potential

$$\frac{1}{\rho}\frac{\partial P}{\partial z} = -\frac{GMz}{(r^2+z^2)^{\frac{3}{2}}}. \tag{2.2.5}$$

We use Eq. (2.2.5) to say something about the scale height H. From our original assumption, $z \sim H \ll r$, giving

$$\frac{1}{\rho}\frac{\partial P}{\partial z} \simeq -\frac{GMH}{r^3}. \tag{2.2.6}$$

We make the approximation $\frac{\partial P}{\partial z} \sim -\frac{P}{H}$ with P now being the pressure on the central plane. We shall take it to be identical to the average pressure. The difference between the two quantities is not enough to affect this line of argument. We can then say $\frac{P}{\rho} \sim c^2$, where c is the local sound speed. We thus have

$$-\frac{c^2}{H} \sim -\frac{GMH}{r^3}. \tag{2.2.7}$$

We use Eq. (2.2.3) to find that

$$\frac{c^2}{H^2} \sim \frac{v_\phi^2}{r^2}, \tag{2.2.8}$$

and thus

$$\frac{r}{H} \sim \frac{v_\phi}{c}. \tag{2.2.9}$$

Thus the condition that the disk be geometrically thin is a requirement that the orbital velocity v_ϕ is highly supersonic. If this thin disk approximation holds then we can see that the pressure and temperature gradients will be largely vertical (i.e. out of the disk plane). Thus the local, vertical structure of the disk essentially becomes decoupled from the gross radial structure. We will return to this point later.

Viscous forces are much smaller in magnitude than the gravitational attraction of the central body. Nevertheless they are critical to the accretion process. Locally they have a dissipative effect on the gas, converting kinetic energy to radiation, circularising gas orbits in the process. On a disk-wide (one hesitates to say global) level, viscous forces are responsible for a net mass flux inwards through the disk and simultaneously for a net outwards flux of angular momentum. We obtain a time scale for this diffusive motion by examining the radial component of the Navier-Stokes equation

$$\frac{\partial v_r}{\partial t} + \ldots = \nu\frac{\partial^2 v_r}{\partial r^2}. \tag{2.2.10}$$

ν is the kinematic viscosity. Very approximately we have

$$\frac{v_r}{t_{visc}} \sim \nu\frac{v_r}{r^2}. \tag{2.2.11}$$

This gives a viscous time scale

$$t_{visc} \sim \frac{r^2}{\nu} \sim \frac{r^2}{c\lambda}, \tag{2.2.12}$$

with c being the sound speed and λ a length characteristic of the viscous motion. This length is restricted by the disk thickness, $\lambda \leq H \ll r$. The dynamical time scale

$$t_{dyn} \sim \frac{r}{v_\phi}. \tag{2.2.13}$$

Hence

$$\frac{t_{dyn}}{t_{visc}} \sim \frac{c\lambda}{v_\phi r} \ll 1. \tag{2.2.14}$$

The dynamical time scale is much shorter than the viscous time scale. The radial drift velocity

$$v_r \sim \frac{r}{t_{visc}}, \tag{2.2.15}$$

and hence $v_r \ll v_\phi$.

As we proceed to describe the radial structure of the disk we shall characterise the disk at radius r by an integrated column density (or mass per unit disk area)

$$\Sigma(r,t) = \int_{-\infty}^{\infty} \rho(z,r,t)\, dz. \tag{2.2.16}$$

A cylindrically symmetric disk is described by three equations; the mass conservation equation

$$r\frac{\partial \Sigma}{\partial t} + \frac{\partial}{\partial r}(r\Sigma v_r) = 0, \tag{2.2.17}$$

the angular momentum conservation equation

$$r\frac{\partial}{\partial t}\left(\Sigma r^2 \Omega\right) + \frac{\partial}{\partial r}\left(r\Sigma v_r r^2 \Omega\right) = \frac{1}{2\pi}\frac{\partial \mathcal{G}}{\partial r}, \tag{2.2.18}$$

and the radial component of the Navier-Stokes equation

$$\frac{\partial v_r}{\partial t} + v_r\frac{\partial v_r}{\partial r} - \Omega^2 r + \frac{\partial \Phi}{\partial r} - \nu\frac{\partial^2 v_r}{\partial r^2} = 0, \tag{2.2.19}$$

Note that we have written Eq. (2.2.19) in a form that assumes ν is constant or slowly varying. In fact the functional form of the viscosity is not yet known. We discuss the viscosity in Section 2.5 . $\Omega = v_\phi / r$ is the angular speed of rotation of the gas. $\mathcal{G}(r,t)$, the viscous torque exerted by a disk annulus at radius r on the gas inside it, is given by

$$\mathcal{G} = 2\pi r \nu \Sigma r^2 \frac{\partial \Omega}{\partial r}. \tag{2.2.20}$$

Let us substitute Eq. (2.2.20) into Eq. (2.2.18) and assume for the moment that the functional form of ν is known. We find we have three equations in three variables; the surface density, the radial velocity, and the angular velocity. It is now that a key assumption is made. In standard thin disk theory Eq. (2.2.19) is replaced by Eq. (2.2.1). As a consequence the angular velocity is found to be independent of time and a function of r only. We are left with the much simpler problem of solving two equations, Eq. (2.2.17) and Eq. (2.2.18), in two variables, Σ and v_r. As our original assumption was that pressure and viscous forces are small compared to the gravitational force in the plane this seems a reasonable thing to do. It severely limits us however. We will find that the radial velocity is completely specified by the density profile. Physically this is unacceptable. For it to be otherwise we must let Ω be time dependent. This point is illustrated in Chapter 4. For the moment, as we are reviewing standard theory, we shall assume that the angular velocity is given by Eq. (2.2.1). Combination of Eq. (2.2.17), Eq. (2.2.18) and Eq. (2.2.20) yields a partial differential equation for the surface density,

$$\frac{\partial \Sigma}{\partial t} = -\frac{1}{r}\frac{\partial}{\partial r}\left(\frac{1}{\frac{d}{dr}\left(r^2\Omega\right)}\frac{\partial}{\partial r}\left(r^3 \nu \Sigma \frac{d\Omega}{dr}\right)\right). \tag{2.2.21}$$

To proceed much further we need the functional forms of the viscosity, and of the rotational velocity. Lynden-Bell and Pringle (1974) solved Eq. (2.2.21) for the general case where both ν and Ω varied as powers of r. They then applied this to two particular cases; one where the rotation curve is due to a point mass and we have Keplerian rotation

$$\Omega = \sqrt{\frac{GM}{r^3}}, \tag{2.2.22}$$

and a second where the azimuthal velocity is a constant, V_0, and the angular velocity

$$\Omega = \frac{V_0}{r}. \tag{2.2.23}$$

This second velocity relation occurs for a self gravitating disk that has surface density inversely proportional to the radius, known as a Mestel disk (Binney and Tremaine, 1987). The viscosity was, for simplicity's sake, assumed to be constant. For both rotation curves Lynden-Bell and Pringle wrote down the stationary solution for the density. They then determined the evolution of the surface density for an initial distribution

$$\Sigma\left(r,0\right) = \frac{1}{2\pi r_1}\,\delta\left(r-r_1\right), \tag{2.2.24}$$

where δ is the Dirac delta function. In this chapter we are primarily concerned with Keplerian disks, so we will continue assuming Eq. (2.2.22) holds. Thus Eq. (2.2.21) reduces to

$$\frac{\partial\Sigma}{\partial t} = \frac{3}{r}\frac{\partial}{\partial r}\left(r^{1/2}\frac{\partial}{\partial r}\left(r^{1/2}\nu\Sigma\right)\right), \tag{2.2.25}$$

which is clearly a diffusion equation for the density. Eq. (2.2.25) tells us that the rate at which matter diffuses in a Keplerian disk is independent of the mass of the central accreting object, depending only upon the viscosity and the existing density distribution. Of course the true functional nature of the viscosity is as yet unknown. It could prove to be dependent upon v_ϕ and hence upon the central body's mass. For the moment we shall note that there is no strong theoretical basis for choosing any one form for the viscosity over any other. Hence we choose the simplest option and assume ν is constant. In this case Eq. (2.2.25) becomes

$$\frac{\partial\Sigma}{\partial t} = \frac{3\nu}{r}\frac{\partial}{\partial r}\left(r^{1/2}\frac{\partial}{\partial r}\left(r^{1/2}\Sigma\right)\right). \tag{2.2.26}$$

We will follow the solution of this equation in a little detail, as we will require the results later for tests of our numerical simulations. We make a change of variable $s = 2r^{\frac{1}{2}}$, giving

$$\frac{\partial\left(s\Sigma\right)}{\partial t} = \frac{12\nu}{s^2}\frac{\partial^2\left(s\Sigma\right)}{\partial s^2}. \tag{2.2.27}$$

This is solved using separation of variables. Let

$$s\Sigma\left(s,t\right) = S\left(s\right)T\left(t\right), \tag{2.2.28}$$

which, on substitution in Eq. (2.2.27) gives

$$\frac{1}{T}\frac{dT}{dt} = \frac{12\nu}{s^2 S}\frac{d^2S}{ds^2} = -\lambda^2, \tag{2.2.29}$$

where λ is a constant. The solution for the density is

$$\Sigma\left(r,t\right) = \frac{e^{-\lambda^2 t}}{r^{\frac{1}{4}}}\left(C_1 J_{\frac{1}{4}}\left(\frac{\lambda r}{\sqrt{3\nu}}\right) + C_2 J_{-\frac{1}{4}}\left(\frac{\lambda r}{\sqrt{3\nu}}\right)\right), \tag{2.2.30}$$

where $J_\nu(x)$ is a Bessel function of the first kind, and C_1 and C_2 are constants of integration. The general solution is a linear superposition of these basis functions. We find

$$\Sigma(r,t) = \int_0^\infty \frac{e^{-\lambda^2 t}}{r^{\frac{1}{4}}} \left(C_1(\lambda) J_{\frac{1}{4}}\left(\frac{\lambda r}{\sqrt{3\nu}}\right) + C_2(\lambda) J_{-\frac{1}{4}}\left(\frac{\lambda r}{\sqrt{3\nu}}\right)\right) d\lambda. \tag{2.2.31}$$

C_1 and C_2 are now functions of λ. They are determined by the initial density distribution $\Sigma(r,0)$ and by a boundary condition at the inner edge of the disk. We will discuss the boundary condition in Section 2.4. At the moment, however, we will consider density distributions which do not come into contact with the central accreting body, being more concerned with the viscous evolution of a density distribution rather than a full time dependent disk solution. As $x \to 0$, $J_{-1/4}(x) \propto x^{-\frac{1}{4}}$. Thus to avoid unbounded behaviour of the solution at small radii we set $C_2 = 0$, to obtain

$$\Sigma(r,t) = \frac{1}{r^{1/4}} \int_0^\infty C(\lambda)\, e^{-\lambda^2 t} J_{1/4}\left(\frac{\lambda r}{\sqrt{3\nu}}\right) d\lambda. \tag{2.2.32}$$

$C(\lambda)$ is now determined purely by the initial density distribution. Setting $t = 0$ and applying a Hankel transformation we find

$$C(\lambda) = \frac{\lambda}{3\nu} \int_0^\infty r'^{5/4}\, \Sigma(r',0)\, J_{1/4}\left(\frac{\lambda r'}{\sqrt{3\nu}}\right) dr'. \tag{2.2.33}$$

We have called the dummy variable r' to distinguish it from the radius r in Eq. (2.2.32). As Lynden-Bell and Pringle did we will find the system's response to a delta function density distribution

$$\Sigma(r,0) = \Sigma_0\, \delta(r - r_0). \tag{2.2.34}$$

Where Σ_0 and r_0 are constants. In this case

$$C(\lambda) = \frac{\lambda}{3\nu} \Sigma_0\, r_0^{5/4}\, J_{1/4}\left(\frac{\lambda r_0}{\sqrt{3\nu}}\right), \tag{2.2.35}$$

and the density distribution at time t is given by

$$\Sigma(r,t) = \frac{\Sigma_0 r_0^{5/4}}{6\nu t r^{1/4}} e^{-\frac{(r_0^2 + r^2)}{12\nu t}} I_{1/4}\left(\frac{r_0 r}{6\nu t}\right). \tag{2.2.36}$$

$I_{1/4}(x)$ is a modified Bessel function of the first kind. As Eq. (2.2.26) is linear in Σ we can obtain from the system's delta function response, the solution for a general initial density distribution

$$\Sigma(r,0) = \Sigma_0(r). \tag{2.2.37}$$

Our general solution for the density is then

$$\Sigma(r,t) = \frac{1}{6\nu t r^{1/4}} \int_0^\infty \Sigma_0(r')\, r'^{5/4} e^{-\frac{(r'^2 + r^2)}{12\nu t}} I_{1/4}\left(\frac{r' r}{6\nu t}\right) dr'. \tag{2.2.38}$$

We can verify Eq. (2.2.38) by substituting Eq. (2.2.33) for $C(\lambda)$ in Eq. (2.2.32) to get

$$\Sigma(r,t) = \frac{1}{r^{1/4}} \int_0^\infty \frac{\lambda}{3\nu} e^{-\lambda^2 t} J_{1/4}\left(\frac{\lambda r}{\sqrt{3\nu}}\right) \int_0^\infty r'^{5/4}\, \Sigma(r',0)\, J_{1/4}\left(\frac{\lambda r'}{\sqrt{3\nu}}\right) dr'\, d\lambda. \tag{2.2.39}$$

We substitute Eq. (2.2.37) into Eq. (2.2.39) and reverse the order of the integrals to obtain

$$\Sigma(r,t) = \frac{1}{3\nu r^{1/4}} \int_0^\infty r'^{5/4}\, \Sigma_0(r') \int_0^\infty \lambda J_{1/4}\left(\frac{\lambda r'}{\sqrt{3\nu}}\right) J_{1/4}\left(\frac{\lambda r}{\sqrt{3\nu}}\right) e^{-\lambda^2 t} d\lambda\, dr'. \tag{2.2.40}$$

Now from a table of integrals (Gradshteyn and Ryzhick, 1965, equation 6.633.2) we find that

$$\int_0^\infty \lambda J_{1/4}\left(\frac{\lambda r'}{\sqrt{3\nu}}\right) J_{1/4}\left(\frac{\lambda r}{\sqrt{3\nu}}\right) e^{-\lambda^2 t} d\lambda = \frac{1}{2t} e^{-\frac{\left(r'^2+r^2\right)}{12\nu t}} I_{1/4}\left(\frac{r'r}{6\nu t}\right). \tag{2.2.41}$$

Substituting Eq. (2.2.41) in Eq. (2.2.40) we once more obtain Eq. (2.2.38).

As mentioned previously, the assumption that the angular velocity is given by Eq. (2.2.1) means that the radial velocity profile $v_r(r,t)$ is determined by the surface density. If we return to Eq. (2.2.17) and Eq. (2.2.18), and assume that ν is constant and that Ω is Keplerian, we find that

$$v_r\left(r,t\right) = -3\nu \frac{\partial}{\partial r} \ln\left(r^{\frac{1}{2}} \Sigma\left(r,t\right)\right). \tag{2.2.42}$$

Thus for the initial density distribution $\Sigma_0(r)$

$$v_r\left(r,0\right) = -3\nu \frac{\partial}{\partial r} \ln\left(r^{\frac{1}{2}} \Sigma_0\right). \tag{2.2.43}$$

We will use Eq. (2.2.43) to set up our simulations in Chapter 4.

2.3. A Specific Example

In this section we take Eq. (2.2.38), the general equation for the density derived in section 1.2, and apply it to a specific extended initial density distribution. We do this, rather than just considering the system's delta function response as Lynden-Bell and Pringle (1974) did, for two reasons. Firstly we find out how useful Eq. (2.2.38) is for determining the evolution of disks as compared to, say, numerically integrating Eq. (2.2.26). Secondly, we need theoretical results with which to test and calibrate the numerical code used in this study.

Specifically we now consider the solution of Eq. (2.2.38) for the initial density distribution

$$\Sigma_0\left(r\right) = \begin{cases} \Sigma_0 & r_1 < r < r_2 \\ 0 & elsewhere \end{cases}. \tag{2.3.1}$$

r_1 and r_2 are constants. Substitution of Eq. (2.3.1) into Eq. (2.2.38) gives

$$\Sigma\left(r,t\right) = \frac{\Sigma_0}{6\nu t r^{1/4}} \int_{r_1}^{r_2} r'^{5/4} e^{-\frac{\left(r'^2+r^2\right)}{12\nu t}} I_{1/4}\left(\frac{r'r}{6\nu t}\right) dr'. \tag{2.3.2}$$

This is not in a very useful form. For large arguments however, we can make the approximation

$$I_{1/4}(x) \simeq \frac{e^x}{\sqrt{2\pi x}} \qquad\qquad x \gg 1. \tag{2.3.3}$$

So, provided $\frac{r'r}{6\nu t} \gg 1$, or $t_{visc}/t \gg 1$ where

$$t_{visc} = \frac{r'r}{6\nu}, \tag{2.3.4}$$

we can write

$$\Sigma\left(r,t\right) = \frac{\Sigma_0}{r^{3/4}\sqrt{12\nu t\pi}} \int_{r_1}^{r_2} r'^{3/4} e^{-\frac{\left(r'-r\right)^2}{12\nu t}} dr'. \tag{2.3.5}$$

Fig. 2.3.1 shows an example calculation with $\Sigma_0 = 1$, $r_1 = 0.25$ and $r_2 = 0.35$. The density is plotted as a function of the radius for $0.1 < r < 0.5$. The plot was not continued to smaller radii as approximation

(2.3.3) breaks down there first. Density profiles for $\nu t = 1.0 \times 10^{-6}, 1.0 \times 10^{-5}, 2.0 \times 10^{-4}$ and 5.0×10^{-4} are shown.

The plot was generated using *Mathematica*. Initially we tried to evaluate Eq. (2.3.2) directly with *Mathematica* but the equation proved too obnoxious. For this reason we used Eq. (2.3.5). In practice we replaced $r_0^{3/4}$ in Eq. (2.3.5) with a tenth order Taylor polynomial centred at $r_0 = r$. This improved the speed of the calculation with no discernible effect on the results. Fig. 2.3.2 was produced in the same manner as Fig. 2.3.1. The same values for constants and initial conditions were used. The three density curves, for $\nu t = 5.0 \times 10^{-4}, 6.0 \times 10^{-4}$ and 7.0×10^{-4}, are plotted on a domain $0.05 < r < 0.5$. They are included to illustrate the behaviour of Eq. (2.3.5) when $\frac{r_1 r}{6\nu t}$ is no longer much greater than one. The density curve looks reasonable for larger radii, however at the inner edge of the plots the density becomes very large. Obviously this is not what should be happening here. We are instead seeing the consequences of the breakdown of approximation (2.3.3).

2.4. Steady State Disks and Boundary Conditions

We shall now consider a disk that has reached steady state. The equation of mass conservation Eq. (2.2.17) becomes

$$(r\Sigma v_r)' = 0 \tag{2.4.1}$$

with the dash indicating the radial derivative. This just states that the mass flow rate $\dot{m}$ is constant and given by

$$\dot{m} = 2\pi r \Sigma v_r. \tag{2.4.2}$$

The equation of angular momentum conservation Eq. (2.2.18) becomes

$$\left(r^3 \Sigma v_r \Omega\right)' = \frac{1}{2\pi}\mathcal{G}'. \tag{2.4.3}$$

Integrating and using Eq. (2.4.2) gives

$$\dot{m}\Omega r^2 - \mathcal{G} = K. \tag{2.4.4}$$

This equation states that the total flux of angular momentum, K, due to mass flow and viscous torques is constant. Substituting for the torque, using Eq. (2.2.20), and rearranging gives

$$\nu\Sigma\Omega' = \frac{\dot{m}}{2\pi r^3}\left(r^2\Omega - L\right), \tag{2.4.5}$$

where $L = \frac{K}{\dot{m}}$ is also a constant.

Now is a suitable time to discuss the inner boundary, where the disk meets the central accreting object. We will assume this object is a star as we are primarily interested in stellar disks. So we define the variable

$$\Omega_k(r) = \sqrt{\frac{GM}{r^3}}. \tag{2.4.6}$$

In other words $\Omega_k(r)$ is the Keplerian angular velocity at radius r. Now if the central star has radius r_*, and rotates with angular velocity Ω_*, then we have a no slip boundary condition

$$\Omega(r) = \Omega_* \qquad\qquad r = r_*. \tag{2.4.7}$$

Now, in practise, Ω_* must be less than $\Omega_k(r_*)$ or the star would break up. If the angular velocity of the disk gas, $\Omega(r)$, is a smooth, continuous function, we then require

$$\frac{d\Omega}{dr} = 0 \qquad\qquad r = r_b \tag{2.4.8}$$

for some radius r_b. The hypothesis is that $\frac{r_b - r_*}{r_*} \ll 1$ and the disk rotational velocity is Keplerian right down to a narrow boundary layer around the star. Now the torque $\mathcal{G} \propto \Omega'$ and so $\mathcal{G} = 0$ at $r = r_b$. If we substitute this into Eq. (2.4.4) we find

$$K = \dot{m}\Omega_b r_b^2, \tag{2.4.9}$$

where Ω_b is the angular velocity of the gas at r_b. Substituting Eq. (2.4.9) into Eq. (2.4.5) gives

$$\nu\Sigma\Omega' = \frac{\dot{m}}{2\pi r^3}\left(r^2\Omega - r^2\Omega_b\right) \tag{2.4.10}$$

In order to obtain a solution for the density, we must now make some assumptions about the angular velocity of the gas. The standard argument at this point (e.g. Frank et al., 1991) is to suggest that the boundary layer is very thin and so to a good approximation

$$\Omega\left(r\right) \sim \Omega_k\left(r\right) \qquad\qquad r = r_b. \tag{2.4.11}$$

Thus Eq. (2.4.10) becomes

$$\nu\Sigma\Omega' = \frac{\dot{m}\left(GM\right)^{\frac{1}{2}}}{2\pi r^3}\left(r^{\frac{1}{2}} - r_b^{\frac{1}{2}}\right). \tag{2.4.12}$$

What is simultaneously done is to substitute $\Omega'(r) = \Omega'_k(r)$ into Eq. (2.4.10) to give

$$\nu\Sigma = -\frac{\dot{m}}{3\pi}\left(1 - \left(\frac{r_b}{r}\right)^{\frac{1}{2}}\right) \tag{2.4.13}$$

This step is justifiable for most of the disk where the gas orbits are Keplerian. At the inner edge however, this is not so. Our boundary condition was $\Omega'(r_b) = 0$ which is inconsistent with $\Omega'(r) = \Omega'_k(r)$. Not surprisingly Eq. (2.4.13) gives the spurious result $\nu\Sigma = 0$ at r_b. If the viscosity is nonzero here, then the implication is that the density goes to zero at r_b. Eq. (2.4.2) then implies that the radial velocity $v_r \to \infty$ here. This is all to say that there is an important caveat on the use of Eq. (2.4.13), that it cannot be used close to the inner edge of the disk. There we must use Eq. (2.4.12). This requires better knowledge of the behaviour of $\Omega(r)$ in this region, which in turn requires a better knowledge of the physics of the boundary layer. Using Eq. (2.4.7) rather than Eq. (2.4.8) as the boundary condition would not have avoided this problem.

So what is happening in the boundary layer? In the Keplerian region of the disk the radial component of the Navier Stokes equation

$$v_r\frac{\partial v_r}{\partial r} - \frac{v_\phi^2}{r} + \frac{1}{\rho}\frac{\partial P}{\partial r} + \frac{GM}{r^2} - \nu\nabla^2 v_r = 0 \tag{2.4.14}$$

reduces to a balance between the gravity and centrifugal forces, the other terms being much smaller. As we approach the central star, Ω decreases from its Keplerian value and the centrifugal term no longer balances gravity. The deficit must be made up by one of the viscous, inertial or pressure terms. Examples of recent attempts to numerically simulate the boundary layer are Paczyński (1991), Popham and Narayan (1991), Kley (1989), and Kley (1991). Paczyński assumed the pressure term balanced the centrifugal deficit. Popham and Narayan used a slightly different model and found inertial forces making up the deficit. To do this supersonic radial velocities were required. These are not favoured (Pringle 1977, Glatzel 1992) as information from the star cannot be propagated outwards against the supersonic flow to the Keplerian disk. Kley favoured the viscous term. This would also require supersonic velocities and is similarly controversial.

The situation is summarised by Glatzel (1992). After discussing various estimates of boundary layer thickness, he solved the azimuthal component of the steady state Navier-Stokes equation for v_ϕ. He found that a boundary layer could not exist if the dynamical viscosity η were constant. A variable viscosity however, could produce a boundary layer. He again solved the Navier-Stokes equation assuming a variable viscosity to find an η and a v_ϕ that have the desired behaviour with $v_\phi(r_*) = v_*$ and $v_\phi(r) \to v_k(r)$ for $r > r_b$, where $v_k(r) = r\Omega_k(r)$ is the Keplerian azimuthal velocity at radius r. The point is that the common use in the literature of the very simple boundary condition Eq. (2.4.8) hides a lot of detail and an issue that is far from resolved.

Observationally, it is important to know what is going on in the boundary layer as approximately half of all the gravitational energy liberated by the disk, is released in that narrow region. It is expected to be very hot and to be the source of high energy radiation. The rest of the disk will be much cooler and so radiate at much longer wavelengths. Depending upon the particular accretion disk system being examined, there may be a problem separating the disk signal from the boundary layer radiation.

From a disk theorist's point of view, how important is the boundary layer? Do the assumptions made about this narrow region affect the predictions of thin disk theory for the whole disk? The short answer is no. The only input the boundary layer has into the equations is to determine the constant in Eq. (2.4.4) or Eq. (2.4.5). It does not affect the functional form of the steady state disk equations. None of the numerical simulations have found Eq. (2.4.8) to be unreasonable, so we can carry on and use Eq. (2.4.13), provided we keep in mind its spurious behaviour for small radii.

The rate at which mechanical energy is dissipated, per unit surface area is

$$D\left(r\right) = \frac{\mathcal{G}\Omega'}{4\pi r}, \tag{2.4.15}$$

noting that the disk has two surfaces. With $\mathcal{G}$ given by Eq. (2.4.4) and assuming Keplerian rotation,

$$D\left(r\right) = \frac{3GM\dot{m}}{8\pi r^3}\left[1 - \left(\frac{r_b}{r}\right)^{\frac{1}{2}}\right]. \tag{2.4.16}$$

In the steady state disk, this energy must be removed at the same rate. As mentioned earlier, the thin disk approximation implies that temperature and pressure gradients will be essentially vertical and heat will be removed in this direction. Thus $D(r)$ will be the source term in any one dimensional energy transport calculation. It should be noted that although $D(r)$ gives the total heat energy generated at a given radius, it gives no indication of the vertical distribution of this heat generation, information that is important for any such energy calculation. To gain an idea of where the dissipation is taking place, we require a knowledge of the viscous mechanism.

2.5. The Viscous Dissipation

Just as the tin man in *The Wizard of Oz* lamented "if I only had a heart", so might we cry " if we only knew the dissipative mechanism". Continuing the analogy, observation found the tin man had feelings and so it was deduced that he must have had a heart. Similarly, disk observations can be explained with a viscous model, which implies the existence of a dissipative mechanism.

Shakura and Sunyaev (1972) focussed attention on possible causes for the dissipation and then condensed the uncertainty into a single dimensionless parameter, α, in the equation for the shear stress between neighbouring annuli of the disk

$$\omega_{r\theta} = \alpha\rho c^2, \tag{2.5.1}$$

and found that $\alpha < 1$. We will briefly discuss the various mechanisms they looked at. The most obvious candidate is the molecular viscosity

$$\nu_{mol} \sim c\lambda, \tag{2.5.2}$$

where c is the sound speed and λ the molecular mean free path. Substitution of typical values for c and λ yields a viscosity that is orders of magnitude too small to account for the dissipation observed in accretion disks.

The next possibility stems from the likelihood that gas flow in disks is turbulent. If that is so, then on length scales larger than that of the turbulent eddies, the effect will mimic a kinematic viscosity given by

$$\nu_{turb} \sim VL. \tag{2.5.3}$$

Here V and L are a velocity and length respectively that are characteristic of the turbulence. Physically, the eddies cannot be larger than the scale height of the disk so $L \sim H(r)$. Furthermore the turbulent flows will be subsonic so $V < c$. This leads to the most commonly stated form of the α parametrisation

$$\nu = \alpha c H \tag{2.5.4}$$

where $\alpha = \frac{V}{c} < 1$. This is often written as

$$\nu = \alpha \frac{c^2}{\Omega} \tag{2.5.5}$$

where we have used Eq. (2.2.9) to substitute for the scale height. Thus "turbulence" is often cited as a possible mechanism. The next problem is then to identify the process by which the flow could become turbulent. We discuss this at the end of the section.

Many accretion flows are dominated by magnetic fields so that rather than a disk being formed, the flow is radial and along magnetic field lines. To see whether magnetic fields dominate the accretion geometry, we compare the energy density of the magnetic field $\frac{B^2}{2\mu}$ to the kinetic energy density $\frac{1}{2}\rho v^2$ and to the thermal energy density $\frac{1}{2}\rho c^2$. The flow régime is determined by the ratio of these three quantities. It is easiest to define the Alfvén velocity v_A by

$$\rho v_A^2 = \frac{B^2}{2\mu}, \tag{2.5.6}$$

giving

$$v_A = \frac{B}{\sqrt{2\mu\rho}}. \tag{2.5.7}$$

We can directly compare the Alfvén, sound and gas speeds to determine whether magnetic fields dominate the flow. In the accretion disk régime, we are starting with the assumption that the magnetic field does not dominate the flow and so $v_A < c < v_\phi$.

Shakura and Sunyaev assumed that any magnetically induced shear stresses in the flow would be proportional to the magnetic energy density

$$\begin{aligned} \omega_{r\theta} &\sim \frac{B^2}{2\mu} \\ &= \rho c^2 \left(\frac{v_A}{c}\right)^2 \\ &= \alpha \rho c^2. \end{aligned} \tag{2.5.8}$$

$\alpha = (\frac{v_A}{c})^2$ is again expected to be less than unity for the reasons outlined above.

When the steady disk equations are taken, together with the α parametrisation of the viscosity, the result is the **steady α-disk model**, which has become the standard starting point for disk analysis.

As it stands, the discussion is rather sterile as we do not know what the fundamental cause of the viscous dissipation is. That may be about to change. Balbus and Hawley (1991) found that any disk that differentially rotated with an angular velocity that decreased with increasing radius, was dynamically unstable in the presence of a weak magnetic field. We paraphrase their explanation of the instability.

Take a differentially rotating disk that is threaded by a (weak) magnetic field running perpendicular to the disk plane. Take one 'parcel' of the disk gas and displace it radially outwards. In addition to the nonmagnetic forces it feels, the parcel will be subject to two magnetic forces. Firstly, the magnetic field will resist being stretched by the displacement of the fluid, and so will exert a restoring force upon the parcel.

But the field will also try to force rigid rotation upon the disk, and so will act to accelerate the parcel. The displaced parcel of fluid will find its azimuthal velocity is too high for its new radius and so will move further outwards. When the latter force is greater, instability results.

The original paper (Balbus and Hawley 1991) outlined a linear analysis of the instability. In the second paper (Hawley and Balbus 1991) they presented a two dimensional numerical study of the instability, verifying the linear analysis and then considering the nonlinear evolution. Hawley and Balbus (1992) performed three dimensional simulations of a small region of the disk. They found that the instability generated turbulent motion, and that angular momentum was transported radially outwards through the disk.

This then is a very promising candidate to be the viscosity mechanism. There is hope that it may soon be incorporated into thin disk theory in a manner consistent with the Shakura-Sunyaev parameterisation.

Goodman (1993) found a local three dimensional instability in disks that are tidally distorted by say a low mass companion to the star at the centre of the disk. Goodman's work followed Pierrehumbert's (1986) discovery that an infinite, incompressible elliptical flow was unstable. Goodman proposed that his instability, through modification of the disk flow, could cause angular momentum transfer to the source of the tidal field. The instability's potential as a viscosity mechanism has not yet been examined in detail. The Goodman instability would appear to be a less likely candidate than the Balbus-Hawley one because it requires a tidal potential. However it is quite possible that both may be important in the case of accretioon disks in cataclysmic variables for example.

2.6. Radiation from the Disk

In this section we obtain a first order picture of the radiation produced by a steady state disk. To do this we will make the simplest possible assumption, that the disk is optically thick and that elements of the surface radiate like blackbodies. This will give us an order of magnitude idea of the radiative signature of the disk.

From the thin disk assumption, the temperature gradient at any radius r in the disk is essentially vertical. The heat energy generated by viscous action $D(r)$ must be removed at an equal rate, by radiative or convective processes, **in the z direction**. The assumption is made that heat is removed radiatively and that the disk is optically thick, i.e. that the viscous action is taking place at infinite optical depth. This lets us write the equation

$$D\left(r\right) = \sigma T^4, \tag{2.6.1}$$

where σ is the Stephan-Boltzmann constant and $T(r)$ is the disk temperature at radius r.

The reality is that the viscous dissipation mechanism is unknown. It could involve turbulent motion on length scales similar to the scale height of disk H. The energy release is then not necessarily going to take place at infinite optical depth. The optically thick disk approximation may not be an entirely accurate one. Further complicating the picture would be any significant atmosphere lying above the disk plane. This would serve to reprocess the disk radiation, reemitting it at longer wavelengths. With these thoughts in mind we shall continue with our optically thick disk.

Using Eq. (2.4.16) we find the temperature as a function of the radius

$$T\left(r\right) = \left(\frac{3GM\dot{m}}{8\pi r^3\sigma}\left(1-\sqrt{\frac{r_*}{r}}\right)\right)^{\frac{1}{4}}. \tag{2.6.2}$$

For $r \ll r_*$ we find

$$\begin{aligned} T\left(r\right) &\simeq \left(\frac{3GM\dot{m}}{8\pi r^3\sigma}\right)^{\frac{1}{4}} \qquad (2.6.3) \\ &\simeq 0.588\left(\frac{GM\dot{m}}{r^3\sigma}\right)^{\frac{1}{4}}. \end{aligned}$$

We see that $T(r)$ has a maximum value at $r = \frac{49}{36} r_*$

$$T_{max} = \left(\frac{3GM\dot{m}}{56\pi\sigma r_*^3} \left(\frac{6}{7}\right)^6 \right)^{\frac{1}{4}} \tag{2.6.4}$$
$$\simeq 0.287 \left(\frac{GM\dot{m}}{r_*^3 \sigma} \right)^{\frac{1}{4}} .$$

We should view Eq. (2.6.2) with suspicion near $r = r_*$ as it relies upon Eq. (2.4.13) whose validity does not extend into the boundary layer. Witness the temperature $T = 0$ at $r = r_*$. In this region the thin disk approximation is in doubt. As discussed previously, significant radial pressure and temperature gradients are postulated for this region with the result that the radial and vertical structures are not decoupled here. T_{max} of Eq. (2.6.4) does however provide some indication of the temperature of the inner edge of the Keplerian disk.

It is important to note the dependence of the blackbody disk temperature upon the radius and upon the mass transfer rate. $T(r)$ is proportional to $r^{-\frac{3}{4}}$ and to $\dot{m}^{\frac{1}{4}}$. The greater the mass flow through the disk, the more dissipation will occur and the hotter the disk will be. Yet T is only a weak function of $\dot{m}$. A one hundredfold increase in $\dot{m}$ will only result in a threefold increase in the temperature. A one hundred fold increase in the radius, on the other hand, reduces the temperature by a factor of thirty. Let us now apply this theory to a specific case, an accretion disk around a white dwarf. We take it to be a one solar mass object of radius $r_* = 10^9$ cm. We will consider the disk to extend from the surface of the white dwarf out to a radius of 10^{11} cm. The mass transfer rate $\dot{m} = 10^{-8}\, M_\odot\, yr^{-1}$. The resulting temperature profile is plotted in Fig. 2.6.1. With this choice of parameters the disk has a maximum temperature $T_{max} \sim 5.6 \times 10^4$ K. At the outer edge of the disk the temperature has dropped to 4000 K. We now use Wien's law

$$\lambda_{max} T = 0.29 \,\mathrm{cm\,K} \tag{2.6.5}$$

to find the wavelength of maximum emission, λ_{max}, for these temperatures extremes. for $T = T_{max}$ we find $\lambda_{max} \sim 5.2 \times 10^{-6}$cm, meaning the hot inner region of the disk radiates most strongly in the ultraviolet – soft X-ray region of the spectrum. For the cool outer disk $\lambda_{max} \sim 8.0 \times 10^{-5}$cm so we expect strongest radiation in the longer wavelength region of the ultraviolet.

We would therefore expect an accretion disk with a white dwarf at the center to radiate at energies up to the soft X-ray, extending down through the ultraviolet and the visible to the infrared. By comparison, if the central object were a neutron star ($r_* = 10^{-6}$cm) or a black hole we should expect radiation up to X-ray and perhaps γ-ray energies. For an accreting main sequence star with r_* orders of magnitude larger than for a white dwarf, the disk would only shine at frequencies up to the low ultraviolet. The question is then, would we be able to distinguish disk radiation from that of the central object. We see that this will depend upon the compactness of the central object in relation to its luminosity.

Chapter 3.
Cataclysmic Variables

3.1. The Classification of Close Binary Systems

Stars in binary systems with short orbital periods (less than a few days) tend to have circular orbits and, unless they are degenerate, to rotate synchronously with each other (Shu, 1982). These **close binaries** are classified according to a system devised by Kopal.

Take two stars, mass m_1 (henceforth known as the primary) and m_2 (the secondary), in circular orbit about one another with orbital speed Ω. Assume they are sufficiently centrally condensed to be well approximated by point masses. In what follows we will choose units so that the total system mass $m = m_1 + m_2$, the interstellar separation d, and Ω are all equal to one (as in Lin & Pringle, 1976). Thus the primary has reduced mass

$$\mu = \frac{m_1}{(m_1 + m_2)} \tag{3.1.1}$$

and the secondary has reduced mass $1 - \mu$.

Select a set of coordinates rotating with the binary, with origin at the system's centre of mass and the primary along the positive x axis at $(1 - \mu, 0, 0)$. The secondary is then at $(-\mu, 0, 0)$. A stationary test particle in this frame experiences a centrifugal force as well as the gravitational attraction of the two stars. This force can be written as the gradient of a potential function Φ_R (the Roche potential) given by

$$\begin{aligned} \Phi_R\,(x, y, z) &= -\tfrac{1}{2}\left(x^2 + y^2\right) - \frac{\mu}{r_1} - \frac{(1-\mu)}{r_2} \\ r_1^2 &= (x + \mu - 1)^2 + y^2 + z^2 \\ r_2^2 &= (x - \mu)^2 + y^2 + z^2 \end{aligned} \tag{3.1.2}$$

Level surfaces of Φ_R are termed Roche equipotentials. The pressure in the two stars will be constant over these. Near either star, the Roche equipotentials are, to a good approximation, concentric spheres centred on that star. Further away, the spheres become distorted into ellipsoids with the major axis along the binary axis. Eventually a level surface about one star is reached that just meets an equivalent surface about the other star. These two critical equipotentials are termed Roche lobes. Further out, the equipotentials surround both stars. The two Roche lobes meet at L_1, the inner Lagrangian point. L_1 is a stationary point of the potential (i.e. a point where $\vec{\nabla}\Phi_R = 0$). In other words, a particle stationary at L_1 would experience no net force. Fig. 3.1 is a contour map of the $z = 0$ plane of Φ_R for a binary with $\mu = 0.85$. As well as plotting the equipotentials, we have used colour to indicate the value of Φ_R around the plane.

Binary systems are categorised according to the size of the two stars relative to their respective Roche lobes as follows:

- **Detached Binaries** The photospheres of both stars lie within their Roche lobes.
- **Contact Binaries** Both stars fill their Roche lobes.
- **Semidetached Binaries** One star fills its Roche lobe whilst the other does not.

3.2. Cataclysmic Variables

The term cataclysmic variable was first used by Kraft (1963) in a paper that showed that several eruptive variable stars were actually binaries with very short orbital periods. Nowadays a cataclysmic variable is defined as being a semidetached binary system with the detached component being a white dwarf. The Roche lobe filling companion is generally a low-mass star (0.1 to $1M_{\odot}$) on or near the main sequence. In discussions of binary systems, depending on one's viewpoint, the more interesting star is referred to as the primary, and the companion as the secondary. In this work, references to the primary are always to the white dwarf.

All cataclysmic variables undergo considerable brightness variations over time. They are categorised according to their observed behaviour into the following classes

- **Novae** Cataclysmic variables distinguished by having undergone at least one nova outburst. During such an event, the system's visual magnitude increases by 8 to 15 magnitudes over a few hours or days. The brightness then decays back to the quiescent magnitude with a timescale of years or decades. They are thought to be nuclear explosions on the surface of the white dwarf. They are further categorised as
    - □ Classical novae (N) for whom only one nova outburst has been observed.
    - □ Recurrent novae (Nr) that have outburst more than once.
- **Dwarf Novae** Cataclysmic variables that exhibit a second type of eruptive behaviour that is less spectacular but more obviously cyclic than novae. A dwarf nova outburst is seen as an increase in brightness, over a few hours, of 2 to 5 magnitudes. The brightness remains at this level for a few days before declining to the quiescent value with a timescale of days. These eruptions occur frequently with semi regular periods of weeks to months. Warner (1974) identified the accretion disk surrounding the white dwarf as the source of these outbursts. Dwarf novae are further subdivided on the basis of additional behavioural traits.
    - ▷ U Gem (UG) stars are archetypal dwarf novae, outbursting at regular intervals of a few weeks to a few months.
    - ▷ Z Cam (ZC) stars behave like U Gem stars but during the decline from outburst they occasionally **stand still** with their brightness roughly 1 magnitude less than at maximum. This can last for days or years before returning to minimum.
    - ▷ SU UMa stars outburst as with UG stars but in addition occasionally undergo **superoutburst** which can last for two weeks and is approximately 1 magnitude brighter than a normal outburst. During such an event, the light curve exhibits a modulation known as **superhump**. This has period a few percent longer than the orbital period of the binary.
- **Nova-like Variables** All other systems that are structurally cataclysmic variables are grouped in this class. The main subclasses are
    - ◁ UX UMa stars are thought to be Z Cam stars in permanent standstill.
    - ◁ VY ScI stars behave like UX UMa systems but occasionally decline to minima similar to those of dwarf novae.
    - ◁ Magnetic systems are cataclysmic variables where the accretion flow from the contact component has been influenced by the magnetic moment of the white dwarf. In such cases the accretion disk will be truncated or even completely disrupted. When the magnetic field is strong enough to have synchronised the rotation of the white dwarf with the binary orbit, the system is identified as an AM Her or polar system. If the synchronisation is not present, the system is termed a DQ Her or intermediate polar system.

Downes and Shara (1993) have catalogued 751 cataclysmic variables, of which 256 have been categorised as novae, 349 as dwarf novae, 98 as novalike variables and 48 remain unassigned.

Ritter (1990) provides a catalogue and summary of observations of 168 cataclysmic variables. He cites period determinations for 165 of them. Only one was found to have a period longer than a day. Different methods give widely different estimates of the masses of the components of cataclysmic variables so they should be viewed with some suspicion. Important for the geometry of the Roche potential is the mass ratio

$$q = \frac{M_{sec}}{M_{wd}} \ , \tag{3.2.1}$$

where M_{wd} and M_{sec} are the mass of the white dwarf and of the secondary respectively. We thus have two sets of terminology to describe the Roche potential geometry; q the mass ratio, and μ the reduced mass of the primary. The former is predominantly used by observers, whilst the latter is sometimes used in numerical papers. They are related by

$$q = \frac{(1-\mu)}{\mu}. \tag{3.2.2}$$

Cataclysmic variables are observed to have $q \lesssim 1$. Gas from the extended star overflows its Roche lobe and falls into the gravitational well of the white dwarf. The overflow occurs in the region of the L_1 point, and takes the form of a stream falling in towards the white dwarf. However, in general the stream will not strike the white dwarf directly. (A typical white dwarf has radius of the order 10^9 cm whereas the binary separation will approach 10^{11} cm). Instead the gas forms a disk around the white dwarf. Mass transfer rates through the L_1 point are thought to be of the order of $10^{-11} to 10^{-7}\ M_\odot\ yr^{-1}$. Shorter period cataclysmic variables have rates at the lower end of the range (Patterson, 1984). The gas stream from the L_1 point was first analysed by Lubow and Shu (1975). Essentially gas free falls from the L_1 point until it encounters the disk. Considerable dissipation occurs at the meeting point of the two streams. Consequently it is known unimaginatively as the disk bright spot or hot spot.

Let us look at one cataclysmic variable in particular, the eclipsing SU UMa system, OY Car. This system has been studied in quiescence (e.g. Wood et al. 1989), in outburst (e.g. Rutten et al. 1992) and in superoutburst (e.g. Naylor et al. 1987). Because it is an eclipsing system, additional data analysis techniques are available to us. In particular we can use the eclipse mapping technque due to Horne (1985) to obtain two dimensional maps of the accretion disk. In Chapter 6 we will compare our numerical simulations with observations, with emphasis on observations of OY Car.

The most easily determined system parameter is the orbital period. In the case of OY Car the period is 0.063121 days ($\lesssim$ 91 minutes). Other measurements are beset by uncertainty. Estimates of the white dwarf mass in OY Car have varied from 0.33 to $1.26 M_\odot$, with different methods producing differing values. For example, Schoembs and Hartmann fitted the observed Doppler shifting of emission lines to theoretical curves for white dwarfs to obtain an estimate of $1 M_\odot$. Wood et al. (1989) used high speed photometric observations of eclipses to find the radius of the white dwarf. They then used the theoretical Hamada-Salpeter mass-radius relationship to estimate that $M_{wd} = 0.685 \pm 0.011 M_\odot$. Wood et al. also determined the mass ratio q of the system by matching the observed position of the disk bright spot to the theoretical trajectory of the mass transfer stream derived by Lubow and Shu (1975). Consequently they found $q^{-1} = 0.102 \pm 0.003$ and knowing M_{wd} they determined that $M_{sec} = 0.070 \pm 0.002 M_\odot$. The system inclination was found to be 83.3°.

Whilst being mindful of the historical variance in estimates for OY Car's parameters, in the following work the Wood et al. values will be used. This is because they utilise the geometry of the system and make a minimum of assumptions. One possible doubt is that white dwarfs embedded in cataclysmic variables, due to the asymmetric nature of their mass gain, are not accurately described by the Hawada-Salpeter relationship.

We will refer in more detail to the observations of OY Car in Chapter 6.

Chapter 4.
Numerical Methods

This chapter is a detailed discussion of the numerical methods used in this study of accretion disks. Initially, the method used (Smoothed Particle Hydrodynamics) is described in general terms. As we proceed, its specific application to the disk problem is explained.

In line with the theory developed in chapter 2, we assume the disk is geometrically thin. The simulations will be two dimensional, with the finite thickness of the disk neglected. Suppressing one dimension dramatically reduces the computational time required for a simulation. The risk is that three dimensional effects, which are ignored, are important for disk evolution.

The disk is much less massive than the accreting white dwarf, so disk self gravity is ignored. This makes the gravitational calculation simply that of the Roche potential. This is a very simple, computationally cheap calculation. By comparison, the pressure and viscous forces are expensive to evaluate. This is important as the gravitational timescale $t_g \propto r^{\frac{3}{2}}$ is small in comparison to the pressure and viscous timescale t_{pv}. With the radii of orbits in the disk varying by a factor of approximately 10^2, the gravitational timescale near the inner edge of the disk is roughly a thousand times smaller than at the outer extremity. It is obviously inefficient to integrate the whole system forward using timesteps appropriate to the inner region of the disk. This chapter details two solutions to this problem. The first is to calculate separate timesteps for each particle. Thus gas near the inner edge is allowed to take many steps for each step taken by gas at the outer edge. At each step, all the forces on the particle being integrated are calculated. The second method is to use operator splitting to separate the gravitational forces from the pressure and viscosity. With this scheme, all the particles are integrated forward to a common time, using just the gravitational force. Each particle takes as many timesteps as needed to get it to that common time. This final state is then used as the initial state for one common pressure/viscosity calculation.

4.1. Smoothed Particle Hydrodynamics

Smoothed Particle Hydrodynamics (SPH) is a particle method for modelling fluids. Originally it was designed to tackle nonaxisymmetric astrophysical problems, but has now found a wide range of applications; from incompressible flow (Monaghan 1994), to elastic fracture problems, to relativistic shocks (Monaghan 1993). Particle methods in general characterise the state of a fluid by the attributes of a collection of particles, and model the evolution of the system with interactions between the particles. For a general introduction to particle methods, the reader is referred to Hockney and Eastwood (1988). Another summary, emphasising the application of particle methods to fluid problems is found in Monaghan (1985). SPH is comprehensively reviewed in Monaghan (1992). Particle methods vary in the way they handle the discretisation of the equations of motion. Many require the use of a grid to calculate spatial derivatives. SPH does not need a grid and so gains a computational advantage in problems with little symmetry. Thus one can concentrate on the physics of the problem without getting bogged down in geometrical difficulties.

SPH is centred around a method of interpolating a function from a disordered set of points (the particles). The integral interpolant A_I of a function $A(\vec{r})$ is defined by

$$A_I(\vec{r}) = \int A(\vec{r}')\, W(\vec{r} - \vec{r}', h)\, dr'. \tag{4.1.1}$$

Formally the integral is over the whole fluid volume. $W(\vec{r}, h)$ is the interpolating function or kernel which weights the contribution of $A(\vec{r}')$ according to distance from $\vec{r}$. h determines the extent of the region which contributes significantly to the integral interpolant. Thus W is a function of $\frac{|\vec{r}-\vec{r}'|}{h}$. h is known as the smoothing length.

The kernel must satisfy two conditions,

$$\int W(\vec{r} - \vec{r}', h) dr' = 1, \tag{4.1.2}$$

and

$$\lim_{h \to 0} W(\vec{r} - \vec{r}', h) = \delta(\vec{r} - \vec{r}'). \tag{4.1.3}$$

In practice, the integral interpolant is replaced by a summation interpolant $A_s(\vec{r})$, with the summation being over the particles. Thus

$$A_s(\vec{r}) = \sum_j m_j \frac{A_j}{\rho_j} W(\vec{r} - \vec{r}_j, h), \tag{4.1.4}$$

where m_j,ρ_j and A_j are the mass, density and A attributes of particle j. In approximating A by A_s there is an error associated with approximating the function by the integral interpolant. The size of this error depends upon the kernel W used. Then there is an error associated with discretising the integral. This is controlled by the relative order/disorder of the particles.

If we choose a differentiable kernel, then the interpolant can be differentiated to give approximations to the derivatives of functions. Hence

$$\vec{\nabla} A_S(\vec{r}) = \sum_j m_j \frac{A_j}{\rho_j} \vec{\nabla} W(\vec{r} - \vec{r}_j, h), \tag{4.1.5}$$

and for a vector interpolant

$$\vec{\nabla} \cdot \vec{v}_S(\vec{r}) = \sum_j \frac{m_j}{\rho_j} \vec{v}_j \cdot \vec{\nabla} W(\vec{r} - \vec{r}_j, h). \tag{4.1.6}$$

This is the essence of SPH. Derivatives of functions in the equations of motion are approximated with the above interpolants. As the equations are evaluated at particle positions, the functions themselves are usually given by the relevant attribute of that particle. Details on the validity and accuracy of the interpolation procedure are to be found in Monaghan (1982).

4.2. The Momentum Equation

In this section we will take the momentum equation

$$\frac{d\vec{v}}{dt} = \frac{1}{\rho} \vec{\nabla} P + \vec{F}, \tag{4.2.1}$$

and obtain an SPH equivalent. Here $\vec{v}$ is the velocity, P is the pressure, ρ is the density and $\vec{F}$ a variable describing any body forces on the fluid. As with finite differencing, there are many ways to discretise an equation with some methods having better properties (stability, high order accuracy, conservation of properties such as linear and angular momentum) than others.

When composing a term to represent the gradient of a function at particle i, it is wise to seek an interpolant that is symmetric in the particle indices i and j. So for the pressure gradient term we make use of the fact that

$$\frac{1}{\rho} \vec{\nabla} P = \vec{\nabla} \left(\frac{P}{\rho} \right) + \frac{P}{\rho^2} \vec{\nabla} \rho. \tag{4.2.2}$$

The summation interpolant approximation to the right hand side of Eq. (4.2.2), evaluated at particle i is then

$$\left(\frac{1}{\rho} \vec{\nabla} P \right)_i = \sum_j m_j \left(\frac{P_i}{\rho_i^2} + \frac{P_j}{\rho_j^2} \right) \vec{\nabla} W(\vec{r}_i - \vec{r}_j, h). \tag{4.2.3}$$

The corresponding interpolant approximation to Eq. (4.2.1) is

$$\frac{d\vec{v}}{dt}_i = \sum_j m_j \left(\frac{P_i}{\rho_i^2} + \frac{P_j}{\rho_j^2} \right) \vec{\nabla} W(\vec{r}_i - \vec{r}_j, h) + \vec{F}_i. \tag{4.2.4}$$

4.3. Kernel

The kernel used in this thesis is the spline function interpolant due to Monaghan and Lattanzio (1985). Appropriately normalised for two dimensions we have

$$W(\vec{r},h) = \frac{10}{7\pi h^2}\begin{cases} 1-\frac{3}{2}x^2+\frac{3}{4}x^3 & 0<x<1 \\ \frac{1}{4}(2-x)^3 & 1<x<2 \\ 0 & x>2 \end{cases} \tag{4.3.1}$$

with $x = \frac{r}{h}$. This particular kernel has compact support, meaning that particles more than $2h$ apart have no influence on one another. It has continuous second derivatives meaning that it is not sensitive to particle disorder and that the error in replacing the integral interpolant by the summation is small. The error in replacing the original function by an interpolant is second order in h (Monaghan, 1992).

In the code used in this work, tables of values for the kernel and its derivative are generated. Whenever kernel estimates are required, they are interpolated from the tables. This is done to save computing time, rather than have the program evaluate kernel estimates anew whenever they are required. Whether the time saved is significant is debateable. The most time consuming part of performing SPH summations is actually determining which particles contribute. This is the problem of finding near neighbours for particles. We discuss this in Section 4.5.

4.4. Artificial Viscosity

An artificial viscosity term was originally added to the SPH momentum equation to improve the method's treatment of shocks (see Monaghan, 1992). Eq. (4.2.4) becomes

$$\frac{d\vec{v}}{dt}_i = -\sum_j m_j\left(\frac{P_i}{\rho_i^2}+\frac{P_j}{\rho_j^2}+\Pi_{ij}\right)\vec{\nabla}W(\vec{r}_i-\vec{r}_j,h). \tag{4.4.1}$$

Various forms for Π_{ij} have been tried. The one most commonly used at the present is

$$\Pi_{ij} = \begin{cases} \frac{-\bar{\alpha}\bar{c}_{ij}\mu_{ij}+\beta\mu_{ij}^2}{\bar{\rho}_{ij}} & \vec{v}_{ij}\cdot\vec{r}_{ij}<0 \\ 0 & \vec{v}_{ij}\cdot\vec{r}_{ij}>0 \end{cases}. \tag{4.4.2}$$

where $\bar{c}_{ij} = \frac{1}{2}(c_i+c_j)$ and $\bar{\rho}_{ij} = \frac{1}{2}(\rho_i+\rho_j)$ are the average values for the sound speed and density of the two interacting particles, and

$$\mu_{ij} = \frac{h\vec{v}_{ij}\cdot\vec{r}_{ij}}{r_{ij}^2+\eta^2}. \tag{4.4.3}$$

η is a softening parameter included to prevent μ_{ij} becoming singular when $r_{ij}\to 0$. In all SPH codes used in this thesis $\eta = 0.1h$. (This method was used by Aarseth (1963) to smooth the gravitational potential in his paper on N-body calculations.)

As it is written above, Π_{ij} has a switch that is on only when $\vec{v}_{ij}\cdot\vec{r}_{ij}<0$. In other words, a particle only feels a viscous force from particles approaching it. In other words viscosity only acts for compression not rarefaction. Originally the artificial viscosity term was included to model shocks, hence the switch. Here we wish to use the term to model shear viscosity so we will disregard the switch and let both approaching and receding particles interact.

There are two free parameters in Eq. (4.4.2). $\bar{\alpha}$ is coefficient to the linear term. Note the use of the bar to distinguish the SPH viscosity coefficient from the Shakura-Sunyaev parameter α. β is coefficient to a nonlinear term that was included to handle strong shocks. These are not a feature of the flows modelled in this thesis so we will set $\beta = 0$. Thus in these simulations we have the simplified viscosity term

$$\Pi_{ij} = -\bar{\alpha}h\,\frac{\bar{c}_{ij}}{\bar{\rho}_{ij}}\,\frac{\vec{v}_{ij}\cdot\vec{r}_{ij}}{r_{ij}^2+\eta^2}. \tag{4.4.4}$$

The 'viscous' acceleration of particle i is then

$$\vec{a}_i = \sum_j m_j \bar{\alpha} h \, \frac{\bar{c}_{ij}}{\bar{\rho}_{ij}} \, \frac{\vec{v}_{ij} \cdot \vec{r}_{ij}}{r_{ij}^2 + \eta^2} \, \vec{\nabla}_i W_{ij}. \tag{4.4.5}$$

We would now like to relate Eq. (4.4.5) to the viscosity term in the fluid equation of motion. To do this we reverse the procedure originally used to generate the SPH summation equations. First we replace the summation by the integral

$$\vec{a} = \int_{support \;\; W_{ij}} \rho_j \bar{\alpha} h \frac{\bar{c}_{ij}}{\bar{\rho}_{ij}} \frac{\vec{v}_{ij} \cdot \vec{r}_{ij}}{r_{ij}^2 + \eta^2} \, \vec{\nabla}_i W_{ij} dV. \tag{4.4.6}$$

We now let the number of particles $N \to \infty$ and the smoothing length $h \to 0$. In other words we seek the continuum limit of Eq. (4.4.6). We follow Pongracic (1988), and Meglicki et al. (1993) to get

$$\vec{a} = \frac{\bar{\alpha} h \kappa}{2\rho} \left(\vec{\nabla} \cdot (c\rho S) + \vec{\nabla} \left(c\rho \vec{\nabla} \cdot \vec{v} \right) \right), \tag{4.4.7}$$

where S is the deformation tensor

$$S_{ab} = \frac{\partial v^a}{\partial x^b} + \frac{\partial v^b}{\partial x^a}. \tag{4.4.8}$$

κ is a constant determined by the kernel. In two dimensions

$$\kappa = \int \int_{support \;\; W} |\frac{1}{r} \vec{\nabla} W| \, \frac{x^2 y^2}{r^2 + \eta^2} \, dx dy. \tag{4.4.9}$$

For the cubic spline kernel in two dimensions

$$\kappa = \frac{1}{4}. \tag{4.4.10}$$

Assume the sound speed and density vary on length scales much larger than the velocity. Then

$$\begin{aligned} \vec{a} &= \frac{\bar{\alpha} h \kappa c}{2} \left(\vec{\nabla} \cdot S + \vec{\nabla} \left(\vec{\nabla} \cdot \vec{v} \right) \right) \\ &= \frac{\bar{\alpha} h \kappa c}{2} \left(\nabla^2 \vec{v} + 2 \vec{\nabla} \left(\vec{\nabla} \cdot \vec{v} \right) \right) \end{aligned} \tag{4.4.11}$$

If the flow is Keplerian, $\vec{\nabla} \cdot \vec{v} = 0$ and

$$\vec{a} = \frac{\bar{\alpha} h \kappa c}{2} \nabla^2 \vec{v}. \tag{4.4.12}$$

For the cubic spline kernel in two dimensions we have

$$\vec{a} = \frac{\bar{\alpha} h c}{8} \nabla^2 \vec{v}. \tag{4.4.13}$$

We have arrived at a term that is identical to the viscosity term in the fluid equation of motion if

$$\nu = \frac{1}{8} \bar{\alpha} c h. \tag{4.4.14}$$

We will test Eq. (4.4.14) in Chapter 5.

4.5. Finding Near Neighbours

When calculating the SPH approximations to pressure and viscous forces, one nominally performs a summation over all particles in the domain. In reality only those particles in the immediate vicinity of a particle influence it. The kernel we are using has compact support so, specifically, we are only concerned with those particles within $2h$ of the subject particle i. We call these particles the **near neighbours** of i. Of course in performing the summations one wants to know which particles are the near neighbours, and not have to consider all n particles.

Finding near neighbours efficiently is a problem that has also arisen in the field of molecular dynamics. The induced dipole-dipole force acts only over a short range. It is described by the Leonard-Jones potential

$$u\left(\vec{r}_{ij}\right) = \begin{cases} 4\epsilon\left[\left(\frac{\sigma}{r_{ij}}\right)^{12} - \left(\frac{\sigma}{r_{ij}}\right)^{6}\right] & r_{ij} < r_{co} \\ 0 & r_{ij} > r_{co} \end{cases} \tag{4.5.1}$$

where r_{ij} is the distance from particle i to particle j. Typically the force is cut off at $r_{co} = 2.5\,\sigma$. Thus we will look at the molecular dynamics solutions to the near neighbour problem. In doing so we must remember that particles in molecular dynamics calculations are likely to move far less relative to one another than particles in fluid dynamics calculations are expected to. In other words we expect that, from timestep to timestep, the near neighbour list of a fluid dynamics particle to change much more dramatically than for a molecular dynamics particle. Thus, algorithms that are efficient for molecular dynamics, may not be for SPH.

The three basic methods underlying most molecular dynamics near neighbour algorithms are; the neighbour table, the link list, and the monatonic logical grid (Morales and Toxvaerd, 1992).

4.5.1. The Neighbour Table

This is self explanatory. For every particle i there is a vector containing the labels of all particles lying within a distance r_s of it. If n_{max} is the maximum number of particles to be found in any sphere of radius r_s, then an array of dimension $n \times n_{max}$ is needed. If $r_s = r_{co}$ then the neighbour table must be updated every timestep. Creating the table is quite time consuming so reducing the frequency of this operation is advantageous. We can do this by letting $r_s > r_{co}$. Then we will only need to update the table every few steps. The exact frequency depends on the value of r_s and the maximum speed of particles in the simulation. The disadvantage of increasing r_s is that $n_{max} \propto r_s^3$. Making r_s too large will result in an unmanageably large neighbour table.

4.5.2. The Link Cell

First the computational domain is divided into a regular lattice of cells. Then, for each cell, a link list is constructed. The list contains the labels of all particles lying in that cell. If the domain is divided into n_{cell} cells then an integer vector of length n_{cell} is required. The ith element of this vector will contain the label of the first particle in the link list of cell i. With n particles, an integer vector of length n is also needed. Element j will contain the label of the next particle in particle j's link list. Provided the cell side length $l \geq r_{co}$, the cutoff length of the kernel/potential, the neighbours of particle j will be it its own cell, or in adjacent cells. Thus finding near neighbours is just a search through the link lists of these cells. As with the neighbour table, we can reduce the frequency with which the link lists need updating by setting $l > r_{co}$. The link cell method is memory efficient as compared to the neighbour table. It is also easy to implement, and requires a minimum of code. In SPH programs with constant smoothing length h, the link cell method is currently the favoured method for finding near neighbours. However, it is not so popular in problems with variable smoothing lengths. A major drawback is that both setting up the link list, and extracting labels from it are recursive operations. As yet the algorithm has not been vectorised.

4.5.3. The Monatonic Logical Grid

For a three dimensional domain, this method involves storing all the particle properties in three dimensional arrays, with the position in the array relating to the physical position of the particle in the domain. Specifically, the particles are ordered in the arrays so that, if the arrays are indexed (i, j, k) the x coordinates of the particles increase monatonically with the index i, the y coordinate increases similarly with j, and z with k. (There is no unique mapping of a particular arrangement of particles onto the arrays). The particles are then said to be on a monatonic logical grid. Particles neighbouring each other in space will find themselves near each other on the grid. The search for near neighbours then becomes a search over a limited volume of the array. In this project, monatonic logical grids were not looked at in detail. The interested reader is referred to Boris, 1986. The suspicion held about this method is that it is far better suited to molecular dynamics than fluid dynamics. Substantial, computationally expensive, reconstructions of the grid could be expected to occur much more frequently in fluid problems.

4.5.4. The Hierarchical Tree

A fourth method used by Hernquist and Katz (1989) in their `TRESPH` code involved using a hierarchical tree data structure to search for near neighbours. They were interested in modelling self-gravitating fluids and so married SPH to a Barnes-Hut N body tree code. `TREESPH` is a three dimensional code suited to a range of applications. They allowed individual particles to have their own value for the smoothing length h which increases the complexity of finding the near neighbours of all particles. The hierachical tree, having already been set up for the gravity solver, proved to be well suited to this task, for a variable smoothing length. Hernquist and Katz did comment however that the linked list method with a cell size of $2h$ appeared to be optimal for problems where the smoothing length was fixed. In this work we use a two dimensional SPH code without self-gravity and with fixed h and in that context we have chosen not to investigate using a tree code to find nearest neighbours.

4.5.5. Relative Merits of the Methods

There is no simple answer to the question 'Which method is the best/quickest/most efficient?' This is because their relative speeds strongly depend on the architecture of the computer being run on. For example, the link cell method runs very quickly on traditional scalar machines. On vector and massively parallel machines however, it is disappointingly slow. This is shown quantitatively below. There is also a suspicion, that it fails to make great use of the new generation of scalar computers. Qualitative results on IBM RISC 6000 and DEC ALPHA machines have not achieved anticipated speedups.

Current molecular dynamics codes tailored for high performance computers use hybrid methods that use both neighbour tables and link lists (see e.g. Grest et al., Morales and Nuevo, and Morales and Toxvaerd).

As an example, an SPH code (using multiple timesteps- see Section 4.7) employing link list near neighbour finding was vectorised on a Fujitsu VP2200. The code was ported to DECstation 5000/125 (a scalar workstation typical of the computers used in this work). Relative speeds for a 5000 timestep trial are tabulated below. The code was shown to be 37% vectorised. In other words, for this particular run, the VP2200 spent 37% of its time performing vector operations. To improve this figure, the near neighbour code ONLY was replaced.

In the new code, link lists were scrapped. To find near neighbours, the domain is covered with a mesh of sidelength l. Rather than use link list, a table of cell occupants is generated. From this, a near neighbour table is created. This second table is updated every timestep. The cell occupant table is only refreshed every few steps. From trial runs, $l = 2.5h$ was shown to be optimum. h is the smoothing length, and the kernel cuts off at $2h$. The resulting code was not much more complicated than the link cell code and was 90% vectorised. This example highlights the point made above, that a near neighbour algorithm that is fast on one machine, may be very inefficient on a different computer.

Having said all this, it is the basic link cell algorithm that is used in the work described in the rest of the thesis. This is for three reasons. Firstly, the algorithm is very simply implemented. As the code underwent substantial revision for other reasons (changing the time stepping, and introducing more complicated physics), simplicity was a high priority. Secondly, most of the computing was carried out on DECstations for which the link cell method is adequately fast. Thirdly it was felt that Murphy's Law of Algorithm

Table 4.5.1: Speed comparison of SPH codes with different near neighbour algorithms

	VP2200	DEC 5000/125
link cell program	78.31 minutes 37% vectorised	708 minutes
cell/neighbour table program	33.86 min 90% vectorised	$\sim$ 1500-2000 min

Improvement was coming into play, 'The time taken to improve the speed of a program is greater than the time the original code takes to run'. Much more substantial speed gains were to be made through changing the timestepping scheme.

4.6. Time Scales

4.6.1. Gravity

Consider a test particle in Keplerian orbit about a star of mass M. The period of the orbit is

$$T = 2\pi \left(\frac{r^3}{GM}\right)^{\frac{1}{2}} \tag{4.6.1}$$

where G is the gravitational constant. We shall assume that to achieve a desired accuracy when numerically integrating along the orbit, we require n timesteps per period. This gives a gravitational timestep

$$\Delta t_{grav} = \frac{2\pi}{n} \left(\frac{r^3}{GM}\right)^{\frac{1}{2}}. \tag{4.6.2}$$

Typically in these simulations we have decided that $n \sim 60 - 100$ will allow us to model the orbit sufficiently well. Thus when calculating the gravitational time scale of an SPH particle we will use

$$\Delta t_{grav} = K \left(\frac{r^3}{GM}\right)^{\frac{1}{2}}. \tag{4.6.3}$$

with $K \simeq 0.1$.

4.6.2. Courant-Friedrichs-Lewy (CFL) Criterion

According to Smith (1985), the CFL condition states that the domain of dependence of a numerical scheme must include the domain of dependence of the original differential equation if it is to be able to model that equation. Put another way, there is a maximum speed with which information can travel throughout the computational domain for any given scheme. For a finite difference scheme that speed is

$$v_{mesh} = \frac{L}{\Delta t}, \tag{4.6.4}$$

with L being the mesh scale, and Δt the timestep. If the scheme is to be adequate, the maximum speed at which information travels in the original system v_{max} must be less than v_{mesh}. Thus we rearrange Eq. (4.6.4) to obtain a condition for the timestep,

$$\Delta t < \frac{L}{v_{max}}. \tag{4.6.5}$$

In practice, for flows with viscosity, this criterion is combined with a viscous time control (see Potter 1973, Monaghan (1992)). From a Von-Neumann stability analysis of finite difference approximations to the diffusion equation, Potter obtains the following stability requirement.

$$\Delta t \lesssim \frac{\Delta^2}{\nu}. \tag{4.6.6}$$

Combination of the two yields

$$\Delta t < \frac{\Delta}{v_{max} + \frac{\nu}{\Delta}}. \tag{4.6.7}$$

In SPH terms, with the viscosity $\nu = \kappa\alpha ch$, we get

$$\Delta t < \frac{h}{c + \kappa\alpha c}. \tag{4.6.8}$$

4.7. Multiple Timestep Method

This scheme was used by Whitehurst (1988 b) to improve the speed of his particle disk code (see Chapter 6 for a review). It has been incorporated into SPH codes by Hernquist and Katz (1989), who developed a general three dimensional SPH code for modelling self gravitating fluids, and by Heller (1993), who was interested in stellar encounters with circumstellar disks.

In the previous section we obtained expressions for the gravitational and pressure/viscous time scales for particles in the disk. We take the minimum of these two quantities, calculated for particle i, and call it δt_i. The basis of this method is that each particle should be integrated individually, taking timesteps appropriate to its own time scale.

Initially we legislate a base timestep for the whole system Δt. That is to say that, for whatever reason, we need to know the state of the whole system at intervals of Δt. The number of steps a particle takes to get from time t to $t + \Delta t$ is determined by its time scale. In fact we only allow particle timesteps Δt_i to have certain values

$$\Delta t_i = \left(\tfrac{1}{2}\right)^m \Delta t \qquad\qquad m = 0, 1, 2, ... \tag{4.7.1}$$

with m chosen so that

$$\left(\tfrac{1}{2}\right)^m \Delta t_i < \delta t_i < \left(\tfrac{1}{2}\right)^{m-1} \Delta t.$$

The process of selecting timesteps for the particles is called binning. Particles with timestep $(\frac{1}{2})^m \Delta t$ are referred to as being in bin m. In practice, for the disk simulations described here, 7–8 bins are required to accommodate all the particles. At the end of each base timestep, a comprehensive binning of particles is done. Whilst a timestep is in progress individual particles may be shuffled between bins as their time scales change.

We shall run through a simple example to clarify the details of the method. Assume we are at the start of a base timestep Δt with all particles having been binned. For the sake of the example we will assume only three bins are required. Those particles in bin 0 have timestep $\Delta t_i = \Delta t$. Those in bin 1 have timestep $\frac{1}{2}\Delta t$ and those in 2 have step $\frac{1}{4}\Delta t$. The order in which particles are integrated is shown in Fig. 4.7.1. The first manœuvre is always to take one step with those particles that have the smallest timestep. In this case, those in bin 2 are brought forward to $t + \frac{1}{4}\Delta t$. These particles have their time scales reevaluated. They can only be redistributed between bin 2 and, if needed, bins with even smaller timesteps (i.e. bins $3, 4, ...$). Even if a particle's time scale lengthens sufficiently for it to warrant it being placed in bin 1 it is prevented from doing so, and it must remain in bin 2. For this example we assume that extra bins are not required. The next substep, numbered 2 in Fig. 4.7.1 brings all particles in bins 1 and 2 one step forward to $t + \frac{1}{2}\Delta t$, with the particles in bin 1 taking a step of size $\frac{1}{2}\Delta t$ and those in bin 2 taking one of size $\frac{1}{4}\Delta t$. They are then redistributed between bins $1, 2, ...$. We now bring particles in bin 2 forward one more step to $t + \frac{3}{4}\Delta t$ and rebin them. Finally all the particles (including those in bin 0) take one step forward to $t + \Delta t$. This completes one base timestep. As stated above, after a particle is stepped, it has its time scale determined anew and it is rebinned. This process is important as during a single base step a particle's time scale may change several times and it may require several different length timesteps. In order that the integration proceeds in an orderly fashion, particles can only be distributed amongst 'active' bins (i.e. those bins involved in the current substep), and any new bins of smaller timestep that may be required.

The timestepping is carried out using a second order predictor- corrector method. In the predictor step, the velocity is calculated to second order accuracy. The position is calculated to third order accuracy. We thus have

$$\vec{v}_1^* = \vec{v}_0 + \Delta t \vec{a}_0 \tag{4.7.2}$$

$$\vec{x}_1 = \vec{x}_0 + \Delta t \vec{v}_0 + \frac{\Delta t^2}{2}\vec{a}_0 \tag{4.7.3}$$

where $\vec{x}_0$, $\vec{v}_0$ and $\vec{a}_0$ are the position, velocity and acceleration of particle i at time t. The pressure, viscous and gravitational forces on particle i at time $t + \Delta t$ are now calculated, to give $\vec{a}_1(\vec{x}_1, \vec{v}_1)$. The velocity is then corrected using the third order accurate equation

$$\vec{v}_1 = \vec{v}_0 + \frac{\Delta t}{2}\left(\vec{a}_0 + \vec{a}_1\right). \tag{4.7.4}$$

Note that the method uses quantities evaluated at the endpoints of intervals rather than at the midpoint, say. This is advantageous when changing a particle's timestep. Hernquist and Katz on the other hand used a leap-frog method which required velocities to be determined at the midpoint of timesteps. When a particle was rebinned, its particle position had to be corrected to account for the change in timestep. No such adjustment need be made with this predictor-corrector. Without considering errors in the force calculations, the error for one step of the above predictor-corrector is $O(\Delta t^3)$ for both the position and velocity. Thus in integrating the system forward to a given time, the error is $O(\Delta t^2)$. This method also conserves angular momentum.

In determining the pressure and viscous forces on a particle, one requires the positions and velocities of all neighbouring particles. Thus the predictor step is also carried out for positions and velocities of all the particles within $2h$ of those being substepped. In terms of computer time this is a very cheap thing to do. It is the calculation of the pressure and viscous forces that is computationally expensive. Consider the interaction between a hot particle (i.e. one being substepped) and one of its neighbours that is not. We have already determined, from the neighbouring particle's time scale, that we do not need to calculate its acceleration yet. We only record its influence upon the hot particle. Thus in a departure from SPH common practice, we lose the symmetry of the force calculation. As a result, the pressure/viscous force summations will no longer conserve linear and angular momentum. Whilst making the multistep method slightly less desirable, it does not deal its validity a crippling blow.

4.8. Operator Splitting

Most of the mass in a disk must lie in its outer reaches where orbital velocities are low. In an SPH disk simulation this is where the great majority of the particles will be found. It would be pointless to update their positions and velocities with the frantic frequency required by those few particles at the disk's inner edge. In the last section we outlined an algorithm that treated particles on an individual basis, integrating each with a steplength appropriate to it. Thus only particles close to the central object took very small steps. Particles further and further away took progressively larger steps.

This section attacks the problem in a different way. First we realise that it is the gravitational force on particles in the inner disk that requires them to take such vanishingly small steps. Yet a gravity calculation is very simple, requiring only a couple of lines of code. It is the calculation of the pressure and viscous forces that are so very time consuming and slow us down. Runtime profiling of SPH codes shows that most of the computational time is spent either in the density and pressure routines or calculating particles nearest neighbours. We have shown already that for any given particle the pressure/viscous time scale is much greater than the gravitational time scale. This suggests that if we could reduce the number of times we calculated the pressure and the viscosity but maintained the rate at which we determined the gravity, there could be much to gain. Thus we turn to operator splitting. The concept is illustrated with a simple example.

Consider solving

$$\frac{dx}{dt} = (c_1 + c_2)\, x, \tag{4.8.1}$$

using a simple Euler scheme. Assume c_1 and c_2 are constant and $|c_1| \gg |c_2|$. Thus

$$x^{n+1} = x^n \left(1 + \Delta t\, (c_1 + c_2)\right). \tag{4.8.2}$$

For the solution to be accurate we need

$$\Delta t\, |c_1 + c_2| \ll 1. \tag{4.8.3}$$

In practice we are interested in the case where c_1 is simple to evaluate while c_2 is complicated. To take account of this we want to mininise the calculation of c_2. To do this we determine a time step for c_1 alone

$$\Delta t_1 < \frac{1}{|c_1|}, \tag{4.8.4}$$

and a time step for c_2 alone

$$\Delta t_2 = k \Delta t_1 < \frac{1}{|c_2|}, \tag{4.8.5}$$

where k is an integer. We can now integrate

$$\frac{dx}{dt} = c_1 x \tag{4.8.6}$$

for k steps each of Δt_1,

$$x_k^* = x^n \left(1 + c_1 \Delta t_1\right)^k \tag{4.8.7}$$

This is justified by the choice of Δt_1. We then use x_k^* as the initial x for one numerical integration step of

$$\frac{dx}{dt} = c_2 x. \tag{4.8.8}$$

We thus have

$$x^{n+1} = (1 + c_2\Delta t_2)\, x_k^*. \tag{4.8.9}$$

Substituting Eq. (4.8.7) for x_k^* into Eq. (4.8.9) we get

$$\begin{aligned} x^{n+1} &= x^n\,(1 + c_2\Delta t_2)\,(1 + c_1\Delta t_1)^k && (4.8.10a) \\ &= x^n e^{\Delta t_2 (c_2 + k c_1) + O(\Delta t_2)^2}. && (4.8.10b) \end{aligned}$$

There is no prescribed order in which the operators have to be treated. We could have taken the large step with c_2 first and then the k smaller steps with c_1 to once again obtain Eq. (4.8.10). This is a special case, in general the two operations will not commute.

Let us now reflect on the numerical implications of operator splitting. In terms of our example we are under no obligation to use the same numerical scheme for both Eq. (4.8.6) and Eq. (4.8.8). We could for example choose an explicit forward difference method for Eq. (4.8.6) and an implicit backward difference scheme for Eq. (4.8.8). This is a strength of the operator splitting method. One has the flexibility to choose a numerical scheme that is appropriate for each operator in terms of accuracy, stability etc..

A second advantage of operator splitting is that you naturally end up with neat, simple, modular code. This is a major consideration when one is developing new code. Operator splitting lies at the heart of ZEUS 2D, a finite difference code for two dimensional magnetohydrodynamics that incorporates radiation transfer. The hydrodynamics algorithms of ZEUS 2D are described in Stone and Norman (1992). This code is mentioned because it has been rigorously tested and detailed comprehensively in the literature, and so it provides a first class example of a sophisticated numerical code that uses operator splitting to considerable advantage. Furthermore, a very similar code to ZEUS 2D was used by Hawley and Balbus (1991, 1992) in their study of a shear instability in weakly magnetized disks. That work is discussed in Section 2.5.

We now apply operator splitting to the problem at hand, which is to solve for each particle the equations

$$\frac{d\vec{v}}{dt} = \vec{a}_{grav} + \vec{a}_{pv} \tag{4.8.11}$$

$$\frac{d\vec{x}}{dt} = \vec{v}. \tag{4.8.12}$$

We discussed previously that the gravitational time scale is much shorter than the pressure/viscous time scale, and that $\vec{a}_{grav}$ is easily calculated compared to $\vec{a}_{pv}$. Thus it is natural to replace Eq. (4.8.11) by

$$\frac{d\vec{v}}{dt} = \vec{a}_{grav} \tag{4.8.13}$$

$$\frac{d\vec{v}}{dt} = \vec{a}_{pv}. \tag{4.8.14}$$

The operator splitting is carried out over a timestep Δt that is less than the viscous/pressure time scales δt_{pv} of all the particles. In general $\Delta t \gg \delta t_{grav}$, the gravitational time scales of the particles.

The disk is not self gravitating and its influence upon the motion of the binary is neglected, thus the gravitational acceleration is given by a simple function of the time and the particle position. For the purposes of this calculation therefore, the particles are independent of one another. The problem of carrying the particles forward Δt is thus very simple. Specifically we use a fourth order Runge-Kutta algorithm, allowing each particle to take as many steps as necessary to reach $t + \Delta t$. More sophisticated integration techniques that can achieve great accuracy, e.g. the Bulirsch-Stoer method (Press et al., 1992) were considered. However there is little point in integrating the gravitational term to very high precision when the SPH pressure/viscosity calculation is limited to second order accuracy in space (limited by the cubic spline kernel), and third order accuracy in time (see below). Because fourth order accuracy is already more than enough, and it is a simple, robust technique, Runge-Kutta was chosen.

We now have $\vec{x}^*(t+\Delta t)$ and $\vec{v}^*(t+\Delta t)$ for all the particles which we use as the initial state for the pressure/viscosity timestep. First we calculate $\vec{a}_{pv}(\vec{x}^*, \vec{v}^*)$. We now use a simple third order explicit scheme to obtain the position

$$\vec{x}\,(t+\Delta t) = \vec{x}^* + \tfrac{1}{2}\Delta t^2 \vec{a}_{pv}\,(\vec{x}^*, \vec{v}^*) \tag{4.8.15}$$

Note that the velocity does not appear in Eq. (4.8.15). This was already accounted for in the gravitational step. We use a predictor-corrector method

$$\vec{v}^{**}\,(t+\Delta t) = \vec{v}^* + \Delta t \vec{a}_{pv}\,(\vec{x}^*, \vec{v}^*) \tag{4.8.16a}$$

$$\vec{v}\,(t+\Delta t) = \tfrac{1}{2}\,(\vec{v}^* + \vec{v}^{**} + \Delta t \vec{a}_{pv}\,(\vec{x}, \vec{v}^{**}))\,, \tag{4.8.16b}$$

to determine the velocity. We now have $x(t+\Delta t)$ and $v(t+\Delta t)$ and this completes a single operator split timestep.

On balance, the operator splitting algorithm appeared better suited to our purposes. A major factor influencing our decision was the modularity and simplicity of the operator split code. By comparison the multistep program was far more involved. It was felt that more complicated physics could be more easily incorporated into the operator split method than into the multstep code. In the comparisons that were run, neither method held a strong advantage in speed. For these reasons, all results described in the rest of this thesis will have been obtained using an operator split SPH code.

Chapter 5.
Testing The SPH Code

The SPH artificial viscosity term has traditionally been used to model shocks. Its performance in this regard has been comprehensively tested (see Steinmetz and Mueller (1993) for a recent critical review). Now several authors are using SPH to model accretion disks. In these calculations the SPH artificial viscosity term is being asked to simulate the disks' viscous shear forces. Nobody has satisfactorily tested the term's ability to perform this task. In Chapter 4, we theoretically investigated the SPH term's application to shear viscosity and obtained an equation estimating the equivalent kinematic viscosity coefficient

$$\nu_{SPH} = \frac{1}{8}\bar{\alpha}ch. \tag{5.1}$$

Hirose (1991), in his doctoral thesis, compared the steady state results of nonaxisymmetric disk simulations with the steady state axisymmetric disk theory to obtain an estimate of the effective viscosity. His simulations included pressure which also acts diffusively. This added a systematic error to his result and so could not be considered a conclusive test of the artificial viscosity term. Artymowicz et al. (1991) used SPH to model disks surrounding an eccentric binary system. They stated that they estimated the viscosity in the simulations from the spreading times of rings. Their calculations also included pressure. These were essentially calibration runs for their code and they were not described in detail. In this Chapter, we compare SPH simulation with axisymmetric disk theory. We test the SPH artificial viscosity term with some rigour in order to determine the validity of Eq. (5.1). In the next section we outline the system to be simulated. We then describe the way we set up the SPH simulation. Results are then discused and compared to axisymmetric thin disk theory. We find that the shear viscosity of the SPH artificial viscosity term is given by Eq. (5.1), accurate to within 10%. Finally we point out that the radial velocity initial condition, imposed upon us by our requirement that v_ϕ is exactly Keplerian, largely determines the evolution of the disk. Other initial conditions are possible if we relax the Keplerian assumption and allow the rotational velocity to be a function of time. We consider the simplest initial condition, $v_r(r,0) = 0$ for all r, and show that the disk responds in a significantly different manner. Finally we postulate that the $v_r(r,0) = 0$ simulation has significance for the modelling of the thermal instability in CV accretion disks.

5.1. The Test

The simulations in this chapter will be of axisymmetric Keplerian disks with, initially, the Gaussian density profile

$$\Sigma_0(r) = \begin{cases} e^{-\frac{(r-r_c)^2}{l^2}} & r_1 < r < r_2 \\ 0 & elsewhere \end{cases}, \tag{5.1.1}$$

with r_1, r_2, r_c and l being constants. We scale the problem using a length scale L, a mass scale M, and a time scale

$$\tau = \sqrt{\frac{L^3}{GM}},$$

where M is the mass of the central body. In these units the gravitational potential due to the central body

$$\phi(r) = -\frac{1}{r}, \tag{5.1.2}$$

and the Keplerian azimuthal velocity in the disk

Table 5.1.1: Summary of constants for the axisymmetric disk simulations

Constant	Value	Comment
$\bar{\alpha}$	0.,10.,20.	SPH artificial viscosity coefficient
h	0.01	SPH smoothing length
c	0.02	sound speed
r_c	0.85	centre of Gaussian
r_1	0.80	inner edge of disk
r_2	0.90	outer edge of disk
l	0.025	length scale of Gaussian
Δr	$\frac{1}{2}h, \frac{5}{13}h$	interparticle spacing

$$v_\phi(r) = \frac{1}{\sqrt{r}}. \tag{5.1.3}$$

The orbital period at radius $r = 1$ is then 2π.

As mentioned in Chapter 1, if the azimuthal velocity is strictly Keplerian, the radial velocity

$$v_r(r,t) = -3\nu\frac{\partial}{\partial r}\ln\left(r^{\frac{1}{2}}\Sigma\right). \tag{5.1.4}$$

Thus, given the density profile of Eq. (5.1.1), the initial radial velocity

$$v_r(r,0) = \frac{-3\nu}{2r} + \frac{6\nu}{l^2}(r - r_0). \tag{5.1.5}$$

Notice that $v_r \propto \nu$. A value for the viscosity is required for the initial radial velocity condition. We will substitute Eq. (5.1) into Eq. (5.1.5) when calculating particles' initial velocity. The aim of the simulations is to determine whether Eq. (5.1) correctly the magnitude of the SPH artificial viscosity term. In order to check this, simulations will be deliberately run with a viscosity that does not match the initial radial velocity.

5.2. SPH Disk Setup

Given the axial symmetry of the problem it is not surprising that setting the particles up in concentric rings produces the cleanest results. If laid down on a square grid, the particles become disordered within a few steps.

The rings are laid down $\Delta r = \frac{1}{2}h$ apart. If $\Delta r \simeq 2h$ then the rings lose contact with one another. If on the other hand the rings are packed too closely together then the program slows down dramatically. The number of particles in each ring is given by

$$N = \frac{2\pi}{\Delta r}. \tag{5.2.1}$$

Thus particles throughout the disk occupy approximately equal areas $A = r\,\Delta r\,\Delta\theta \simeq (\frac{1}{2}h)^2$. To achieve a Gaussian density profile, the particles' masses were given by.

$$m(r) = e^{\frac{-(r-r_c)^2}{l^2}}\,r\,\Delta r\,\Delta\theta. \tag{5.2.2}$$

5.3. Results

5.3.1. Initial Tests

The SPH simulations in this section were configured as per Table 5.1.1. The base value for $\bar{\alpha}$ was set at 10.0. Using Eq. (5.1) and c and h from Table 5.1.1 we obtain $\nu = 2.5 \times 10{-}4$. This value was used to determine the initial radial velocity of all disk simulations described in this section. The initial setup is shown in Fig. 5.2.1. The figure includes a closeup plot of part of the disk itself to illustrate how the particles were initially arranged. The other three diagrams show various attributes of all 22,400 particles as a function of radius. As the particles are arranged in rings, only 21 distinct points are visible on each graph.

A typical run would be 150 timesteps long with the steplength $\Delta t = 0.01$ in our scaled units. We are thus following the disk up to a time $t = 1.50$. In that time, gas at a radius $r = 0.85$ will have executed about 0.3 of an orbit about the central object. In Chapter 2, by looking at the radial Navier Stokes equation, we estimated that the viscous time scale

$$t_{visc} \sim \frac{r^2}{\nu}.$$

In fact, in Section 2.3 we more precisely defined it as

$$t_{visc} = \frac{r^2}{6\nu}. \tag{5.3.1}$$

But in these simulations, the natural length scale is not r, the radius of the disk, but l, the scaling factor in Eq. (5.1.1). We thus have

$$t_{visc} = \frac{l^2}{6\nu}. \tag{5.3.2}$$

Substituting Eq. (5.1) into Eq. (5.3.2) gives

$$t_{visc} = \frac{4l^2}{3\bar{\alpha}ch}. \tag{5.3.3}$$

This result is not surprising as the initial radial velocity

$$v_r\left(r,0\right) \simeq \frac{6\nu}{l^2}\left(r - r_0\right). \tag{5.3.4}$$

Now $r - r_0 \sim l$ and $t \sim \frac{l}{v_r}$ so we have again $t \sim \frac{l^2}{6\nu}$. If we take $\bar{\alpha} = 10.0, h = 0.01$ and $l = 0.025$ we find $t_{visc} \sim 0.4$ scaled time units. We expect significant changes in the radial profile to occur on this time scale. In this simulation the viscous time scale is much shorter than the dynamical time scale.

Gas pressure will also cause the ring to spread out. It is the main purpose of these simulations to compare the SPH artificial viscosity term with the viscous torques of the axisymmetric theory, described in Chapter 2, so we will start by switching the pressure off.

It is quite apparent that the initial spreading of the ring is due to $v_r(r,0)$. So how does the viscous shear term affect the evolution of the ring? Will its influence be completely overshadowed by the initial radial velocity and therefore undetectable? To explore this question three simulations were run with identical initial density and radial velocity conditions. Disk parameters were also kept fixed, except for the SPH artificial viscosity coefficient $\bar{\alpha}$ which was set at $0.0, 10.0$ and 20.0 in the different simulations. With $\bar{\alpha} = 0$ and no pressure, the particles are simply moving independently of one another in the gravitational potential of the central object. Their initial condition was a Keplerian angular velocity plus a small radial velocity. The particles will thus all follow slightly eccentric orbits in the plane. As a result, when we look at the density profile of the disk, we will see it oscillate between a broad flattened shape, and a tall, narrow profile.

We have seen that the viscous torque between adjacent rings is given by

$$\mathcal{G} = 2\pi r \nu \Sigma r^2 \frac{\partial \Omega}{\partial r}.$$

If Ω is a decreasing function of r (as is the Keplerian law of rotation) then the viscous torques will transfer angular momentum outwards. Thus inner rings will fall further in and outer rings will move further out. The disk will then tend to continue spreading rather than contracting.

So what we specifically want to look at is the rate of spread of the disks with the three different viscosities. Their initial evolution is shown in Fig. 5.3.1 ($\bar{\alpha} = 10.0$), Fig. 5.3.2 ($\bar{\alpha} = 0.00$) and Fig. 5.3.3 ($\bar{\alpha} = 20.0$). In each plot we see density profiles of the disk at intervals of 0.1 scaled time units, starting at $t = 0.0$, up to $t = 1.5$. The general behaviour of the three disks are similar with the initially rapid and subsequently slower spreading being the most apparent features.

A clearer picture emerges when we plot the maximum density of the three disks as a function of time for 600 timesteps (Fig. 5.3.4). We see the inviscid disk behaving as expected with the peak density oscillating. As stated before, the inviscid disk is actually a collection of noninteracting particles and we are just seeing the effect of their synchronised orbits. The peak of the $\bar{\alpha} = 10.$ disk decays more slowly than the inviscid disk indicating that the viscous term is having a significant effect. Eventually its peak density also rebounds slightly. This effect is caused by the increasing spacing between rings in the disk. The SPH viscous interaction occurs over a length scale h. Particles further than $2h$ apart will not viscously interact. Particles within the same ring have negligible viscous interactions because $\vec{v}_{ij} \cdot \vec{r}_{ij} \simeq 0$. Thus, when the rings get sufficiently far apart, the particles cease interacting and we see the same effect of the synchronised orbits as with the inviscid simulation.

The $\bar{\alpha} = 20.0$ disk decays at an even slower rate than the other two. Its decay continues past that of the $\bar{\alpha} = 10.0$ case before levelling off abruptly. Here the simulation has run up against the limits of its own resolution. A particle's density is obtained with a summation over all nearest neighbours. These can be split into two groups; those on its own ring, and those on other nearby rings. As the simulation proceeds, the rings separate and the contribution of particles on other rings declines. The ring itself expands only slightly (particularly so for the ring at the peak of the density curve which hardly moves at all) so particles on the ring remain at roughly constant distances from one another and the contribution of these neighbours remains roughly constant with time. The flat section of the $\bar{\alpha} = 20.0$ curve between $t = 2$ and $t = 4$ is an example of this effect.

If we were to increase the number of particles in the simulation by decreasing the particle separation, Δr, both along and between rings, we would find that a particle's density was obtained by a summation over more particles and thus the contribution of each neighbour is diminished. The total number of neighbours $\propto \frac{1}{(\Delta r)^2}$, but the number of neighbours within a particle's own ring is only $\propto \frac{1}{\Delta r}$. Thus decreasing Δr also reduces the relative importance of neighbours on the same ring. We can thus achieve lower densities before cutoff occurs. Of course, increasing the particle number also increases the computational time and so a compromise must be made.

Another method of studying the results of SPH simulations is to plot all the particles, coloured, for example, according to their density. These can be viewed as a sequence of still frames or be put together to make an animation of the disk. There is often much information in the animations that is not apparent in the more traditional graphs and figures we have seen above. Fig. 5.3.5 shows the disk at six equally spaced times with the particles coloured according to disk surface density (scale at right of figure). They clearly show that the greatest change in the disk peak density of the disk occurs over the first few frames (i.e. over a time of ~ 0.4 scaled units in agreement with the estimate of the viscous time scale we made above). The latter frames show a more leisurely rate of change in the density occurring, accompanied by a significant spreading of the initially narrow ring.

Let us summarise what we have learnt from these simulations. Firstly, the initially rapid spreading of the disk is due to the initial radial velocity condition. Secondly, viscosity slows down the spreading of the disk. This is a significant effect which is clearly seen. We have seen that the SPH simulations have a resolution limit related to the particle number density. Finally, there is a second problem in the simulations caused by the increasing distances between rings. When the ring separation becomes comparable to the length scale of the SPH interpolating kernel, SPH can't model the viscous shear between rings and the calculations lose their validity.

5.3.2. SPH Meets Axisymmetric Disk Theory

In this section we compare the evolution of our SPH disk simulations with solutions to the time dependent axisymmetric thin disk equations derived in Chapter 2.

We start by considering the $\bar{\alpha} = 10.0$ simulation described in the previous sections. The interparticle spacing $\Delta r = \frac{1}{2}h$. Fig. 5.3.6 shows density profiles for this simulation taken at 20 timestep intervals from $t = 0.00$ to $t = 0.80$. On the same axes we have plotted (solid lines) the theoretically obtained disk profile for the same time. These curves were obtained by taking the general equation for the density at time t, Eq. (2.2.38) and substitute Eq. (5.1.1) for the initial density and Eq. (5.1) for the viscosity to give

$$\Sigma(r,t) = \frac{4}{3\bar{\alpha}chtr^{\frac{1}{4}}} \int_{r_1}^{r_2} e^{-\frac{(r_0-r_c)^2}{l^2}} r_0^{\frac{5}{4}} e^{-\frac{2\left(r_0^2+r^2\right)}{3\bar{\alpha}cht}} I_{1/4}(\frac{4r_0 r}{3\bar{\alpha}cht}) dr_0. \tag{5.3.5}$$

This was numerically integrated with **`Mathematica`**, using the same approximations as in Section 2.3. The agreement between SPH and thin disk theory appears to be very good here. We will go on to investigate the extent of the agreement. For the moment, note two things. Firstly the height of the initial SPH density curve (topmost set of points) is about 5% less than it should be (as given by Eq. (5.1.1), the topmost solid line). The failure is due to the narrowness of the initial Gaussian relative to the length scale h. As we mentioned in the previous section, a particle's density is determined via a summation over all particles within its neighbourhood (i.e. less than $2h$ distant). Changes in the density over length scales shorter than this tend to be smoothed out. The problem can be removed by increasing l the length scale of the Gaussian. However the viscous time scale is proportional to l^2 so by broadening the Gaussian we also dramatically slow down the viscous evolution of the ring.

The second point to note is that the decline of the density in the simulation is very slightly slower than theory predicts. If we compare simulation and theory at slightly later times, Fig. 5.3.8 we see that the agreement has started to deteriorate. It is still quite good at $t = 1.00$ (100 timesteps) but fairly poor at $t = 1.50$ (150 timesteps). The deterioration appears to be due to the resolution limitation discussed in the previous section. As the rings move apart, a particle's density is more and more dependent upon its neighbours within the same ring. If this is so, then increasing the number of particles in the simulation will, as previously discussed, extend the agreement of theory and simulation to a later time.

In Fig. 5.3.7 we plot the maximum density of the simulated disk as a function of time against the theoretical $\Sigma(r_c,t)$, where r_c is the centre of the initial density distribution. In actuality the density peak migrates inwards with time albeit very slowly. As a result, at later times $\Sigma(r_c,t)$ will be an underestimate of the peak density. This effect is however very small. This diagram again demonstrates the very close agreement the simulation has achieved with the theory. However, the two points of difference raised above are again apparent.

To test the hypothesis that the mismatch at later times is due to the excessively high proportion of neighbours in the same ring a second simulation was run. All the disk parameters were kept fixed, as were the initial velocity and density profiles. The interparticle and inter ring spacing δr was reduced from $\frac{1}{2}h$ to $\frac{5}{13}h$ $(\simeq .38h)$. The setup now required 37478 particles in 27 rings. We find, as expected that closer particle spacing means better agreement with the theory over a longer period of time. Fig. 5.3.9 shows the $t = 1.00$ and $t = 1.50$ profiles of the new simulation with the corresponding theoretical curves. The $t = 1.0$ curves agree almost perfectly and the $t = 1.5$ curves display good agreement. In Fig. 5.3.10 we see a marked improvement in the agreement of the peak densities. One can still detect that the SPH disk is decaying a fraction more slowly than the the theoretical curve. This effect could equally as well be due to the migration inwards of the peak and our underestimate of the theoretical value. Finally we compare the peak densities of the two $\bar{\alpha} = 10.0$ disks (Fig. 5.3.11) and see that the second simulation with more particles is capable of going to lower densities than the original one. We can now proceed with reasonable assurance that we can understand the mismatch between theory and simulation.

In the previous section we showed that the effects of the viscous shear on disk evolution were not completely overshadowed by the initial radial velocity. In Fig. 5.3.12 we display the $t = 0.60$ density curves of the three simulations described in the previous section (all with particles $\frac{1}{2}h$ apart). To reiterate, all these runs start with the initial radial velocity appropriate to the $\bar{\alpha} = 10.0$ disk. They evolve with $\bar{\alpha} = 0.0, 10.0$ and 20.0 respectively. On the same axes we have plotted the theoretical density profile corresponding to $\bar{\alpha} = 10.0$. This figure shows how well the theory and simulation agree. If Eq. (5.1) was not holding even approximately then we would see it on this graph. In Fig. 5.3.13 we have attempted to put fairly rigorous error bounds upon the match between theory and simulation. This time we are comparing simulations with $\bar{\alpha} = 8.0, 10.0$ and 12.0 with the theory. Near the peak itself, the theory clearly best matches the $\bar{\alpha} = 10.0$ curve. At the edges of the ring the differences between the three curves are too small to judge the best fit. Overall we could fairly safely place error bounds of $\pm 10\%$ upon Eq. (5.1), at least for these simulations.

5.3.3. Angular Momentum Conservation

The SPH programs used in this chapter were written in `FORTRAN` and run in both single and double precision. Here we just wish to detail the performance of the code in conserving angular momentum for the $\bar{\alpha} = 10.0$ disk used in previous sections (with $\Delta r = \frac{1}{2}h$). This gives some sort of indication that the operator split algorithm is working effectively. Fig. 5.3.14 shows the change in the angular momentum of the disk over a double precision run of 150 timesteps. The angular momentum is conserved to great precision with a maximum variation from the original value of $\pm 3 \times 10^{-7}$. The precision is significantly degraded in single precision. This is to be expected as the truncation errors are approximately seven orders of magnitude larger. Fig. 5.3.15 plots the angular momentum as a function of time for 600 steps of a single precision run. The variation is now up to $\pm 4 \times 10^{-5}$. The variability shows no signs of increasing with time and there is no immediately obvious trend in the data. This is just a quick, simple test of the algorithm and program. It would not necessarily show up every fault or bug, however if the test failed then there would certainly be a fault somewhere in our work.

5.3.4. The Effect of Pressure

Previous simulations in this chapter have had the pressure set to zero. Here we consider how a nonzero pressure affects disk evolution. For simplicity we consider an isothermal equation of state

$$P = c^2 \rho, \tag{5.3.6}$$

with c, the sound speed, being constant. The pressure term in the radial component of the Navier-Stokes equation is

$$a_{pr} = c^2 \frac{\partial \ln \rho}{\partial r}. \tag{5.3.7}$$

With $\Sigma(r, 0)$ given by Eq. (5.1.1) we have initially

$$\begin{aligned} a_{pr} &= -\,2\,(r - r_0)\,\frac{c^2}{l^2} \\ &\simeq \frac{c^2}{l}. \end{aligned} \tag{5.3.8}$$

The gravitational acceleration

$$a_{gr} \sim \frac{1}{r^2}.$$

Therefore

$$\frac{a_{pr}}{a_{gr}} \sim \frac{c^2 r^2}{l} \ll 1. \tag{5.3.9}$$

So the effect of the pressure will be small. However it will cause an additional spreading of the ring. A comparison of a simulation including pressure with theory will lead us to underestimate the viscosity. We ran a standard $\bar{\alpha} = 10.0$ disk with $\delta r = \frac{1}{2}h$ and all other parameters as in Table 5.1.1. In particular the sound speed $c = 0.02$. This gives us a Mach number $\mathcal{M} \simeq 50$. Fig. 5.3.16 shows the density profile of the simulation every 10 steps, from $t = 0.00$ up to $t = 1.50$. The addition of pressure has done little to change the basic character of the disk evolution.

In Fig. 5.3.17 we plot (as we did with the purely viscous disks) radial profiles against theoretical curves. The increased spread of the disks is clearly evident. Whereas for the purely viscous disks (Fig. 5.3.6) the simulation and theory aligned quite well, now we see at each time that the simulated disk has decayed further than the theory.

In Fig. 5.3.18 we plot the peak density vs time curves of the $\bar{\alpha} = 10.0$ simulations with and without pressure. We see once more that the pressure accelerates the spreading of the disk and the decline in the peak density. As mentioned in the introduction to this chapter, Hirose (1991) and Artymowicz et al. (1991) attempted to determine the viscosity from simulations that included pressure. They will thus have measured some sort of overall diffusion coefficient rather than finding the diffusion due to the artificial viscosity term. In our simulations we saw that the viscous term slowed the rate of spread of the disk. The pressure on the other hand added to the spreading. Thus in our case, if we had not removed pressure from our early simulations, we would have underestimated the artificial viscosity term.

5.4. The $v_r = 0$ Case

As discussed in Chapter 1, if we legislate that the angular velocity of gas in the disk be a function of the radius only, in an initial value problem we are free to select only one of the density and the radial velocity at $t = 0$ but not both. The angular velocity assumption restricts us to a small class of solutions. But are these always the most physically interesting solutions?

Let us consider a disk with the Gaussian initial density function used previously in this chapter. Let us now specify the initial radial velocity to be

$$v_r\,(r,0) = 0, \qquad \text{all r} \tag{5.4.1}$$

and the angular velocity to be Keplerian. If the gas is inviscid, there are no torques between neighbouring annuli of the disk. There will be no radial diffusion and the disk will remain unchanged in its initial state. How will the disk respond if the viscosity is suddenly switched on? Let us take the three disk equations, Eq. (2.2.17),Eq. (2.2.18) and Eq. (2.2.19), and substitute the above initial conditions. Note that Eq. (5.4.1) implies that

$$\frac{\partial v_r\,(r,0)}{\partial r} = 0 \qquad \text{all r.} \tag{5.4.2}$$

From the equation of mass conservation we initially have

$$\frac{\partial \Sigma\,(r,0)}{\partial t} = 0. \tag{5.4.3}$$

The Navier-Stokes equation tells us that

$$\frac{\partial v_r\,(r,0)}{\partial t} = 0, \tag{5.4.4}$$

and from the momentum conservation equation we have at $t = 0$

$$r^2 \Sigma \frac{\partial v_\phi}{\partial t} = \frac{1}{2\pi}\frac{\partial \mathcal{G}}{\partial r}. \tag{5.4.5}$$

The equations tell us that the disk's initial response will be to the sudden application of viscous shear forces will be entirely in the angular velocity. The density and radial velocity functions are initially stationary.

5.4.1. Results

In this section we consider a disk simulation with the same setup as those of previous sections. The basic parameters are given by Table 5.1.1. The viscosity coefficient, $\bar{\alpha} = 10.0$, the interparticle spacing $\Delta r = \frac{1}{2}h$, and the density profile is given by Eq. (5.1.1). This disk will not have its initial radial velocity given by Eq. (5.1.5), but will instead have it set to zero. We will refer to this disk as the *stationary* disk, as opposed to the standard disk described in previous sections which has $v_r(r, 0)$ given by Eq. (5.1.5).

As we have done with previous simulations, we have plotted density profiles of the disk taken at ten timestep intervals from $t = 0.0$ to $t = 1.5$ in Fig. 5.4.1. The dramatic initial decline in the density peak characteristic of previous simulations is not seen here. Instead the density peak seems to remain virtually constant for a period of time before eventually starting to decay and spread.

Fig. 5.4.2 is a sequence of views of the disk, coloured to indicate surface density. The density-colour key (to right) is identical to that in Fig. 5.3.5 and we have taken the frames at identical times, so the two figures can be quickly compared. In the stationary disk, a red band indicating an area of high density is visible even in the $t = 0.6$ frame, whereas in Fig. 5.3.5 the high density region had already decayed away by the time of the second frame ($t = 0.2$) which could perhaps be compared with the $t = 1.00$ frame in the stationary disk. Clearly the initial radial velocity has a strong influence on the course of a disk's evolution.

In Fig. 5.4.3 we display the peak density vs time curve of the stationary disk simulation on the same axes as the theoretical peak density curve for the standard disk. The rapid decline in the standard disk peak contrasts with the stationary disk peak which remains at its initial value before beginning a slow decline. If we were to define a disk's half life as the time it took for the peak density to drop to half its initial value, this stationary disk has a half life roughly three times as long as the comparable standard disk.

We now want to look at the azimuthal velocity to see how far the stationary disk departs from Keplerian behaviour. In Fig. 5.4.4 we have plotted, for several times, the azimuthal velocity of the particles in the standard disk as a function of radius. We have marked on each plot the Keplerian azimuthal velocity curve as a solid line. We note that even the standard disk departs slightly from Keplerian rotation. This occurs most noticeably at the inner and outer edges of the disk. Overall however the disk rotates to a good approximation in Keplerian fashion.

The same is not true of the stationary disk (Fig. 5.4.5, Fig. 5.4.6 and Fig. 5.4.7). The first few plots show the inner rings decelerating and the outer rings accelerating until the azimuthal velocity profile is almost flat. During this time angular momentum is being transferred outwards through the disk via the viscous torques. Having lost angular momentum, the inner rings fall further inwards, whilst the outer regions of the disk are flung further out. After a while the azimuthal velocity regains a reasonably Keplerian profile. This occurs once the initially sharp density gradients in the disk have been smoothed out. A second simulation was perormed with the particle separation $\Delta r = \frac{5h}{13}$. This confirmed that the azimuthal velocity plots were not contaminated by the particle number density effect.

5.4.2. Discussion

By assuming that $v_\phi = \sqrt{\frac{GM}{r}}$ we are ignoring a host of interesting solutions to the disk equations. We may even be misled into making erroneous conclusions about disk behaviour. Let us look at one particular area of research into disks where it could be important to consider the angular velocity to be time dependent, the modelling of dwarf nova outbursts. We have already decsribed outbursts in Chapter 3. One model, originally proposed by Osaki (1974), explains outbursts as periods of enhanced mass transfer through the accretion disk caused by some form of instability within it. What would cause such unstable behaviour was not known until Meyer and Meyer-Hofmeister (1981) identified a thermal instability likely to arise in CV accretion disks. The essence of the instability is that much of the disk gas flow occurs under conditions near to those needed to ionise hydrogen. Ionisation significantly affects the gas properties and the viscosity of the gas flow. For detailed summaries of the thermal instability, the reader is referred to Smak (1984) or more recently Meyer-Hofmeister and Ritter (1991). It is proposed that for low surface densities the gas is largely un-ionised and the gas flow is relatively inviscid. The tendency is for matter to accumulate in these regions as there is insufficient viscosity to cause it to drift radially inwards. The density and temperature increase and the gas ionises. It is assumed that one one consequence of the ionisation is a greatly enhanced viscosity, with the dramatic change in the gas properties occurs over the disk's thermal time scale which is much shorter than either of the dynamical or the viscous time scales.

The increased viscous dissipation in the region implies an increase in the thermal energy radiated away by the disk. The outburst is supposedly caused by large areas of the disk coherently jumping to the hot ionised state. However the enhanced viscosity increases the radial mass flow, causing the region to drain of mass and the surface density to drop. Eventually it will drop far enough for the ions to recombine and the region to return to its inviscid state. If we are to determine whether this essentially local instability has the capacity to cause an essentially diskwide disturbance, we need to how the density responds to a suddenly increased viscosity. Up until now, numerical studies of this thermal instability (Lightman (1974b), Meyer and Meyer-Hofmeister (1984) , Bath and Pringle (1981) and Lin et al. (1985)) have made use of the assumption of strictly Keplerian rotation. Specifically they have started from the radial diffusion equation for the density Eq. (2.2.25) (some authors adding source terms to simulate mass transfer from the secondary). Yet the standard theory on the other hand implicitly assumes that any change in the viscosity will occur on a very long time scale. If we relax our constraint upon the azimuthal velocity then we can handle more rapid changes in the viscosity. Our simulation neatly illustrates the point. By giving the disk zero radial velocity at $t = 0$, we are saying that prior to this time it was inviscid and no diffusion occurred. We start the simulation with a positive viscosity which is equivalent to saying the disk suddenly became viscous at $t = 0.0$ (via for example the thermal instability). This is apparently a physically important situation which cannot be modelled using standard theory.

Chapter 6.
SPH Simulations of Accretion Disks in Binary Potentials

6.1. Numerical Studies of CV Accretion Disks

Numerical studies of accretion disks in cataclysmic variables can generally be put into three classes; finite difference solutions of the axisymmetric thin disk equations, finite difference solutions allowing non-axisymmetric motion, and particle scheme simulations. Let us briefly consider their roles in the development and application of disk theory.

The axisymmetric equations for a geometrically thin disk in Keplerian rotation can be easily be put in finite difference form and solved approximately. The thin disk approximation means we can painlessly add to the basic density evolution equation (Eq. (2.2.38)) quite complicated radiation physics. As a result such axisymmetric calculations are used as diagnostic tools to help determine the detailed physics of observed disks, and as simple test beds for hypotheses (e.g. the thermal instability model for outbursts in dwarf novae). Pringle, Verbunt and Wade (1986), and Wood (1990) are two papers that illustrate this use for axisymmetric calculations. These models ignore the angular variation in disk properties as being unimportant in the determination of its gross response, with the only concession to asymmetry being the addition of a bright spot to the basic model. A second concern is the reliance of these calculations upon the assumption of Keplerian rotation. This point has already been expanded upon in Chapter 5.

The second and third categories of simulation put more emphasis upon the dynamics of the disk, and in particular upon the influence of the binary gravitational potential, at the expense of incorporating complicated gas thermodynamics. The two types of simulation, finite difference solutions to the fluid equations and particle based simulations, are in general not directly comparable as they approach the problem from different directions and rely upon different assumptions e.g. about the disk viscosity. A general remark about both types of simulation is that their purpose has been to guide and verify the general theory. Because of the absence of detailed radiation physics they have not been suited for use as tools for directly interpreting observations.

Fully two dimensional finite difference solutions of the fluid equations have been used to investigate a theory for angular momentum transfer alternative to the Shakura and Sunyaev model. Rather than assuming a viscously shearing disk, it is assumed that the disk is inviscid and that angular momentum is transferred outwards via a set of spiral shock waves. The observations however do not fit the spiral shock model. A recent set of simulations is detailed in Matsuda et al. (1990). These calculations are not easy or cheap, requiring large amounts of time on supercomputers and so at this moment are less accessible as modelling tools.

Particle based simulations are also being used to study disks in the full binary potential. The complicated geometry of the gravitational potential greatly increases the complexity of a finite difference scheme. In particular the mesh required to cover the computational domain is not simple, and must be recalculated for each binary mass ratio. The complexity of truly Lagrangian particle methods on the other hand is not significantly influenced by the potential's geometry. In this thesis we have used the same SPH code to run both axisymmetric disk simulations and calculations in the full binary potential. The relative simplicity of particle methods implies that they are cheaper to run than the equivalent finite difference calculations. On the other hand the finite difference path is well trodden with stability and accuracy problems being well understood. By comparison much less work has been done with particle methods and there is the perception, well founded or not, that they are somehow less reliable than finite difference methods. In fact early particle simulations of disks used quite an ad hoc approach to modelling viscous shear. One of the central aims of this project has been to critically evaluate the SPH artificial viscosity term's ability to model viscous shear forces, and to quantify its dissipative effects. As there are several groups around the world using SPH to model disks it is important that this basic work be done. The particle schemes used to date can be roughly divided into three groups; SPH codes, Particle In Cell (PIC — a method due to Harlow) schemes, and methods based upon the viscous particle method of Lin and Pringle (1976). The last was developed specifically to simulate thin disks in binary systems. Lucy (1977) cited the Lin and Pringle work as the 'direct stimulation' for his development (simultaneously with Gingold and Monaghan (1977)) of SPH. So we might describe the viscous particle method as being one of the ancestors of SPH. In fact PIC is also seen as an SPH forebear.

In view of its central role in disk modelling, we will have a brief look at the viscous particle method. The accretion disk is represented by a collection of particles moving in two dimensions in the plane of the binary. As we have previously discussed, in the plane, pressure forces are small compared to gravity. In this method they are neglected completely. Viscous forces, because of their role in redistributing angular momentum throughout the disk, cannot be ignored. They are simulated with periodic instantaneous reactions between the particles. In between interactions particles move completely independently of one another as if they were test particles in the restricted three body problem. The interactions occur at regular time intervals Δt when the computational domain is covered with a square grid of cell size l. Particles can only interact with others in the same cell, and not with particles in other cells. This is a point of difference with SPH which is purely Lagrangian with particle-particle forces being determined completely independently of any grid. So, the position and velocity of the centre of mass, $\vec{r}_{cm}$ and $\vec{v}_{cm}$, of all particles within a cell are determined. Particle velocities are then adjusted to put them in rigid rotation about this centre of mass. The angular velocity Ω is chosen so as to conserve the total angular momentum of the particles in the cell. The particles new velocities are given by

$$\vec{v}_i = \vec{v}_{cm} + (\vec{r}_i - \vec{r}_{cm}) \times \vec{\Omega}. \tag{6.1.1}$$

Particle positions are not altered during the interaction, effectively making it instantaneous. Both linear and angular momentum are conserved at the cell level. For a given angular momentum the state of lowest energy is rigid rotation. Thus the effect of the interaction is a net removal of kinetic energy from each cell. This loss is intended to correspond to the energy dissipation viscous shear would cause in the region. In line with thin disk theory this energy is transported vertically out of the disk plane. In this case it is assumed to be instantaneously radiated away.

We see that Lin and Pringle have taken an ad hoc approach to modelling the viscosity in the disk. Let us consider its advantages and disadvantages. Firstly we note that it is a simple numerical scheme that appears to address the basic dynamical issues. As we stated in Chapter 2, very little is known about the mechanism producing the dissipation. In the absence of such knowledge it is probably wise to keep the model simple. In previous chapters we have discussed the relative length of the disk's viscous and radiative time scales. Any simulation run to study a disk's viscous evolution will have to run for many orbital periods. It is important therefore to have a method that is simple and computationally efficient. Viscous particle simulations have been run for hundreds of binary orbital periods. Without the dedicated use of a very powerful computer for long periods of time this simulation length is beyond the capacity of finite difference schemes. SPH lies between finite difference schemes and the viscous particle method in its simplicity and thus we expect SPH calculations to be somewhat more time consuming than the equivalent viscous particle simulation but also to be much more rapid than finite differencing.

A disadvantage of the viscous particle method is that it has little theoretical underpinning. We can't, as we did in Chapter 4, theoretically estimate the magnitude of the dissipation. What we can say is that, using a dimensional argument, for a given grid of size l and a timestep between interactions Δt

$$\nu = C\frac{l^2}{\Delta t}. \tag{6.1.2}$$

But the magnitude of the constant C has to be determined by comparing simulations with other results. Furthermore the physics it describes is strictly limited and can't be extended in any systematic way. The SPH equations by comparison have been developed from the fluid equations of motion in a straightforward way. Thus if we wish to alter the physics being simulated we just return to the original fluid equations, modify them and then derive an equivalent SPH set of equations. Theoretically we can include as many different physical processes in our SPH algorithm as we wish. In practice the code must also satisfy accuracy, stability and computing speed constraints. Another key aim of this thesis is to bridge the gap between particle simulations and observations by incorporating some radiative physics into the code.

Lin and Pringle in their original work concluded simulations for three different mass ratios

$$q = \frac{m_{sec}}{m_{wd}} = \frac{5}{2}, \frac{1}{2}, \frac{2}{5}.$$

In each case they started with no particles in the simulation, injecting them at a steady rate from the inner Lagrangian point L_1 with a velocity vector as calculated by Lubow and Shu (1975). They followed each for several tens of orbital periods and found them all to reach a steady state.

Whitehurst (1988 a,b) heavily modified the Lin and Pringle method. He replaced the Lin and Pringle pseudo-viscous interaction so that a particle no longer interacted with all particles in its cell but instead with a single near (not necessarily nearest) neighbour. This eliminated any artificial grid from the calculations. Instead of adjusting velocities as above, Whitehurst chose to give the particles, upon interaction, an additional acceleration

$$a_i = \begin{cases} \frac{C^2}{r} + \frac{Qu^2}{r} & u < 0 \\ \frac{C^2}{r} & u \geq 0 \end{cases}, \tag{6.1.3}$$

where $u = (\vec{v}_i - \vec{v}_j) \cdot (\vec{r}_i - \vec{r}_j)$ and $r = |\vec{r}_i - \vec{r}_j|$ for particle i and its near neighbour j. If $u < 0$ then the two particles are approaching each other. The $\frac{C^2}{r}$ simulates a pressure force between the two particles. The original Lin and Pringle algorithm neglected pressure. The $\frac{Qu^2}{r}$ term is the dissipative term. Note that it is nonlinear. Whitehurst (1988 b) showed that it is similar to the nonlinear β component of the SPH artificial viscosity term. He argued that because the flow is highly supersonic, this rather than the $\bar{\alpha}$ component is needed to prevent problems of particle interpenetration. We remark that the β term was included to control penetration in shocks. With the shearing force in these disks, shocks are not a feature and particle penetration is not a major problem. We have chosen to set $\beta = 0$ and only use the linear component. Other authors have also done this. We also note that in our case we have removed the switch on the viscosity term. Other authors have kept it in place.

Whitehurst did not use any form of interpolation when calculating pressure and viscous forces and so had to restrict himself to interacting with a fixed number (one) of near neighbours. In other simulations that he carried out with interactions evaluated for all neighbours within a cutoff radius r_{co}, the forces were found to be proportional to the particle number density. Whitehurst also devoted considerable energy to developing a fast, efficient algorithm. He did away with the concept of a single timestep for all particles and introduced a binary tree of time steps (see Section 4.7 for details).

The algorithm Whitehurst ends up with is almost a halfway house between the viscous particle method and SPH. It is truly Lagrangian but does not use interpolation to calculate gradients. Unlike SPH it is not derived from the fluid equations, instead its underpinning is that basic constants of the motion are conserved in the method (mass, linear and angular momentum). In fact, in a summary of the capabilities of various methods for modelling disks, Whitehurst and King (1992) incorrectly criticise SPH for introducing a "scalar numerical viscosity which will tend to destroy the genuine momentum transfer of the disc by non conservation of *local* angular momentum". The simulations in Chapter 5 found that SPH accurately modelled the angular momentum transport due to viscous shear. Other tests of angular momentum transport are noted in Monaghan (1988), all of which found SPH to perform satisfactorily. We note that the artificial viscosity term conserves both linear and angular momentum and is Galilean invariant.

Whitehurst simulated a disk in a system with mass ratio $q = 0.15$. Rather than achieving a steady state disk with a shape that was approximately constant with time, he found one that was quite eccentric and rotated around the white dwarf. In the frame of the binary this disk motion was in the opposite sense to the binary's with a fractionally longer period (1.035 times that of the binary). In the inertial frame the disk was seen to rotate slowly in the same sense as the binary.

Osaki (1985) had previously proposed an eccentric disk as the cause of the superhumps observed in SU UMa stars in superoutburst. He identified the eccentricity as the one-armed eigenmode of the disk which had an eigenfrequency ω_{pr} which was close to but not equal to zero. The superhump frequency ω_s would then be given by

$$\omega_s = \omega_b + \omega_{pr} \tag{6.1.4}$$

where ω_b is the angular velocity of the binary. To estimate the precessional frequency Osaki considered the orbits of isolated particles at radii appropriate to the outer edge of the disk. He approximated

$$\omega_{pr} \sim \Omega - \kappa \tag{6.1.5}$$

where Ω and κ are the angular velocity and epicyclic frequency respectively of such an isolated particle orbit. Osaki found

$$\frac{\omega_{pr}}{\omega_b} \sim \frac{3}{4}\frac{qr_d^{\frac{3}{2}}}{\sqrt{1+q}} \tag{6.1.6}$$

where r_d is the radius of the outer edge of the disk in units of the interstellar separation. Eq. (6.1.6) fits the observed superhump frequencies quite well. Osaki did not identify any mechanism by which the disk could become eccentric. Whitehurst's simulation showed that a tidal mechanism existed but did not identify it exactly.

Hirose and Osaki (1990) carried out simulations for a range of mass ratios using a standard Lin and Pringle algorithm. They found that an elliptic, precessing disk resulted for mass ratios $0.05 < q < 0.25$. In the same paper they investigated the cause of the eccentricity. Now Paczynski (1977) had claimed that gas orbits in these accretion disks were well approximated by a family of simple periodic solutions of the restricted three body problem. He found that orbits at the centre of the disk were approximately circular but at larger radii they become progressively more distorted. Far enough out the orbits are distorted enough to cross over orbits with smaller mean radii. Gas travelling along these outer orbits would experience considerable dissipation in the neighbourhood of these crossings. Paczynski's proposal was that the disk was effectively tidally truncated at the outermost periodic nonintersecting orbit (hereafter referred to as the last nonintersecting orbit or LNO).

Hirose and Osaki used the method due to Hénon (1966) to investigate the stability of those periodic orbits within the LNO. The analysis came down to integrating a test particle along a periodic orbit. A small perturbation was added to the particle's initial conditions. If after integrating for a full period the perturbation had grown, the orbit was said to be unstable. They found that for $q < 0.25$ the outermost orbits in the truncated disk were unstable. For very small q however the outermost orbits were marginally stable once more with the disk having a much reduced unstable region. Investigating further, Hirose and Osaki did a linear perturbation analysis of these noninteracting particle orbits. They were found to be unstable when their angular velocity in the inertial frame was three times that of the binary. In other words the instability mechanism was a 3:1 parametric resonance.

For the unstable disk simulations they measured a 'superhump' period which was simply the disk period in the frame corotating with the binary. The period was found to vary from 1.043 ± 0.010 for a $q = 0.1$ disk to 1.083 ± 0.025 for a $q = 0.2$ disk. They also conducted a second set of simulations with double the grid size, giving them a fourfold increase in the viscosity but a reduction in the resolution. These simulations produced unstable disks for a larger range of mass ratios. In fact all the coarse grid calculations resulted in eccentric disks except for a $q = 1$ simulation. It is possible that the decreased resolution and increased dissipation resulted in the disks somewhat overcoming the tidal truncation and extending further past the LNO than the fine mesh disks did. Hence the resonance region would still lie within the disk for larger mass ratios and the eccentric behaviour would still occur. Hirose and Osaki then compared the resulting disk periods with Eq. (6.1.6) and found a small but significant difference. The simulation results were fractionally larger. This also put them slightly larger than the observed superhump periods. They repeated the analysis in Osaki (1985) using a higher order approximation to the tidal potential to obtain

$$\frac{\omega_{pr}}{\omega_b} \sim \frac{3}{4}\frac{qr_d^{\frac{3}{2}}}{\sqrt{1+q}}\left(1+\frac{15}{8}r_d^2\right). \tag{6.1.7}$$

With r_d the disk radius taken to be 0.47 in units of the interstellar separation Eq. (6.1.7) was found to agree with the viscous particle results. The simulation periods were still systematically larger than the observations. Hirose (1991) extended the analysis of Osaki (1985) by numerically calculating the eigenvalue corresponding to the disk's eccentric mode. He assumed the disk was to first order axisymmetric with an axisymmetric equation of state. Though his results depended upon the sound speed, his values were still systematically lower than the simulation periods.

Lubow (1991 a,b) continued the study of the tidal instability. He pointed out that the orbits of non-interacting particles will not give a good indication of a fluid disk's behaviour at resonance because of the considerable pressure and viscous forces expected there. Consequently he performed a perturbation analysis of the cylindrically symmetric fluid equations under the action of a small tidal potential due to the secondary star. The $3:1$ resonance identified by Hirose and Osaki as the cause of the disk eccentricity is then simply the $3:1$ inner Lindblad resonance. Thus Lubow considered in detail (1991 a) the disk response to the $m=3$ component of the tidal potential

$$\Phi_m\left(r,\theta,t\right) = \Phi_m\left(r\right) cos\left[m\left(\theta-\omega_b t\right)\right], \tag{6.1.8}$$

with θ, r being cylindrical coordinates centred on the primary and ω_b defined as before. The disk responses are sinusoidal with argument $k\theta - l\omega_b t$. In general, to first order, the mth component of the tidal potential Φ_m gives rise to a $k=l=m$ tidal response in the disk. Now Lubow found that at the 3:1 inner Lindblad resonance, the $k=l=3$ tide coupled with any initial eccentricity (a $k=1$, $l=0$ mode) to induce a $k=2$, $l=3$ response. This is a two armed spiral that travels with speed $\frac{\omega_b}{2}$ in the rotating frame. This in turn coupled with the initial tidal response to generate an increase in the eccentricity. Thus Lubow had found that the mechanism for eccentrically destabilising the disk was a positive feedback loop . The growth of the eccentric mode strength was found to be exponential with rate

$$\lambda = 2.08 \times 2\pi\omega_b q^2 r_{res}^2 \frac{\Sigma_0\left(r_{res}\right) e\left(r_{res}\right)}{M\langle e\rangle}, \tag{6.1.9}$$

where r_{res} is the radius of the resonance, $e(r)$ is the disk eccentricity at radius r, M is the total disk mass and $\langle e\rangle$ is the mass averaged eccentricity. The calculation is valid for a disk with pressure and a small viscosity. Extending it to the high viscosity régime, one expects the travelling $k=2$, $l=3$ wave to be damped and the growth rate of the eccentricity to be diminished.

To verify his analysis Lubow (1991 b) conducted several two dimensional SPH simulations of fluid annuli orbiting a central point mass and subject to various small perturbing potentials. The code he used, incorporating a variable smoothing length, had been previously tested on galactic problems involving shocks. He broke the disk response down into its various components by Fourier analysing the particle distributions as functions of angle and time. In summarising the work of Hirose and Osaki we noted that the $3:1$ resonance only occurs within the disk for low mass secondaries. When it does occur within the disk it is always near the outer edge where particle orbits start to intersect one another.

Lubow felt that these intersections implied a large amount of dissipation occurred in this part of the disk. This in turn he took to imply that the density would be low here. According to Eq. (6.1.9) this would slow the growth of the eccentric mode. For that reason he initially used only the $m=3$ component of the tidal potential in his simulations. In this case the orbit crossings and the resonance region are more widely separated. Furthermore the analysis focussed upon the $m=3$ mode so this was a natural thing to do. Lubow found the eccentricity grew exponentially with a rate predicted by the theory. The two armed spiral wave was actually visible in the particle plots as well as showing up in the Fourier analysis. Eventually the eccentricity's exponential growth was slowed as higher order modes became excited and the the dissipation increased.

Lubow also performed simulations in the full binary potential. In this case he found there was a strong tidal response to the $m=2$ component of the potential which interfered with the travelling spiral wave so its full rotation could no longer be seen. With the mass ratio $q=0.10$ the disk was found to precess in a prograde fashion with $\frac{w_{pr}}{w_b}=0.025$. With $r_d=0.48$ Eq. (6.1.6) gives $\frac{w_{pr}}{w_b}\sim 0.024$. The equivalent Hirose and Osaki simulation found $\frac{w_{pr}}{w_b}=0.041$. Again there appears to be a small but significant difference between Lubow's, and Hirose and Osaki's results. To determine the reason why, we must consider the radial density profiles of the various disks. In the Lubow calculation an annulus was used so the density went to zero for small radii. Hirose and Osaki on the other hand had substantial mass in the inner disk. The density distribution depends upon the viscosity so by allowing ν to have a radial dependance we can alter the relative densities in the inner and outer disk and perhaps change its precession frequency.

SPH is now being used by several groups to look at CV accretion disks. Hirose (1991) used two dimensional SPH calculations to verify the viscous particles results of Hirose and Osaki (1990) detailed above. He found that his SPH simulations were more time consuming and he was prevented from exactly duplicating his unstable viscous particle runs. He was forced to use a very large viscosity to reduce the total number of particles. He also altered the injection procedure so that new particles were added to the system by placing them in a Keplerian orbit about the primary. The radius of the orbit was set at the Lubow-Shu or circularisation radius. With these modifications, Hirose ran a $q = 0.15$ simulation and obtained an elliptical, precessing disk in agreement with his viscous particle results. Hirose's work highlighted the importance of developing an efficient SPH code. In this Chapter we will describe longer and more detailed SPH simulations.

At this point we take time out to define the circularisation radius. Take a test particle injected at the L_1 point and follow its motion. Also consider the simple periodic orbits about the primary that intersect the test particle's path. At each point on its path, take the component of the test particle's velocity that is tangent to the periodic orbit at that point and compare it to the orbital velocity. At some point the two will match. We refer to the average radius of this critical periodic orbit (which is to good approximation circular) as the circularisation radius.

Meglicki et al. (1993) performed a three dimensional SPH accretion disk simulation which they were able to carry forward about one and three quarter orbital periods. With their injection stream no longer restricted to the orbital plane they found significant changes in the stream /disk interaction. In particular some of the stream passed over the outer disk, only encountering it at smaller radii. In that short simulation time they found that a dense ring formed at the circularisation radius within a less dense disk that extended roughly out to the last intersecting orbit. They interpreted this as being a long term feature of the disk. This is very surprising when one considers that the two dimensional simulations must be run for several orbits in order to follow the disk's viscous evolution.

6.2. Isothermal Simulations

We now move on to our own isothermal simulations. In this section we set down the basic assumptions and approximations, the boundary conditions, etc. for the calculations. The next two sections will be concerned with particular simulations. The calculations use the two dimensional operator split SPH algorithm described in Chapter 4, and tested in Chapter 5.

The simulations have been carried out in a similar fashion to those of Lin and Pringle (1981), Whitehurst (1988 a,b) and Hirose and Osaki (1990). We treat the binary as a pair of point masses in circular orbit about one another. We scale the problem by choosing our unit of length to be d the interstellar separation, our unit of mass to be the combined mass of the the two stars m and our unit of time to be $\tau = \sqrt{\frac{d^3}{Gm}}$ the reciprocal of the angular velocity of the two stars. In these units the primary has a reduced mass μ and the secondary $1-\mu$. The binary thus has a mass ratio

$$q = \frac{1-\mu}{\mu}. \tag{6.2.1}$$

The orbital period of the system is 2π. The gravitational acceleration of a test particle due to the stars is

$$\vec{a}_{grav} = -\frac{1}{r_1^3}\vec{r}_1 - \frac{1}{r_2^3}\vec{r}_2, \tag{6.2.2}$$

where $\vec{r}_1$ and $\vec{r}_2$ are the position vectors of the test particle relative to the primary and the secondary respectively.

We work in two coordinate systems, both with origin at the centre of mass of the binary. The first set, in which the program works, is fixed in space. In these coordinates the primary and secondary have position vectors

$$\vec{r}_p = (1-\mu)\left(\cos t\,\vec{i} + \sin t\,\vec{j}\right) \tag{6.2.3}$$

and

$$\vec{r}_s = -\mu \left(\cos t\, \vec{i} + \sin t\, \vec{j} \right). \tag{6.2.4}$$

The second coordinate system rotates with the binary, with the primary and secondary having fixed positions $(1-\mu, 0)$ and $(-\mu, 0)$. These coordinates are used to display results.

To this binary system we add a disk. The total mass of the disk is assumed so small that it has no effect on the stellar orbits. Disk self gravity is also ignored. We use the isothermal equation of state

$$P = \Sigma c^2. \tag{6.2.5}$$

with c the sound speed equal to a constant. Now we know that considerable heat is generated in the disk via viscous shear forces. In the isothermal approximation not only is this heat instantaneously removed but the entire disk is in contact with some huge heat source that maintains the disk at some nonzero temperature T_0. Obviously this is completely unrealistic but it is done so we can consider the disk dynamics in isolation. In the next section we will take the disk out of the air-conditioned laboratory and add some thermodynamics. Whitehurst (1988 a) made a similar decision to fix the sound speed.

The simulations are completed in two stages. In the first step we start with no disk at all around the primary. We then follow the long term buildup of the disk under steady mass transfer from the secondary. This involves following the disk for over a hundred binary periods. In the second phase of the study we look at the fully established disk in more detail studying it over intervals of a couple of binary orbits.

The mass flow from the secondary is assumed to be steady. It is modelled by injecting a single particle every timestep from the inner Lagrangian point, L_1 with a velocity and trajectory in accordance with the results of Lubow and Shu (1975).

Particles are removed from the system if they end the timestep within the white dwarf radius r_{wd}, within the Roche lobe of the secondary, or at a distance greater than r_{cutoff} from the white dwarf.

In practice when we test whether a particle lies within the secondary's Roche lobe we check if the Roche potential at that point $\Phi_R(\vec{r}) < \Phi_{Rcrit}$, the value of the Roche potential on the Roche lobe. If it is and the particle's distance from the secondary's centre of mass is less than the distance from the secondary to L_1, we assume the particle is within the secondary's Roche lobe.

The simulation effectively has open boundary conditions with the density going to zero at the edges of the disk. This may be OK at the outer edge of the accretion disk but is not so realistic where the disk meets the white dwarf. We have already covered the boundary condition debate in Section 2.4. Our choice of inner boundary condition (essentially to have a hole in the domain of radius r_{wd}) was made because it is very easy to implement. It is in line with the inner boundary conditions of previous particle simulations. We have restricted the computational domain to a circle of radius r_{cutoff} for convenience's sake. In order to determine particles' near neighbours, the program places a grid of cells (side length $2h$) over all the particles. Occasionally a lone particle is flung far from the disk. If left in the calculation this single particle can hugely increase the number of grid cells required and slow the program down to a crawl. A typical accretion disk calculation has of the order of 10^4 particles, so discarding the odd one now and again has very little effect.

With so many particles, a lot of computer memory is required to record the complete state of the disk. For each particle we must store the position, velocity, mass, density, force, and rate of energy dissipation. It is neither practical nor desirable to store the state of the disk at the end of every timestep. On the other hand a single run of 10^5 timesteps can take several weeks to run on a DEC station 5000, so we must save the disk state at regular intervals in order that we can restart from a crash, or consider an interesting stage in the disk's development in more detail, without having to return to $t = 0$. As a compromise between saving time and space, we save the disk state every 5000 timesteps (i.e. about every eight orbital periods). In a separate file, constantly being overwritten, we store the disk state at the end of the previous step. Once we have completed the major run, we return to various points in the evolution and produce more detailed data.

Table 6.3.1: Summary of constants for the $\mu = \frac{1}{2}$ simulation. All values are in our scaled units (see section 5.2).

Constant	Value	Comment
$\bar{\alpha}$	10.0	artificial viscosity coefficient
h	0.01	SPH smoothing length
c	0.02	sound speed
v_{inj}	0.1	initial velocity of particles injected at L_1 point (in rotating frame)
θ_{inj}	0.3491	angle to binary axis at which particles are injected (in radians)
Δt	0.01	timestep
r_{wd}	0.02	radius white dwarf

6.3. The $\mu = \frac{1}{2}$ Case

In this section we describe a simulation completed with equal mass primary and secondary stars. As a matter of fact no such cataclysmic variables are observed and there are theoretical arguments to suggest that they do not exist, so this does not appear to be an immediately useful case study.

However, the aim is to compare results with the viscous particle simulations of Lin and Pringle (1976), and Hirose and Osaki (1990). In both cases the simulations resulted in steady state disks. Hirose and Osaki compared their results with axisymmetric steady state. In so doing they were able to estimate the viscous shear produced by the viscous particle method. We conducted a similar comparison between our simulation and steady state theory as a further test of our methods.

With the Lin and Pringle viscous particle method, the kinematic viscosity is given by

$$\nu = C\frac{l^2}{\Delta t}, \tag{6.3.1}$$

where l is the length scale of the viscous grid cells, Δt is the time between viscous interactions and C is a constant of proportionality. Hirose and Osaki compared the azimuthally averaged density profile of their steady state result with the axisymmetric Eq. (2.4.13)

$$\nu\Sigma = \frac{\dot{m}}{3\pi}\left(1 - \left(\frac{r_b}{r}\right)^{\frac{1}{2}}\right). \tag{6.3.2}$$

With l and δt both set to 0.01 they found $\nu = 2.02 \times 10^{-4}$. Lin and Pringle chose $l = 0.02$ and so from Eq. (6.3.1) we expect the shear viscosity in their simulation to be roughly four times that in Hirose and Osaki's. We have selected the various parameters in our simulation to keep broad agreement with Hirose and Osaki's paper. Their values are listed in Table 6.3.1.

We wished our viscous interaction to have a comparable length scale to that of Hirose and Osaki so we set the smoothing length $h = 0.01$. We then chose the sound speed to give a highly supersonic azimuthal velocity i.e. so that

$$\mathcal{M} = \frac{\mu}{cr^{\frac{1}{2}}} \gg 1. \tag{6.3.3}$$

We chose $c = 0.02$. Setting $\bar{\alpha} = 10.0$ gives, via Eq. (4.4.14), $\nu_{sph} = 2.5 \times 10^{-4}$. Our choice was also influenced by practical considerations. From Eq. (2.4.13) we know that the mass of a steady state disk $M_d \propto \nu^{-1}$.

With equal mass particles this implies that the total number of particles in the disk $n \propto \nu^{-1}$. Setting a high viscosity reduces the number of particles required for the simulation. It also reduces the viscous time scale and so decreases the simulation time the disk requires to reach its final state (if any). On the other hand we do not want to set the viscosity so high that the results have little relation to reality.

Hirose and Osaki set the radius of the white dwarf $r_{wd} = 0.01$. We have chosen to double it for two reasons. Firstly if $r_{wd} = h$, the SPH particles would be able to 'see' one another across the hole. Particles that should not be influencing one another will affect each other's pressure and density, and interact viscously. A second consideration is that increasing the size of the white dwarf increases the minimum gravitational timestep used in the simulation. This was a more important criterion with the multi step method. With operator splitting, it is not the gravitational integration that consumes the most time in a timestep and so we save less by increasing r_{wd}. Changing it will also have a minor effect on the number of particles required for the simulation. Referring to Chapter 3, we see that 0.02 is still in accord with the observations.

The simulation initially run for this section had the pressure set to zero and only the viscous term in operation, however the results proved less than satisfactory. With the pressure turned off, particles were able to approach one another very closely. The artificial viscosity term acted to damp their relative motion. Every now and then a pair of particles became "stuck " together. As a result of being so close to one another these particles had extremely high densities. We have included a typical density versus radius plot for one such zero pressure simulation (Fig. 6.3.1). The majority of particles didn't experience this pairing and their densities are broadly in line with axisymmetric disk theory. These are the points clustered along the base of the plot. Above it we see a scattering of isolated points with very high densities that are the particle pairs we speak of. This is quite simply a defect in the simulation and is not a 'physical' phenomena. For this reason the simulation was repeated with the pressure term included. In all subsequent simulations in this work, the term is kept on. When particles approach one another very closely, there is a very large associated density gradient. The pressure force acts to smooth out these gradients and force the particle pair apart. As we saw in Chapter 5, adding a pressure term will affect the radial diffusion in the disk and reduce the accuracy of Eq. (4.4.14). This is a difference with the simulations of Hirose and Osaki, and Lin and Pringle, who ignored pressure forces.

We first consider the evolution of the accretion disk from zero mass to steady state. Fig. 6.3.2 shows the number of particles in the disk as a function of time. The particles have equal mass, so this plot effectively shows the growth of the disk mass with time. After about 600 time units, it has reached a steady value. The particle number vs time plots of Hirose and Osaki, and Lin and Pringle are very similar to Fig. 6.3.2. With an estimated viscosity of $\nu = 2.02 \times 10^{-4}$, Hirose and Osaki's disk reached a steady state size of 12,200 particles after a similar time ($\sim$ 600 time units). When we consider that particle number is inversely proportional to the viscosity, the two results agree quite well. In a second simulation with four times their original viscosity, Hirose and Osaki found the disk reached a steady size of 2,900 particles in a much shorter time. Lin and Pringle's disk (which also had $l = 0.02$) finished with 2,700 particles , achieving that size in approximately 120 time units. This is in agreement with the disk's viscous time scale being inversely proportional to the viscosity.

The spatial growth of the disk is displayed in Fig. 6.3.3. This is a series of six particle plots of the disk with particles coloured according to their density. We have elected to use a logarithmic scale (key to right). This visually enhances broad trends in the data at the expense of some resolution. The Roche lobe and last nonintersecting simple periodic particle orbit (LNO) are included as blue lines. The snapshots are taken in the coordinate system corotating with the binary. The secondary star is to the left in each frame. In discussing various regions of the disk we will always assume that we are looking upon it as in Fig. 6.3.3. Thus when we refer to the left of the disk we mean the half of the disk closer to the secondary star, and so on. In referring to the individual frames we shall number them 1–6 from left to right, then top to bottom. The frame number is not shown on these figures. The integer to the far left in each frame refers to the image making process. The middle integer is the number of time steps from the beginning of the simulation, the number to the far right is the simulation time (dimensionless units) of the frame.

When the Paczyński orbits do intersect one another it is on the left hand side of the Roche lobe, approximately along the binary axis. At the top and bottom of the disk, the periodic orbits become more broadly spaced before drawing together once more on the disk's right hand side (though the orbits do not cross each other here). If the Paczyński orbits were similar to the gas streamlines in the disk, gas would experience to compressions and two rarefactions upon each circuit of the white dwarf.

The first five frames of Fig. 6.3.3 show the disk at 5000 timestep (~ 8 binary orbit) intervals. A glance at Fig. 6.3.2 reveals that the disk mass is growing steadily over this period. Spatially however, the disk appears to have reached full size quite early in its evolution. We can see little change in the disk's size from $t = 250.00$ (when its mass is still growing) to $t = 1000.00$ (the end of the simulation long after the disk mass has stabilised). The left hand edge of the full size disk, lies just inside the LNO. On the right hand side a low density fringe actually extends beyond it. Hirose and Osaki found their disk extended a little beyond the LNO, but in terms of the total disk mass, the amount of disk lying beyond the LNO was very small.

We notice the development of a high density ridge along the left hand side of the disk coincident with the region where Paczyński's outer periodic orbits intersect the inner ones. In fact this is where the Paczyński streamline argument leads us to expect a high density region. The gas is moving anticlockwise around the white dwarf. We look at the gas in the outer disk. We see a compression in the flow at the top of the disk. This becomes the high density ridge around the left hand side. The ridge is not uniform but contains knots of very high density gas. These have condensed out of inhomogeneities apparent in the flow on the disks upper right edge. In fact nowhere around its circumference is the disk edge that smooth. Alongside the ridge, the disk edge wraps around the high density knots. As we follow the flow we see the disk edge develop a sawtooth structure. On the right hand side the disk is quite ragged with small clumps actually breaking off from the main disk and travelling on more eccentric orbits before rejoining it at the disk's top.

We gain more information from Fig. 6.3.4. This is another particle plot of the disk at $t = 1000.00$, this time with the particles coloured according to their radial velocity. As before, for similar reasons, we have used a logarithmic scale for v_r. Because relatively high radial velocities were concentrated in the injection stream and the inner region of the disk, we have masked these areas out. This enables us to see the radial motion occurring in the outer reaches of the main disk. The pink/red areas of the disk are moving radially outwards whilst the blue/green areas are moving inwards. We can see the compression at the top of the disk where the ridge is forming. It is apparent that orbits in the outer disk are elliptical. In the pink region on the lower left of the disk we see a lone green particle. This is in fact from the injection stream. As it was not simply stopped dead at the very edge of the but managed to penetrate a reasonable way into the disk we must conclude that the stream has a reasonable momentum relative to the disk edge. (This phenomenon has been identified in other frames and is definitely not a pigment of the imagination!)

In Fig. 6.3.5 we have plotted the density and radial velocities of all the particles in a small region with bounds $0.16 < x < 0.32$ and $-0.2 < y < -0.05$. This box includes the region of impact of the disk and injection stream. We have suppressed the y coordinate and plotted the properties against x. The stream particles have density $\Sigma \sim 0.01$. At the disk edge there appear to be three separate trends in the density with peaks at $\Sigma = 0.12, 0.075$ and 0.05. These correspond to three knots in the high density ridge. Obviously there is a good deal of variation in densities at the disk edge and so there will be a wide variation in collision conditions experienced by particles in the injection stream. On the radial velocity plot we see that by the time it strikes the disk the injection stream is moving with a radial velocity of 0.1 scaled units which is five times the sound speed. The disk edge on the other hand is at this point moving radially outwards with velocities approaching but not quite reaching the sound speed. The injection stream penetrates the disk from $x = 0.20$ to $x = 0.26$ where it is finally stopped. In this case the stopping distance was of the order of 6 to $10h$. If a dense knot should be passing under the injection stream, the stopping distance will be a lot shorter than otherwise. One could query how well the details of the stream's impact upon the disk are being handled. However one has to recognise that the simulation will handle basic features of the collision such as conservation of linear and angular momentum quite adequately and so the gross influence of the stream's impact upon disk behaviour should be well modelled.

We followed the disk evolution for a few hundred timesteps, recording the trajectories of a small selection of the particles (Fig. 6.3.6). Six of the nine particles were initially within the LNO. These particles followed orbits that were to good approximation circular. They could be described as being Paczyński periodic orbits with a small eccentricity and inwards radial drift superimposed. The three particles that started outside the LNO had far more eccentric paths. As with the Paczyński orbits, these particles all cross over the LNO. Initially this only occurs on the far left hand side of the disk, but as they lose angular momentum and drift inwards, larger and larger fractions of their orbits fall within the LNO. Even if the particle orbits are not precisely as predicted by Paczyński, they are similar enough that the argument should apply. The high density ridge then is just the region where orbits intersect and viscous particle interactions are strong.

Before we continue on to discuss the steady state disk we note that during the whole 100,000 step simulation not a single particle returned to the secondary or was flung out of the computational domain. This implies that the angular momentum removed from the disk was extracted by tidal torques. In the full system this would be returned to the binary's orbit but in this simulation it is simply lost. This result agrees with those of Hirose and Osaki, and of Whitehurst.

Hirose and Osaki compared their steady state disk with axisymmetric theory. Here we do likewise. First we azimuthally averaged the various properties of the disk. To do this we dropped all the particles in a set of radial bins corresponding to annuli of equal width. For each bin we then found the mean value of the property and the mean particle radius. For each bin we plot one point on the curve. In these figures the annuli were set to be 0.01 units wide. In Fig. 6.3.7 we have plotted the azimuthally averaged density for the $\mu = \frac{1}{2}$ disk at $t = 1000.00$. On the same axes are shown the solutions to Eq. (2.4.13) for $(\nu, r_b) = (2.40 \times 10^{-4}, 0.016)$ and $(2.35 \times 10^{-4}, 0.017)$. For all ν and r_b these values were found to give the best fit to the simulation data. We have obtained an estimate for the viscosity that agrees well with our theoretically derived value of 2.5×10^{-4} (verified to within $\pm 10\%$ in Chapter 5). Our range does however lie a fraction lower than the predicted value. But we have included pressure in this simulation and we know the pressure affects the radial diffusion. Given that the simulation is asymmetric and gas orbits are not exactly circular, this is perhaps the best agreement that we can reasonably expect. The matching of the theoretical solutions and the simulation is not so good for the innermost two or three simulation points. This should not concern us as we have seen in Section 2.4 that the theoretical solution fails near $r = r_b$, as it gives the result that the $\Sigma(r_b) = 0$. Our boundary condition should give a similar result except that SPH will smear the drop in density out over about a smoothing length. Of more concern is the hump in the simulation density curve at approximately $\log r = -1.3$. This is of course due to the ridge we discussed earlier. This plot tells us that the highest densities are to be found in the disk edge. We would expect that any model of the disk must somehow take account of this ridge. The gas extending beyond the ridge is by comparison very tenuous. This suggests a possible two component model for steady state disks in binary potentials consisting of a steady state axisymmetric disk, with a high density ridge superimposed along its left hand edge. With good accuracy the outer edge of the disk is given by the LNO.

So how believable are calculations that are run for up to one hundred thousand timesteps? Are the results overwhelmed by an accumulation of numerical errors? This question must be asked not just of our simulations, but also of those of Whitehurst, Lin and Pringle, and Hirose and Osaki. In fact we cannot answer directly. In the axisymmetric simulations of Section 5.3.3 we found our code conserved angular momentum well, over short periods of time. In the reduced three body problem there is only one constant of the motion, the Jacobi integral. In addition the disk mass is constantly changing, so we really cannot complete such quantitative tests. The best indication that results are reliable for such long simulations is the good agreement of steady state results with axisymmetric theory, and in particular that the viscosity giving best fit to the simulation agrees with our theoretical value for ν.

We have also considered the rate of viscous dissipation of energy per unit disk surface area. With our thin disk approximation we are effectively considering the disk luminosity per unit surface area. Adjusted for our scaled units, steady state theory gives us

$$D(r) = \frac{3\dot{m}}{8\pi r^3}\left(1 - \left(\frac{r_b}{r}\right)^{\frac{1}{2}}\right). \tag{6.3.4}$$

We have plotted the azimuthally averaged rate of viscous dissipation in the simulation at $t = 1000.00$ in Fig. 6.3.8. On the same axes we have plotted the theoretical solution for $r_b = 0.017$. The two curves agree brilliantly. This is a favourable result both for our simulation and the axisymmetric theory. It is interesting that the agreement between theory and simulation is better than it was for the density. Note that Eq. (6.3.4) does not depend upon the viscosity. The jagged peaks in the simulation data at larger radii are due both to the ridge and to the point where the stream impacts the disk (the hot spot). Compared to their immediate surrounds these two asymmetric features will be quite luminous. The radiation will however be dominated by the axisymmetric central regions of the disk where the viscous dissipation is very large. Current attempts to extract information from photometric observations of light curves model the disk as being axisymmetric with a superimposed hot spot. They do not take account of the high density ridge. This must be looked at further.

We now consider the role of the injection stream in the determination of the disk structure. We started from a steady state ($t = 1000.00$) disk and allowed it to evolve in the absence of any mass inflow from the secondary. Fig. 6.3.9 is a particle plot taken at $t = 1020.00$ (i.e. 2000 timesteps after the stream was switched off). The particles are coloured according to their density using a logarithmic scaling as before. We thus compare it with frame 6 of Fig. 6.3.3. With the injection switched off, the disk has spread further to the right and top, and the edge is generally more ragged with streamer like arms now a feature to the lower right. The streamer at the top middle that is the precursor to the high density ridge has become more prominent and extended. The ridge itself is perhaps more prominent with the knots now more convoluted. Overall, turning off the injection stream has lead to the disk spreading out and becoming more disordered. However, following the disk over an extended period, it was noticed that it was only the outer disk that was being disordered. That portion of the disk lying within the LNO remained undisrupted. To confirm this picture we have included a a particle path diagram (Fig. 6.3.10), with initial conditions identical to those in Fig. 6.3.6, that follows our no injection simulation. We see that the trajectori.e.s of the six inner particles are more or less unaffected by the injection stream. The orbits of the outer three particles however have become less regular in (Fig. 6.3.10). In particular the outermost particle has taken a distinctly more eccentric path in the no injection case.

We explain the disk spreading by referring to Fig. 6.3.5 . There we saw that the injection stream struck the disk with a very large radial velocity. Even though it is much less dense than the gas at the disk's edge, it still imparts a reasonable impulse in the negative radial direction. The impact region is located so that this impulse tends to decrease the eccentricity of particle paths at the edge of the disk. It also acts to restrict the fraction of the disk's mass that extends beyond the LNO, almost like a small potential barrier. When the stream is switched off (and the barrier removed) we have a problem analogous to those of Chapter 5. In these simulations we followed the spreading of rings after some similar release at $t = 0$. In this case we have additional effects caused by the binary potential. Density gradients in the disk caused it spread both inwards and outwards. However the gas that moved outwards beyond the LNO experienced increasing tidal forces that, in the absence of any damping from the injection stream, increased the eccentricity of its motion. As it travelled along these orbits, this gas underwent strong interactions with the edge of the disk and had its motion further disrupted. That fraction of the gas lying within the LNO however, continued moving along simple periodic nonintersecting paths. We will discuss the stability of these paths in the context of simulations for differing mass ratios μ.

As the simulation continued (it was followed for a total of 50,000 timesteps), no gas either left the system or returned to the secondary star. All particles removed from the simulation were accreted by the white dwarf. Even with the added kick from tidal forces, the gas in the disk's outer reaches is still bound to the primary. These tidal torques still remove net angular momentum from the disk, returning it to the binary orbit, as if the disk is acting as a small fly wheel in the system. The decay of the disk mass is shown in Fig. 6.3.11. This process was not simply the reverse of the initial disk growth from zero mass. In that case the gas formed a tightly coherent ring. As more gas was injected the ring gradually spread to fill the LNO. As it faded away however the density profile throughout the LNO was almost uniform. For about 100 scaled time units the disk mass decays at a constant rate, after which the decay appears to be exponential. Eventually all that was left was a sparse swarm of particles that interact with each other only weakly. They represent a tenuous gas that would be all that remained after the disk decayed away.

Table 6.4.1: Summary of constants for the $\mu = 0.85$ simulation (in scaled units).

Constant	Value	Comment
$\bar{\alpha}$	10.0	artificial viscosity coefficient
h	0.01	SPH smoothing length
c	0.02	sound speed
v_{inj}	0.1	initial velocity of particles injected at L_1 point (in rotating frame)
θ_{inj}	.366519	angle to binary axis at which particles are injected (in radians)
Δt	0.01	time step
r_{WD}	0.02	radius white dwarf

6.4. The $\mu = 0.85$ Case

In this section we discuss disk simulations for a binary with a primary of reduced mass $\mu = 0.85$ (i.e. a mass ratio of $q = \frac{3}{17}$). Rather than attempting to cover the entire parameter space we have concentrated upon a single mass ratio which matched an observed dwarf nova. We selected the well observed SU UMa system OY Car, described in some detail in Chapter 2.

The simulations of this section are once more isothermal. The majority of parameters are the same as for the last section. In accordance with the work of Lubow and Shu (1975) the angle of injection for the stream has been adjusted for the new mass ratio. The constants are recorded in Table 6.4.1. As before we start with an empty Roche lobe and proceed by injecting SPH particles at a constant rate (one per time step). We follow the simulation for 100,000 time steps (160 binary periods).

The number of particles in the simulation is shown as a function of time in Fig. 6.4.1. This diagram is very similar in character to Figure 5 of Hirose and Osaki 1990 (for a $q = 0.15$ calculation). Both figures show the disk mass reaching a maximum value after about 400 scaled time units (in our case it reaches a maximum size of 19592 particles at $t = 470$). In both simulations the disk mass then drops to a lower stable value. In this calculation the final value was roughly 18800 particles. Hirose and Osaki had maximum and final values of 22800 and 17500 particles respectively.

Hirose and Osaki found that the maximum in the disk mass coincided with the start of a periodic loss of particles back to the secondary star. The disk had previously become eccentric and started to rotate in the binary's frame. It kept growing until about $t = 400$ when, in the process of precessing, it began to just brush the secondary star's Roche lobe. The mass subsequently dropped before stabilising at a lower value as the disk found a balance between injection from the L_1 point, accretion onto the white dwarf and loss to the secondary. Our simulation results agree with their conclusion. The maximum in the disk mass coincided with the onset of particle return to the secondary. We also saw a few particles be flung out to large radii $r > r_{cutoff}$ where they were removed from the simulation. Their total number was however much less than the number of particles that returned to the secondary. Unfortunately, for this simulation, we do not have a complete record of the fates of all the particles. We can say that at $t = 830$ there were 18814 particles in the disk. At $t = 1000$ there were 18803. Over that period 17000 particles were injected at the L_1 point, 118 returned to the secondary, none left the system entirely and 16893 were accreted onto the white dwarf. Of the particles that left the system, 99.3% were accreted and 0.7% returned to the secondary. We can take these as being steady state figures.

Fig. 6.4.2 is a sequence of particle plots of the $\mu = 0.85$ simulation showing the disk's initial growth to maximum mass. As we have done before, we have coloured particles according to their density using a logarithmic scale. In each frame we have drawn the last nonintersecting orbit of a noninteracting particle

(LNO). As we discussed previously Paczynski (1977) predicted that the disk would be tidally truncated at the LNO. A second orbit has also been drawn in. This is the last stable noninteracting particle orbit (LSO) as calculated by Hirose and Osaki (1990). This approximately marks the location of the $3:1$ inner Lindblad resonance. Note that it lies inside the LNO. After the work of Hirose and Osaki, and Lubow (1991 a,b), when the disk edge encounters the Lindblad resonance we expect the disk to become eccentric and precess in a prograde fashion. This is indeed what the figure shows. The first few frames show a disk developing in a very similar fashion to the $\mu = \frac{1}{2}$ simulation. The steadily growing disk appears approximately axisymmetric with a high density ridge along its outer edge. By $t = 300$ (frame 4) the disk extends out to the LNO and indeed beyond it on the upper right hand side. Up until this time the disk appears to have been unaffected by the Lindblad resonance.

By $t = 350$ however its influence has become apparent. The disk is now eccentric and in prograde precession. We note that in this particular frame the major axis of the disk is approximately vertical (perpendicular to the binary axis). The high density ridge is less regular than in previous frames with a knotted structure becoming apparent. The eccentricity is even more apparent in the last frame where its major axis is now horizontal. Rather than a single ridge we now have a two armed spiral. This is the $k = 2, l = 3$ travelling wave identified in Lubow's analysis and seen in his SPH simulations. As we know, the $3:1$ resonance almost coincides with the region where simple periodic particle orbits start intersecting one another. Lubow stated that these intersections would lead to a density reduction here. This in turn would lead to a reduction in the growth rate of the eccentricity. By implication this would reduce the influence of the resonance upon the disk. Rather than a drop in the density we see an enhancement. Lubow did not see a ridge in his simulations due to his choice of initial conditions. Rather than allowing a disk to grow under steady mass transfer from the secondary he created an annulus of particles all travelling on simple periodic orbits of the potential. We have discussed the density ridge in relation to the $\mu = \frac{1}{2}$ simulation already. Similar density enhancements have been observed in two dimensional simulation by other authors (Hirose and Osaki 1990, Lin and Pringle 1976). Nobody has completed a three dimensional simulation that is of any use in this regard, so to what extent this feature is diminished in 3D remains to be seen. Its presence in three dimensions would strengthen the case for disk eccentricity being the cause of superhump.

We now consider the changes in particle orbits as the disk becomes eccentric. These will indicate the influence of the resonance upon fluid streamlines. In Fig. 6.4.3 and Fig. 6.4.4 we have plotted the trajectories of a small number of particles randomly chosen at $t = 300$ (frame 4 Fig. 6.4.2) and $t = 400$ (frame 6 Fig. 6.4.2) respectively. At $t = 300$ the orbits are all roughly simply periodic. The trajectories of the innermost particles are approximately circular with a small eccentricity and a net inwards radial drift. Further out the paths are more eccentric. The semi major axes of these orbits are not precisely vertical but actually rotated a few degrees in the clockwise direction. Now the simple periodic orbits of nonintersecting particles are exactly symmetric about the binary axis. The difference must therefore be caused by the inter-particle forces (pressure and viscosity).

Hirose (1991) also noticed that the disk's semi-major axis was slightly tilted. He noted that as a result of the tilt the net tidal torque experienced by a particle due to the secondary star was nonzero. Evaluating the total tidal torque upon the disk in one of his simulations he found that it was negative, meaning that angular momentum was being extracted from the disk. If the particles' orbits had been symmetric about the binary axis then the net tidal torque would have been zero.

On each trajectory plot we have drawn the LNO and inside it the LSO, as solid lines. Now the outermost particle trajectories extend beyond the LNO, particularly at the right hand side of the disk. As a consequence we see a certain amount of orbit crossing along the disk edge, largely on the left hand side. This region of orbit intersection corresponds to the high density ridge seen in Fig. 6.4.2. The important point to be gathered from Fig. 6.4.3 is that although the disk is starting to spill over the LSO particle orbits are still approximately simply periodic. The influence of the Lindblad resonance upon streamlines in the outer disk has yet to become significant. By $t = 400$ (Fig. 6.4.4) the story has changed. Particles in the outer disk are now following eccentric orbits that are approximately doubly rather than singly periodic with apastrons occurring at angular separations of roughly $\frac{4\pi}{3}$. In other words the azimuthal frequency (in the frame rotating with the binary) ω_θ and the radial frequency ω_r are approximately related by

$$\omega_\theta = \frac{2}{3}\omega_r. \tag{6.4.1}$$

This corresponds to the two armed spiral travelling wave mentioned previously. The particle orbits do not close exactly due to pressure and viscous forces and also due to the excitation of other modes in the disk. In his simulation using the full potential Lubow noted that other modes interfered with this spiral wave. We see that now orbital intersections are occurring over a much larger area of the disk and can be seen at smaller radii than in Fig. 6.4.3. The very inner part of the disk however remains unaffected by the resonance. Particle orbits here are still approximately circular and concentric.

Fig. 6.4.5 is a particle trajectory plot for $t = 1000$, by which time the disk has reached a non-stationary steady state. The double periodicity of orbits in the outer regions is still clearly apparent. It has not been overwhelmed by other modes or been destroyed by pressure and viscous forces. We know then that the two armed spiral is still moving round the disk. Overall the fraction of the disk dominated by the motion appears larger than in Fig. 6.4.4. Orbit intersections are occurring over more of the disk again though this is not quantified. Only at very small radii are disk orbits apparently nonintersecting and simply periodic. Fig. 6.4.3, Fig. 6.4.4 and Fig. 6.4.5 support the statement of Lubow (1991 a) that noninteracting particle orbits cannot be used to represent the disk in the region of resonances. All the orbit crossings highlight the importance of fluid forces in determining the disk response.

We now consider the growth of the disk's eccentricity by examining the motion of its centre of mass. Fig. 6.4.6, Fig. 6.4.7 and Fig. 6.4.8 follow it for 5000 time steps (50.00 scaled time units) from $t = 300.00, 400.00$ and 1000.00 respectively. Each figure consists of four plots. They show; the trajectory of the centre of mass in the inertial frame, and in the rotating frame, and its radial and angular coordinates (in the rotating frame) as functions of time. Collectively the plots in Fig. 6.4.6 show a periodic motion with uniformly increasing amplitude. Recall that at $t = 300.00$ the disk still appeared approximately axisymmetric. (frame 4 Fig. 6.4.2).

We have captured, in Fig. 6.4.6 then, the initial growth of the eccentricity as the disk encounters the $3:1$ eccentric inner Lindblad resonance. In Fig. 6.4.10 we fit two exponential curves to the peaks of the radius versus time graph (plot c) of Fig. 6.4.6. Now if the disk were perfectly axisymmetric, its centre of mass would of course be at $r = 0.0$. But even in the absence of the Lindblad resonance the disk will be distorted by the asymmetry of the potential. Hence the mean radius of the centre of mass is approximately $r = 0.355$. The amplitude of the oscillations in Fig. 6.4.10 give an indication of the energy in the eccentric mode. If the mode had an exponential growth rate we would expect the oscillations' amplitude to grow exponentially as well. We now look at the Eq. (6.1.9) prediction for the growth rate at $t = 300.00$. We assume that the eccentricity at the resonant radius (which we take to be $r_{res} = 0.48$) equals the mass averaged value. We get

$$\lambda = 9.38 \times 10^{-2} \frac{\Sigma_0 \left(r_{res} \right)}{M}. \tag{6.4.2}$$

At $t = 300.00$ in our simulation $\Sigma_0(0.48) = 2.03 \times 10^{-2}$ whilst the total disk mass $M = 1.6460 \times 10^{-2}$. We thus have

$$\lambda = 0.116. \tag{6.4.3}$$

Even accounting for the several assumptions made and that in Fig. 6.4.10 we are not directly plotting the growth of the energy in the eccentric mode, the simulation eccentricity is growing much more slowly than predicted. The coefficients differ by a factor of 100. We must conclude that eccentricity is being suppressed in the simulation. The obvious candidate is the injection stream which we have already seen in the previous section reduced the eccentricity of particle orbits in the outer disk, and also restricted its outward expansion.

When Lubow conducted a simulation in the full potential, the eccentricity grew quadratically rather than exponentially. Simulations using only the $m = 3$ component of the potential however did show an exponential growth rate that agreed with his analysis. He found that in the full simulation, other modes (the $k = l = 2$ mode in particular) interfered with the growth mechanism. So even in the absence of an injection stream the eccentricity grew more slowly than simple theory suggested.

We must point out that Lubow's simulations are not directly comparable to ours. His disks had a smoothly varying density profile and no mass injection. We also note that during this eccentricity growth, the mass of our disk was not stationary but still increasing. We would expect the distribution of this additional mass to be affected by the resonance. We would then expect it in turn to influence the disk's response to the resonance.

To summarise then, in our simulation the disk eccentricity grew much more slowly than predicted by Lubow's analysis (1991 a). We strongly suspect the injection stream of suppressing the growth rate. The presence of other modes in the disk, excited by the full binary potential, may also interfere with the eccentricity growth. Simulations with the gas injected at the circularisation radius rather than at L_1, would help answer this question.

By $t = 400$ the amplitude of the motion of the centre of mass has increased greatly (Fig. 6.4.7). The disk is now visibly eccentric (frame 6 Fig. 6.4.2). The motion does not, however, continue to grow at the same rate. At $t = 1000.00$ the disk has reached a steady state. But now, unlike in the $\mu = \frac{1}{2}$ case, it is a precessing rather than stationary state. Whitehurst (1994) Fourier analysed the disk's radial mass profile with respect to time in order to determine its precession rate. After a lot of hard work he obtains a figure which we can read straight off Fig. 6.4.8. Indeed plotting the trajectory of the disk's centre of mass is a cheap method of probing the disk motion. We have already used it above to estimate the growth rate of the eccentricity.

The character of the disk precession is shown in Fig. 6.4.9. This is a sequence of six particle plots at 100 time step (1.00 time unit) intervals. They thus approximately cover a full period of the disk's eccentric motion. The two armed spiral mentioned earlier is visible in several frames, though not always clearly. We can also see the major axis of the disk moving clockwise (in the opposite sense to the particle motion). In frames 3 and 4 ($t = 1002.00$ and $t = 1003.00$) the disk appears stressed in the sense that the ridge/spiral is disrupted with high density knots in it. Frames 5 and 6 ($t = 1004.00$ and $t = 1005.00$) on the other hand show a relaxed disk. The spiral structure here is more pronounced and uniform.

The data for plot c of Fig. 6.4.8 was used to determine the period of the disk motion (i.e. the 'superhump' period). Over six full cycles the period P_s ranged from 6.74 to 6.84 scaled time units with a mean value of 6.79. Thus over this interval the value of the ratio of the superhump to the binary period $\frac{P_s}{P_b} = 1.08 \pm 0.01$. In a viscous particle simulation conducted by Hirose and Osaki (1991) for a system with $q = 0.175$ and $\nu = 2.0 \times 10^{-4}$ the ratio was found to be 1.081 ± 0.043 (if significant figures were watched closely this would probably have been written as 1.08 ± 0.04). Now we have already stated that the isothermal SPH simulations described here closely followed the viscous particle simulations of Hirose and Osaki. There were small differences between the models; our white dwarf had twice the radius of Hirose and Osaki's, and we included pressure forces. In other words the simulations are directly comparable as they incorporate the same assumptions, the principle ones being that the disk is isothermal and that the viscosity is constant throughout. Because the calculations used different techniques they can be used to verify each other's results.

For $q = \frac{3}{17}$ and $r_d = 0.48$ Eq. (6.1.6) gives $\frac{\omega_{pr}}{\omega_b} \simeq 0.041$ and hence $\frac{P_s}{P_b} \simeq 1.04$. Using Eq. (6.1.7) we get $\frac{P_s}{P_b} \simeq 1.06$. Formally these values agree with Hirose and Osaki's simulation to within the uncertainties. However in the light of our simulation there does appear to be a small but significant difference between the particle simulations and the theory (and with the observations for that matter). Lubow in his SPH simulation (1991 b) with the full binary potential for a $q = 0.10$ system found $\frac{P_s}{P_b} = 1.026$ which agrees closely with Eq. (6.1.6) whereas Hirose and Osaki found for a similar system $\frac{P_s}{P_b} = 1.043 \pm 0.010$. Why does Lubow obtain such a low value for the 'superhump' period? We now look at the differences between his simulation and ours.

Firstly Lubow considered an annulus rather than a broad disk. Secondly his radial density profile was very different to ours. He also had a sound speed $c = 0.05$ in our scaled units which is two and a half times our value. Consequently pressure forces would be more important in his simulation. But Hirose and Osaki completely discounted pressure forces and their results are very close to ours so perhaps these are not important. It appears that Lubow's simulation was much less dissipative than ours. His value for ν would have been roughly 20 times less than ours. From this discussion it is apparent that for a given mass ratio q, the disk precession period is not as tightly constrained as we would have hoped, but in fact depends upon assumptions made about the physics of the disk. Hirose and Osaki were confident of the uniqueness of the period for a given q. We are not so sure. As the range of values obtained in simulations and theoretical calculations includes the observed 'superhump' periods we believe that disk eccentricity is a very good candidate to be the cause of the phenomenon. Tightening the constraints on the disk period will require better knowledge of the physics and structure of the disk. We may even use numerically obtained disk periods as a test of various disk structures.

We now consider the time dependence of the energy dissipation in the disk. Once released, this energy is assumed to be radiated vertically through each of the disk's two faces. In the thin disk approximation, vertical temperature gradients are much sharper than those in the plane so we neglect radial radiation transport. In order to determine the spectrum produced by the disk a radiative transfer calculation must be performed at each particle using the local dissipation rate as the source term. The problems with such calculations were described in Chapter 2. A simple bolometric picture of the disk radiation can be obtained by simply looking at the rate at which energy is dissipated in the disk as a function of time. Fig. 6.4.11, Fig. 6.4.12 and Fig. 6.4.13 plot this for different radii for periods commencing at $t = 300.00, 400.00$ and 1000.00 respectively. The top curve in each figure is the total dissipation for the disk. There is clearly a lot of high frequency noise in this plot that is absent from those for the outer regions of the disk. This is easily explained. The thin disk theory outlined in Chapter 2 showed that the dissipation per unit area is greatest in the inner regions. Indeed this is the dominant component of the total dissipation. But in our SPH calculations there are relatively few particles in the inner disk. The accretion onto the white dwarf of even a single particle is a significant event in terms of the luminosity of the inner regions. Thus the dissipation curve is quite noisy. If we were to repeat the calculation with a smoothing length that increased with r we could improve our resolution in the inner regions by increasing the number of particles there. As a result we would expect a smoother signal.

In Fig. 6.4.11 we see an apparently linear increase in the dissipation rate over time throughout the disk. We relate this trend to the disk's mass which is still increasing at this point. In addition to the linear trend we see an emerging periodic component that is caused by the disk's tidal instability that is only starting to manifest itself at $t = 300$. We are thus looking at the changes in the disk luminosity as it begins to precess. By $t = 400.00$ (Fig. 6.4.12) the amplitude of the motion has increased and there is a corresponding increase in the amplitude of the periodic component of the disk luminosity. The constant size of any particular peak across the three curves is an indication that the periodic luminosity is sourced in the outer disk. The linear trend in the background luminosity is still apparent with the disk mass still increasing. It is of course absent at $t = 1000.00$ (Fig. 6.4.13) as the disk mass has stabilised by then. A general observation regarding the peaks in Fig. 6.4.12 and Fig. 6.4.13 is that they are not of constant height. There is a tendency for the peak size to alternate between two values. This does not however always occur.

The luminosity curve from the outer disk is sufficiently noisy to introduce considerable uncertainty into the timings of luminosity maxima. We could have processed the signal using some form of low bandpass filter. Instead we took the simple option and obtained the mean period for the seven cycles shown in Fig. 6.4.12. In units of the orbital period this is found to be 1.07 ± 0.02. This clearly matches the period of the disk precession.

So now we know the disk precession gives rise to a similar periodicity in the luminosity of the disk. We would still like to determine exactly where and how this excess dissipation arises. Fig. 6.4.14 traces the dissipation rate in the outer disk for a little over one and a half periods. It shows the peak lasts about a third of a cycle. In addition to the major peak we see a second broad hump (from about $t = 400$ to $t = 600$). These secondary humps seem to be general feature of the cycle but due to the noisy signal they are quite difficult to resolve. Fig. 6.4.15 is a sequence of particle plots coloured according to luminosity per unit area. In order to highlight the structure in the outer disk we have masked out rather more of the central region ($r < 0.15$) than we did to generate Fig. 6.4.14. Fig. 6.4.15 goes a long way to explaining the cyclic behaviour of the dissipation rate. Frame 3 ($t = 1001.5$) almost exactly coincides with the largest spike in the first hump in Fig. 6.4.14. Frames 2 and 4 correspond to the shoulders of that same peak. The other frames show the disk at various times when its luminosity is reduced to the background level.

In what became known as the 'elliptic disk model' for superhump, Vogt (1983) proposed that the excess luminosity occurred in or near the bright spot where the injection stream strikes the disk edge. The reasoning was as follows. As the disk precesses, at any given angular position θ, the radial coordinate of the disk edge is a periodic function of time. The position of the bright spot must then also vary periodically. Now when the disk edge moves inwards, gas from the L_1 point must fall further from the L_1 point before striking it. At the point of impact then it will have more kinetic energy. This energy is largely dissipated in the collision. Hence we expect the bright spot to be brightest when it is at smallest radius. Conversely, when the disk edge moves outwards and the bright spot retreats along the free fall path back towards the L_1, the in-falling gas has less energy when it strikes the disk and the spot will be dimmer. The proposal was then that the advance and retreat of the bright spot is the source of superhump. This was not the case in our simulation.

Frames 2 to 4 of Fig. 6.4.15 show that during the luminosity peak, considerable energy is being released in a narrow band extending from the disk bright spot anticlockwise around the bottom edge of the disk. A glance at Fig. 6.4.2 shows that this band corresponds to the high density ridge/spiral travelling wave discussed earlier. To verify that the luminosity excess is occurring in this ridge we have included another dissipation versus time plot, Fig. 6.4.16. This time we evaluated the total dissipation occurring at radii $r > 0.15$ to match Fig. 6.4.15. The leftmost point of the masked out zone in the centre of the disk has coordinates $(0, 0)$ in the rotating frame. From Fig. 6.4.15 we observe that the bright spot is always to the left of this point (i.e. the x coordinate of the bright spot is always negative). A considerable portion of the high density ridge on the other hand lies to the right of this point and so the simplest way of separating the dissipation from the two features was to plot two dissipation curves, one for the left side of the disk and one for the right side with the separator being the line $x = 0$.

Fig. 6.4.16 shows two interesting things. Firstly that the luminosity peak occurs almost entirely in the right hand side of the disk confirming our view that it is the ridge rather than the bright spot that is the source of the peaks. It appears that the greatest dissipation occurs in the region where the ridge makes it closest approach to the white dwarf (at say $\theta \sim 0$). The second point of note is the difference in smoothness between the two curves. The signal from the left hand side has considerably more high frequency 'noise' than that from the right. This is undoubtedly due to the rapid changes in collision conditions experienced by the injection stream as it strikes the jagged edge of the disk. In other words the high frequency variation of the luminosity curve is coming from the bright spot.

Referring back to Fig. 6.4.15 we see that not only is the position of the point of impact moving, but also the angle with which the stream strikes the disk is varying. In frame 6 ($t = 1005.00$) the stream and disk edge are moving almost perpendicularly when they collide. The angle is much more acute in frame 4 ($t = 1002.00$). Reducing the angle of incidence between the two gas flows reduces their relative velocities and hence the viscous dissipation occurring here. We thus also have an explanation for the longer period variability observable in the signal from the left hand side of the disk.

Relative to the left hand side, the signal from the right side of the disk is very smooth. The luminosity hump is still not a simple, single peak but consists of several peaks close together. This is explained by the lumpiness of the ridge. Rather than being smooth along its length it contains various knot like structures. When these knots make their closest approach to the white dwarf there is a corresponding peak in the luminosity. We note that in this region considerable compression and large velocity shear must feature, resulting in the excess dissipation.

What is causing the peak amplitude to alternate between two values? This phenomenon may be due to the rotation of the two armed spiral travelling wave which has a period twice that of the binary. We hypothesise that due to the interaction with other modes the two arms are not identical. Lubow noticed that in a full binary simulation the travelling wave was disrupted by other tidal modes. This line of thought has not been pursued.

6.5. Discussion of Isothermal Simulations

We have spent considerable time discussing and evaluating the SPH artificial viscosity term and we concluded that it generates a viscous shear equivalent to a kinematic viscosity

$$\nu = \frac{1}{8}\bar{\alpha}ch.$$

In the simulations described in this section $\bar{\alpha}$, c and h were fixed which gave rise to a constant ν. We now discuss the realism of this choice, and relate it to other models, in particular the Shakura-Sunyaev parameterisation, for the dissipation. Recall Eq. (2.5.5) for the parameterisation

$$\nu = \alpha\frac{c^2}{\Omega}.$$

As discussed in Chapter 2 we are largely ignorant of the source of the dissipation. Hydrodynamic turbulence is widely suspected in which case it is accepted that $\alpha \sim 1$. In this case

$$\nu \simeq c^2\Omega. \tag{6.5.1}$$

Taking the Keplerian rotation law and assuming the disk is isothermal we have

$$\nu \sim r^{\frac{3}{2}}. \tag{6.5.2}$$

Thus our constant ν disk is not exactly comparable to a Shakura-Sunyaev turbulent disk and will give rise to a different density profile. Consider a steady state disk for which the density profile is given by

$$\Sigma = \frac{-\dot{m}}{3\pi\nu}\left(1 - \sqrt{\frac{r_b}{r}}\right) \tag{6.5.3}$$

where r_b is a constant (see Chapter 2). Thus a Shakura-Sunyaev disk will be more centrally condensed than our constant ν simulation. This has implications for the disk's interaction with the Lindblad resonance. Lubow (1991 a) found that the disk's eccentricity growth was proportional to the relative density at the resonance. We would thus expect the eccentricity to grow more slowly in a Shakura-Sunyaev disk than in ours and we might possibly find that the influence of the resonance is reduced. The disk's 'superhump' period would also change. The natural thing to do now would be to perform an appropriate SPH simulation. Equating the SPH and Shakura-Sunyaev viscous terms we have

$$\frac{1}{8}\bar{\alpha}ch = \frac{\alpha c^2}{\Omega}. \tag{6.5.4}$$

Thus

$$\bar{\alpha} = \frac{8\alpha c}{h\Omega} \tag{6.5.5a}$$

$$= \frac{8\alpha c r^{\frac{3}{2}}}{h\mu^{\frac{1}{2}}}. \tag{6.5.5b}$$

With $\alpha = 1, c = 0.02, h = 0.01$ and $\mu = 0.15$ we have

$$\bar{\alpha} = 41.3r^{\frac{3}{2}}. \tag{6.5.6}$$

Now if the disk extends from $r = 0.02$ out to $r \simeq 0.5$ we find a range for the SPH artificial viscosity coefficient of

$$0.1 < \bar{\alpha} < 15. \tag{6.5.7}$$

We note that our previous simulations used $\bar{\alpha} = 10.0$. Thus if we were to perform another isothermal simulation changing only the prescription for $\bar{\alpha}$ to Eq. (6.5.5) and leaving the methods and other parameters fixed, the resulting disk would require many more particles than previous calculations did. These particles would then be concentrated in the inner regions of the disk.

The operator split algorithm should be able to cope quite well with a centrally condensed disk. The multiple time stepping algorithm investigated as an alternative would have handled the problem less effectively. The fact remains however that increasing the particle number will increase the CPU time required by the simulation. At the time of writing the department was installing a set of DEC-Alpha workstations. Tests on a demonstration machine had shown our code to run $6-8$ times faster than on our existing workstations. That would have been enough for us to contemplate performing this simulation. As it was time constraints have prevented us from including such a run in this thesis work. Other ways to reduce the CPU time required would be to change the system parameters. We could for example reduce the particle injection rate to say a third of its present value and perhaps change the method of injection as was done by Hirose (1991). Ultimately though we would want to run a calculation that was directly comparable with the simulations of Hirose and Osaki and also with our constant viscosity work. As SPH is fully Lagrangian it is very easy to introduce a variable viscosity. All we need do is let $\bar{\alpha}$ become another particle property like the mass or the density. It would take more effort to introduce a variable viscosity into the viscous particle method. Let us relate our constant viscosity simulation to the Shakura-Sunyaev parameterisation. Rearranging Eq. (6.5.5a) we have

$$\alpha = \frac{h\mu^{\frac{1}{2}}\bar{\alpha}}{8cr^{\frac{3}{2}}}. \tag{6.5.8}$$

Substituting the values from Table 6.4.1 we have

$$\alpha = 0.24r^{-\frac{3}{2}}. \tag{6.5.9}$$

Assuming the disk extended between $r = 0.02$ and $r = 0.5$ we find

$$0.68 < \alpha < 86. \tag{6.5.10}$$

This means that with the parameters that we used in these simulations, the viscosity was too large to have been due to hydrodynamic turbulence. As Hirose and Osaki used similar parameter values this statement can be extended to their simulations as well. Of course we do not know that the dissipation is caused by such turbulence. Other mechanisms have been proposed but they too, when expressed in a Shakura-Sunyaev fashion, seem to result in α parameters of a similar magnitude or smaller than the hydrodynamic one. We do not believe that the high α values used in these simulations invalidates our results. It merely means that they must be used with care. Measured 'superhump' periods in particular must be viewed in the light of the various assumptions made about the disk.

Table 6.6.1: Representative values for K^*

System	Mass	Period	K^*		
	$M_\odot$	(days)	($\bar{m}_w = 1$)	($\bar{m}_w = \frac{1}{2}$)	($\bar{m}_w = 0.615$)
Z Cha !	0.62	0.074499	0.445	0.890	0.723
SW UMa !	0.81	0.05681	0.40	0.81	0.66
OY Car †	0.755 ± 0.013	0.063121	0.415	0.831	0.675
AH Her !	1.71	0.258116	0.263	0.525	0.427

! (Lang, 1991)
†(Wood et al, 1989)

6.6. Blackbody Disks

The simulations in the previous sections effectively ignored the thermodynamic properties of the disk flow. In reality the viscous heating must affect the gas properties. In this section we improve upon the isothermal assumption. If we are to do this then we must solve, in addition to the mass and momentum conservation equations, the energy equation. This calculation is problematic as we know little about the local structure of the disk. The thin disk approximation however helps us considerably. It allows us to assume that vertical temperature gradients are much larger than those in the plane, and thus that the thermal energy generated by viscous action is all transported in the vertical direction. For the moment we assume this transport to be radiative rather than convective. So, at any point on the disk plane we need only solve a one dimensional energy equation with the source term being the local rate of dissipation of energy, D. With the radiative time scale being very short compared to other time scales, at any time t, we can equate the radiative flux through a point on the disk surface to $D/2$ (the disk has two surfaces).

We mentioned in the introduction that previous particle based simulations essentially neglected radiative transfer, concentrating instead on the disk dynamics. All the two dimensional particle simulations to date have been essentially isothermal (Lin and Pringle (1974), Whitehurst (1988 a,b), Lubow (1991 b), Hirose and Osaki (1990)). Heat generated by viscous action was assumed to be immediately radiated away, and to have no effect on the disk.

Meglicki et al. (1993), on the other hand, in their three dimensional SPH calculation ignored radiative losses and assumed the disk to be adiabatic. It is not surprising therefore that the gas heated up and they found disk formation was inhibited. The three dimensional simulations of Lanzafame et al. were similarly limited. They assumed the gas to be polytropic with index γ. They also found that the gas heated up and that disk formation was inhibited except when $\gamma \rightarrow 1.00$. Because we can make use of the thin disk approximation, it is easier to incorporate radiation physics into a two dimensional simulation than into a three dimensional one. Up until now, when theoretical disk radiation profiles were required, axisymmetric finite difference codes were used so that any non-axisymmetric variation in the signal were neglected. The work done in this section is the first step in bridging the gap between axisymmetric finite difference codes and particle scheme. Hence we use the simplest approximation possible regarding the disk's vertical structure. We assume the dissipation is occurring at infinite optical depth and that each element of the disk's surface radiates like a blackbody with temperature

$$T_b = \left(\frac{D}{2\sigma}\right)^{\frac{1}{4}}, \tag{6.6.1}$$

where σ is the Stephan Boltzmann constant. This is certainly adequate to provide basic information about the disk radiation. If at a later stage we wished to replace Eq. (6.6.1) with a more sophisticated treatment of the radiation, it would be very easy to do so. We now assume that T_b is characteristic of the gas flow at that radius and use it in the equation of state

$$\frac{P}{\rho} = c^2 \tag{6.6.2a}$$

$$= \frac{k_b T_b}{\bar{m}_w m_p} \tag{6.6.2b}$$

where k_b is the Boltzmann constant, m_p is the mass of a proton, and $\bar{m}_w$ is the (dimensionless) mean molecular weight of the gas. $\bar{m}_w = 1$ for neutral hydrogen and $\frac{1}{2}$ for fully ionised hydrogen. Frank (1985) gives $\bar{m}_w = 0.615$ as being appropriate for a fully ionised 'cosmic' mix of gases. We thus have

$$\frac{P}{\rho} = \frac{k_b}{\bar{m}_w m_p}\left(\frac{D}{2\sigma}\right)^{\frac{1}{4}}. \tag{6.6.3}$$

This can be written as

$$\frac{P}{\rho} = K D^{\frac{1}{4}} \tag{6.6.4}$$

where

$$K = \frac{1}{\bar{m}_w} \times 4.49804 \times 10^5 \qquad \mathrm{m^2 kg^{-\frac{1}{4}} s^{-\frac{5}{4}}}. \tag{6.6.5}$$

We scale the equations in the same way as we did in the last section, according to the total mass of the binary M, the interstellar distance d, and the reciprocal of the orbital angular velocity ω_b^{-1}. Scaling Eq. (6.6.4) gives us

$$\frac{P^*}{\rho^*} = c^{*2} = K^* D^{*\frac{1}{4}} \tag{6.6.6}$$

where

$$K^* = \left(\frac{\omega}{M^5 G^8}\right)^{\frac{1}{12}} K \tag{6.6.7}$$

For the moment we use $*$ to denote dimensionless quantities. G is the gravitational constant. Table 6.6.1 lists the system parameters for four cataclysmic variables and the corresponding values for K^*. Though its precise value depends upon $\bar{m}_w$, it is apparent that K^* will be a parameter of order unity in Eq. (6.6.6). This equation essentially closes the feedback loop. The sound speed is now determined by the dissipation rate. The kinematic viscosity is in turn proportional to the sound speed. We have thus introduced a (very weak) positive feedback.

In the isothermal simulations described previously, we were able to arbitrarily set the SPH particle mass, $m_{sph} = 10^{-6} M$. We realised that it simply scaled quantities like the density and the dissipation rate. Because the equation of state fixed the sound speed independently of these quantities m_{sph} was essentially irrelevant to the simulation. In this case however, because of the feedback loop we must determine an appropriate particle mass. We let m^* be the dimensionless particle mass, so

$$m_{sph} = m^* M. \tag{6.6.8}$$

Now, unless otherwise mentioned, in the various simulations we inject particles singly at intervals

$$\delta t = \frac{1}{100}\frac{T}{2\pi}. \tag{6.6.9}$$

Using Eq. (6.6.8) and Eq. (6.6.9), we find the mass transfer rate in the simulation

$$\dot{m} = 2\pi \times 100\, m^* \frac{M}{T}. \qquad (6.6.10)$$

In general, mass transfer rates in cataclysmic variables are thought to be of the order of 10^{-11} to $10^{-7} M_\odot \mathrm{yr}^{-1}$, in other words there is a 10^4 variation over the class. Systems with shorter orbital periods are observed to have rates at the lower end off this range (Patterson, 1984).

Mass transfer is thought to occur in the following way. The binary systematically loses orbital angular momentum causing the interstellar separation (and the binary period) to decrease. As a result, the secondary's Roche lobe contracts until it reaches the surface of the star itself. Material then leaks out of the Roche lobe via the inner Lagrangian point. $\dot{m}$ is then determined by the rate at which orbital angular momentum is lost. We do not wish to enter a discussion of the various mechanisms and models here. The reader is referred to Livio (1993) for further details. We do note however that for systems with periods less than two hours, gravitational quadrupole radiation removes sufficient angular momentum to account for observed $\dot{m}$. OY Car, having a period of one and a half hours, clearly falls into this category.

$\dot{m}$ cannot be directly measured but has to be inferred indirectly. For example Wood et al (1989) calculated the bright spot luminosity and temperature of OY Car in quiescence. The bright spot luminosity is fairly clearly related to $\dot{m}$ as it is simply the region where the stream from L_1 strikes the disk. Thus they estimated $\dot{m}_q \simeq 10^{-11}$ to $10^{-10}\, M_\odot \mathrm{yr}^{-1}$ for OY Car. That is probably quite a reliable estimate, for quiescence. It has not yet been established whether this rate is approximately constant throughout a dwarf nova's outburst cycle. This is because during outburst the disk luminosity increases, swamping the signal from the bright spot. More indirect methods must then be used. Rutten et al. (1992) used eclipse mapping techniques to obtain radial disk brightness temperature profiles for OY Car in normal outburst. By fitting these profiles to steady state axisymmetric solutions (see Section 1.6) they obtained an outburst mass flux $\dot{m}_o \simeq 1 \times 10^{-9} M_\odot \mathrm{yr}^{-1}$. This is a factor of ten to a hundred greater than $\dot{m}_q$. Now $\dot{m}_o$ is strictly a measure of the mass transfer within the disk itself. If one one believes the thermal instability model for superhump, this enhanced mass flux is due to enhanced dissipation in the disk. On the other hand, according to the mass transfer burst model the flow rate from the secondary greatly increases. For our purposes this argument is irrelevant. We are just seeking a mass flux that is characteristic of OY Car in outburst. We then impose that as the mass flux from the secondary. So, in order to determine an appropriate dimensionless particle mass we rearrange Eq. (6.6.10) and use Table 6.6.1 to get, for OY Car,

$$m^* = 3.64 \times 10^{-7} \dot{m}. \qquad (6.6.11)$$

Substituting $\dot{m}_q$ into Eq. (6.6.11) we have

$$m^* \simeq 10^{-18} \text{ to } 10^{-17}, \qquad (6.6.12)$$

and for outburst

$$m^* = 3 \times 10^{-16}. \qquad (6.6.13)$$

With these values being so small, we were wary of introducing large roundoff errors into the calculations. So we kept the SPH particle mass m_{sph} at its isothermal value,

$$m_{sph} = 10^{-6} M, \qquad (6.6.14)$$

and instead change the equation of state Eq. (6.6.6) to get

$$\frac{P^*}{\rho^*} = \left(\frac{m^*}{10^{-6}}\right)^{\frac{1}{4}} K^* D^{*\frac{1}{4}}. \qquad (6.6.15)$$

We define a new constant

$$L = \left(\frac{m^*}{10^{-6}}\right)^{\frac{1}{4}} K^*. \qquad (6.6.16)$$

Table 6.7.1: Summary of constants for the $\mu = \frac{1}{2}$ simulation

Constant	Value	Comment
μ	0.5	scaled mass of primary
$\bar{\alpha}$	10.0	artificial viscosity coefficient
h	0.01	SPH smoothing length
L	4.0×10^{-3}	sound speed coefficient
v_{inj}	0.1	initial velocity of particles injected at L_1 point (in rotating frame)
θ_{inj}	0.3491	angle to binary axis at which particles are injected (in radians)
Δt	0.01	timestep
r_{wd}	0.02	radius white dwarf

We then simply set L at the beginning of the simulation. Now the smaller L is, the lower the sound speed is. The kinematic viscosity is directly proportional to the sound speed so reducing L increases the computational time required for a simulation. This happens in two ways. Firstly the viscous time scale increases, so the simulation has to be carried further for the system to reach some equilibrium state. Secondly the number of particles required increases, thus increasing the computations required time step. In fact we were forced to set

$$L = 4.0 \times 10^{-3}$$

in order that the simulations ran to completion in a reasonable time. Working backwards, assuming $\bar{m}_w = 0.615$, this value for L implies a mass transfer rate $\dot{m} \simeq 3.4 \times 10^{-9} M_{\odot}\mathrm{yr}^{-1}$. This is perhaps a factor three higher than the figure quoted in Rutten et al. but it can be said to be characteristic of OY Car in outburst and superoutburst.

6.7. Blackbody $\mu = \frac{1}{2}$ Simulation

In this section we describe a blackbody disk simulation performed in a system with a primary of reduced mass $\mu = \frac{1}{2}$ (i.e. a mass ratio $q = 1.0$). We have already detailed an isothermal simulation for such a system. That disk was found to evolve to a stationary state. The purpose of this simulation is to test the theory and code before we tackle a more interesting (and realistic) mass ratio. The system parameters are as listed in Table 6.7.1. They are largely the same as those in the equivalent isothermal calculation. In fact the sole difference between the simulations is that the sound is no longer constant but is determined by Eq. (6.6.15).

Fig. 6.7.1 shows that the evolution of the $\mu = \frac{1}{2}$ blackbody disk is identical in character to that of the isothermal case, with the total mass increasing uniformly from zero to a steady state value. Of course, given the different equations of state, the two disks achieve different steady state masses after differing periods of time. We will expand upon this later. For the moment however the take home message from this diagram is that the assumption that disk elements radiate like blackbodies has not affected the dynamic stability of an accretion disk in a $\mu = \frac{1}{2}$ system.

We now consider the final steady state of the blackbody simulation. Fig. 6.7.2 shows azimuthally averaged density versus radius curves for the isothermal and blackbody disks at $t = 1000.00$. We take it that these reflect the steady state profiles. In fact even at steady state the curves are not completely stationary, but the variability is not significant. We have truncated the plot at $r = 0.40$ to eliminate the injection stream from the picture. We see the profiles are fundamentally similar, differing only in the detail. They both show a steadily increasing density in the region $0.05 < r < 0.25$. This is the approximately axisymmetric interior of the disk. Then from $0.25 < r < 0.30$ the two curves have in common a broad peak. This is the non-axisymmetric outer region of the disk. The peak is due to the high density ridge along the LNO that we examined in our isothermal simulations. The two curves then drop away as we encounter the disk edge. In both profiles we observe a halt in the decline at $r \simeq 0.35$ (actually a spike for the isothermal disk) where the injection stream strikes the disk and causes some compression. From this figure we draw the qualitative conclusion that the new equation of state has had little effect upon the radial mass distribution of the steady state disk. To quantify this we plot

$$M_D(r) = \frac{\int_0^r \int_0^{2\pi} r' \Sigma\left(r', \theta\right) d\theta dr'}{\int_0^\infty \int_0^{2\pi} r' \Sigma\left(r', \theta\right) d\theta dr'} \tag{6.7.1}$$

for the two disks (Fig. 6.7.3). $M_D(r)$ is just the fraction of the total disk mass lying interior to r. Obviously $0 < M_D(r) < 1$. In fact the two disks have very similar radial mass distributions. The isothermal one is however slightly more centrally condensed than the black body. We explain this thus. In the isothermal disk the sound speed c is a constant. Therefore the SPH artificial viscosity term with constant $\bar{\alpha}$ and h will give a kinematic viscosity ν that is independent of r. The steady state density profile (assuming axisymmetry)

$$\Sigma_{iso}(r) \propto \left(1 - \sqrt{\frac{r_b}{r}}\right). \tag{6.7.2}$$

For an axisymmetric steady state black body disk however, the sound speed

$$c(r) \propto D(r)^{\frac{1}{8}} \tag{6.7.3a}$$

$$\propto \frac{1}{r^{\frac{3}{8}}}\left(1 - \sqrt{\frac{r_b}{r}}\right)^{\frac{1}{8}}. \tag{6.7.3b}$$

Except when $r \simeq r_b$ we can to very good approximation say

$$c(r) \propto r^{-\frac{3}{8}}. \tag{6.7.4}$$

Thus for constant $\bar{\alpha}$ and h

$$\nu(r) \propto r^{-\frac{3}{8}} \tag{6.7.5}$$

and

$$\Sigma_{bl}(r) \propto r^{\frac{3}{8}}\left(1 - \sqrt{\frac{r_b}{r}}\right). \tag{6.7.6}$$

We see that the density of the black body disk increases more rapidly with r. If the two disks are truncated at the same outer radius r_o then the isothermal disk will be the more centrally condensed of the two. In our case r_o is the tidal radius. We return to Fig. 6.7.3 and see that the two curves rise with steepening gradients before levelling off quite sharply at $r \simeq 0.30$. The disks are truncated through a combination of tidal forces and the inward pressure of the injection stream. We see that for these two disks approximately 7 to 8% of the disk mass lies beyond the truncation radius (this figure includes the particles in the injection stream). We could increase this fraction by increasing the viscosity or reducing the injection rate but the turn off in the curve would remain at the same point as it is independent of the disk properties and is only a function of the system geometry. Overall, the change in the equation of state has only resulted in minor alterations to the disk's steady state configuration.

Table 6.8.1: Summary of constants for the black body simulation of OY Car

Constant	Value	Comment
μ	0.85	scaled mass of primary
$\bar{\alpha}$	10.0	artificial viscosity coefficient
h	0.01	SPH smoothing length
L	4.0×10^{-3}	sound speed coefficient
v_{inj}	0.1	initial velocity of particles injected at L_1 point (in rotating frame)
θ_{inj}	0.366519	angle to binary axis at which particles are injected (in radians)
Δt	0.01	timestep
r_{wd}	0.02	radius white dwarf

Fig. 6.7.4 plots the speed of sound for all the disk particles at $t = 1000.00$ against their radius. We see over the whole disk a variation of only about a factor of four in c. In the axisymmetric interior, for a given r, the sound speed is quite tightly constrained. But in the non-axisymmetric outer reaches of the disk where we find the ridge, there are wide variations in the sound speed for any particular radius. From this figure we can deduce that there are large viscosities both in the very inner part of the disk and in the ridge around the disk edge.

In deriving the blackbody disk equations we are using in these simulations, we assumed that the disk was geometrically thin. This is equivalent to assuming that $\frac{v_\phi}{c} \gg 1$ i.e. that the azimuthal motion is highly supersonic. In Fig. 6.7.5 we test this assumption. $\frac{v_\phi}{c}$ is plotted for all the particles at $t = 1000.00$. We see indeed that this assumption holds. For most of the disk $10 < \frac{v_\phi}{c} < 20$. In the very inner disk $\frac{v_\phi}{c}$ reaches values approaching 40. With the ratio decreasing with increasing radius, in the axisymmetric region at least, we find that the disk gets geometrically thicker as we move outwards. Once we reach the non-axisymmetric outer region, the figure shows there will be considerable height variations in the disk. This perhaps indicates that the flow here has a three dimensional character. The exact nature of these billows in the outer disk and the question of whether there is turbulent motion here are points that are yet to be determined. Part of the campaign to learn more about this region should be a series of three dimensional simulations. As mentioned before, because of a failure to adequately include radiative processes, the three dimensional simulations so far performed by other authors have not been of any use in this regard.

Our objectives in this section were fairly limited. We wished to evolve a disk to a steady state in order to test the code and to examine the influence that the altered equation of state has upon the disk's final state. We found there to be only small differences with the isothermal disk. Using the SPH artificial viscosity term with constant $\bar{\alpha}$ and h we found a steady state blackbody disk to have relatively more mass in its outer regions than an equivalent isothermal disk.

6.8. Blackbody Disk Model of OY Car

In this section we describe a simulation of OY Car in outburst and superoutburst. The parameter values are listed in Table 6.8.1. Most of the settings have already been discussed in previous sections. The simulation format is identical to previous ones. The calculation was followed for 1500.00 scaled time units (239 orbital periods).

The evolution of the disk mass is shown in Fig. 6.8.1, with the equivalent isothermal curve included for comparison. Recall the development of the isothermal disk. During the initial growth the disk remained stationary in the frame of the binary and was approximately axisymmetric. By $t \simeq 300$, the disk had begun to interact with the inner Lindblad resonance. Thereafter it became eccentric and started precessing. All this while the disk mass was still increasing. The disk became gradually more eccentric until by $t \simeq 400$ it had developed a 'tail' which extended a little beyond the Roche lobe. On passing between the two stars, this would lose particles back to the secondary. This additional mass loss was large enough to cause the disk mass to peak, and then drop monotonically to an equilibrium value. The blackbody disk evolved in a similar fashion. The major difference was that after the mass peaked it did not drop uniformly to a stable value but underwent several oscillations of gradually decreasing amplitude. Now in the previous section we found that a steady state $\mu = \frac{1}{2}$ blackbody disk had relatively more mass in its outer regions than an equivalent isothermal one. This observation also applies to the $\mu = 0.85$ case. As a result, when the blackbody disk began precessing it returned more mass per cycle to the secondary than did the isothermal disk. Hence we see a more rapid decline in the blackbody curve. As the disk's mass decayed, so to did its size. By $t \simeq 500$ the disk had shrunk so far that the mass loss to the secondary was significantly reduced Again the balance between addition and removal of particles shifted and the disk mass rose. This increase, with some mass loss to the secondary still occurring, was less rapid than the initial rise. By $t \simeq 700$ the tail had again grown so it encountered the secondary every pass. This process continued until an approximate equilibrium state was reached. The blackbody disk mass had still not reached a stationary value by $t = 1500.00$, the conclusion of the simulation.

We quantify the above argument by examining the records of particles leaving the system. We look in particular at a period of slightly less than ten thousand timesteps, $t = 1406.04$ to $t = 1500.00$, during which the disk mass exhibited a slow decay. The total particle number decayed from $141,604$ at $t = 1406.04$ to $141,120$ at $t = 1500.00$. Thus to good approximation the disk mass, and the disk itself, could be considered to have reached equilibrium. In the rest of this section, we will assume that the disk over this period is typical of the blackbody disk in equilibrium. This presumes that if we had carried the simulation further, the disk would have reached a state where there was no secular change in its attributes. Rather than do this we will draw our conclusions based upon the behaviour of the disk between $t = 1406.04$ and $t = 1500.00$. Over this interval a total of 9396 particles (one per time step) were injected at L_1. Thus 9880 left the system in various ways. 8859 (89.67%) were accreted onto the white dwarf, 1014 (10.26%) were returned to the secondary, and 7 particles (0.07%) became gravitationally unbound and escaped to infinity. Comparing these figures with the steady state figures for the isothermal disk we find that approximately 10% of the particles removed from the blackbody disk returned to the secondary, whereas only 0.7% of those removed from the isothermal disk did so. In absolute terms we compare 1014 for the blackbody calculation with 118 in twice the time for the isothermal simulation. This strongly supports our explanation for the differences in evolution of the two disks.

The mass of the blackbody disk peaked at $t = 365$, whereas the isothermal maximum occurred at $t = 470$. This indicates that the blackbody disk encountered the $3:1$ resonance and subsequently became unstable at an earlier time than did the isothermal one. We confirm this observation with a look at the motion of the disk's centre of mass. In Fig. 6.8.4 the increasing amplitude oscillation due to the tidal instability becomes apparent at $t \simeq 250$. For the isothermal disk this occurred approximately 50 scaled time units later at $t \simeq 300$. This is all consistent with the blackbody disk developing with relatively more mass in the outer regions than the isothermal disk did.

There is further confirmation in Fig. 6.8.2 which plots the radial mass distribution function $M_D(r)$ (see Eq. (6.7.1)) for the two disks at $t = 250.00$. At this time both disks were stationary and approximately axisymmetric. Recall $M_D(r)$ is the proportion of the disk's mass lying interior to r so that $\frac{dM_D}{dr}$ indicates the proportion of the disk's mass lying near radius r. The isothermal disk is shown to be the more centrally condensed of the two. At later times, when the tidal instability set in, M_D became a function of the phase of the disk and we could no longer compare radial mass distributions in the same way. Fig. 6.8.5 shows two exponential fits to the amplitude of the radial motion of the disk centre of mass. A glance at Fig. 6.4.10 reveals that these are the same exponentials used in the isothermal case. We thus see that the growth rate of the instability is unaffected by the change in equation of state.

From the scaled dissipation rate we can obtain a blackbody temperature using

$$T = \frac{L^*}{K^*}\left(\frac{M}{2\sigma}\left(\frac{2\pi}{P_b}\right)^3 D^*\right)^{\frac{1}{4}} \tag{6.8.1}$$

where P_b is the period of the binary, σ is the Stephan-Boltzmann constant, and M is the mass of the white dwarf. If we take the molecular weight $\bar{m}_w = 0.615$, $L^* = 4.0 \times 10^{-3}$, and the values of K^*, M and P from Table 6.6.1 we get

$$T = 7.05 \times 10^4 D^{*\frac{1}{4}}. \tag{6.8.2}$$

Fig. 6.8.9 shows an azimuthally averaged disk temperature profile for the simulation at $t = 250.00$. At this stage the disk mass is still increasing but only on the viscous timescale which is very much longer than the dynamical and orbital timescales. To first order, and in the absence of the tidal instability which has not yet begun to manifest itself, we can consider the disk to be in steady state. The standard model of dwarf novae in outburst incorporates a steady state blackbody disk. We thus compare the simulation disk at $t = 250.00$ with the observations of Rutten et al. (1992) of OY Car in outburst. They obtained radial brightness temperature profiles of OY Car's disk not only in outburst, but also in quiescence, and in the rise to outburst. The outburst profiles clearly showed the $r^{-\frac{3}{4}}$ dependance characteristic of steady state axisymmetric disks. Quiescent disks in general have a much flatter profile (see also Wood, 1990). We stated that the simulation disk at $t = 250.00$ was very nearly in steady state. To verify this we replot the temperature profile on logarithmic axes to determine its radial dependance (Fig. 6.8.10). We find $T \propto r^{-0.70\pm0.05}$, very close to the steady state relationship. In fact we have plotted the temperature as a function of $\frac{r}{r_L}$, where r_L is the distance from the white dwarf to L_1, to allow direct comparison with the brightness temperature profiles of Rutten et al. (their fig 4b).

As we have already mentioned, Rutten et al. deduced a mass flow rate for the outbursting disk by fitting steady state axisymmetric solutions to their observations. We used this information to set our mass transfer parameters, and so our simulation results are not totally independent of their simulations. We should expect therefore the simulated disk to have temperatures that are of the same order as the observed disk. Rutten et al. found that the centre of OY Car's disk reached a temperature of 3×10^4K. In our simulation we found temperatures in the inner disk regions were typically of the order of 4×10^4K. The inner boundary condition is likely to prevent better agreement. Temperatures in the outer disk of OY Car were observed to drop below 10^4K. The minimum temperature in the simulation was approximately 5000K. The general impression then is that the model and the observations agree well. This is not only a good indication that the blackbody SPH code is working, but also that the parameter settings are indeed appropriate for OY Car in outburst and superoutburst.

We see a blip in the simulation temperature profile at $r \simeq 4.3$, caused by the heating in the stream-disk impact zone. This feature is not apparent in observational curves. In fact a common feature of outbursts is the disappearance of the bright spot. Perhaps more correctly, the radiative flux from the rest of the disk increases sufficiently during an outburst to swamp any bright spot luminosity. Rutten et al. state that the bright spot can be distinguished in their data for the quiescent disk. It becomes less apparent in the rise to outburst, and by outburst maximum the bright spot has completely disappeared. Recall that in the simulation we set the mass transfer rate from the secondary $\dot{m}$ to be equal to the mass flow rate calculated for the disk in outburst, $\dot{m}_o$, obtained by Rutten et al.. We must conclude that in actuality $\dot{m} \ll \dot{m}_o$. Of course this means that the disk is not in equilibrium but is losing mass. This is consistent with the thermal instability model for outbursts. According to this model, during quiescence the disk is cool and relatively inviscid. During this time the disk gains mass. Eventually the thermal instability is triggered by rising temperatures and pressures. Corresponding to the sudden leap in temperatures is a dramatic increase in viscosity. As a result the mass flow rates and luminosities increase as well. The simulation result is not consistent with the mass transfer burst model because it shows that if $\dot{m}$ were to be of the order of $\dot{m}_o$, the bright spot would be visible.

We present in Fig. 6.8.7 six snapshots of the steady state blackbody disk that follow a single precession period of the disk. A similar figure was produced for the isothermal disk (Fig. 6.4.9) There are striking similarities between the two figures. The disk in frame 1 of Fig. 6.8.7 is at the same phase in its precession as the disk in frame 4 of Fig. 6.4.9, and so on. Clearly the main features of the disk motion remain unchanged. As before we see the disk precessing clockwise, in the opposite sense to the motion of the gas and of the binary. Again the two armed spiral structure is visible at various points in the cycle (frames 1-4). More prominent in the blackbody simulation is the disruption of the stream caused by the disk itself. In frames 4 and 5 the centre of mass of the disk makes its closest approach to the secondary. Gas from L_1 only has a short distance to fall before striking the disk. By frame 5 the collision is a glancing one. Thus when the disk centre of mass moves further clockwise in frame 6 we see a tortuous trail of matter from the stream and the disk edge. This disruption however quickly disappears. It is not seen to nearly the same extent in the isothermal disk.

To better see the differences in the two disks' cyclic behaviour we look at the motion of their centres of mass (Fig. 6.8.6 and Fig. 6.4.8 for the blackbody and isothermal disks respectively). The motion of the blackbody disk centre of mass clearly has a larger amplitude than that of the isothermal disk. This agrees with all we have seen so far. Furthermore when we look at the trajectory of the centre of mass in the rotating frame (upper right), we see that the blackbody disk centre of mass passes L_1 more closely which explains why we see a stronger disruption of the stream in the blackbody case. From the radial motion of the centre of mass (lower left graph) we determine the precession period of the disk. Over the interval $t = 1406.04$ to $t = 1500.00$, the ratio of the disk precession period to the binary orbital period was measured to be

$$\frac{P_s}{P_b} = 1.07 \pm 0.02. \tag{6.8.3}$$

The equivalent ratio for the isothermal disk, was 1.08 ± 0.01. Thus, given the uncertainties in the two figures, we can say the two disks precessed at the same rate. We will not go over once more our discussion of possible factors affecting the speed of precession (see Section 6.4). However we note that the change in equation of state only resulted in a minor alteration to the radial mass distribution. Although it was enough to alter the disk's evolution, and enough to increase the amplitude of the precession, it may not have been sufficient to change the period of the motion. To properly address this question we must run simulations with alternate forms for the dissipation law.

In deriving our equations (Section 6.6) we assumed the disk was geometrically thin. We now check that the results from this simulation are consistent with that assumption. In an axisymmetric disk , this was equivalent to assuming that the azimuthal velocity was highly supersonic. At larger radii in this disk, the orbits are clearly not axisymmetric. Thus we redefine the Mach number, $\mathcal{M}$, of a particle to be the ratio of the particle's physical speed to its sound speed. In Fig. 6.8.8 we plot $\mathcal{M}$ for a subset of the disk particles at times corresponding to the six frames in Fig. 6.8.7. This figure clearly shows that for all but a very few particles at large radii ($r > 0.6$), $\mathcal{M} \gg 1$ and the geometrically thin assumption holds good. It has not been determined whether those few low $\mathcal{M}$ particles are indicative of some three dimensional structure at the very edge of the disk, or are just points where the model departs from reality. The inner disk ($r < 0.25$) remains largely unaffected by the tidal instability, and the Mach number radius relationship is roughly time independent in this range. At radii larger than 0.25 however the plots show considerable variation. However whether the flow has a Mach number of 50 or 100, it will still be geometrically thin. In other words these differences may not be observable.

We plot the energy dissipation rate as a function of time for the blackbody simulation. This equates to the total disk luminosity (through both disk faces). We thus compare this curve with photometric disk observations. In particular we compare the periodic component of the energy dissipation plots with superhumps. Fig. 6.8.11 shows not only the total figure for the disk, but also that component of the signal generated by the outer regions (lower two curves) for $t = 1406.04$ to $t = 1500.00$. In common with the isothermal simulation, the signal from the inner disk is very noisy. Before plotting, we averaged the dissipation over ten timesteps (giving us approximately 63 points per binary period). This removed the high frequency component of the data and made comparison with observations more easy. We note that although the time resolution of their observations was much finer, Amerongen et al. (1987) used 50 data points per period to plot average superhump light curves of VW Hydri. Other superhump observations used for comparison with our simulation were by Schoembs and Vogt 1983 (VW Hydri), and Patterson et al. 1993 (VW Aquarii).

A detailed description of the superhump phenomenon is found in Warner (1985). When they initially appear in a superoutburst, superhumps have an amplitude as great as 30 to 40% of the background disk luminosity. This declines over the course of the supermaximum. The shape of the superhumps also evolves. Initially they have quite sharp peaks, with a steeper rise than decline. Later on the profiles become smoother, and the period decreases fractionally (but it is always a few percent greater than the orbital period). Now in this simulation we sought a steady state precessing disk. We did not attempt to model the disk's evolution over a superoutburst. Thus we do not see any of the superhump evolution described above.

In Fig. 6.8.12 we show 20 scaled time units of the $r > 0.10$ luminosity curve. The luminosity is shown on a logarithmic scale for ease of comparison with observations. Both in Fig. 6.8.11 and Fig. 6.8.12 large narrow spikes in the luminosity are clearly visible. They occur regularly and always at the same phase in the disk precession. The spikes are not seen in the observational data. Their presence in the simulation can however be explained.

At the same phase each precession period, the disk throws off a number of particles into the neighborhood of the inner Lagrangian point. The material tends to gather here, colliding with the injection stream (frames 1 and 2, Fig. 6.8.14). This gas 'blob' eventually falls towards the primary (frames 3 and 4), getting compressed as it does so. After an oblique encounter with the disk, the blob's angular momentum carries it around the primary, where it finally merges with the main disk flow. Frames 5 and 6 show the huge rent in the disk along the blob's path. It is this violent collision that causes the spike in the luminosity. The injection stream plays some role in the creation of these blobs. However in a second blackbody simulation in which gas was injected in a circular orbit at the disk circularisation radius, the blobs still formed and the narrow spikes were still visible in the luminosity curve (Fig. 6.8.13). In other words the gas thrown off by the disk each rotation is sufficient to form the blobs. This phenomenon is a symptom of the simulation disk's large eccentricity. As real superhump lightcurves do not show these spikes, it appears that CV disks are more centrally condensed and less eccentric than ours. Again, to follow this point further, we must conduct simulations with the Shakura-Sunyaev viscosity.

Warner and O'Donoghue (1988) and O'Donoghue (1990) have made detailed studies of eclipse lightcurves of Z Cha in superoutburst with the objective of obtaining a two dimensional map of the superhump light source. Now previous studies had found the source to be an extended region in the outer disk with a temperature somewhat less than 10^4K. For example Naylor et al. (1987) estimated that the superhump light from OY Car came from a region that was optically thick with a temperature approximately 8000K, and an area of the order of that of the whole disk. Warner and O'Donoghue attacked the problem by writing a code that generated synthetic light eclipse curves for given disk luminosity distributions. Using trial and error, they then sought the distribution which produced eclipses that best matched observations. Their basic assumption was that the source had a fixed position in the binary's frame (ie that it did not move over the course of the superhump). They simply modulated the source's brightness using the time variation of an uneclipsed hump. This process was clearly quite ad hoc. However it was reasonably effective in excluding some candidate source configurations. Their fundamental discovery was that the source definitely was not axisymmetric. Secondly, they analysed two eclipses in detail and found them to be incompatible with light variations in the hot spot (the Vogt elliptic disk model for superhump). Best matches with observations were obtained when the superhump source was modelled as a ring with a brightness function of the form

$$B(\theta, t) = f(\theta) \times g(t) . \tag{6.8.4}$$

Specifically, the fit was best for a ring that was brightest near the binary axis on the side near the secondary and then decayed away to either side.

O'Donoghue (1990) improved the technique by utilising Horne's eclipse mapping method. Firstly he decomposed observed eclipse lightcurves into two components; from the background disk, and from the superhump source. There was of course considerable uncertainty involved in this process. He then performed a maximum entropy deconvolution on the superhump signal. The resulting two dimensional superhump 'maps' are more detailed than the results of Warner and O'Donoghue but are still constrained by the same assumptions; that the superhump light source is stationary, and that it has a uniform brightness modulation given by the time variation of an uneclipsed hump. He considered four eclipsed superhumps in detail. In each case he found the superhump source to be located on the edge of the disk in the approximate direction of the secondary. In three eclipses the source could be resolved into three components; a compact source on the disk edge almost in line with the binary axis, and two flanking extended sources that followed the disk rim. The relative brightness of the three sources changed from eclipse to eclipse. The fourth eclipse had quite a different superhump map consisting of a single peak located near where the stream encounters the disk.

If we discount the narrow spikes, the simulation lightcurves somewhat resemble observational profiles. In common with superhump, over each cycle the luminosity rises steeply and then declines more slowly. The amplitude of the oscillation (without spikes) is very approximately one quarter the magnitude of the steady signal from the outer disk. In fact, there are two humps per cycle, a large one with a steep rise to maximum and a second smaller one that occurs about half a cycle later.

Fig. 6.8.15 is a set of six disk luminosity maps, corresponding to the density plots of Fig. 6.8.7, and to the first cycle of the lightcurve in Fig. 6.8.12. The centre of the disk ($r < 0.10$) has been masked out in each plot, and a logarithmic scale used, in order to highlight the structure in the outer disk. In frames 2 and 3 ($t = 1408$ and $t = 1409$) we see a pink (i.e. high luminosity) trail extending downstream of the point of impact of the stream with the disk. Recall Fig. 6.8.13, the lightcurve for the blackbody disk without an injection stream. The second hump is absent, having been replaced by an extended minimum. Thus the smaller cyclical hump in the lightcurve is caused by variations in the hotspot luminosity in accordance with the Vogt elliptic disk model for superhump. Now the data analysis of Warner and O'Donoghue, and of O'Donoghue, specifically excluded the hotspot as the superhump light source in several observed eclipses. In one case however, O'Donoghue found that the hotspot did appear to be responsible. So what is happening?

The amplitude of the hot spot hump will be proportional to the eccentricity of the disk. The blackbody simulation produces a disk that is more eccentric than the isothermal one and, we suspect, more eccentric than observed disks. Thus we would expect the hot spot hump to be most prominent for the blackbody disk. Indeed it is far less visible in the isothermal simulation. Within the context of the thermal instability model, we expect the disk to evolve considerably during a superoutburst. As mass drains away onto the white dwarf, the disk's moment of inertia and eccentricity will be affected. Changes in the nature of the superoutburst are not unreasonable. As a final comment we note that at the very end of a supermaximum, a phenomena known as 'late superhump' is observed. These oscillations have a period very similar to standard superhumps but are shifted 180° out of phase.

Now we turn to the larger of the two humps. Frames 5 and 6 of Fig. 6.8.15 show a very bright ridge along the bottom of the disk. Referring to Fig. 6.8.7, we see that it is dense as well as luminous. Splitting the signal into components from the right and left hand sides of the disk (as we did for the isothermal simulation), reveals that the right hand side contributes most of the luminosity. In fact if we follow the ridge from left to right, the luminosity increases to a maximum at the endpoint of the ridge. Thus the large hump is formed in exactly the same manner as in the isothermal simulation. This result is clearly inconsistent with the detail of O'Donoghue's analysis of observations. There is no evidence in either simulation of a bright spot on the left hand side of the disk near the binary axis.

The particle plots of Fig. 6.8.15 have been redrawn in Fig. 6.8.16, this time colouring the particles according to temperature. Fig. 6.8.16 shows that temperatures in the ridge at the bottom of the disk range from approximately 2×10^4 to 3×10^4 K. These temperatures are a factor of two or three greater than the temperature estimates by Naylor et al. (1987) of the superhump source.

Rutten et al. (1992) note that the eclipse lightcurves may include some light from sources other than the disk. Unless this extraneous luminosity is correctly removed, the deconvolution process will give incorrect results. In particular the disk luminosity map will have a spurious ring structure. They mention that this may be affecting Warner and O'Donoghue's results. As a check they suggest adjusting the resolution of the deconvolution. Spurious structure will then reveal itself by changing position. Genuine disk features will be unaffected. Now in their analysis of OY Car in outburst, Rutten et al. found up to 15% of the total system luminosity came from off the disk plane.

The eclipse mapping technique was originally used to find luminosity maps for stationary disks. To apply it to a time dependent light source, O'Donoghue had to make assumptions about its nature. It was assumed that the source was stationary in the binary frame and that the entire source brightened and dimmed in phase. Considering our simulations, we find that these may not be good assumptions. It is entirely possible that the source is moving and that the time dependence of its luminosity is not uniform.

We have already mentioned the importance of the disk's radial mass distribution in determining its properties. It is quite possible that the location of the time dependent signal could be different in a simulation with a more centrally condensed disk. We recall that our $\mu = \frac{1}{2}$ disks developed high density ridges along their left hand edge (looking on the disk in the same sense as in all our particle plots). However these disks were stationary and did not precess.

O'Donoghue compared his results with Whitehurst's (1988 a) simulations. He thought Whitehurst's assumption that heat energy was instantaneously radiated away was unrealistic. Whitehurst, and ourselves, have equated the instantaneous radiation approximation to the assumption that the disk is geometrically thin. Strictly however, this argument only applies to axisymmetric, stable disks in which temperature changes are slow relative to the dynamical timescale. In our unstable, precessing disks we find both sharp horizontal temperature gradients and temperatures that change in a fraction of a binary period. It is thus possible that the approximation is not very good in the non-axisymmetric regions of tidally unstable disks.

Let us perform a thought experiment and assume the approximation breaks down locally in the region of the superhump luminosity. How would our results be affected? Firstly the large horizontal temperature gradients would result in some thermal energy transport in the plane (convective or radiative). secondly some of the energy released by viscous action would be taken up as internal energy of the gas. Thus some energy would be convected away along streamlines. The superhump energy then will be radiated away over a larger surface area than in our simulation. As a result the superhump region will have a lower temperature than ours. We also expect the high frequency components of the signal to be diminished. We do not believe however that relaxing the instantaneous radiation assumption on its own could account for the differences between our results and those of O'Donoghue.

So there is disagreement as to the location of superhump in the disk. We do not feel that either simulation or observational analysis is yet at a stage where a strong statement can yet be made on this point. We would like to complete a simulation with a Shakura-Sunyaev viscosity. Then we must consider our assumption that heat generated by viscous dissipation is immediately radiated out of the plane. On the observational side we would like to see more eclipses analysed. Currently the sample size is too small. We also feel that an observational attempt to locate the superhump source that is independent of the assumptions of Warner and O'Donoghue must be made.

6.9. Blackbody Disk Conclusions

On the whole, the attempt to incorporate some simple radiation physics into a two dimensional particle based disk simulation has been quite successful. The strength of particle methods is their ability to model the dynamics of disk flow. Up until now however, direct comparison between particle simulation and observation has been lacking. This has detracted from the credibility of these methods. We have tested a very simple blackbody model against observations. We knew *a priori* that the disks of dwarf novae in outburst had blackbody temperature profiles. Our simulation proved capable of reproducing the long time scale features of an outbursting disk, particularly the $r^{-\frac{3}{4}}$ temperature profile. The greater visibility of the bright spot in our simulation than in observations was taken as supporting evidence for the thermal instability model for outburst.

Our change in equation of state yielded other useful information. We found first of all that it caused a small change in the radial mass distribution, upon which the strength of the disk's tidal instability proved strongly dependent. A slight increase in the proportion of the disk mass in its outer regions (near the resonance) resulted in an earlier onset of the instability. The amplitude of the disk precession was then found to be larger. The nature of the cyclic component of the energy dissipation was also affected. A clear future direction for this research then will be to complete a set of simulations with a Shakura-Sunyaev viscosity law.

The simulations (both blackbody and isothermal) provide quite strong circumstantial evidence that the tidal instability is the cause for superhump. The disk precession periods obtained are significantly higher than superhump values but are consistent with results of other authors and can possibly be explained in terms of the differing moments of inertia in observed and simulated disks. The cyclic dissipation curve in our blackbody simulation bears some similarity to observed superhumps. We are not so confident regarding the detail of the signal. In particular our initial simple assumption that all energy viscously released at a point in the disk is instantaneously radiated through the disk faces may not hold in and around the superhump source. We have not thoroughly investigated the degree to which this may be a problem. At first glance however, it appears that rectifying it would not significantly affect the global disk behaviour but just increase the size of the periodic source and reduce its high frequency variability. Perhaps the bright spot and other non axisymmetric regions will also have to be considered in this regard.

Notwithstanding the above concerns, we should be encouraged by the results. The way appears clear to incorporate more complicated radiation physics in order to model quiescent dwarf novae disks for example.

Chapter 7.
The Stability of a Ring of 'Viscous' Particles

7.1. Background

Whilst conducting axisymmetric simulations similar to those of Chapter 5, we noticed that eventually the disks became disordered. This was found to be due to an instability associated with the SPH artificial viscosity term. The behaviour is illustrated in Fig. 7.1 and Fig. 7.2. Frame 1 (top left) of Fig. 7.1 shows the initial setup of the disk. We placed particles in 7 rings with a separation, both within and between rings set at $\frac{5h}{13}$. This gave the annulus an intial radial extent, $0.2385 < r < 0.2615$. The values of the various parameters are listed in the caption to Fig. 7.1. To simplify matters we used a constant particle mass. As a result the density has a $\frac{1}{r}$, discontinuously dropping to zero at the disk edges. All particles with positive x coordinates are plotted in bold. This highlights the differential rotation of the disk. Initially it evolves as we would expect, spreading out radially. By $t = 1.00$ (approximately one and a quarter periods of the annulus) the disk has already spread out considerably and become quite diffuse. In particular, ring 1 (starting at the inside and counting out) has moved sufficiently far inside of the next innermost ring (2) to become almost independent of it. We see for the first time a small 'wobble' on that innermost ring of particles. 0.10 time units later (frame 3) the 'wobble' has become much larger, giving ring 1 a sawtooth appearance. After a further ten timesteps it has become completely disrupted. We now see a slight wobble on the next innermost ring. It is unclear whether the destabilisation of ring 2 is increased through interactions with the remnants of ring 1. The disk's continuing evolution is shown in Fig. 7.2, frame 1 of which tells a curious story. With the second inner ring now well disrupted, the third ring is also starting to wobble. The fourth, fifth and sixth rings at this point are still holding their form but the outermost ring is showing signs of disorder. Thus the instability occurs initially at both edges of the disk and progresses inwards to the interior of the disk (rings 4 and 5). This indicates that the presence of neighbouring rings on both sides inhibits the growth of the viscous instability. The remaining three frames of Fig. 7.2 show the progressive disruption of the disk. By $t = 2.2$ very little remains of the initial ring structure.

To simplify the problem further we reduced the disk to a single ring of viscous particles. This becomes disordered in exactly the way ring 1 did. We show this in Fig. 7.3. The parameters for this calculation were identical to those of the previous simulation. Once more we used an initial particle separation of $\frac{5h}{13}$. In this case the ring showed signs of disorder after approximately 2.5 scaled time units which is two and a half times longer than it took ring 1 in the previous calculation. By $t = 2.80$ the particles form a narrow annulus rather than a single ring. As the simulation proceeds this annulus simply becomes broader.

7.2. Stability Analysis

Below we describe a linear stability analysis of a single circular ring of SPH particles in Keplerian orbit about a massive central body. We neglect gravitational and pressure forces between the particles. Thus the only forces we do consider are their viscous interactions and the gravitational attraction of the central body. The equilibrium state of the ring is for the particles to continue in their circular orbits of radius r and angular velocity $\omega = \sqrt{(\frac{GM}{r^3})}$. In this equilibrium state the viscous forces between particles are exactly zero. We consider the linear growth of a small perturbation to the ring. The problem is scaled by setting the mass of the central body M, the equilibrium radius of the ring and the particles' angular velocity equal to unity. The analysis is modelled on Maxwell's (1856) treatment of a gravitating ring.

Take two particles in the ring which we shall label P and Q. In the equilibrium ring, at time t, particle P has polar coordinates (r_{p0}, φ_{p0}) where

$$r_{p0} = 1 \tag{7.2.1}$$

and

$$\varphi_{p0} = S_p + t. \tag{7.2.2}$$

S_p is the angular coordinate of P in the frame corotating with the ring. $\vec{r}_{p0}$ then is the position vector of that particle in the equilibrium ring. It is of course a unit vector. $\vec{\Omega}_0$ is the angular velocity vector. The motion is anticlockwise so

$$\vec{\Omega}_0 = \vec{k}, \tag{7.2.3}$$

with $\vec{k}$ being the unit vector in the positive z direction. $\vec{\Omega}_0 \times \vec{r}_{p0} = \vec{k} \times \vec{r}_{p0}$ completes the orthonormal triad, being a unit vector tangent to the motion of particle P. The coordinates of particle Q are similarly defined. The equilibrium angular separation of the two particles is independent of time

$$\zeta_{pq} = S_q - S_p. \tag{7.2.4}$$

Let there be N particles equally spaced about the ring. Then

$$\zeta_{pq} = \frac{2\pi j}{N}, \tag{7.2.5}$$

with j being an integer such that $0 \le j \le N$. We then apply a small perturbation to the ring, giving particle P new coordinates (r_p, φ_p) where

$$\begin{aligned} r_p &= r_{p0} + \rho_p && (7.2.6a)\\ &= 1 + \rho_p && (7.2.6b) \end{aligned}$$

and

$$\begin{aligned} \varphi_p &= \varphi_{p0} + \sigma_p && (7.2.7a)\\ &= S_p + t + \sigma_p. && (7.2.7b) \end{aligned}$$

The situation is illustrated in Fig. 7.4. $\vec{r}_p$ then is the position vector of P in the perturbed ring.

$$\begin{aligned} \vec{r}_p &= r_p \vec{r}_{p0} + r_p \sigma_p \left(\vec{k} \times \vec{r}_{p0}\right) && (7.2.8a)\\ &= (1+\rho_p)\,\vec{r}_{p0} + (1+\rho_p)\,\sigma_p \left(\vec{k} \times \vec{r}_{p0}\right). && (7.2.8b) \end{aligned}$$

ρ_p and σ_p are assumed to be small. Thus to first order

$$\vec{r}_p \simeq (1+\rho_p)\,\vec{r}_{p0} + \sigma_p \left(\vec{k} \times \vec{r}_{p0}\right). \tag{7.2.9}$$

The velocity vector of P in the perturbed ring

$$\begin{aligned} \vec{v}_p &= \dot{\rho}_p \vec{r}_{p0} + (1+\dot{\sigma}_p)(1+\rho_p) \left(\vec{k} \times \vec{r}_{p0}\right) && (7.2.10a)\\ &\simeq \dot{\rho}_p \vec{r}_{p0} + (1+\dot{\sigma}_p+\rho_p) \left(\vec{k} \times \vec{r}_{p0}\right). && (7.2.10b) \end{aligned}$$

This stability study then is just an analysis of the linear growth of the perturbation functions $\rho(S,t)$ and $\sigma(S,t)$ where we have chosen to use coordinates corotating with the ring. We then have

$$\rho_p(t) \equiv \rho(\varphi_p - t, t) \tag{7.2.11a}$$
$$= \rho(S_p + \sigma_p, t) \tag{7.2.11b}$$
$$\simeq \rho(S_p, t) \tag{7.2.11c}$$

and

$$\sigma_p(t) \equiv \sigma(\varphi_p - t, t) \tag{7.2.12a}$$
$$\simeq \sigma(S_p, t)\,. \tag{7.2.12b}$$

We now proceed by linearising the equations of motion and solving them for ρ and σ for the initial conditions

$$\rho(S, 0) = \rho_0(S) \tag{7.2.13a}$$
$$\dot\rho(S, 0) = \dot\rho_0(S) \tag{7.2.13b}$$
$$\sigma(S, 0) = \sigma_0(S) \tag{7.2.13c}$$
$$\dot\sigma(S, 0) = \dot\sigma_0(S)\,. \tag{7.2.13d}$$

The equation of motion in the radial direction is

$$\ddot r - r\dot\varphi^2 = -\frac{1}{r^2} + R \tag{7.2.14}$$

where R is the radial component of the viscous force per unit mass. In the azimuthal direction we have

$$r\ddot\varphi + 2\dot r\dot\varphi = T \tag{7.2.15}$$

with T being the tangential component of the viscous force per unit mass. Linearising Eq. (7.2.14) we have

$$\ddot\rho - 3\rho - 2\dot\sigma = R \tag{7.2.16}$$

and from Eq. (7.2.15) we get

$$\ddot\sigma + 2\dot\rho = T. \tag{7.2.17}$$

For a moment consider the inviscid case, $R = T = 0$. We have

$$\ddot\rho - 3\rho - 2\dot\sigma = 0 \tag{7.2.18}$$

and

$$\ddot\sigma + 2\dot\rho = 0. \tag{7.2.19}$$

With the initial conditions given by Eq. (7.2.13), this system has solution

$$\rho(S, t) = \rho_0(S)(4 - 3\cos t) + \dot\rho_0(S)\sin t + \dot\sigma_0(S)(1 - 2\cos t) \tag{7.2.20a}$$
$$\sigma(S, t) = 6\rho_0(S)(\sin t - t) + \sigma_0(S) + 2\dot\rho_0(S)(\cos t - 1) + \dot\sigma_0(S)(4\sin t - 3t)\,. \tag{7.2.20b}$$

If we rewrite the solution, ordering terms according to their time dependence we get

$$\rho(S,t) = 2\left(\dot{\sigma}_0(S) + 2\rho_0(S)\right) + \dot{\rho}_0(S)\sin t - \left(2\dot{\sigma}_0(S) + 3\rho_0(S)\right)\cos t \tag{7.2.21a}$$

$$\begin{aligned}\sigma(S,t) &= \left(\sigma_0(S) - 2\dot{\rho}_0(S)\right) - 3\left(\dot{\sigma}_0(S) + 2\rho_0(S)\right)t \\ &\quad + 2\left(2\dot{\sigma}_0(S) + 3\rho_0(S)\right)\sin t + 2\dot{\rho}_0(S)\cos t.\end{aligned} \tag{7.2.21b}$$

Consider an isolated particle in a circular orbit about a central mass. There are of course nearby orbits that are circular but with slightly different radii and angular velocities. If we apply a (small) perturbation to the particle we may observe two phenomena. Firstly the particle may be shifted to a neighbouring circular orbit. Secondly it may execute small 'epicyclic' oscillations with the new circular orbit as its 'guiding centre'. The epicyclic period is determined by the radius of the circular orbit.

Returning to the ring, the constant term in Eq. (7.2.21a) and the term of order t in Eq. (7.2.21b) represent a shift to a neighbouring circular orbit. We call this the secular response of the ring. The sinusoidal terms represent the epicyclic or oscillatory response. Note that the epicycles are of unit frequency (period 2π) as a result of our scaling of the problem. With an appropriate choice of $\rho_0, \dot{\rho}_0, \sigma_0$ and $\dot{\sigma}_0$ we can of course eliminate either the shift to a new guiding centre, or the epicyclic motion.

We now consider the viscous case. The standard SPH artificial viscosity term gives rise to a force per unit mass on particle P

$$\vec{F}_p = \sum_Q \frac{m_q \bar{c}\bar{\alpha} h}{\bar{\rho}} \frac{\vec{v}_{pq}\cdot\vec{r}_{pq}}{r_{pq}^2 + \eta^2 h^2} \vec{\nabla}_p W_{pq}, \tag{7.2.22}$$

where the summation is over all particles in the ring. We replace the mean values for the sound speed and density, $\bar{c}$ and $\bar{\rho}$ by the constants c and D respectively. All particles have equal mass m. Now the SPH artificial viscosity always has an $\eta^2 h^2$ term in the denominator to prevent it from becoming singular at very small r_{pq}. For the purposes of this stability analysis however, it can be neglected. Thus Eq. (7.2.22) simplifies to

$$\vec{F}_p = \frac{\bar{\alpha} chm}{D} \sum_Q \frac{\vec{v}_{pq}\cdot\vec{r}_{pq}}{r_{pq}^2} \vec{\nabla}_p W_{pq}. \tag{7.2.23}$$

For the purposes of this analysis we shall assume that the kernel is a Gaussian normalised for two dimensions,

$$W_{pq} = \frac{1}{\pi h^2} e^{-\frac{r_{pq}^2}{h^2}}. \tag{7.2.24}$$

We thus have

$$\vec{\nabla}_p W_{pq} = -\frac{2\vec{r}_{pq}}{\pi h^4} e^{-\frac{r_{pq}^2}{h^2}} \tag{7.2.25a}$$

$$= -\frac{2}{h^2}\vec{r}_{pq} W_{pq}. \tag{7.2.25b}$$

Then

$$\vec{F}_p = -\frac{2\bar{\alpha} chm}{Dh^2} \sum_Q \frac{\vec{v}_{pq}\cdot\vec{r}_{pq}}{r_{pq}^2} \vec{r}_{pq} W_{pq} \tag{7.2.26a}$$

$$= -f \sum_Q \frac{\vec{v}_{pq}\cdot\vec{r}_{pq}}{r_{pq}^2} \vec{r}_{pq} W_{pq}. \tag{7.2.26b}$$

$$f = \frac{2\bar{\alpha} chm}{Dh^2} \tag{7.2.27}$$

is then just a constant reflecting the strength of the viscous interactions, it having the dimensions of a kinematic viscosity. In the undisturbed ring there is no relative motion of the particles and hence the viscous forces between them are all zero. The problem now is to determine the viscous forces between the particles in a slightly perturbed ring. Dotting Eq. (7.2.9) and Eq. (7.2.10) we get, to first order,

$$\vec{v}_p \cdot \vec{r}_p = \dot{\rho}_p + \sigma_p. \tag{7.2.28}$$

Dotting the velocity vector for Q with the position vector for P we find

$$\vec{v}_q \cdot \vec{r}_p = \left(\dot{\rho}_q \vec{r}_{q0} + (1 + \dot{\sigma}_q + \rho_q)\left(\vec{k} \times \vec{r}_{q0}\right)\right) \cdot \left((1 + \rho_p)\,\vec{r}_{p0} + \sigma_p\left(\vec{k} \times \vec{r}_{p0}\right)\right) \tag{7.2.29}$$

Neglecting all terms of higher than first order

$$\vec{v}_q \cdot \vec{r}_p \simeq \dot{\rho}_q \vec{r}_{q0} \cdot \vec{r}_{p0} + (1 + \dot{\sigma}_q + \rho_q + \rho_p)\left(\vec{k} \times \vec{r}_{q0}\right) \cdot \vec{r}_{p0} + \sigma_p\left(\vec{k} \times \vec{r}_{q0}\right) \cdot \left(\vec{k} \times \vec{r}_{p0}\right). \tag{7.2.30}$$

Now

$$\left(\vec{k} \times \vec{r}_{q0}\right) \cdot \left(\vec{k} \times \vec{r}_{p0}\right) = \vec{r}_{q0} \cdot \vec{r}_{p0}. \tag{7.2.31}$$

Hence

$$\vec{v}_q \cdot \vec{r}_p \simeq (\dot{\rho}_q + \sigma_p)\,\vec{r}_{q0} \cdot \vec{r}_{p0} + (1 + \dot{\sigma}_q + \rho_q + \rho_p)\left(\vec{k} \times \vec{r}_{q0}\right) \cdot \vec{r}_{p0}. \tag{7.2.32}$$

Therefore

$$\vec{v}_{pq} \cdot \vec{r}_{pq} = (\dot{\rho}_p + \sigma_p + \dot{\rho}_q + \sigma_q)(1 - \vec{r}_{q0} \cdot \vec{r}_{p0}) + (\dot{\sigma}_q - \dot{\sigma}_p)\left(\vec{k} \times \vec{r}_{q0}\right) \cdot \vec{r}_{p0} \tag{7.2.33}$$

to first order. Recall that ζ_{pq} is the equilibrium angular separation of P and Q. Thus

$$\vec{r}_{q0} \cdot \vec{r}_{p0} = \cos\zeta_{pq} \tag{7.2.34}$$

and

$$\vec{r}_{p0} \times \vec{r}_{q0} = \sin\zeta_{pq}\,\vec{k}. \tag{7.2.35}$$

Hence

$$\vec{v}_{pq} \cdot \vec{r}_{pq} = (\dot{\rho}_p + \sigma_p + \dot{\rho}_q + \sigma_q)(1 - \cos\zeta_{pq}) + (\dot{\sigma}_q - \dot{\sigma}_p)\sin\zeta_{pq}. \tag{7.2.36}$$

Now for small angles ζ_{pq}, $1 - \cos\zeta_{pq}$ is a second order term whereas $\sin\zeta_{pq}$ is first order. Therefore

$$\vec{v}_{pq} \cdot \vec{r}_{pq} \simeq (\dot{\sigma}_q - \dot{\sigma}_p)\sin\zeta_{pq} \tag{7.2.37}$$

and the viscous force per unit mass

$$\vec{F}_p \simeq -f \sum_Q \frac{(\dot{\sigma}_q - \dot{\sigma}_p)}{r_{pq}^2}\sin\zeta_{pq}\,\vec{r}_{pq} W_{pq}. \tag{7.2.38}$$

Using Eq. (7.2.34) we have

$$r_{pq}^2 \simeq 2\left(1 - cos\zeta_{pq}\right). \tag{7.2.39}$$

Thus we resolve the viscous force into radial component

$$R \simeq -\frac{f}{2} \sum_Q \left(\dot{\sigma}_q - \dot{\sigma}_p\right) \sin \zeta_{pq} \, W_{pq}, \tag{7.2.40}$$

and tangential component

$$T \simeq \frac{f}{2} \sum_Q \left(\dot{\sigma}_q - \dot{\sigma}_p\right) \left(1 + \cos \zeta_{pq}\right) W_{pq}. \tag{7.2.41}$$

Note that σ itself does not appear either as a term on the left hand side of the equations of motion, Eq. (7.2.16) and Eq. (7.2.17), or in the viscous force term Eq. (7.2.38). Thus we define the perturbation in terms of ρ and $\dot{\sigma}$, and assume it to be of the form

$$\rho\left(S,t\right) = Ae^{i(lS+nt)} \tag{7.2.42a}$$
$$\dot{\sigma}\left(S,t\right) = Be^{i(lS+nt)}. \tag{7.2.42b}$$

In other words we assume the perturbation is sinusoidal with mode number l. Substitution of Eq. (7.2.42) into Eq. (7.2.16) yields

$$\left(-n^2 - 3\right) A - 2B = -\frac{fB}{2} \sum_Q \left(e^{il(S_q - S_p)} - 1\right) \sin \zeta_{pq} \, W_{pq}. \tag{7.2.43}$$

The summation is over all N particles in the ring. However as we know that only nearby particles will contribute to the sum, we can replace the finite sum with an infinite one from $Q = -\infty$ to $Q = +\infty$. It is now clear that the odd component of the sum must vanish. Therefore

$$\left(n^2 + 3\right) A + 2B = \frac{ifB}{2} \sum_Q \sin l\zeta_{pq} \, \sin \zeta_{pq} \, W_{pq}. \tag{7.2.44}$$

From Eq. (7.2.17) we get in the same fashion

$$inB + 2inA = -\frac{fB}{2} \sum_Q \left(1 - \cos l\zeta_{pq}\right) \left(1 + \cos \zeta_{pq}\right) W_{pq}. \tag{7.2.45}$$

We let

$$\Psi = \frac{1}{2} \sum_Q \sin l\zeta_{pq} \, \sin \zeta_{pq} \, W_{pq} \tag{7.2.46}$$

and

$$\Phi = \sum_Q \left(1 - \cos l\zeta_{pq}\right) \left(1 + \cos \zeta_{pq}\right) W_{pq}. \tag{7.2.47}$$

From Eq. (7.2.44) we have

$$\left(n^2 + 3\right) A = \left(2i + f\Psi\right) iB \tag{7.2.48}$$

and from Eq. (7.2.45)

$$2inA = \left(\frac{if}{2}\Phi - n\right) iB. \tag{7.2.49}$$

Elimination of A and B from Eq. (7.2.48) and Eq. (7.2.49) yields the cubic equation in n,

$$n^3 - \frac{if\Phi}{2}n^2 + (2if\Psi - 1)\,n - \frac{3if}{2}\Phi = 0. \tag{7.2.50}$$

If $f = 0$ (ie there is no viscosity) we have

$$n_0^3 = n_0 \tag{7.2.51}$$

which has solutions

$$n_0 = 0, \pm 1. \tag{7.2.52}$$

We immediately identify the $n_0 = \pm 1$ solutions with the oscillatory terms in Eq. (7.2.20) and the $n_0 = 0$ root with the linear component. We now assume a **weak** viscosity and hence look for solutions of Eq. (7.2.50) of the form

$$n = n_0 + \epsilon \tag{7.2.53}$$

where $\epsilon \ll 1$. We look at the three distinct solutions of Eq. (7.2.51) individually. First we let

$$n = 1 + \epsilon. \tag{7.2.54}$$

Substitution of Eq. (7.2.54) into Eq. (7.2.50) yi.e.lds

$$(1+\epsilon)^3 - \frac{if\Phi}{2}(1+\epsilon)^2 + (2if\Psi - 1)(1+\epsilon) - \frac{3if\Phi}{2} = 0 \tag{7.2.55}$$

Neglecting all second and higher order terms in ϵ we find

$$\epsilon_1 = if\,(\Phi - \Psi) \tag{7.2.56}$$

If we take

$$n = -1 + \epsilon \tag{7.2.57}$$

we get

$$\epsilon_{-1} = if\,(\Phi + \Psi)\,. \tag{7.2.58}$$

Finally, if we take

$$n = \epsilon \tag{7.2.59}$$

we find

$$\epsilon_0 = -\frac{3if}{2}\Phi. \tag{7.2.60}$$

Now the time dependence of the perturbation functions is given by

$$e^{int} = e^{i(n_0+\epsilon)t}.$$

With all three solutions of Eq. (7.2.50), n is real and ϵ is imaginary. The linear stability of a perturbation is thus determined by the sign of ϵ. If it is positive then the perturbation will die away. If on the other hand it is negative, the perturbation will grow exponentially at a rate

$$\lambda = -\epsilon. \tag{7.2.61}$$

We must now examine Φ and Ψ in a little detail. First we consider Φ. If there are N particles in the ring and W_{pq} is given by Eq. (7.2.24) then

$$\Phi = \frac{1}{\pi h^2} \sum_{j=1}^{N} \left(1 - \cos\left(jl\Delta\theta\right)\right) \left(1 + \cos\left(j\Delta\theta\right)\right) e^{-2(1-\cos(j\Delta\theta))/h^2} \tag{7.2.62}$$

where

$$\Delta\theta = \frac{2\pi}{N}. \tag{7.2.63}$$

The mode number l is an integer such that $0 \leq l \leq N$. In order to compare summations for rings with different N, we will refer to the scaled mode number $\frac{l}{N}$. Now, given Eq. (7.2.63) for $\Delta\theta$ we can easily show that

$$\cos\left(lj\Delta\theta\right) = \cos\left(\left(N - l\right) j\Delta\theta\right) \tag{7.2.64}$$

and

$$\sin\left(lj\Delta\theta\right) = -\sin\left(\left(N - l\right) j\Delta\theta\right). \tag{7.2.65}$$

Thus , in terms of Φ, a perturbation with mode number l is indistinguishable from one with mode number $N - l$. The graph of Φ as a function of $\frac{l}{N}$ then will be symmetric about $\frac{l}{N} = \frac{1}{2}$. Fig. 7.5 plots $\pi h^2 \Phi$ for three values of $\frac{\Delta\theta}{h}$, the ratio of the particle separation to the smoothing length. The curves were obtained by directly computing the summation and are indeed symmetric about the line $\frac{l}{N} = \frac{1}{2}$. We see that Φ increases uniformly from zero at $\frac{l}{N} = 0$ to a maximum at $\frac{l}{N} = \frac{1}{2}$. As $\frac{\Delta\theta}{h} \to 0$ the maximum becomes very broad and flat with $\Phi \simeq$ constant for increasingly large ranges of $\frac{l}{N}$. Thus, from Eq. (7.2.60), the $n_0 = 0$ modes are always unstable with the short wavelength modes growing most rapidly. In other words the secular component of the ring's response to a perturbation is unstable for perturbations of all length scales. We now consider analytically the cases $\frac{l}{N} \to 0$ and $\frac{l}{N} = \frac{1}{2}$ in order to place bounds on the behaviour of Φ. Firstly we make some simplifying approximations. We note that $h \ll 1$. Thus $e^{-2(1-\cos(j\Delta\theta))/h^2} \to 0$ except if $1 - \cos(j\Delta\theta) \to 0$. In other words the only non negligible terms in the summation have $j\Delta\theta \ll 1$. In this limit

$$1 - \cos\left(j\Delta\theta\right) \simeq \tfrac{1}{2}\left(j\Delta\theta\right)^2 \tag{7.2.66}$$

and

$$1 + \cos\left(j\Delta\theta\right) \simeq 2. \tag{7.2.67}$$

Thus

$$\Phi \simeq \frac{2}{\pi h^2} \sum_{j=1}^{N} \left(1 - \cos\left(jl\Delta\theta\right)\right) e^{-\left(\frac{j\Delta\theta}{h}\right)^2}. \tag{7.2.68}$$

Now if l is small, that is the perturbation is of long wavelength, we can say

$$1 - \cos\left(jl\Delta\theta\right) \simeq \tfrac{1}{2}\left(jl\Delta\theta\right)^2. \tag{7.2.69}$$

Then

$$\Phi \simeq \frac{l^2}{\pi h^2 \Delta\theta} \sum_{j=1}^{N} \left(j\Delta\theta\right)^2 e^{-\left(\frac{j\Delta\theta}{h}\right)^2} \Delta\theta. \tag{7.2.70}$$

This is just a Riemann sum. If the particle separation is small in comparison to the smoothing length, we can approximate Eq. (7.2.70) with the integral

$$\Phi \simeq \frac{2l^2}{\pi h^2 \Delta\theta} \int_0^\infty x^2 e^{-\left(\frac{x}{h}\right)^2} dx. \tag{7.2.71}$$

Hence

$$\Phi \simeq \frac{l^2 h}{2\sqrt{\pi}\Delta\theta}. \tag{7.2.72}$$

On the other hand if $l = \frac{N}{2}$ (the short wavelength limit) we have

$$1 - \cos(jl\Delta\theta) = 1 - (-1)^j \tag{7.2.73}$$

and

$$\Phi \simeq \frac{2}{\pi h^2 \Delta\theta} \sum_{j=1}^{\frac{N}{2}} e^{-\left(\frac{2j\Delta\theta}{h}\right)^2} 2\Delta\theta. \tag{7.2.74}$$

Again if the particle separation is small in comparison to the smoothing length, we can approximate Eq. (7.2.74) with an integral to find

$$\Phi\left(l = \frac{N}{2}\right) \simeq \frac{2}{h\sqrt{\pi}\Delta\theta}. \tag{7.2.75}$$

Eq. (7.2.75) gives a maximum value for Φ from which we conclude that the maximum growth rate of a $n_0 = 0$ mode is

$$\lambda_{max} = \frac{3f}{h\sqrt{\pi}\Delta\theta}. \tag{7.2.76}$$

Now we turn to Ψ. We have plotted $\pi h \Psi$ for three values of $\frac{\Delta\theta}{h}$ in Fig. 7.6. The curves are antisymmetric about the line $\frac{l}{N} = \frac{1}{2}$. In each case $\Psi = 0$ at $\frac{l}{N} = 0, \frac{1}{2}$ with a single peak in between. As $\frac{\Delta\theta}{h} \to 0$ the x intercept at $\frac{l}{N} = \frac{1}{2}$ becomes an extended region whilst the peak becomes narrower and taller. As we did with Φ, we write

$$\Psi = \frac{1}{\pi h^2} \sum_{j=1}^{N} \sin(jl\Delta\theta) \sin(j\Delta\theta)\, e^{-2(1-\cos(j\Delta\theta))/h^2}. \tag{7.2.77}$$

The antisymmetry of Ψ about $\frac{l}{N} = \frac{1}{2}$ becomes apparent when we look at Eq. (7.2.77) in the light of Eq. (7.2.65). Again noting $j\Delta\theta \ll 1$ we have

$$\Psi \simeq \frac{1}{\pi h^2} \sum_{j=1}^{N} \sin(jl\Delta\theta)\, j\Delta\theta e^{-\left(\frac{j\Delta\theta}{h}\right)^2}. \tag{7.2.78}$$

In the long wavelength limit, $l \to 0$, we find

$$\Psi \simeq \frac{lh}{4\sqrt{\pi}\Delta\theta}. \tag{7.2.79}$$

Thus in this régime

$$\begin{aligned}\Phi - \Psi &\simeq \frac{lh}{4\sqrt{\pi}\Delta\theta}(2l - 1) \\ &> 0.\end{aligned} \tag{7.2.80}$$

Table 7.3.1: Summary of constants used the single ring simulations.

Constant	Value	Comment
M	1	central mass
r	1	ring radius
$\bar{\alpha}$	0.02	SPH artificial viscosity coefficient
h	0.01	SPH smoothing length
c	0.02	sound speed
N	1256	particle number
$\frac{D}{m}$	1.3635×10^{4}	normalised surface density
f	5.87×10^{-6}	viscosity constant
ϵ	10^{-6}	amplitude of perturbation

Table 7.3.2: Comparison of linear theory and simulation results for the growth rate of the single ring instability for different wavelength perturbations.

	growth rate	
l	theory	simulation
50	1.47×10^{-2}	1.44×10^{-2}
100	5.53×10^{-2}	5.52×10^{-2}
200	1.74×10^{-1}	1.66×10^{-1}

And so for small l, Eq. (7.2.56) and Eq. (7.2.58) tell us that the $n_0 = \pm 1$ modes are stable. For short wavelengths we see from Fig. 7.6 that $\Psi \to 0$ and so again the $n_0 = \pm 1$ modes are stable. Therefore we conclude that the periodic component of the ring's response is damped by the viscosity.

7.3. Numerical Results

We now test the linear analysis with some numerical calculations. We set up a single circular ring of particles in Keplerian orbit about a central mass with parameters as listed in Table 7.3.1. The analysis showed that the the secular component of a ring's response to a general perturbation was unstable whereas the oscillatory component was stable. We wish to measure the growth rate of the instability so we apply a perturbation that only generates a secular response. Thus we set

$$\rho_0(S) = \epsilon \cos lS \tag{7.3.1a}$$
$$\dot{\rho}_0(S) = 0 \tag{7.3.1b}$$
$$\sigma_0(S) = 0 \tag{7.3.1c}$$
$$\dot{\sigma}_0(S) = -\frac{3}{2}\rho_0(S)\,. \tag{7.3.1d}$$

The linear solution for such a perturbation is

$$\rho(S,t) = \rho_0(S)\, e^{\frac{3}{2}f\Phi t} \tag{7.3.2a}$$

$$\dot{\sigma}(S,t) = -\frac{3}{2}\rho_0(S)\, e^{\frac{3}{2}f\Phi t}. \tag{7.3.2b}$$

We define, as a measure of the total perturbation of the ring at time t

$$\gamma(t) = \sqrt{\sum_{j=1}^{N} \rho_j^2(t)}\,. \tag{7.3.3}$$

Using Eq. (7.3.2) we have

$$\gamma(t) = e^{\frac{3}{2}f\Phi t}\sqrt{\sum_{j=1}^{N} \rho_j^2(0)}\,. \tag{7.3.4}$$

Thus $\gamma(t)$ grows at the same rate as $\rho(t)$. We ran simulations for three values of l; 50, 100, and 200. Such large values were chosen to ensure the perturbation grew reasonably quickly. Fig. 7.7 shows $\ln(\gamma(t)/\gamma(0))$ as a function of time for the three calculations. The initial increase in γ is clearly exponential in all three cases. The gradients of the initial linear sections of the curves are summarised in Table 7.3.2 alongside the growth rates predicted by Eq. (7.3.2). Note that in the computational work we used the cubic spline kernel given by Eq. (4.3.1) rather than the Gaussian kernel used in the analysis. Calibrating the results is however a simple matter and is not discussed here. The simulation results are in agreement with the linear theory. Although the initial growth of the perturbation is exponential, in agreement with the theory, eventually the response becomes nonlinear. In the $l = 50$ case we see a second phase of exponential growth between $t \simeq 80$ and $t \simeq 95$ but with an increased rate. We presume that energy has been dumped into higher l, faster growing modes. This phenomenon is also apparent but to a lesser extent in the $l = 100$ simulation. We do not see it in the 200 calculation. In all three cases the growth eventually levels off. To carry the analysis of the simulations further we would use Fourier analysis techniques, just as Lubow (1991 b) did in his study of the tidal instability of disks in low mass ratio binaries.

7.4. Conclusions

We know, from the work of Lynden-Bell and Pringle (1974), that a shearing disk of gas spreads out radially. Over time there is an outwards flux of angular momentum and an inwards mass flux. In Chapter 5 we discussed SPH simulations that accurately modelled such evolution. We note that the disks in the simulations were set up with smoothly varying (Gaussian) density profiles and a radial extent that was significantly larger than the smoothing length. In this chapter we have found that a single ring of particles orbiting a central body, for which the only interparticle forces are SPH artificial viscosity interactions, is in unstable equilibrium. This behaviour is quite distinct from that of an extended disk. In the unperturbed ring, the viscous forces between particles are identically zero. Thus the ring is in equilibrium. If however the particle orbits are disturbed, the ring spreads out into a narrow disordered annulus. This may then indeed spread further in accordance with the standard disk theory. With linear analysis we determined the growth rate of the single ring instability. Numerical simulations gave results in agreement with the theory.

The instability is of a similar nature to the one found by Julian and Toomre (1966) who looked at the response of a self-gravitating disk to a perturbing mass orbiting in its plane. They found the disturbance generated spiral-like structures in the disk. To find the basic instability mechanism they analysed the motion of a single star in the disk as it was disturbed by a point mass moving more rapidly past it on an interior orbit. As in our problem, the force between two particles is along their line of centres. The gravitational force however is always attractive whereas the SPH viscous force is only attractive between two particles moving apart from one another. It is repulsive for two approaching particles.

Julian and Toomre found that as the star and the point mass approached one another the star experienced a force in the azimuthal direction. This acted to reduce the star's angular momentum and bring it in to a smaller radius orbit that was closer to the point mass. When the particles had passed one another the azimuthal force on the star changed sign, restoring angular momentum. However the interaction was not exactly symmetric in this sense and the star experienced a net change in its angular momentum. Thus the mean radius of its orbit was altered by the interaction. Over the course of the encounter, the point mass also imparted a net radial impulse upon the star, setting it moving in little epicycles. When all the individual stellar responses were combined, the disk developed spiral structures throughout. Toomre and Kalnajs (1991) described the instability as amplifying preexisting grainy structures in the disk.

We take a single ring and displace a single particle a distance $\frac{1}{2}h$ inwards. Give this 'rogue' particle the Keplerian velocity appropriate to its new radius and a mass one hundred times greater than that of the other particles. Fig. 7.8 shows that portion of the ring nearest the 'rogue' particle (marked with a star) in a frame corotating with the ring. The displaced particle, on a smaller Keplerian orbit, is rotating slightly more rapidly than the ring. Because of its much larger mass, the 'rogue' particle hardly feels the viscous interactions with the ring and continues in its circular orbit. We concentrate then upon the encounter of the 'rogue' with the ring particle initially immediately to its left (shown in bold). This is analogous to the single encounter discussed by Julian and Toomre. Rather than pulling the ring particle towards itself, the 'rogue' pushes it out of the ring. In frame 3 (middle left) the 'rogue' and the ring particle are just passing one another. The relative velocity along their line of centres will thus be (approximately) zero and the viscous acceleration drops away. This then is a point of difference with the gravitational instability. In that case the radial effect on the star can be approximately given by a single impulse at the moment of closest approach. We would thus expect the epicyclic response of the ring particle to be more significant in the gravitational case than in the viscous case. This perhaps explains why spiral structures were not observed in the extended disk simulation shown in the introduction to this chapter, (Fig. 7.1 and Fig. 7.2). As the rogue passes the ring particle, the sign of both the radial and azimuthal components of the viscous force change and the particle is brought back into the ring. The encounter is not however completely symmetric, leaving it with a small net change in angular momentum. The rogue particle meanwhile continues on its merry way, disturbing more particles as it goes.

Lyubarskij et al. (1994) found an eccentric particle instability that was relevant to gaseous accretion disks. Consider a single particle in an eccentric orbit in a gravitational potential. If for some reason the particle experiences a braking torque when it is near apocentre, the eccentricity of its orbit increases. On the other hand if the braking occurs near pericentre, the orbit becomes more circular. They found that, depending on the viscosity law used, fluid disks could be susceptible to this eccentric instability. The standard Shakura-Sunyaev viscosity parametrisation for example gave rise to an unstable disk. This instability is clearly different to the single ring instability found in this Chapter. It remains to be seen how important their instability is in real astrophysical situations.

The Julian and Toomre instability applies to disks of discrete matter. We are interested in this thesis, on the other hand, in modelling gaseous or continuum disks. However the single ring must be considered a particulate rather than a continuous initial condition. As such the single ring instability is not relevant to our modelling of disks. Yet we have already seen that the instability can occur in a simulation of an extended disk (Fig. 7.1 and Fig. 7.2). But it only occurred in rings that had become detached from the rest of the disk. In other words at the edges the disk was noticing the individual particles and their approximation to a continuum was breaking down. There are two things that can be done to prevent the instability occurring. Firstly we use smooth radial density profiles. The density profile in the disk simulation above was discontinuous at the boundaries. The rate of transfer of angular momentum via viscous torques between rings is proportional to the radial derivative of the density. Thus with the discontinuity in the density at the boundaries, the outside rings are very rapidly spun up/down. The ring radius then changes and they lose contact with the disk. Thus there is rapid breakdown of such simulations at the boundaries. With smooth density profiles, the spin up or down of the outside rings is more controlled. This was one of the major rasons we chose to use Gaussian density profiles in Chapter 4 despite the complexity this added to the analysis over say a top hat profile.

The second tactic is to periodically add extra rings to the disk in between the existing ones to prevent the gaps between them becoming to large. Of course this has to be done in such a way as to conserve basic quantities such as disk mass, energy and angular momentum. Thus whenever a ring is added the properties of all particles (old and new) will have to be recalculated by interpolation from the old particle distribution. We were able to avoid using this scheme however it would be relatively easy to implement.

Chapter 8.
Summary of Results

The various physical processes in accretion disks; gravity, radiation, viscosity etc. can have time scales that differ by many orders of magnitude.In particular, dynamical time scales are much shorter than viscous time scales. This creates problems when designing simulations to follow an accretion disk's viscous evolution. In response, we developed a new SPH algorithm that incorporates operator splitting. This allows us to treat the gravitational and viscous forces upon a particle separately, using timesteps appropriate to them. The gain in speed over a standard SPH code is large, though the exact speedup of course varies from simulation to simulation. The operator split algorithm could find many applications, not only in problems involving vastly differing time scales, but also in situations where the different forces require different numerical techniques (for stability, accuracy etc).

The SPH code was tested against axisymmetric thin disk theory. Simulations of gaseous annuli spreading via viscous shear were compared with analytical results. This allowed us to verify that the SPH artificial viscosity term could adequately model viscous shear forces. We found quantitatively that it behaved as predicted.

In the course of these tests we found that the disk's evolution was strongly constrained by the assumption that the azimuthal velocity of the gas was a function of r only. Small deviations from Keplerian rotation significantly affected the rate at which the disk spread out radially. Such deviations will occur when the viscosity changes in a time that is short compared to the dynamical time scale. It is possible that the thermal instability found by Meyer and Meyer-Hofmeister (1981) would cause such a sudden change. Up till now, in numerically studying the thermal instability model for outburst, authors have assumed strictly circular Keplerian orbits. We recommend that appropriate simulations be completed, without making this assumption. We feel results may be significantly affected.

We conducted isothermal disk simulations in two different binary potentials. First we considered a system with equal mass primary and secondary stars. Disks in such binaries had previously been found to be tidally stable. We ran a simulation for 160 binary orbital periods during which the disk evolved to a stationary state. The outer edge of the disk approximately coincided with Paczynski's last nonintersecting orbit of a noninteracting particle. The stationary disk could be approximately described as the superposition of an axisymmetric steady state solution with a nonuniform high density rim along the outer edge. With the exception of the inner and outer boundaries, the simulation disk closely matched the appropriate steady state solution. The injection stream was found to restrict the outward expansion of the disk. When the injection stream was switched off, the last nonintersecting orbit was found to approximately mark the boundary between a disordered outer disk and an ordered axisymmetric inner disk.

We also performed an isothermal simulation for a system with mass ratio $q = 0.15$. Disks in such low mass ratio binaries had previously been found to be tidally unstable (Whitehurst 1988 a, Hirose and Osaki 1990). When it encountered the $3:1$ inner Lindblad resonance, the disk became eccentric and began to precess. Superhump in Su UMa systems in superoutburst had been proposed as a visible signature of the tidal instability.

Following the trajectory of the disk centre of mass was found to be an accurate, yet simple method of monitoring the instability. Our disk became unstable and precessed in a prograde fashion. The disk centre of mass then executed simple harmonic motion with the same frequency as the precession. Lubow (1991 a) had theoretically calculated the growth rate of the disk eccentricity and then verified the result with SPH simulations using only the $m = 3$ mode of the (perturbing) binary potential. When he used the full binary potential he found the eccentricity growth was inhibited by other modes in the disk. In our simulation the eccentricity grew much more slowly than Lubow's theory predicted. We concluded that this was due to the full binary potential, and to the presence of the injection stream.

Our simulation was set up in a similar fashion to those of Hirose and Osaki, and used a constant viscosity of similar magnitude to theirs. The precession rate of our disk agreed with Hirose and Osaki's results but differed with the results of others (Whitehurst, Lubow) and with observed superhump periodicities. We postulate that this difference is a result of the differing radial mass distributions in the various disks. Now this depends upon the form of the viscosity function. In particular we have shown that a Shakura-Sunyaev viscosity law would result in a more centrally condensed disk than does our constant viscosity. We have proposed but not completed a set of simulations using the Shakura-Sunyaev parameterisation.

The rate of viscous energy dissipation in the disk gives a simple bolometric indication of its luminosity. When plotted as a function of time for the precessing disk, a cyclic component is seen. This has the same period as the disk's precession. This then is the luminous signature of the tidal instability in our simulation. The periodic signal was found to come from a high density region in the outer disk about a quarter turn downstream of the disk bright spot. The luminosity source was incompatible with the Vogt (1983) elliptic disk model for superhump.

We then incorporated the condition that elements of the disk radiated like blackbodies into our model. We then ran simulations corresponding to our isothermal calculations.

From the steady state ($q = 0.5$) simulation we found that the blackbody disk evolved with a slightly larger fraction of its mass in the outer regions then did the isothermal disk.

The various parameters for the $q = 0.15$ blackbody disk simulation were fixed to enable comparisons with the eclipsing Su UMa system OY Car in outburst and in superoutburst. As before, we found that the disk was tidally unstable. Before the onset of the instability however, the simulation compared well with observations of OY Car in outburst. In particular we obtained the $r^{-\frac{3}{4}}$ temperature dependance of a steady state blackbody disk (as observed in OY Car in outburst). Actual temperatures in the simulation agreed to within an order of magnitude with observations.

With relatively more mass in the outer regions, we found that the blackbody disk interacted more strongly with the $3 : 1$ resonance than did the isothermal disk. Though the eccentricity grew at the same rate in the two simulations, the amplitude of the final disk motion was larger in the blackbody case. The precession rate was however unchanged.

We compared the viscous dissipation in the blackbody simulation with observations of superhump. Our findings were not absolutely conclusive with both simulation and observation requiring further attention. With respect to the observations, we would like to know how severely the assumptions made about the superhump source affect the results of the eclipse mapping studies of superoutbursts. We would then like to see the observational data set built up. It is entirely possible that as the disk evolves through a superoutburst, the precise nature of the superhump source changes. The degree of variation from outburst to outburst, and from system to system is also an issue.

The blackbody simulation dissipation curve displayed tall narrow spikes not seen in real superhump lightcurves. These were caused by small blobs of gas thrown off by the disk in the course of its precession. This phenomenon was not seen in the isothermal disk in which the precession was slightly less pronounced. We conclude that the blackbody simulation was more eccentric than an actual disk. The location of the remaining signal did not match observations. In addition to the source seen in the isothermal simulation, there was a pronounced periodic signal from the bright spot. Again we attribute this to the relatively large eccentricity of the blackbody disk. One observed superhump was identified as coming from the bright spot.

The temperature of the simulation source was a factor of three or so higher than the observational case. We suggest that the initial assumptions made in incorporating blackbody radiation into the simulation may not be appropriate in regions where the temperature changes rapidly. In such places, rather than all the viscously released energy being instantaneously radiated through the disk surfaces, as assumed, significant fractions may be transported in the plane or be taken up as internal energy. The brightness temperature of the superhump source would be reduced and the area increased to be more in line with observations.

To summarise, we found that the energy released in a tidally stressed disk had a cyclic component with many similarities to superhump. This much was already known from previous work. But there were also significant differences between our simulation and observed superhumps. The two signals differed slightly in their periods, in their shape, and more significantly, in their point of origin. The temperatures of the two sources also did not exactly agree. However we feel that we can account for these differences and that none of them present any severe difficulties for the model. Some (minor) improvements to the model, and a more comprehensive set of observations will bring the two closer together. We believe that the results have strengthened the case that tidal instability is the cause of superhump.

Previous particle based simulations have yielded much information on the dynamics of accretion disks. They have however suffered a credibility problem because of their apparent ad hoc treatment of the processes involved. Testing of such codes for accuracy and stability has been very limited. By comparison these properties are well understood for finite difference methods. Yet the complicated geometry of the binary potential posed far greater problems for finite difference schemes than for particle methods. Smoothed Particle Hydrodynamics showed great promise in this regard. It is particle based and so holds no fears regarding complicated gravitational potentials. Secondly its equations can be obtained from the fluid equations of motion. Thus SPH allows one to systematically modify the physics in the simulation. Its stability and accuracy had been previously tested on a wide range of problems, but not specifically on shearing disks. As several people were turning to SPH to study accretion disks, it was important to quantitatively test the scheme against disk theory. This we did. We then demonstrated that one can successfully incorporate enough disk physics into SPH disk simulations to enable meaningful comparison with observations

References

1. Aarseth, S. J., Mon. Not. R. Astr. Soc. 126 (1963) 223.
2. Artymowicz, P., Clarke, C. J., Lubow, S. H. and Pringle, J. E., Astrophys. J. 370 (1991) L35.
3. Balbus, S. A., and Hawley, J. F., Astrophys. J. 376 (1991) 214.
4. Bath, G. T., Nature Phys. Sci. 246 (1973) 84.
5. Bayly, B. J., Physical Rev. Let. 57 (1986) 2160.
6. Binney, J. J. and Tremaine, S., *Galactic Dynamics*, Princeton University Press, 1987.
7. Boris, J., J. Computational Physics 66 (1986) 1.
8. Bruch, A. and Duschl, W. J., Astron. Astrophys. 275 (1993) 219.
9. Cannizzo, J. K., in: *Accretion Disks in Compact Stellar Systems*, ed J. C. Wheeler, World Scientific, 1993.
10. Downes, R. A. and Shara, M. M., Publ. Astr. Soc. Pacific 105 (1993) 127.
11. Frank, J., King, A. and Raine, D., *Accretion Power in Astrophysics*, Cambridge University Press, 1992.
12. Gingold, R. A., and Monaghan, J. J., Mon. Not. R. Astr. Soc. 181 (1977) 375.
13. Glatzel, W., Mon. Not. R. Astr. Soc. 257 (1992) 572.
14. Goodman, J., Astrophys. J. 406 (1993) 596.
15. Grest, G. S., Dünweg, B. and Kremer, K., Computer Physics Commun. 55 (1989) 269.
16. Haefner, R., Schoembs, R., and Vogt, N., Astron. Astrophys. 77 (1979) 7.
17. Hawley, J. F. and Balbus, S. A., Astrophys. J. 376 (1991) 223.
18. Hawley, J. F. and Balbus, S. A., Astrophys. J. 400 (1992) 595.
19. Heller, C., Astrophys. J. 408 (1993) 337.
20. Hernquist, L. and Katz, N., Astrophys. J. Suppl. 70 (1989) 419.
21. Hirose, M., *Tidal Instability of Accretion Disks in Close Binary Systems*, Doctoral Thesis, University of Tokyo, 1991.
22. Hirose, M. and Osaki, Y., Publ. Astr. Soc. Japan 42 (1990) 135.
23. Hockney, R. W. and Eastwood, J. W. *Computer Simulations Using Particles* Adam Hilger, 1988.
24. Horne, K., Mon. Not. R. Astr. Soc. 213 (1985) 129.
25. Julian, W. H. and Toomre, A., Astrophys. J. 146 (1966) 810.
26. Kley, W., Astron. Astrophys. 208 (1989) 98.
27. Kley, W., Astron. Astrophys. 247 (1991) 95.
28. Kopal, Z., *The Roche Problem*, Kluwer, 1988.
29. Lang, K., R., *Astrophysical Data: Planets and Stars*, Springer-Verlag, New York, 1991.
30. Lanzafame, G., Belvedere, G., Molteni D., Mon. Not. R. Astr. Soc. 258 (1992) 152.
31. Lanzafame, G., Belvedere, G., Molteni D., Mon. Not. R. Astr. Soc. 263 (1993) 839.
32. Lightman, A. P., Astrophys. J. 194 (a1974) 419.
33. Lightman, A. P., Astrophys. J. 194 (b1974) 429.
34. Lin, D. N. C., Papaloizou, J. and Faulkner, J., Mon. Not. R. Astr. Soc. 212 (1985) 105.
35. Lin, D. N. C. and Pringle, J. E., in: *Structure and Evolution of Close Binary Systems*, eds P.Eggleton, S.Mitton, and J.Whelan, D. Reidel Publishing Company, Dordrecht, 1976.
36. Livio, M., in: *Interacting Binaries*, eds H. Nussbaumer, and A. Orr, Springer-Verlag, 1993.
37. Lubow, S. H., Astrophys. J. 381 (a1991) 259.
38. Lubow, S. H., Astrophys. J. 381 (b1991) 268.
39. Lubow, S. H. and Shu, F. H., Astrophys. J. 198 (1975) 383.
40. Lucy, L. B., Astronomical J. 82 (1977) 1013.

41. Lynden-Bell, D., and Pringle, J. E., Mon. Not. R. Astr. Soc. 168 (1974) 603.
42. Lyubarskij, Y. E., Postnov, K. A., and Prokhorov, M. E., Mon. Not. R. Astr. Soc. 266 (1994) 583.
43. Maxwell, J. C., *On the Stability of the motion of Saturn's Rings*, an essay which obtained the Adam's Prize for the year 1856, in the University of Cambridge, in: *The Scientific Papers of James Clerk Maxwell*, ed Niven, W. D., Dover, 1965.
44. Matsuda, T., Sekino, N., Sawada, K., and Shima, E., in: *Status Reports of Supercomputing Astrophysics in Japan, KEK 1989*, National Laboratory for High Energy Physics, 1990.
45. Meglicki, Z., Wickramasinghe, D., and Bicknell, G. V., Mon. Not. R. Astr. Soc. 264 (1993) 691.
46. Meyer, F. and Meyer-Hofmeister, E., Astron. Astrophys. 104 (1981) L10.
47. Meyer, F. and Meyer-Hofmeister, E., Astron. Astrophys. 132 (1984) 143.
48. Meyer-Hofmeister, E. and Ritter, H., in: *Close Binaries*, eds J. Sahade, Y. Kondo, G. McClyskey, Kluwer Academic Publishers, 1991.
49. Molnar, L. A. and Kobulnicky, H. A., Astrophys. J. 392 (1992) 678.
50. Molteni, D., Belvedere, G., and Lanzafame, G., Mon. Not. R. Astr. Soc. 249 (1991) 748.
51. Monaghan, J. J., SIAM J. Sci. Stat. Comput. 3 (1982) 422.
52. Monaghan, J. J., Comput. Phys. Rep. 3 (1985) 71.
53. Monaghan, J. J., Ann. Rev. Astron. Astrophys. 30 (1992) 543.
54. Monaghan, J. J., *Relativistic Smoothed Particle Hydrodynamics I Special Relativity*, Monash University Applied Mathematics Report 93/46.
55. Monaghan, J. J., J. Computational Physics 110 (1994) 399.
56. Monaghan, J. J. and Lattanzio, J. C., Astron. Astrophys. 149 (1985) 135.
57. Morales, J. J. and Nuevo M. J., Computer Physics Commun. 60 (1990) 195.
58. Morales, J. J. and Toxvaerd, S., Computer Physics Commun. 71 (1992) 71.
59. Naylor, T., Charles, P. A., Hassall, B. J. M., Bath, G. T, Berriman, G., Warner, B., Bailey, J., and Reinsch, K., Mon. Not. R. Astr. Soc. 229 (1987) 183.
60. Naylor, T., Bath, G. T., Charles, P. A., Hassall, B. J. M., Sonneborn, G., van der Woerd, H., van Paradijs, J., Mon. Not. R. Astr. Soc. 231 (1988) 237.
61. O'Donoghue, D., Mon. Not. R. Astr. Soc. 246 (1990) 29.
62. Osaki, Y., Publ. Astr. Soc. Japan 26 (1974) 429.
63. Osaki, Y., Astron. Astrophys. 144 (1985) 369.
64. Paczyński, B., Astrophys. J. 216 (1977) 822.
65. Paczyński, B., Astrophys. J. 370 (1991) 597.
66. Patterson, J., Astrophys. J. Suppl. 54 (1984) 443.
67. Patterson, J., Bond, H. E., Grauer, A. D., Shafter, A. W., Mattei, J. A., Publ. Astr. Soc. Pacific 105 (1993) 69.
68. Pierrehumbert, R. T., Physical Rev. Let. 57 (1986) 2157.
69. Popham, R. and Narayan, R., Astrophys. J. 370 (1991) 604.
70. Potter, D., *Computational Physics*, John Wiley and Sons, 1973.
71. Press, W. H., Teukolsky, S. A., Vetterling, W. T., and Flannery, B. P., *Numerical Recipes in* `FORTRAN`, *Second Edition*, Cambridge University Press, 1992.
72. Pringle, J. E., Mon. Not. R. Astr. Soc. 178 (1977) 195.
73. Pringle, J. E., Ann. Rev. Astron. Astrophys. 19 (1981) 137.
74. Pringle, J. E., Verbunt, F., and Wade, R. A., Mon. Not. R. Astr. Soc. 221 (1986) 169.
75. Ritter, H., Astron. Astrophys. Suppl. 85 (1990) 1179.
76. Rutten, R. G. M., Kuulkers, E., Vogt, N., and van Paradijs, J., Astron. Astrophys. 265 (1992) 159.

77. Schoembs, R. and Vogt, N., Astron. Astrophys. 91 (1980) 25.
78. Shakura, N. I., and Sunyaev, R. A., Astron. Astrophys. 24 (1973) 337.
79. Shu, F. H., *The Physical Universe An Introduction to Astronomy*, University Science Books, 1982.
80. Smak, J., Publ. Astr. Soc. Pacific 96 (1984) 575.
81. Smith, G. D., *Numerical Solution of Partial Differential Equations: Finite Difference Methods*, Oxford University Press, 1985.
82. Steinmetz, M. and Mueller, E., Astron. Astrophys. 268 (1993) 391.
83. Stone, J. M. and Norman, M. L., Astrophys. J. Suppl. 80 (1992) 753.
84. Toomre, A., and Kalnajs, A. J., in: *Dynamics of Disc Galaxies*, ed B. Sudelius,1991.
85. van Amerongen, S., Bovenschen, H., and van Paradijs, J., Mon. Not. R. Astr. Soc. 229 (1987) 245.
86. Warner, B., Mon. Not. R. Astr. Soc. 168 (1974) 235.
87. Warner, B., in: *Interacting Binaries*, eds P. P. Eggleton and J. E. Pringle, D. Reidel, 1985.
88. Warner, B. and O'Donoghue, D., Mon. Not. R. Astr. Soc. 233 (1988) 705.
89. Whitehurst, R., Mon. Not. R. Astr. Soc. 232 (a1988) 35.
90. Whitehurst, R., Mon. Not. R. Astr. Soc. 233 (b1988) 529.
91. Whitehurst, R., Mon. Not. R. Astr. Soc. 266 (1994) 35.
92. Whitehurst, R. and King, A., Mon. Not. R. Astr. Soc. 249 (1991) 25.
93. Wood, J. H., Mon. Not. R. Astr. Soc. 243 (1990) 219.
94. Wood, J. H.,Horne, K.,Berriman, G. and Wade, R., Astrophys. J. 341 (1989) 974.

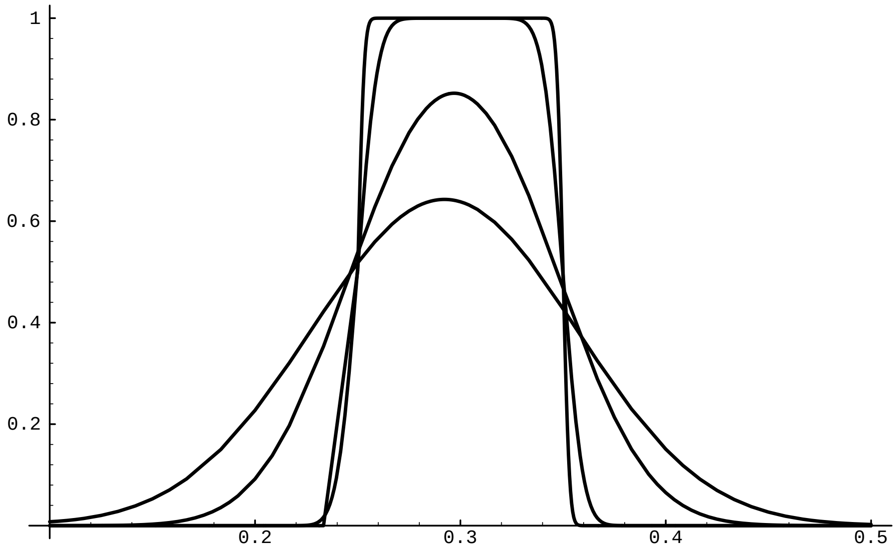

Figure 2.3.1: Evolution of an annulus with initial density profile given by Eq. (2.3.1). $r_1 = 0.25$ and $r_2 = 0.35$. From top to bottom the curves are for $\nu t = 1.0 \times 10^{-6}, 1.0 \times 10^{-5}, 2.0 \times 10^{-4}$ and 5.0×10^{-4}.

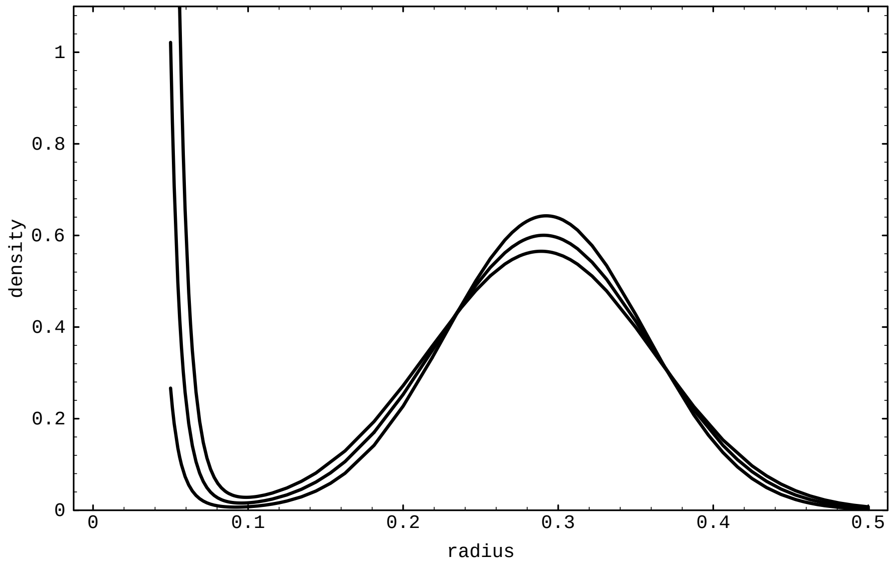

Figure 2.3.2: Plots of Eq. (2.3.5) for $\nu t = 5.0 \times 10^{-4}, 6.0 \times 10^{-4}$ and 7.0×10^{-4}. This figure illustrates the breakdown of Eq. (2.3.5).

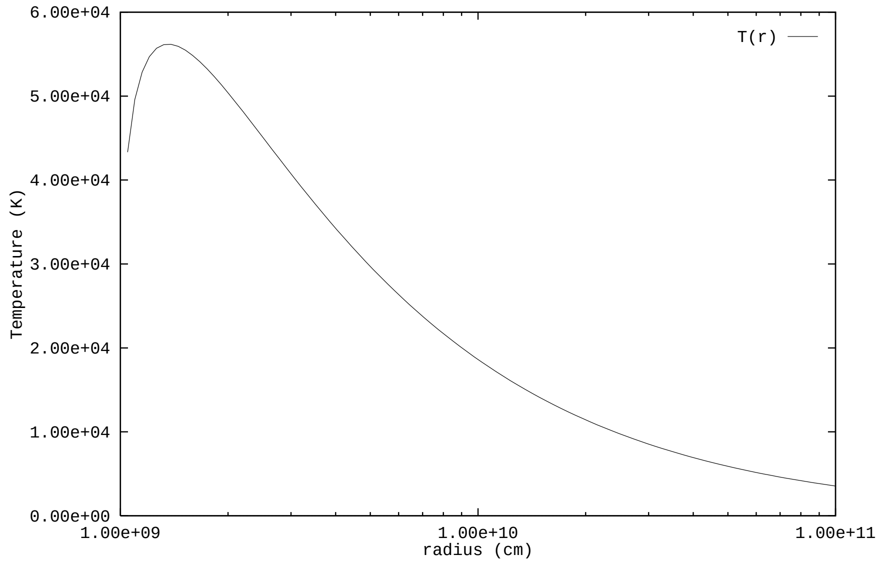

Figure 2.6.1: Example steady state temperature profile for a 'blackbody' disk about a white dwarf.

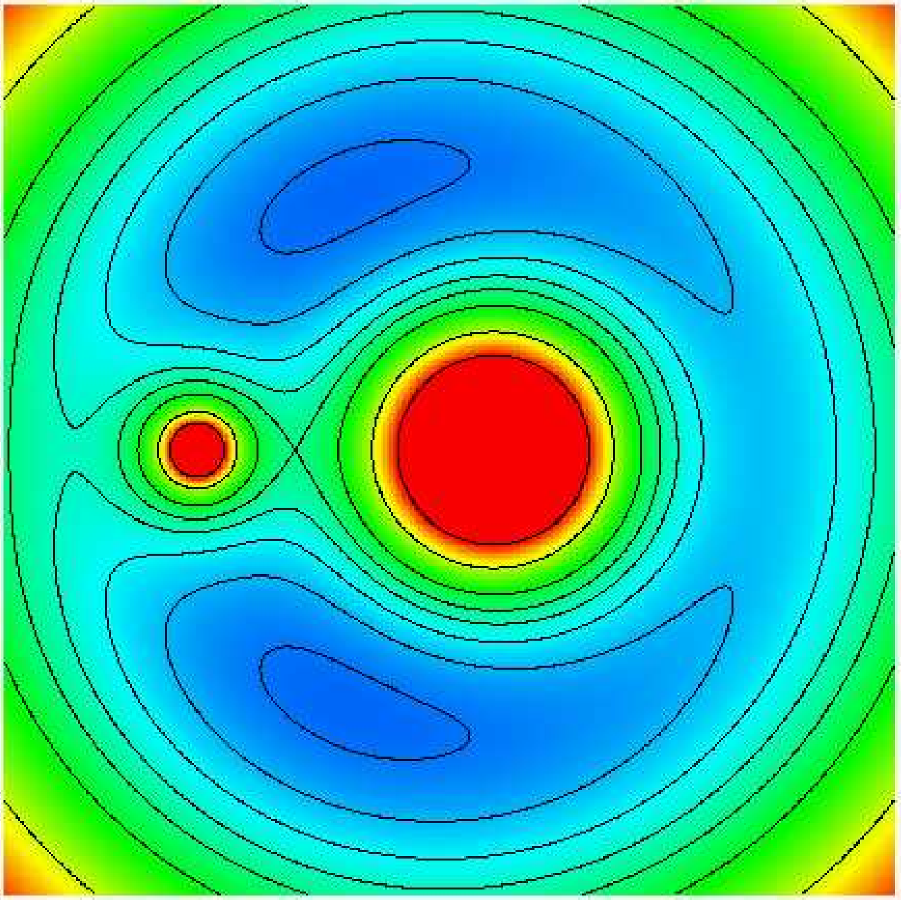

Figure 3.1: Contour map of the $z = 0$ plane of the Roche potential Φ_R for $\mu = 0.85$. As in a standard geographical contour map, the contours are marked in black whilst the colour indicates altitude (in this case depth of the potential well). In order of increasing depth the colours are blue, green, yellow and red. The primary is at the centre of the red circular well to the right. The low mass secondary lies in the red circular well to the left.

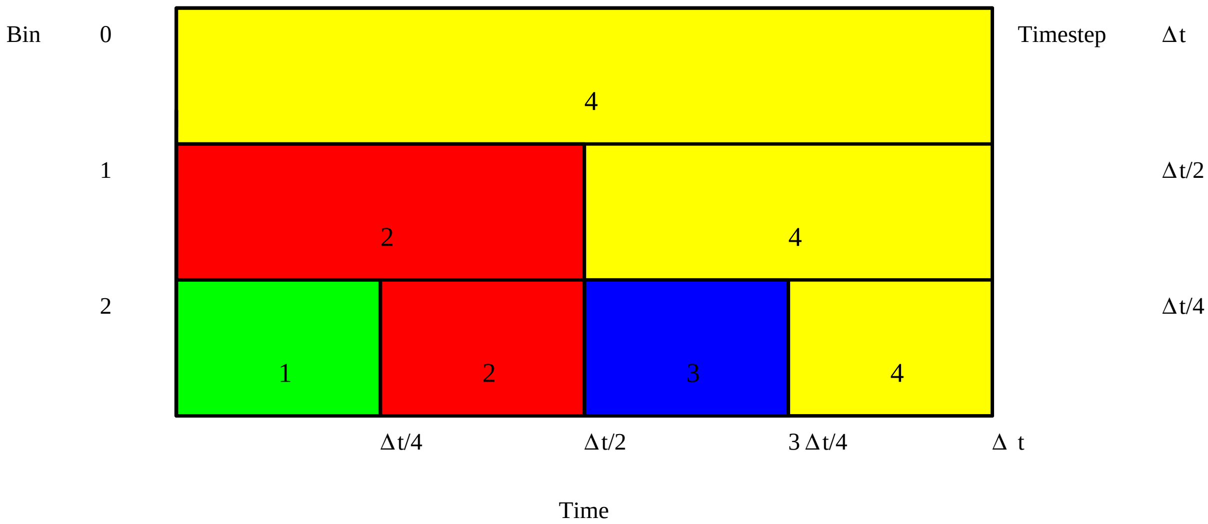

Figure 4.7.1: Division of a timestep into substeps showing the order in which the bins are integrated. (Based on a diagram in Whitehurst, 1988b)

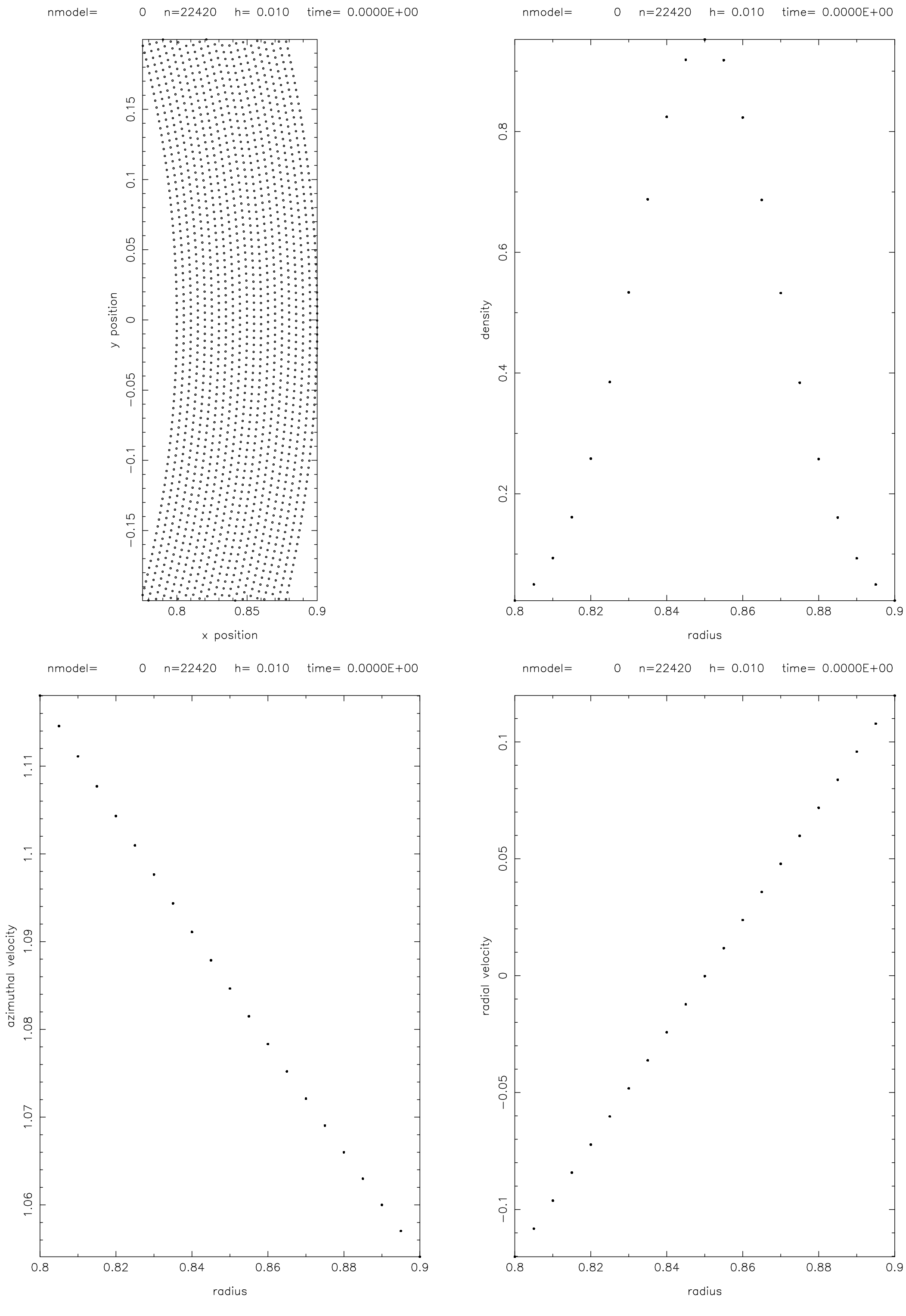

Figure 5.2.1: Initial state

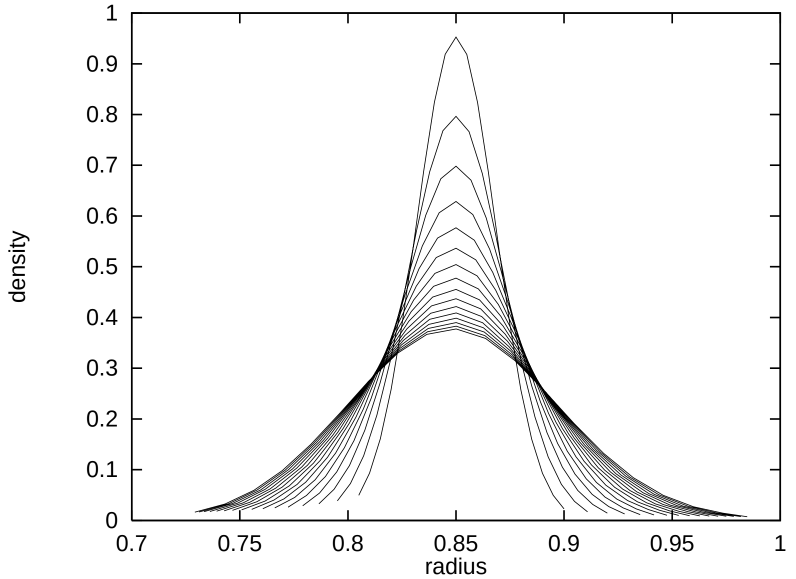

Figure 5.3.1: Density profiles of $\bar{\alpha} = 10.0$ disk for every 0.1 scaled time units from $t = 0.0$ to $t = 1.5$.

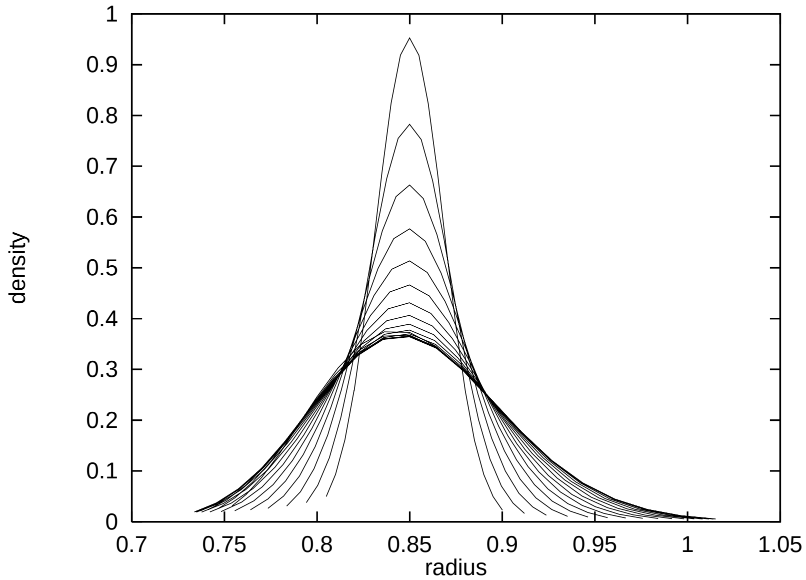

Figure 5.3.2: Density profiles of $\bar{\alpha} = 0.0$ disk for every 0.1 scaled time units from $t = 0.0$ to $t = 1.5$.

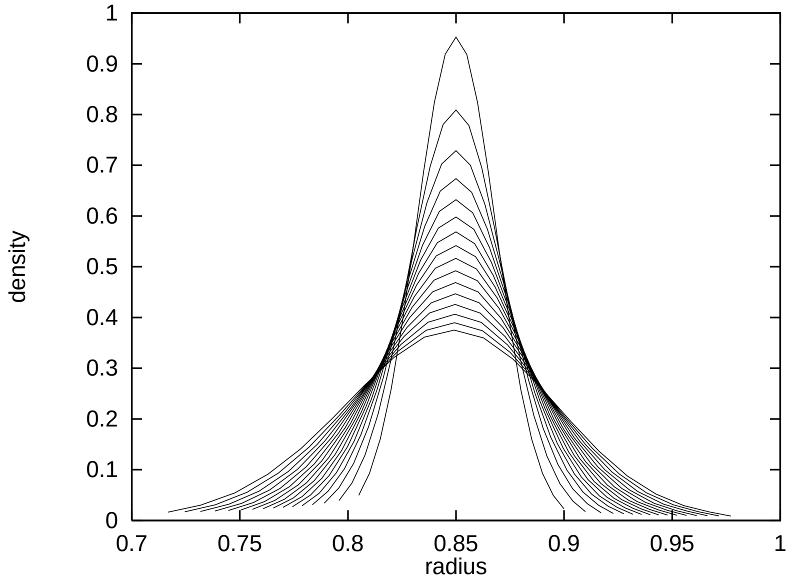

Figure 5.3.3: Density profiles of $\bar{\alpha} = 20.0$ disk for every 0.1 scaled time units from $t = 0.0$ to $t = 1.5$.

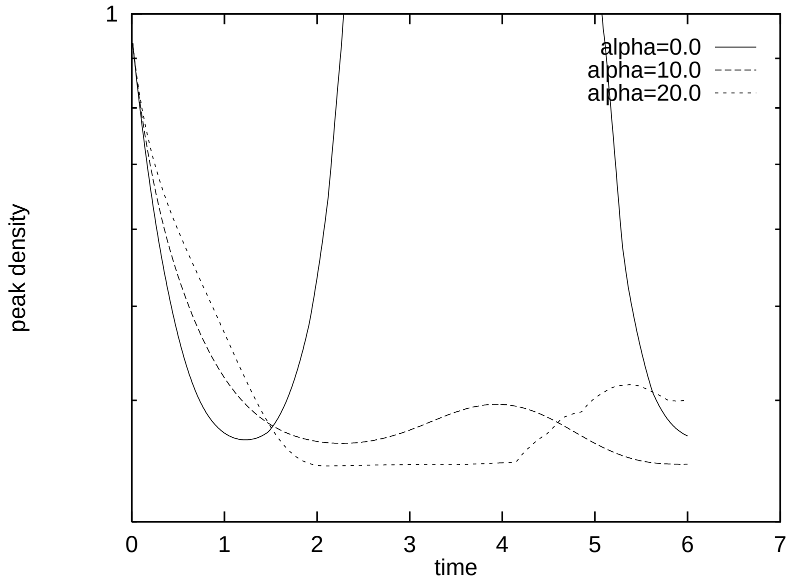

Figure 5.3.4: Peak density as a function of time for the $\bar{\alpha} = 0.0, 10.0, 20.0$ disks.

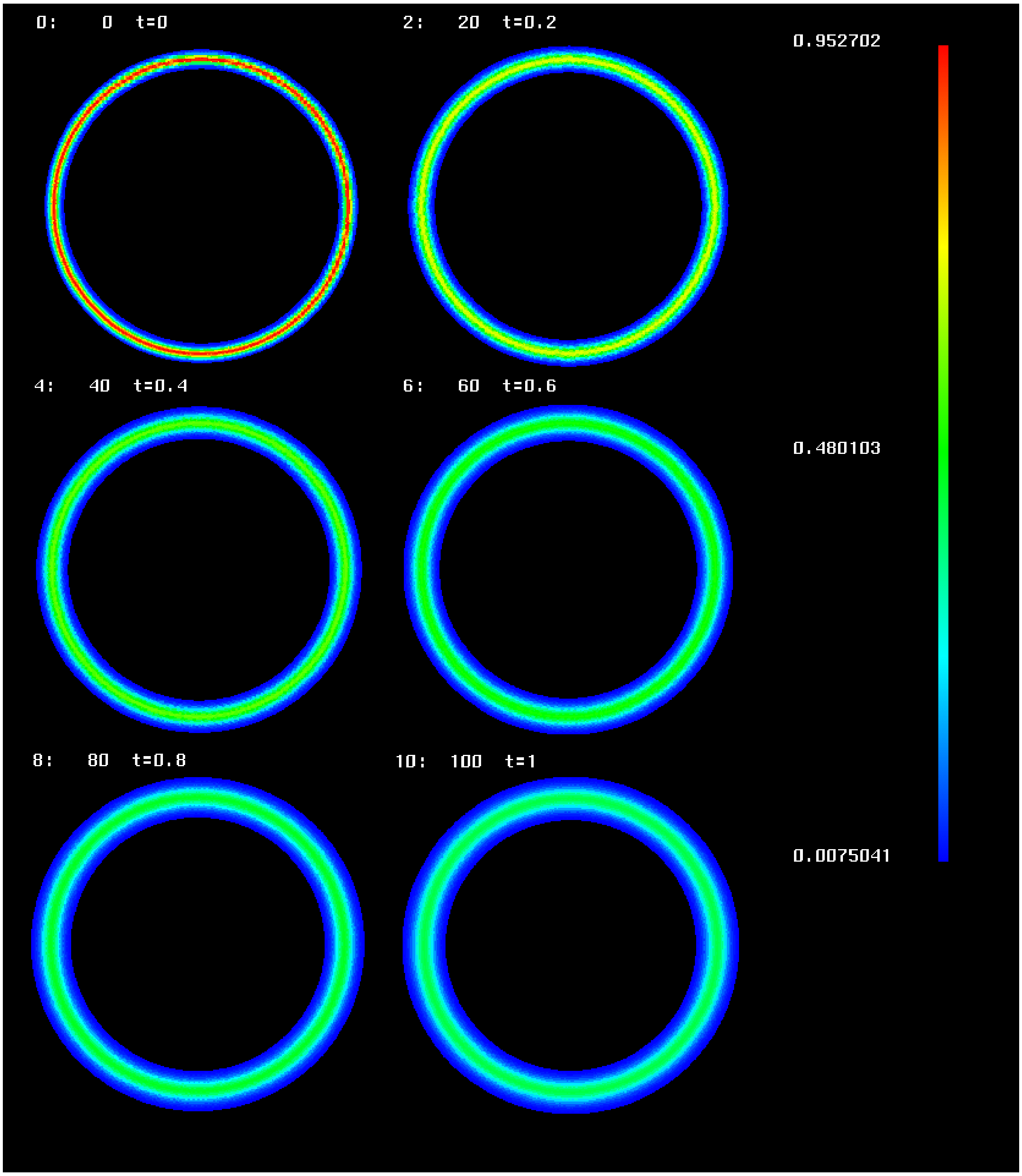

Figure 5.3.5: Six snapshots of the ring at the times shown. The particles are coloured according to density (key to the right).

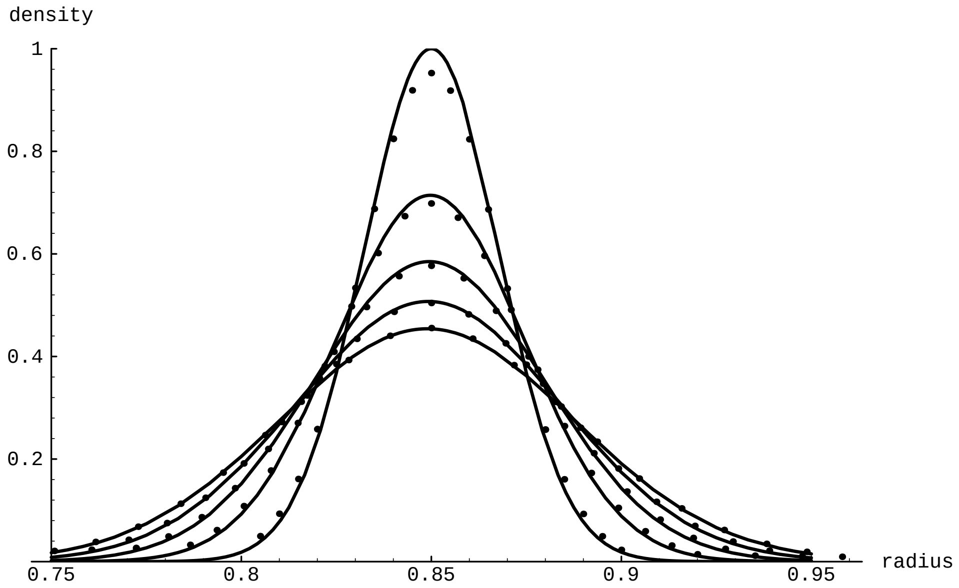

Figure 5.3.6: $\bar{\alpha} = 10.0$ disk evolution (points) plotted at 0,20,40,60,80 timesteps against the theoretical derived density curves.

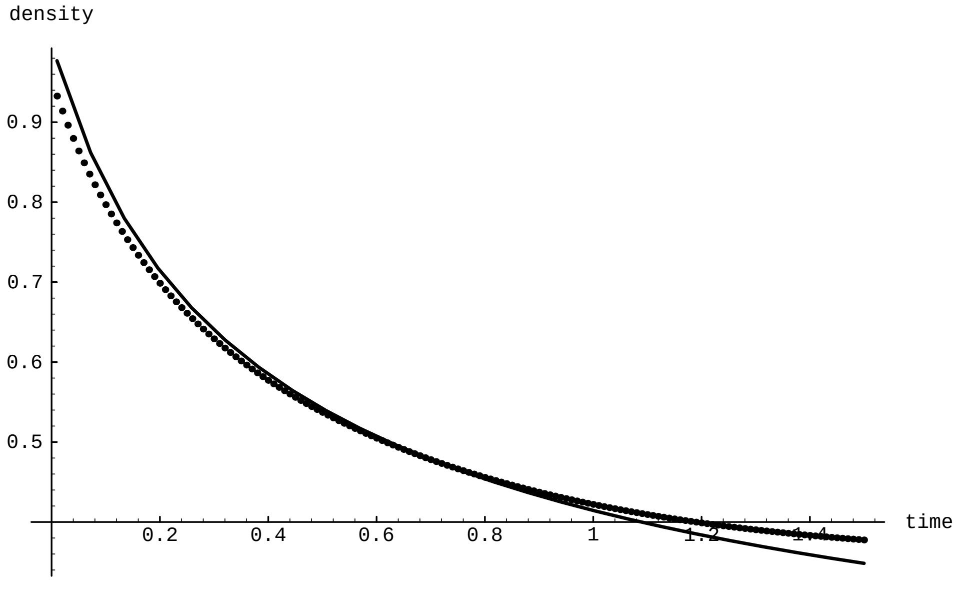

Figure 5.3.7: $\bar{\alpha} = 10.0$ disk peak density (points) plotted against the density at $r = r_c$ for the theory (solid line).

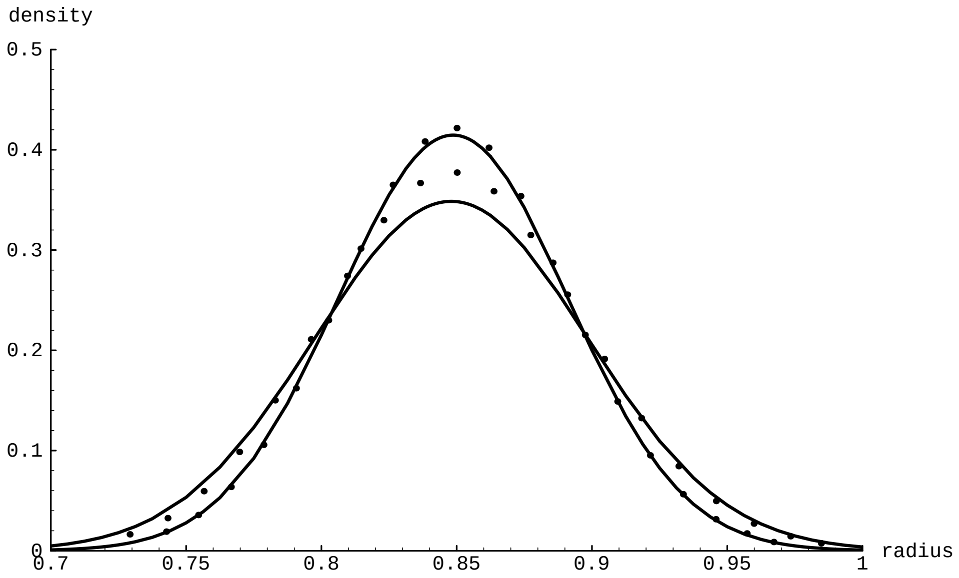

Figure 5.3.8: $\bar{\alpha} = 10.0$ disk evolution (points) plotted at 100 and 150 timesteps against the theoretical derived density curves.

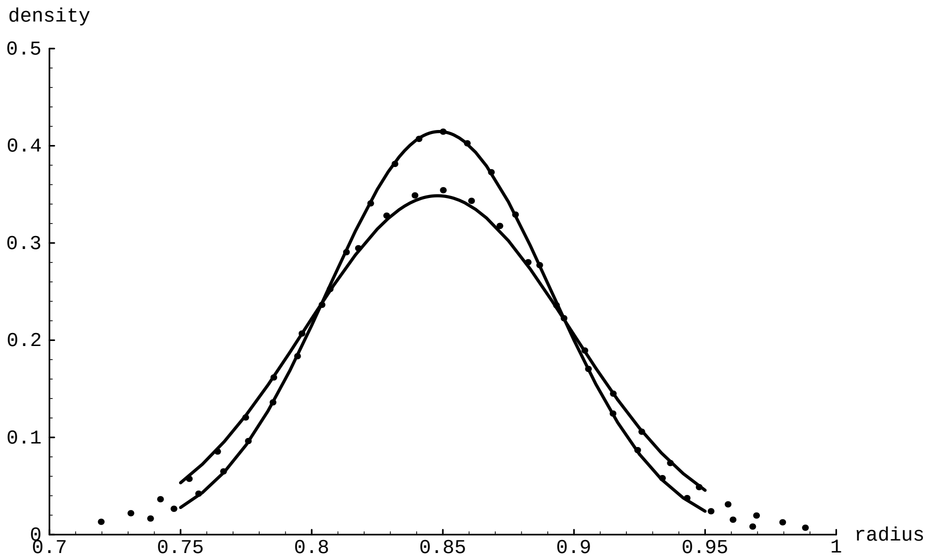

Figure 5.3.9: $\bar{\alpha} = 10.0$ disk evolution (points) plotted at 100 and 150 timesteps against the theoretical derived density curves. This disk is set up with more rings (and particles) than standard.

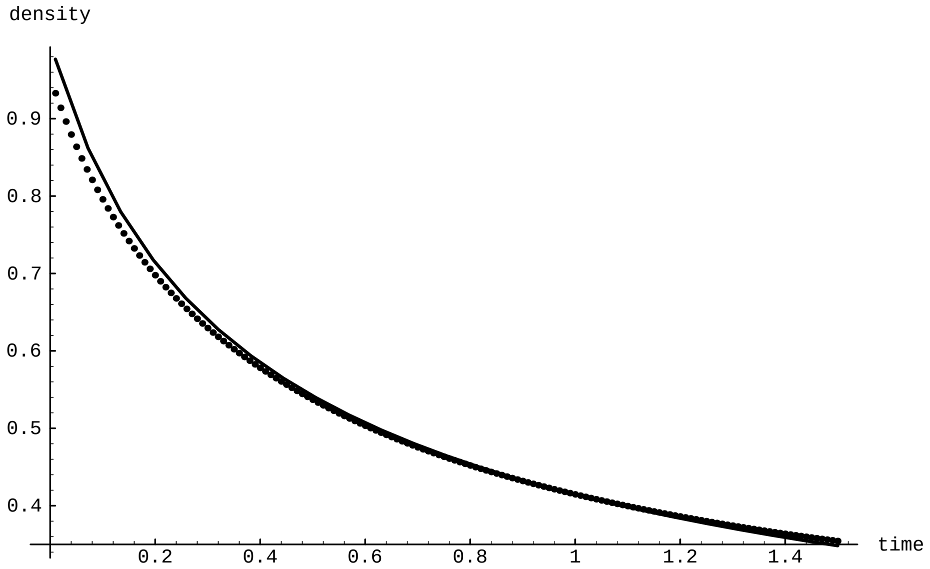

Figure 5.3.10: Peak density for $\bar{\alpha} = 10.0$ disk with 37478 particles (points) plotted against the theoretical $\Sigma(r_c, t)$ (solid line).

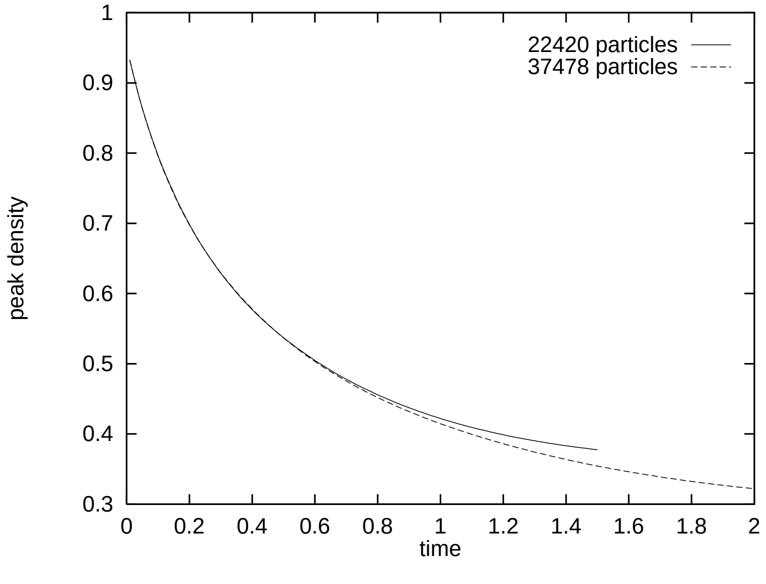

Figure 5.3.11: Peak density as a function of time for the two $\bar{\alpha} = 10.0$ simulations.

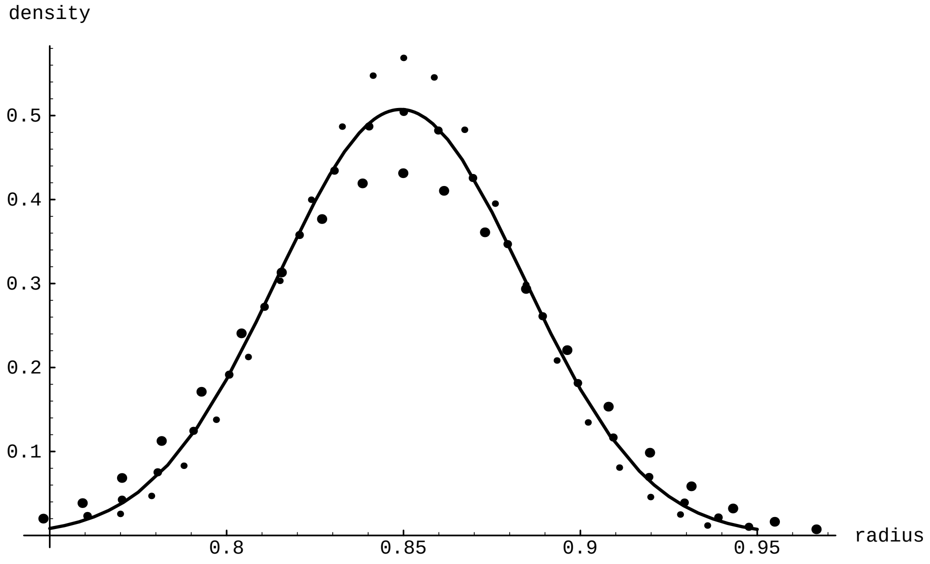

Figure 5.3.12: Theoretical disk profile (solid line) for $t = 0.60$ plotted with $\bar{\alpha} = 20.0$ (smallest points), $\bar{\alpha} = 10.0$ (midsize points) and $\bar{\alpha} = 0.0$ (largest points) SPH simulation results.

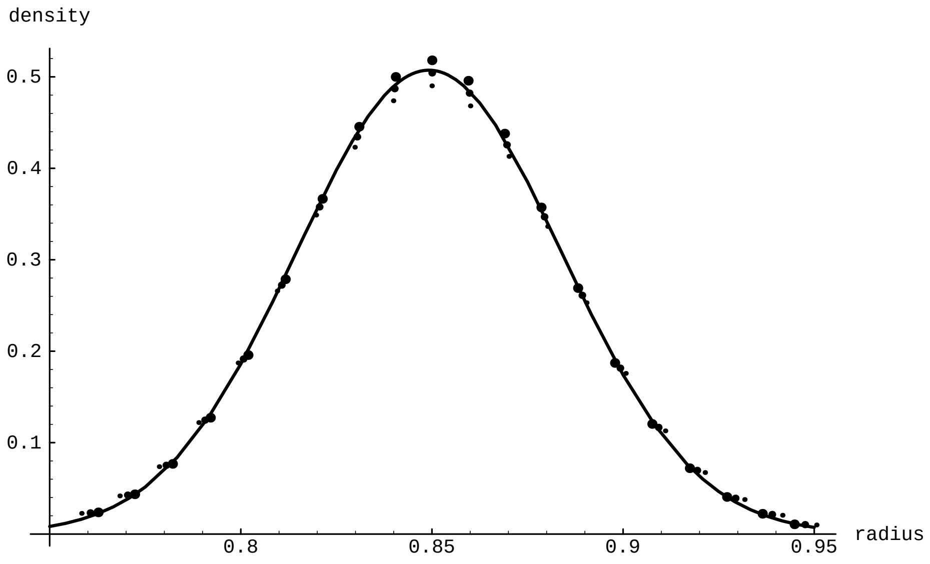

Figure 5.3.13: Theoretical disk profile (solid line) for $t = 0.60$ plotted with $\bar{\alpha} = 8.0$ (smallest points), $\bar{\alpha} = 10.0$ (midsize points) and $\bar{\alpha} = 12.0$ (largest points) SPH simulation results.

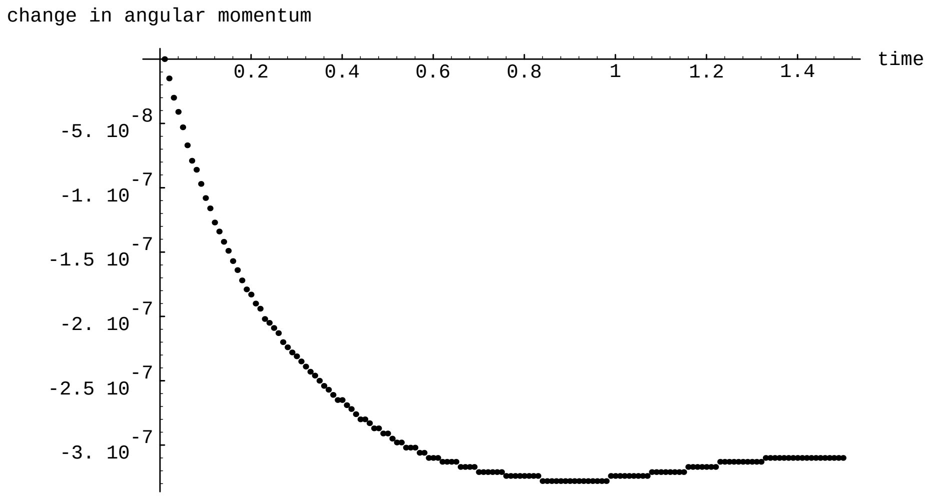

Figure 5.3.14: Change in the angular momentum with time from the original $3.4862772E-02$ Double precision

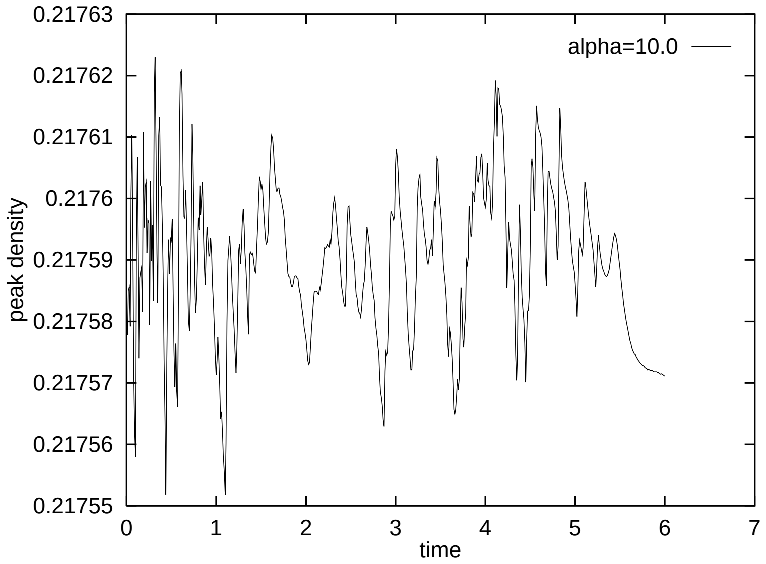

Figure 5.3.15: Angular momentum as a function of time (22480 particles). single precision

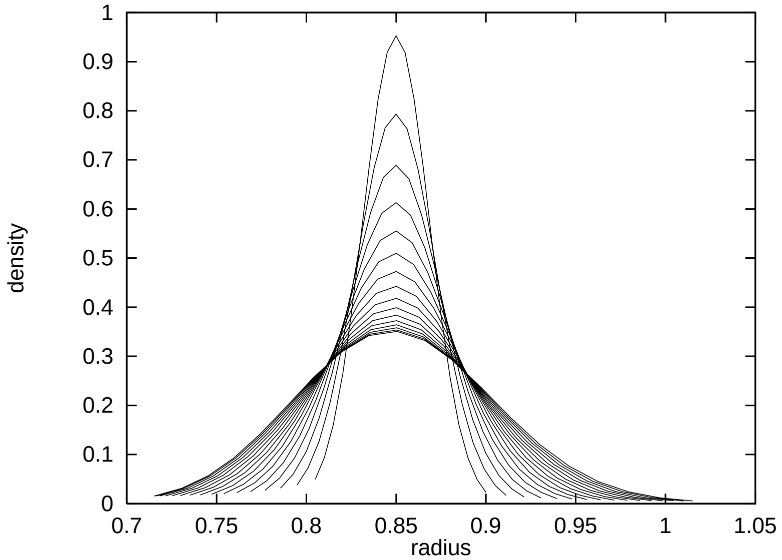

Figure 5.3.16: Density profiles of $\bar{\alpha} = 10.0$ disk for every 0.1 scaled time units from $t = 0.0$ to $t = 1.5$.

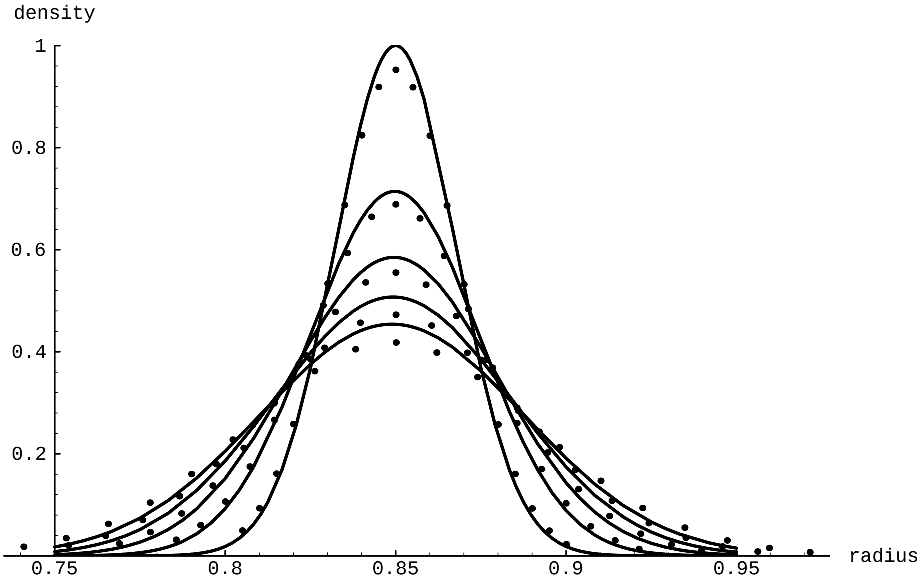

Figure 5.3.17: $\bar{\alpha} = 10.0$ disk with pressure evolution (points) plotted at 0,20,40,60,80 timesteps against the theoretical derived density curves.

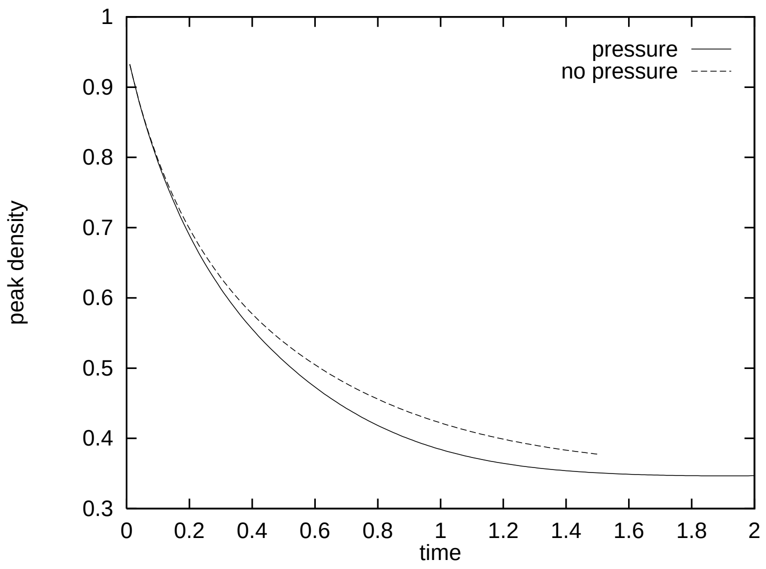

Figure 5.3.18: Peak density as a function of time for the $\bar{\alpha} = 10.0$ disks with and without pressure.

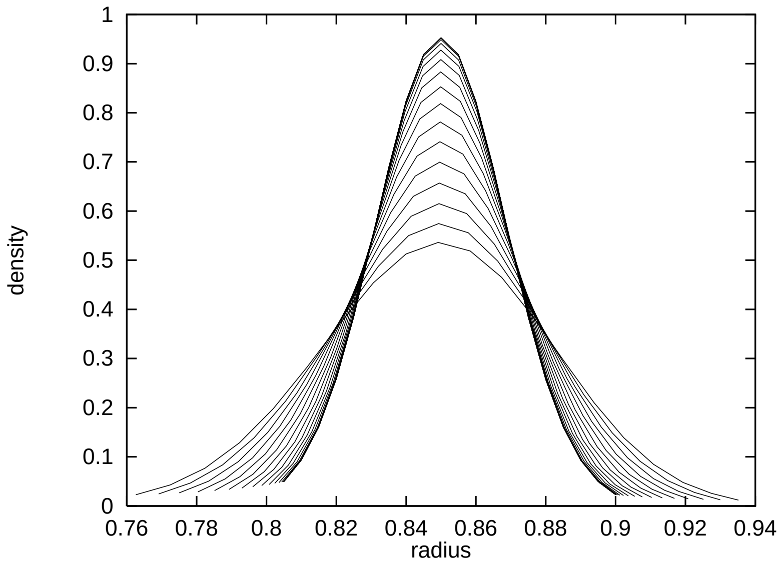

Figure 5.4.1: Density profiles of $\bar{\alpha} = 10.0$ disk for every 0.1 scaled time units from $t = 0.0$ to $t = 1.5$.

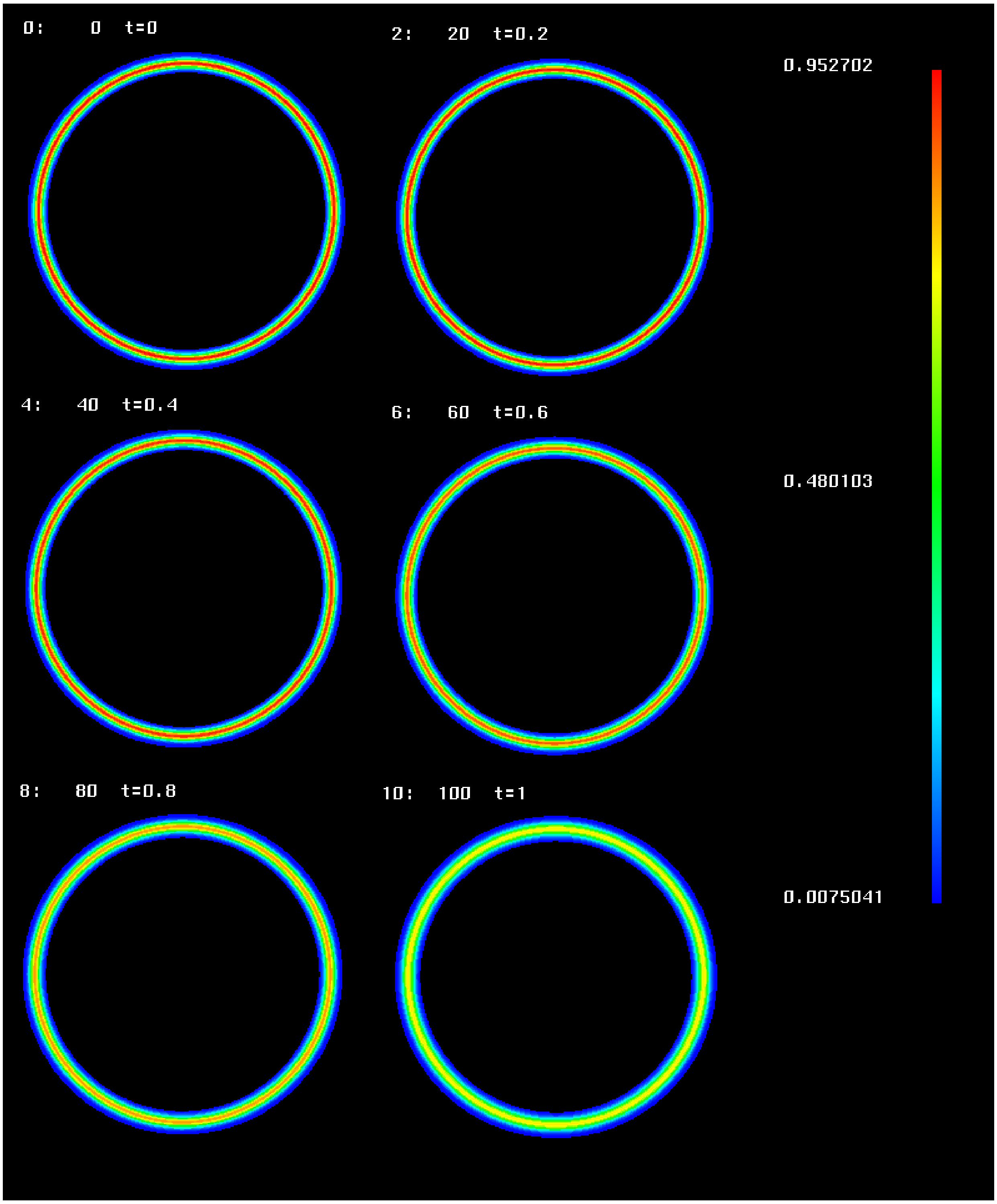

Figure 5.4.2: Evolution of initially stationary ring. Particles are coloured according to density (key to right).

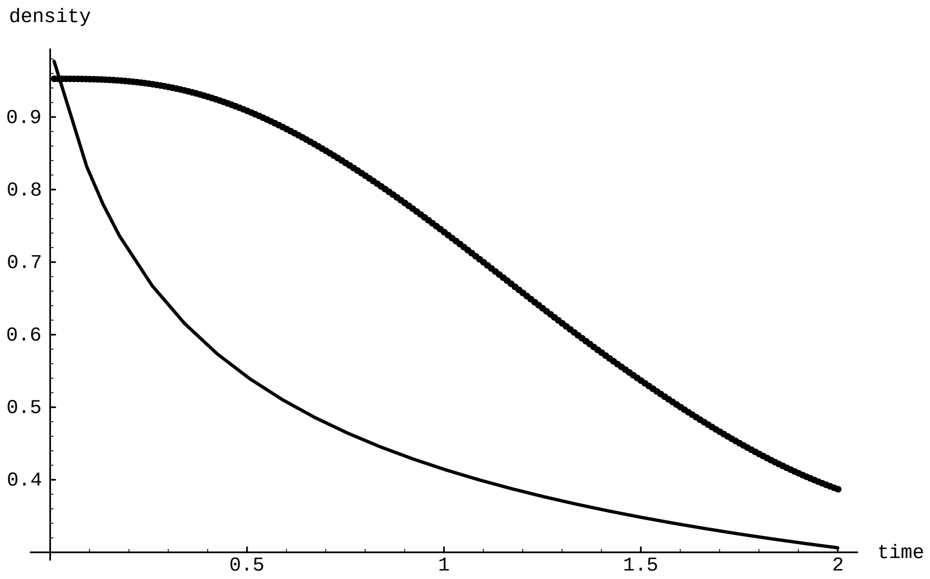

Figure 5.4.3: $\bar{\alpha} = 10.0$ disk peak density plotted against theoretical $\Sigma(r_c, t)$

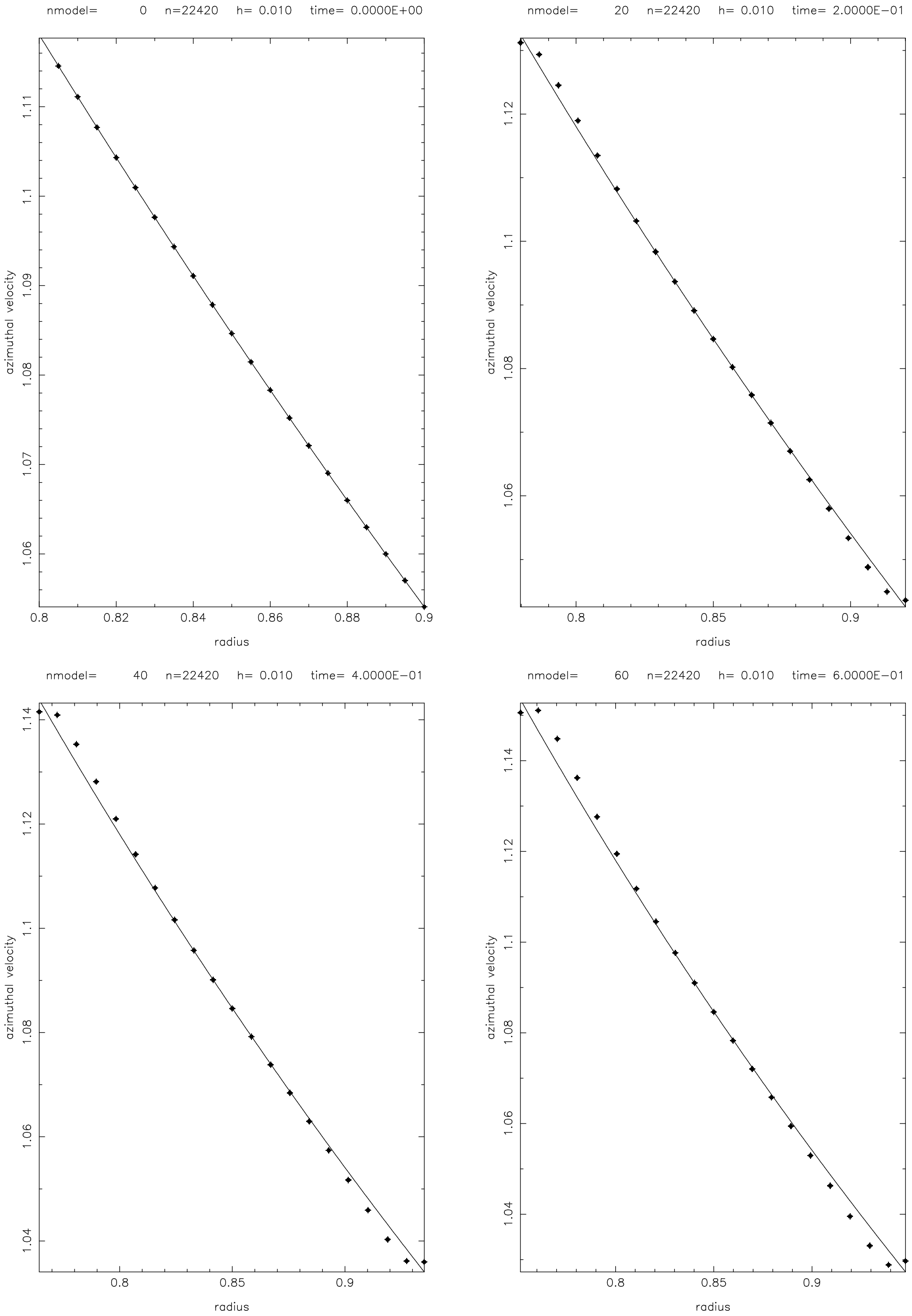

Figure 5.4.4: Angular velocity as a function of radius at $t = 0.0, 0.2, 0.4$ and 0.6 for the standard disk simulation (points). The Keplerian velocity curve is marked on the plots as a solid line.

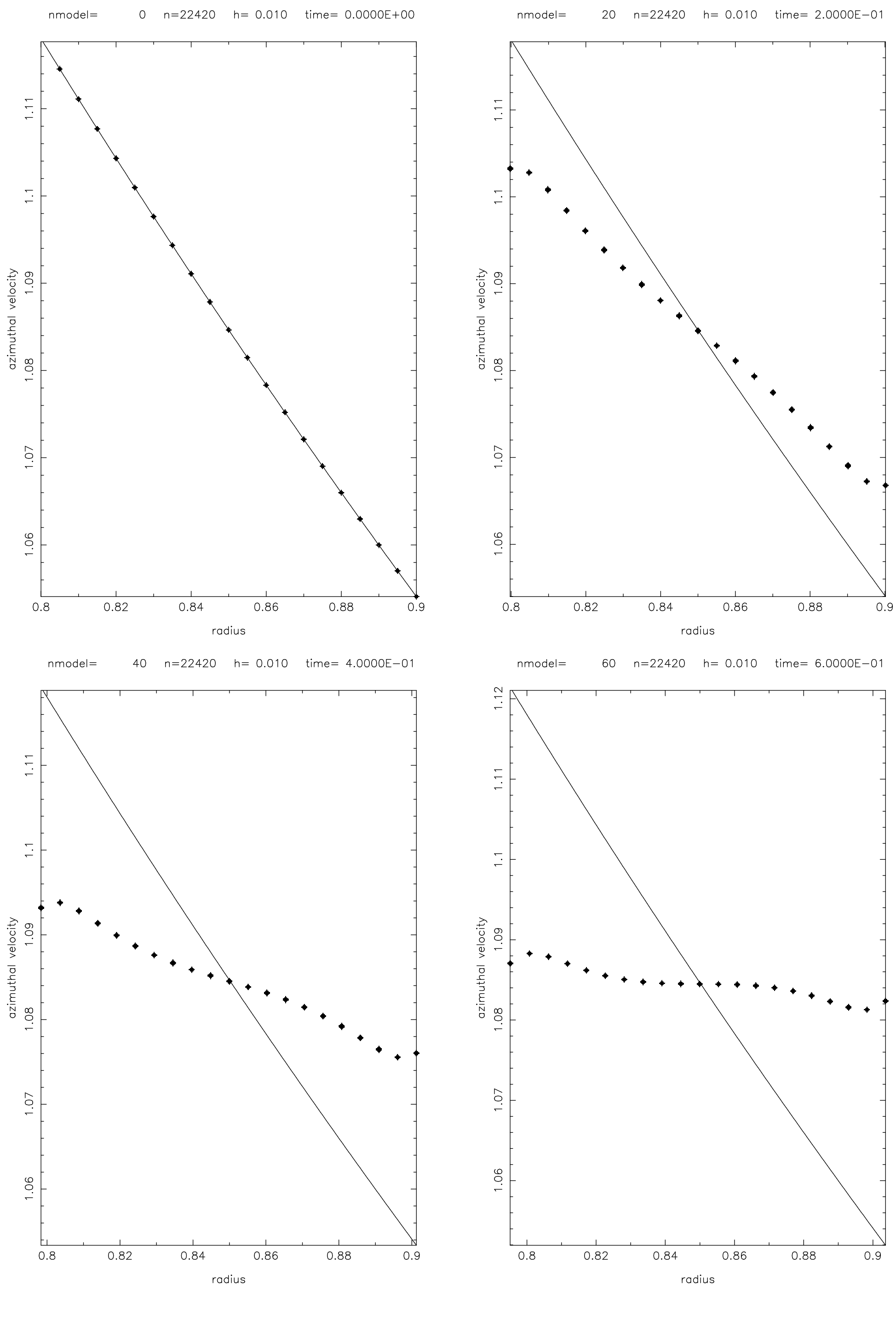

Figure 5.4.5: Angular velocity as a function of radius at $t = 0.0, 0.2, 0.4$ and 0.6 for the stationary disk simulation (points). The Keplerian velocity curve is marked on the plots as a solid line.

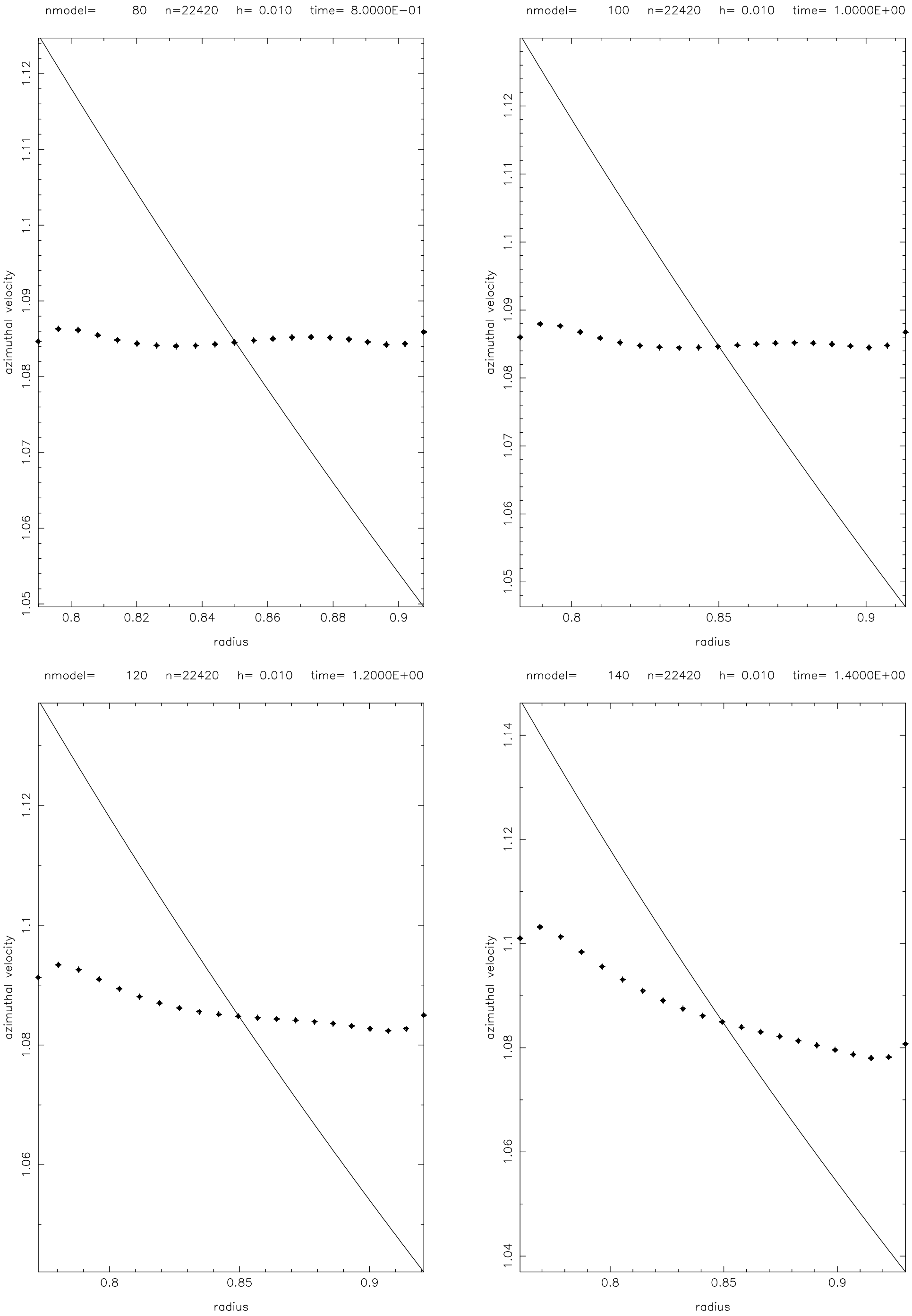

Figure 5.4.6: Angular velocity as a function of radius at $t = 0.8, 1.0, 1.2$ and 1.4 for the stationary disk simulation (points). The Keplerian velocity curve is marked on the plots as a solid line.

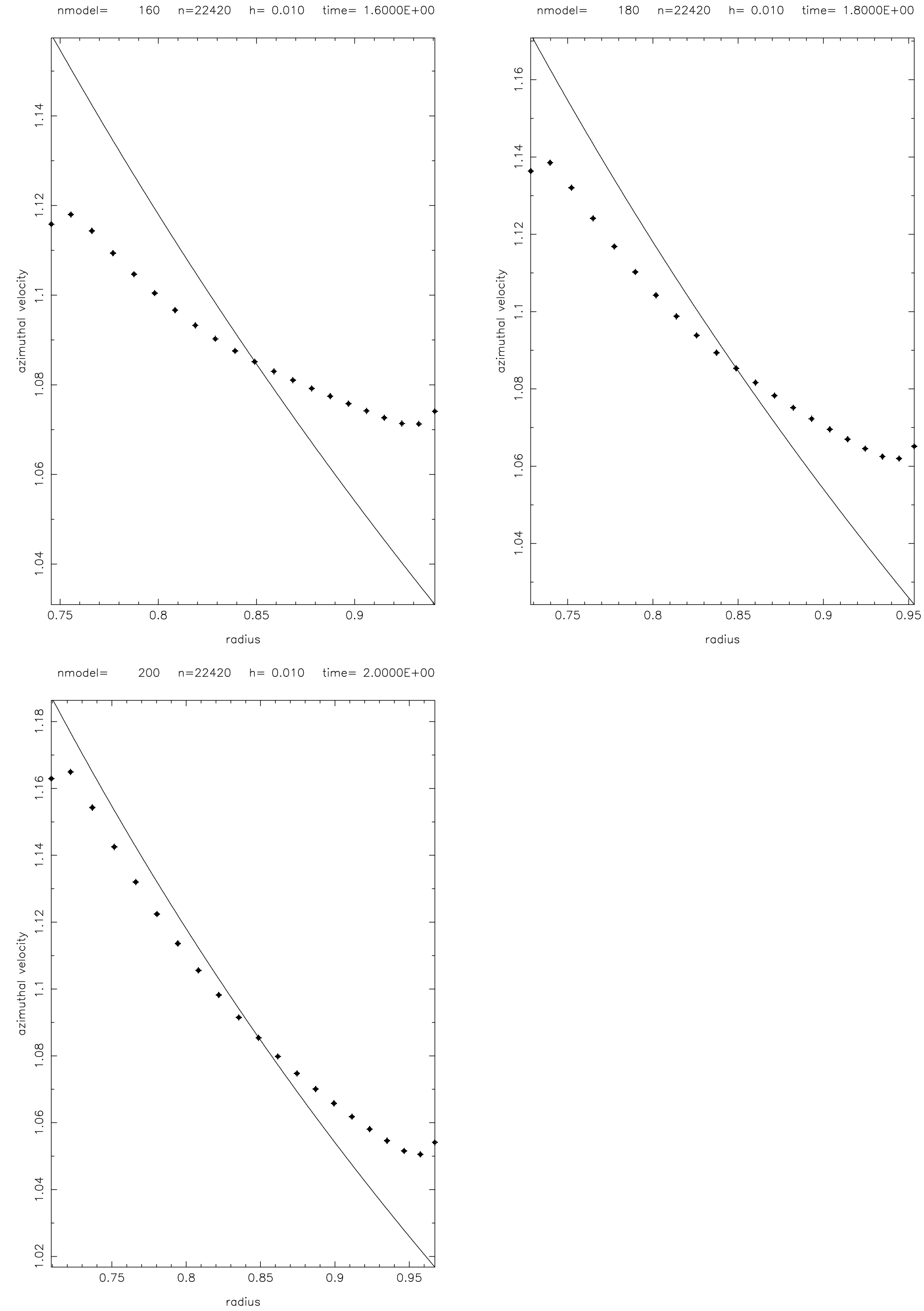

Figure 5.4.7: Angular velocity as a function of radius at $t = 1.6, 1.8$ and 2.0 for the stationary disk simulation (points). The Keplerian velocity curve is marked on the plots as a solid line.

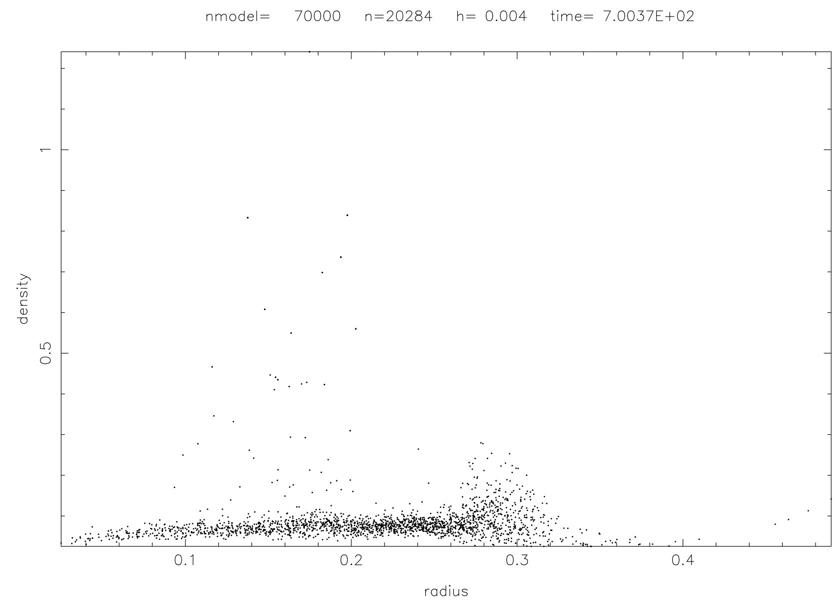

Figure 6.3.1: Density of every tenth particle plotted against the radius for a $\mu = \frac{1}{2}$ disk with zero pressure.

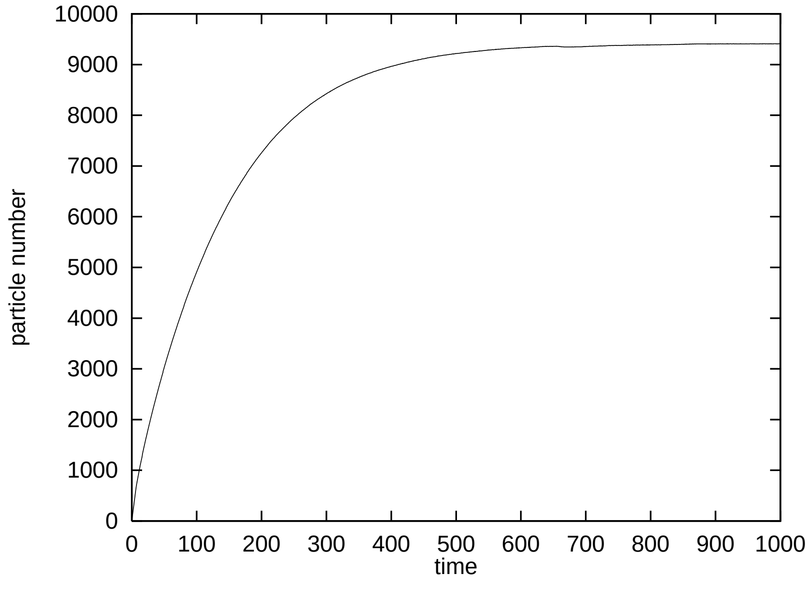

Figure 6.3.2: Plot of particle number against time for the $\mu = \frac{1}{2}$ disk.

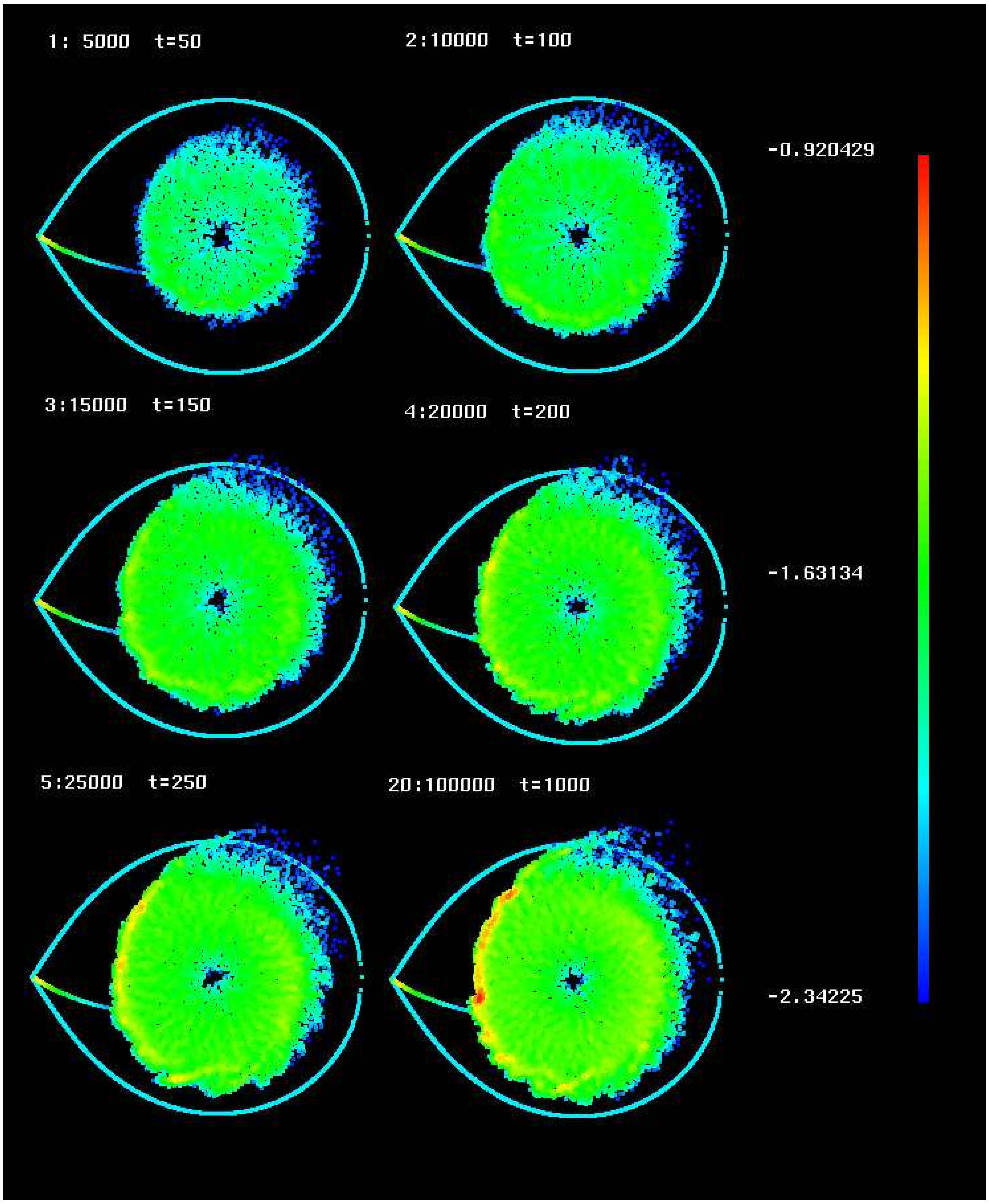

Figure 6.3.3: Particle plots for the $\mu = \frac{1}{2}$ disk at the times shown. The disk is coloured according to surface density using a log scale (key to right)

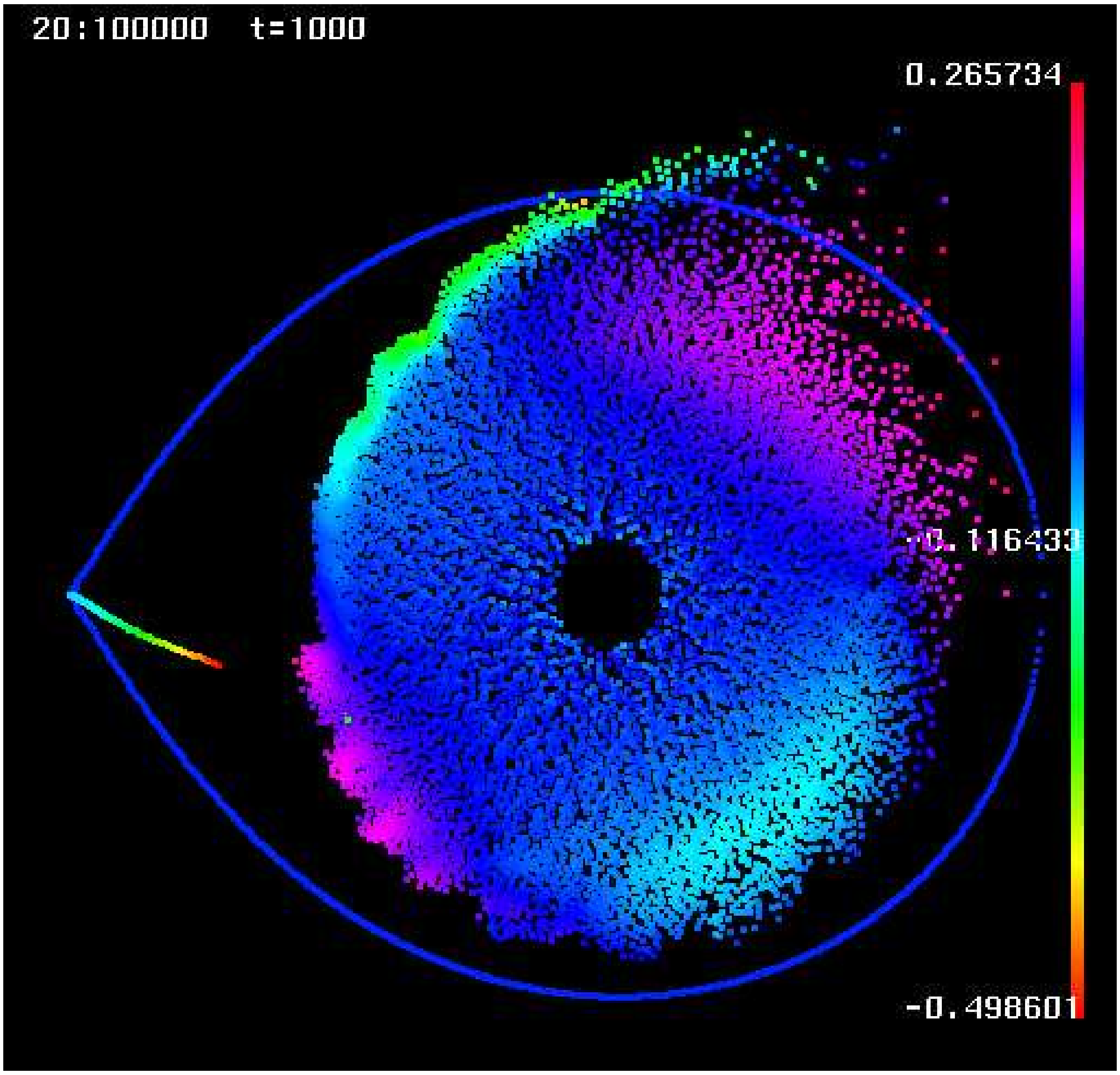

Figure 6.3.4: Particle plot of the $\mu = \frac{1}{2}$ disk coloured to show radial velocity (key to right). The inner region of the disk ($r < 0.05$) and part of the injection stream have been masked out of the plot to better resolve the behaviour of the radial velocity in the main body of the disk.

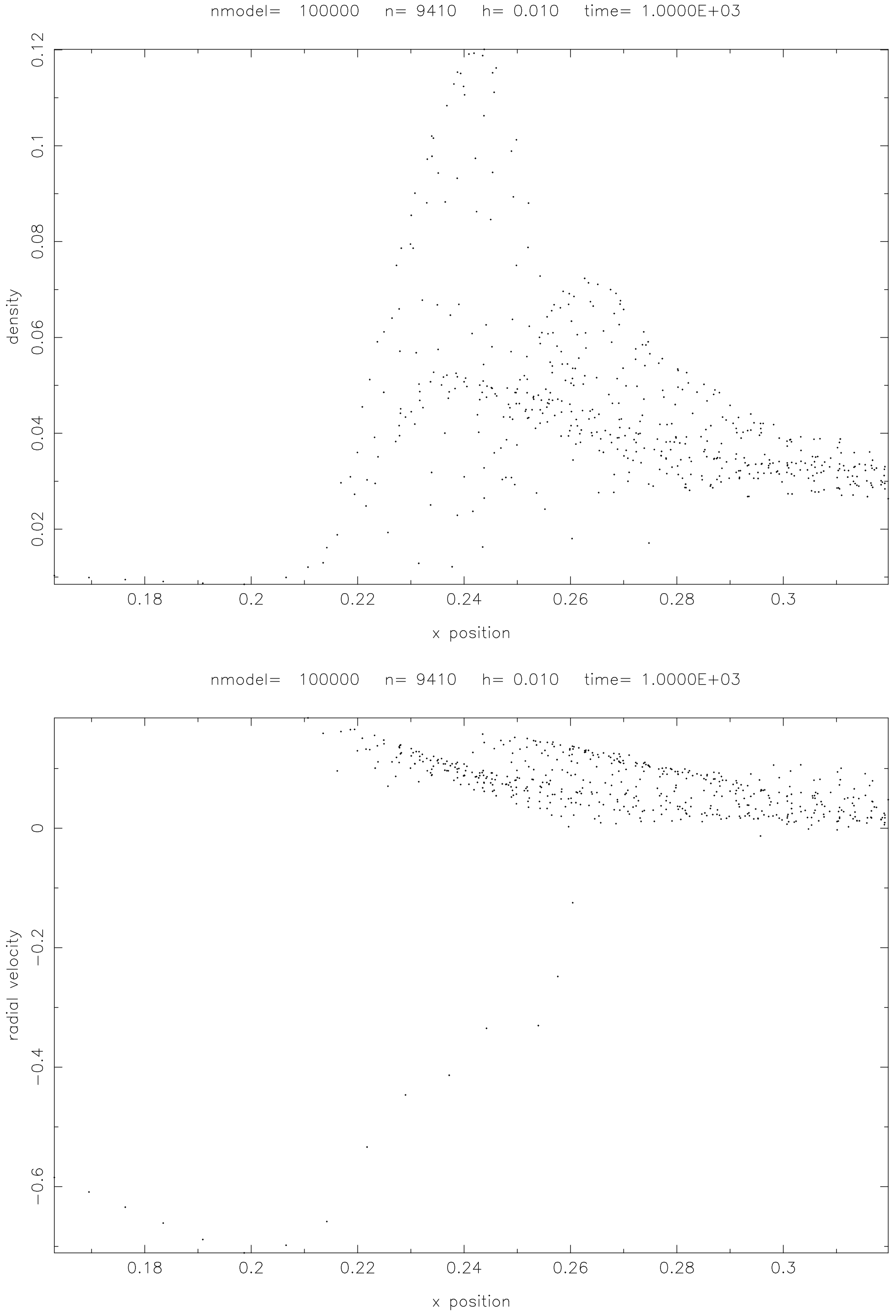

Figure 6.3.5: Density and radial velocities for all particles in the region $0.16 < x < 0.32$, $-0.20 < y < -0.05$ for the $\mu = \frac{1}{2}$ disk.

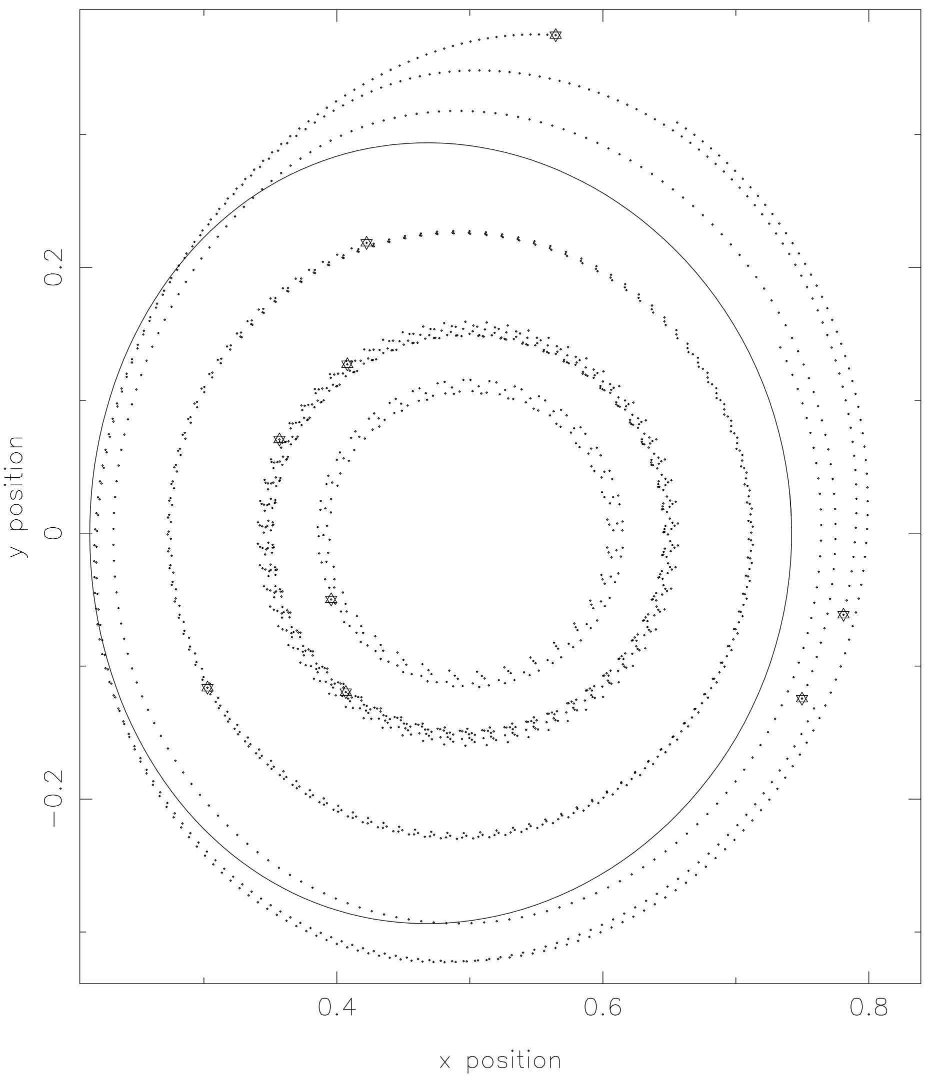

Figure 6.3.6: The paths of nine SPH particles in the $\mu = \frac{1}{2}$ disk. The large points mark the particle positions at $t = 1000.00$ with a small point recording its position every timestep after that. The particles are followed for 600 timesteps. The last simple nonintersecting periodic orbit is marked in as a solid line.

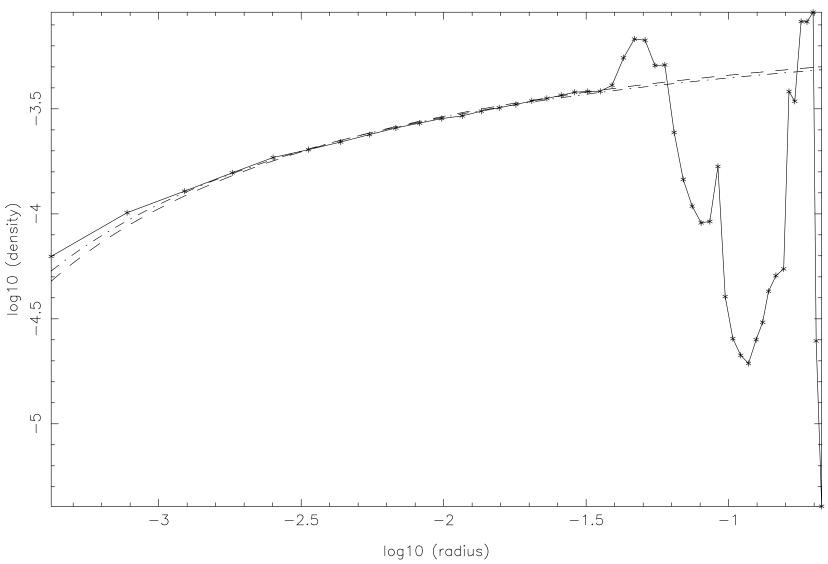

Figure 6.3.7: Azimuthally averaged density as a function of radius for the $\mu = \frac{1}{2}$ disk at $t = 1000.00$ (solid line with stars) plotted against axisymmetric disk theory, shown by the dashed line ($r_* = 0.017, \nu = 2.35 \times 10^{-4}$), and the dot dash line ($r_* = 0.016, \nu = 2.40 \times 10^{-4}$).

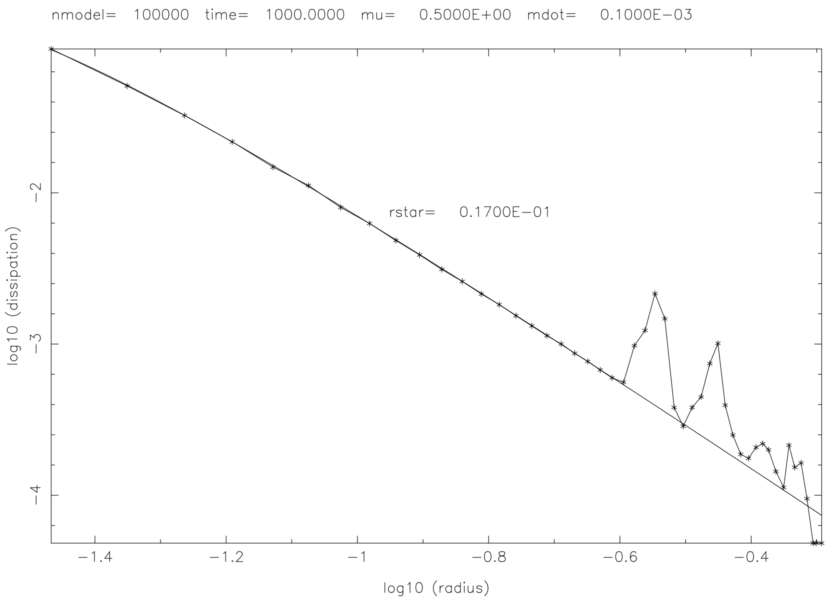

Figure 6.3.8: Azimuthally averaged energy dissipation rate as a function of radius for the $\mu = \frac{1}{2}$ disk at $t = 1000.00$ (solid line with stars) plotted against the theoretical curve for $r_* = 0.017(solidline)$.

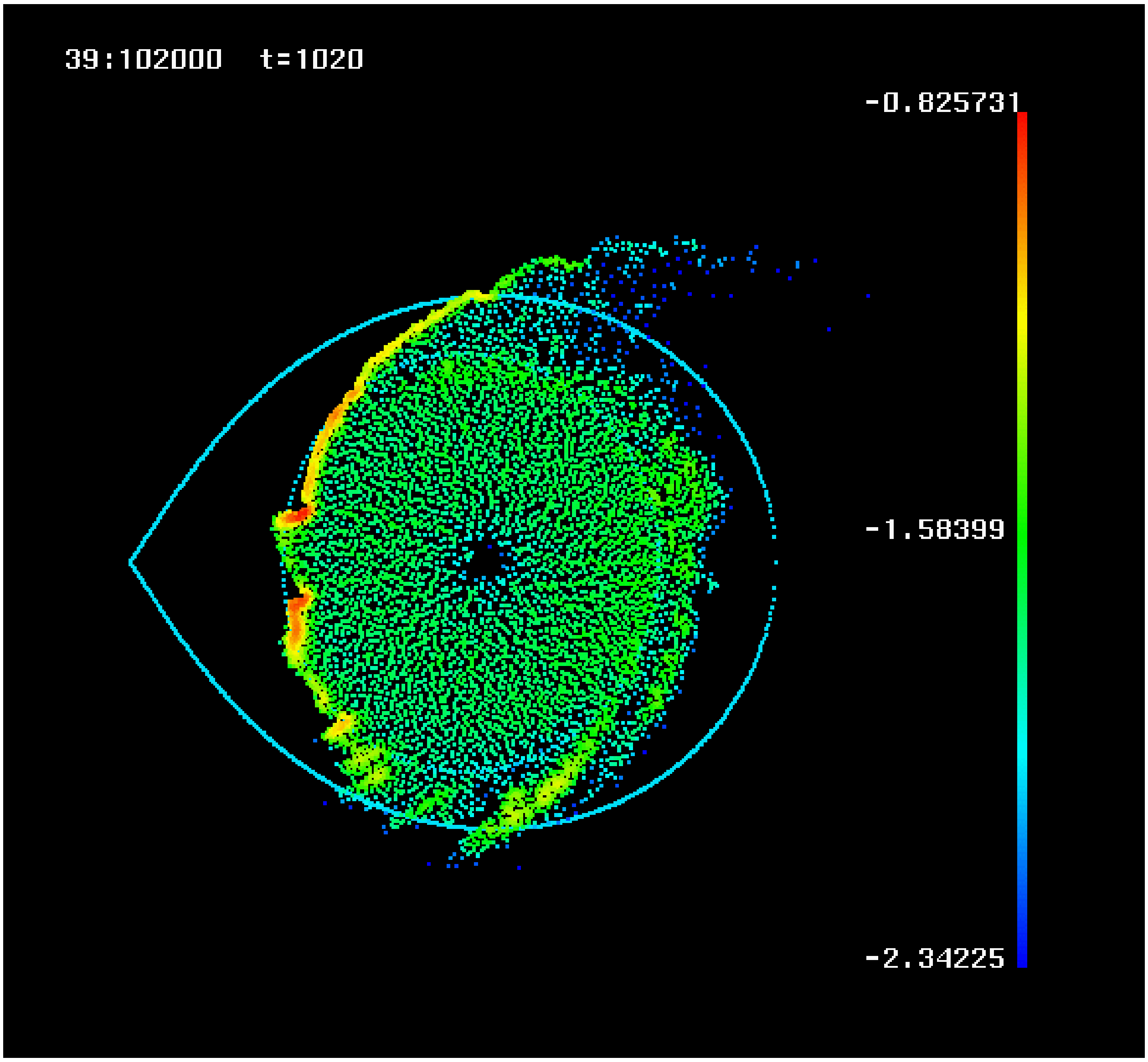

Figure 6.3.9: Particle plot of the $\mu = \frac{1}{2}$ disk 2000 steps after the injection stream has been switched off (i.e. 20.00 scaled time units after frame 6 Fig. 6.3.3). The particles are coloured according to their density using a logarithmic scale.

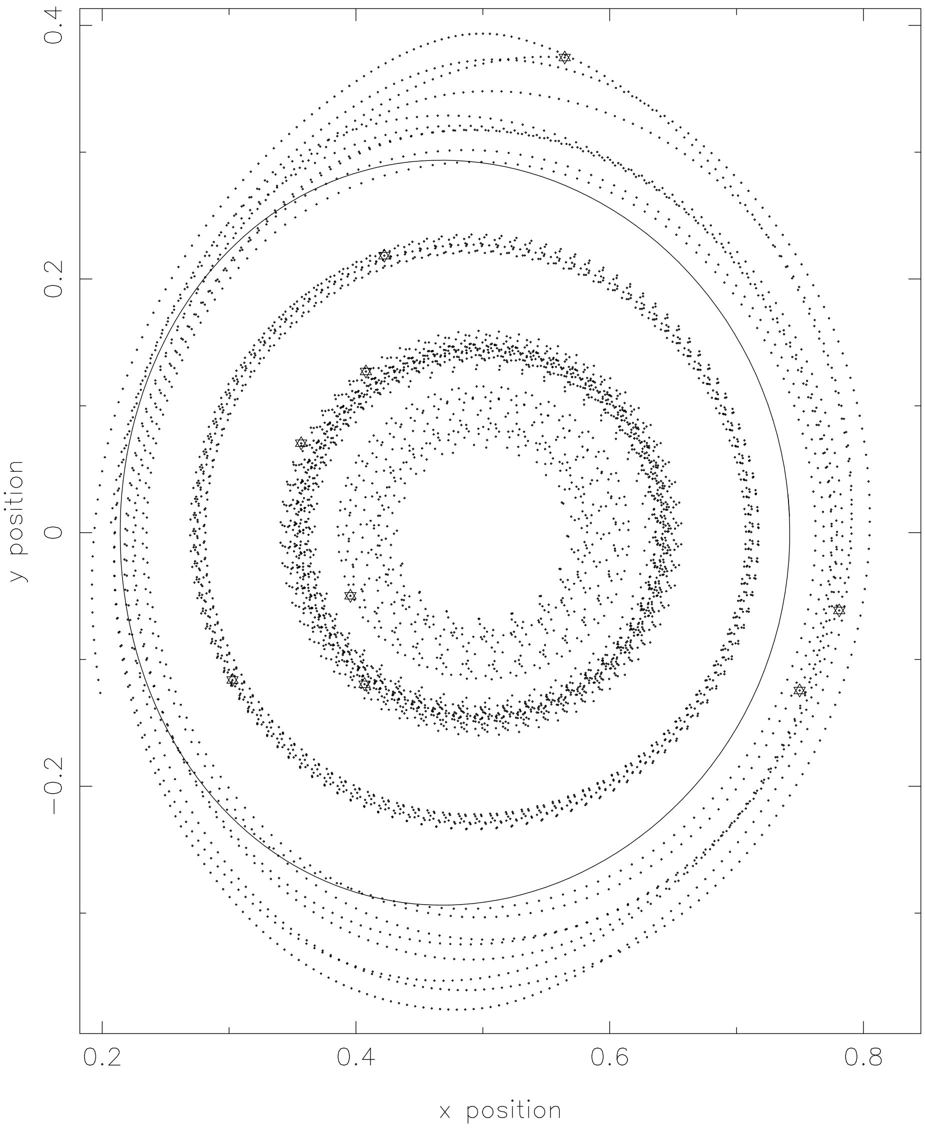

Figure 6.3.10: The paths of nine SPH particles in the $\mu = \frac{1}{2}$ disk. The large points mark the particle positions at $t = 1000.00$ with a small point recording its position every timestep after that. The particles are followed for 600 timesteps. The injection stream has been switched off. The last simple nonintersecting periodic orbit of a noninteracting particle (LNO) is marked in as a solid line.

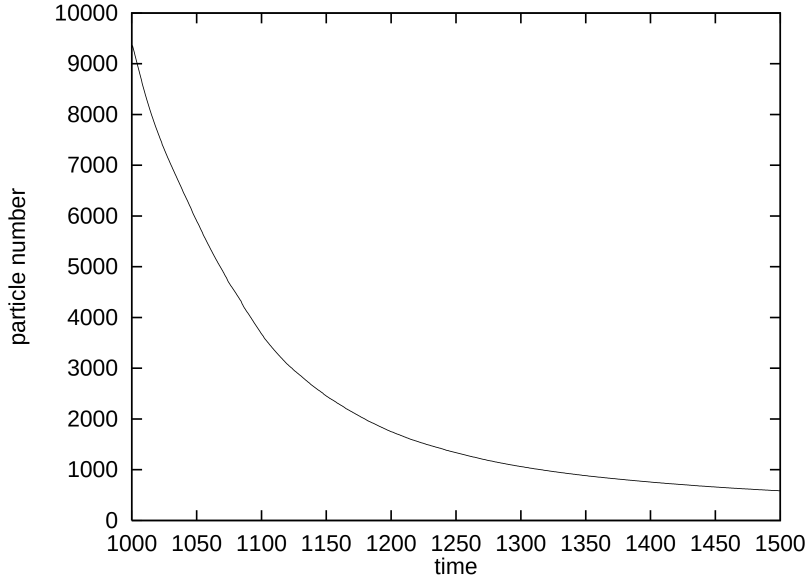

Figure 6.3.11: Plot of particle number against time for the $\mu = \frac{1}{2}$ disk with the mass injection from the secondary switched off.

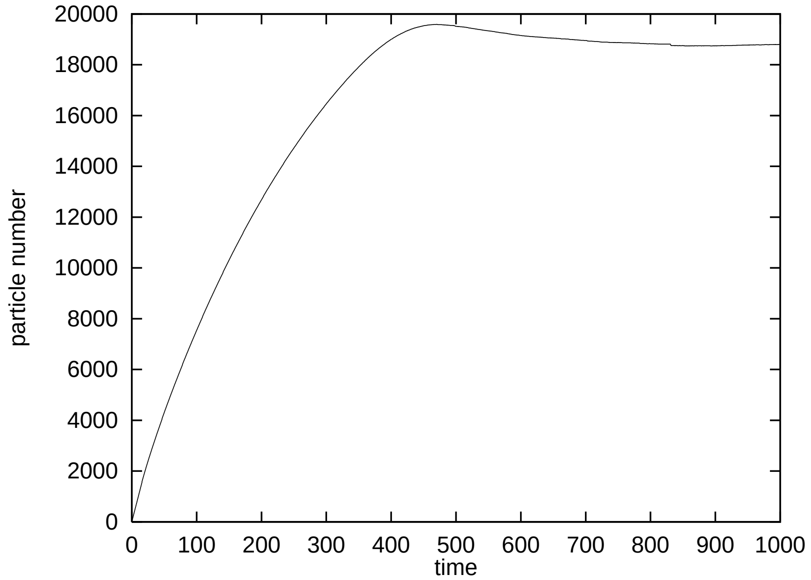

Figure 6.4.1: Plot of particle number against time for the $\mu = 0.85$ disk.

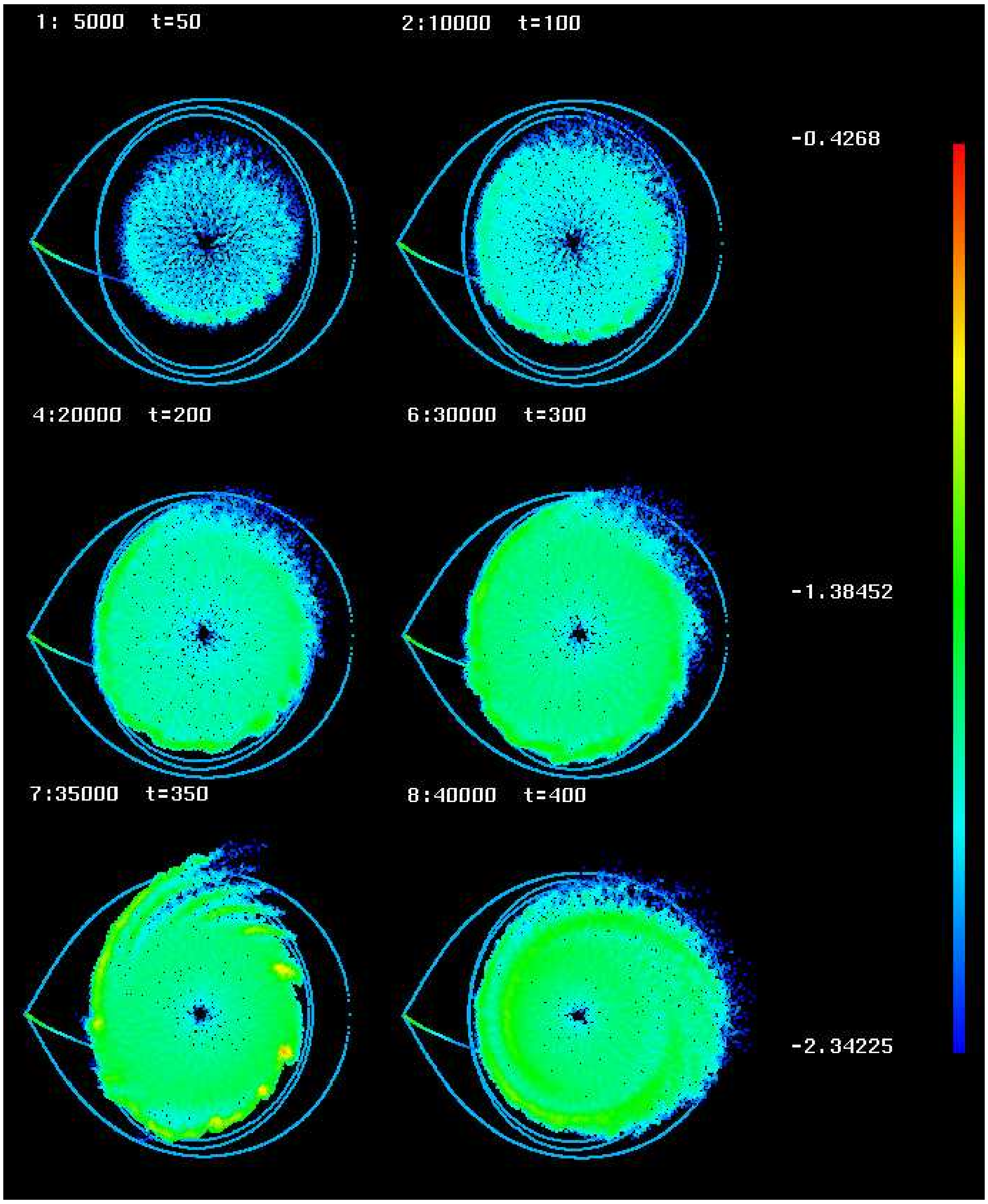

Figure 6.4.2: Particle plots for the $\mu = 0.85$ disk at the times shown. The disk is coloured according to surface density using a log scale (key to right)

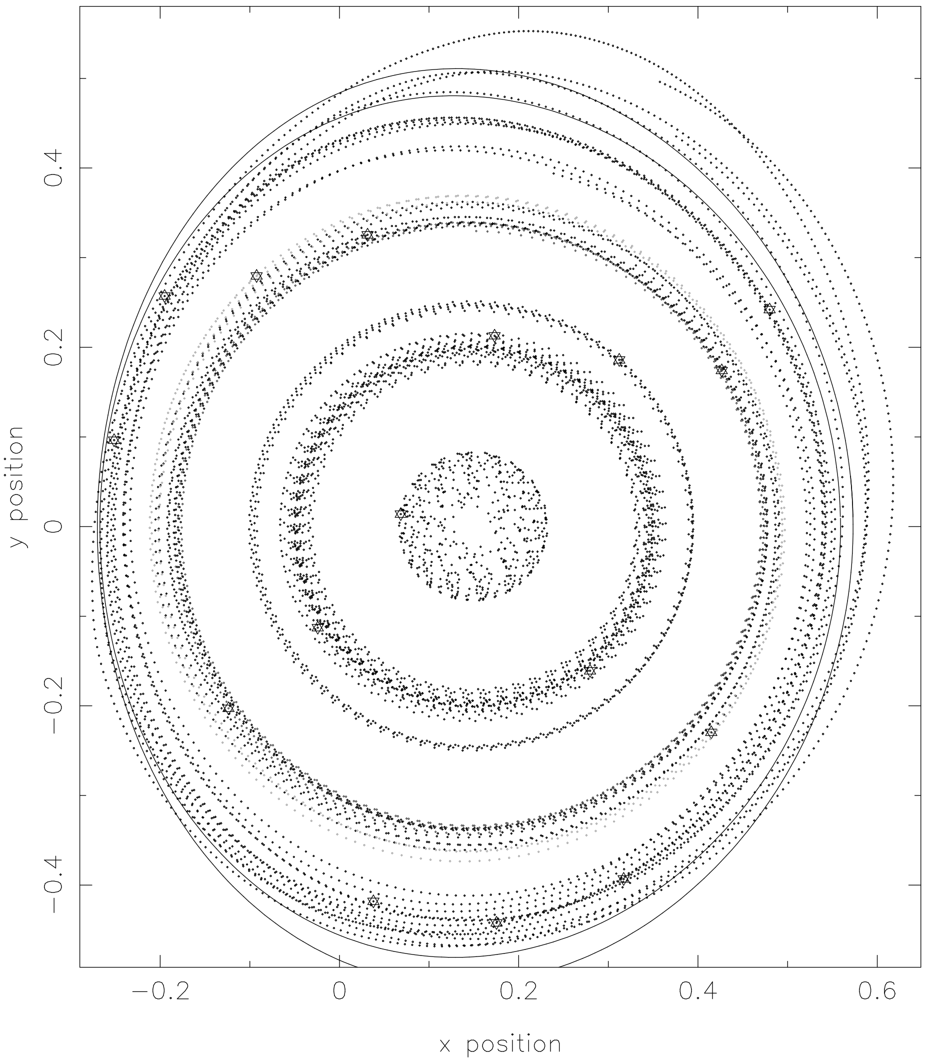

Figure 6.4.3: The paths of sixteen SPH particles in the $\mu = 0.85$ disk. The large points mark the particle positions at $t = 300.00$ with a small point recording its position every time step after that. The particles are followed for 600 time steps. The last nonintersecting periodic orbit (LNO)and the last stable periodic orbit (LSO) have been marked in with solid lines.

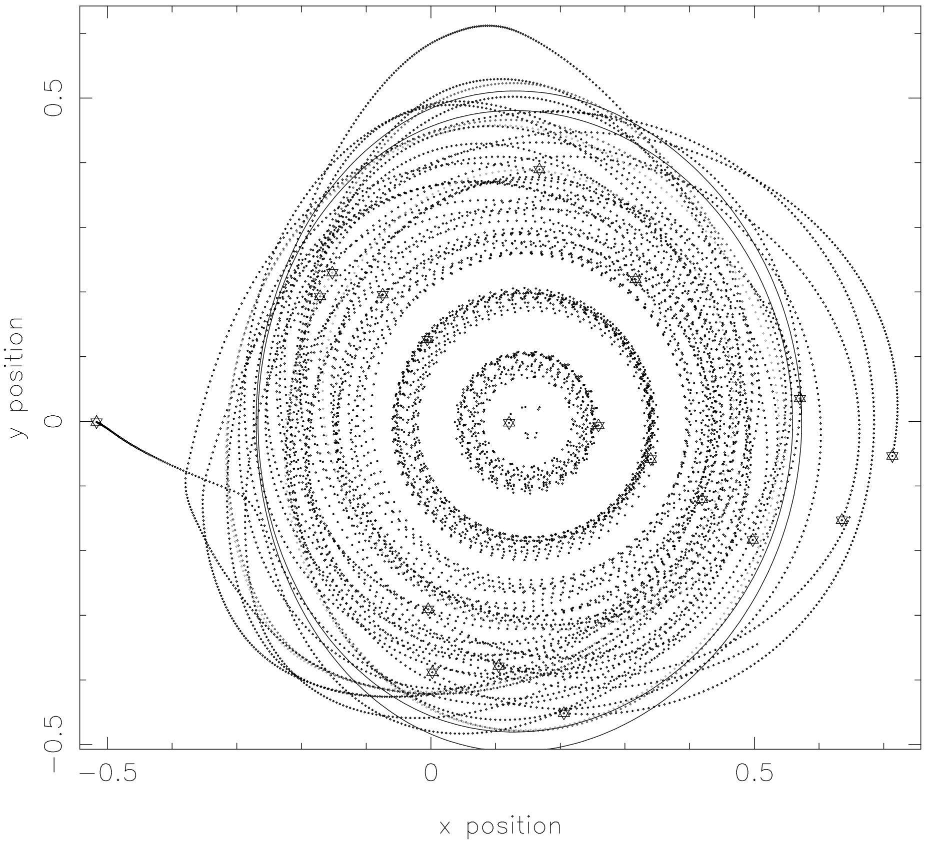

Figure 6.4.4: The paths of nineteen SPH particles in the $\mu = 0.85$ disk. The large points mark the particle positions at $t = 400.00$ with a small point recording its position every timestep after that. The particles are followed for 600 time steps. The LNO and LSO have been marked in with solid lines.

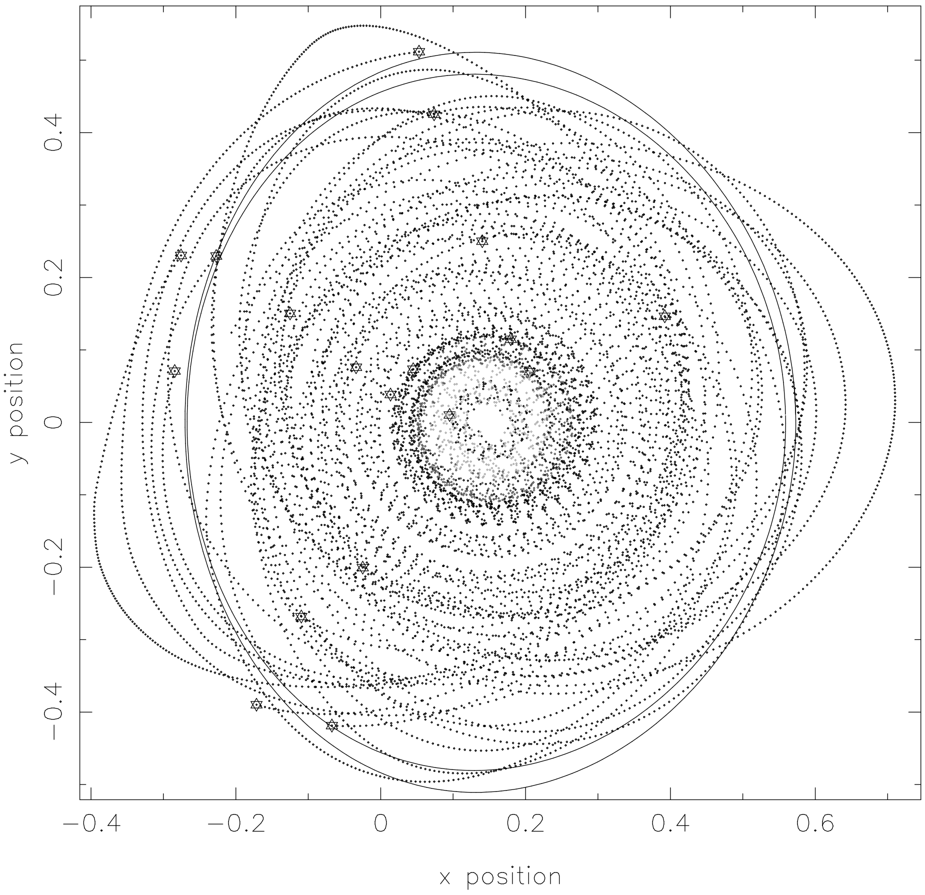

Figure 6.4.5: The paths of eighteen SPH particles in the $\mu = 0.85$ disk. The large points mark the particle positions at $t = 1000.00$ with a small point recording its position every time step after that. The particles are followed for 600 time steps. The LNO and LSO have been marked in with solid lines.

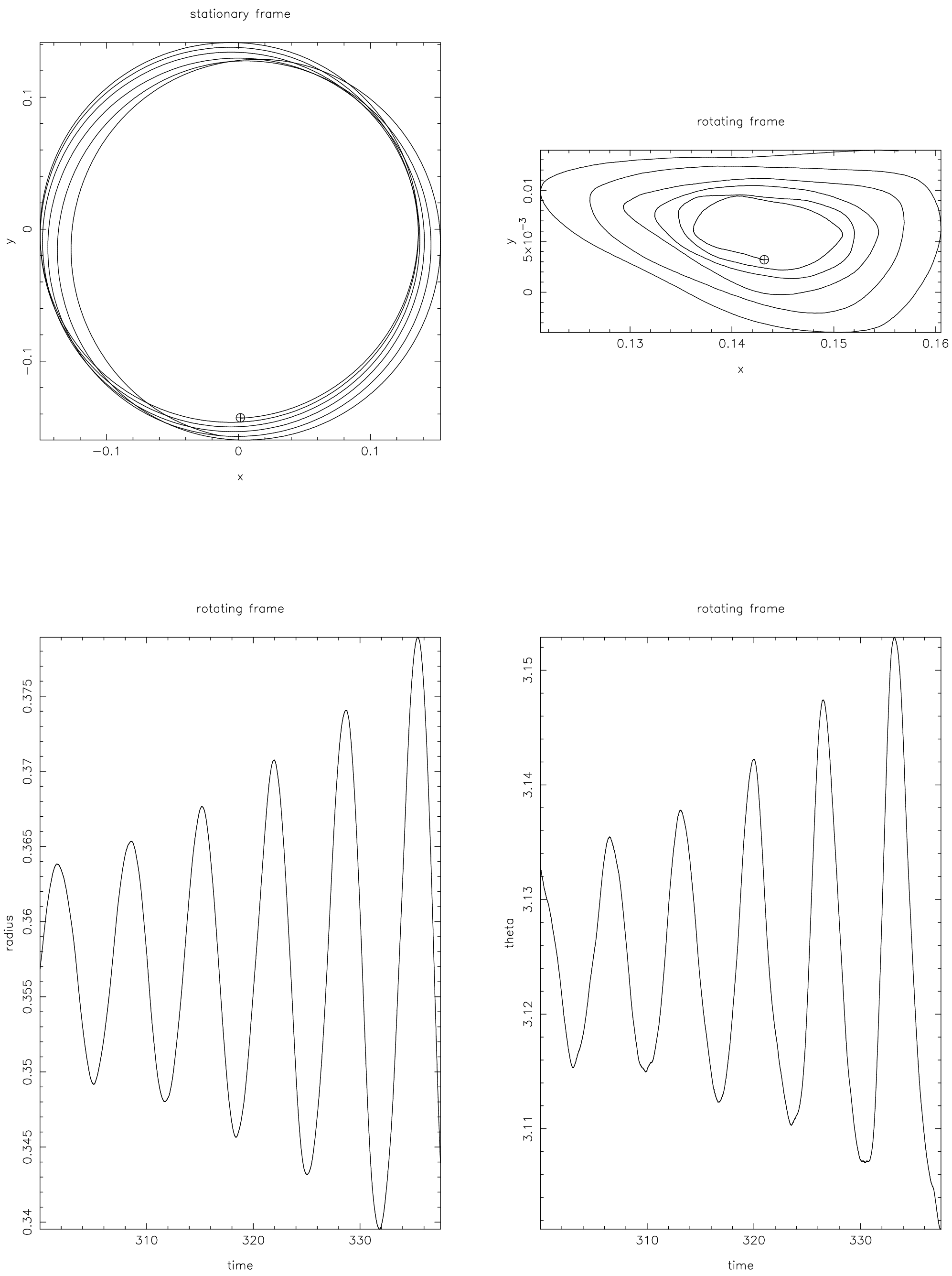

Figure 6.4.6: Plots of the motion of the centre of mass of the accretion disk for 5000 steps (50.00 scaled time units) starting from $t = 300.00$. The top two diagrams show its trajectory in the stationary and rotating frames. The lower figures show its radial and angular position with respect to the white dwarf primary as a function of time.

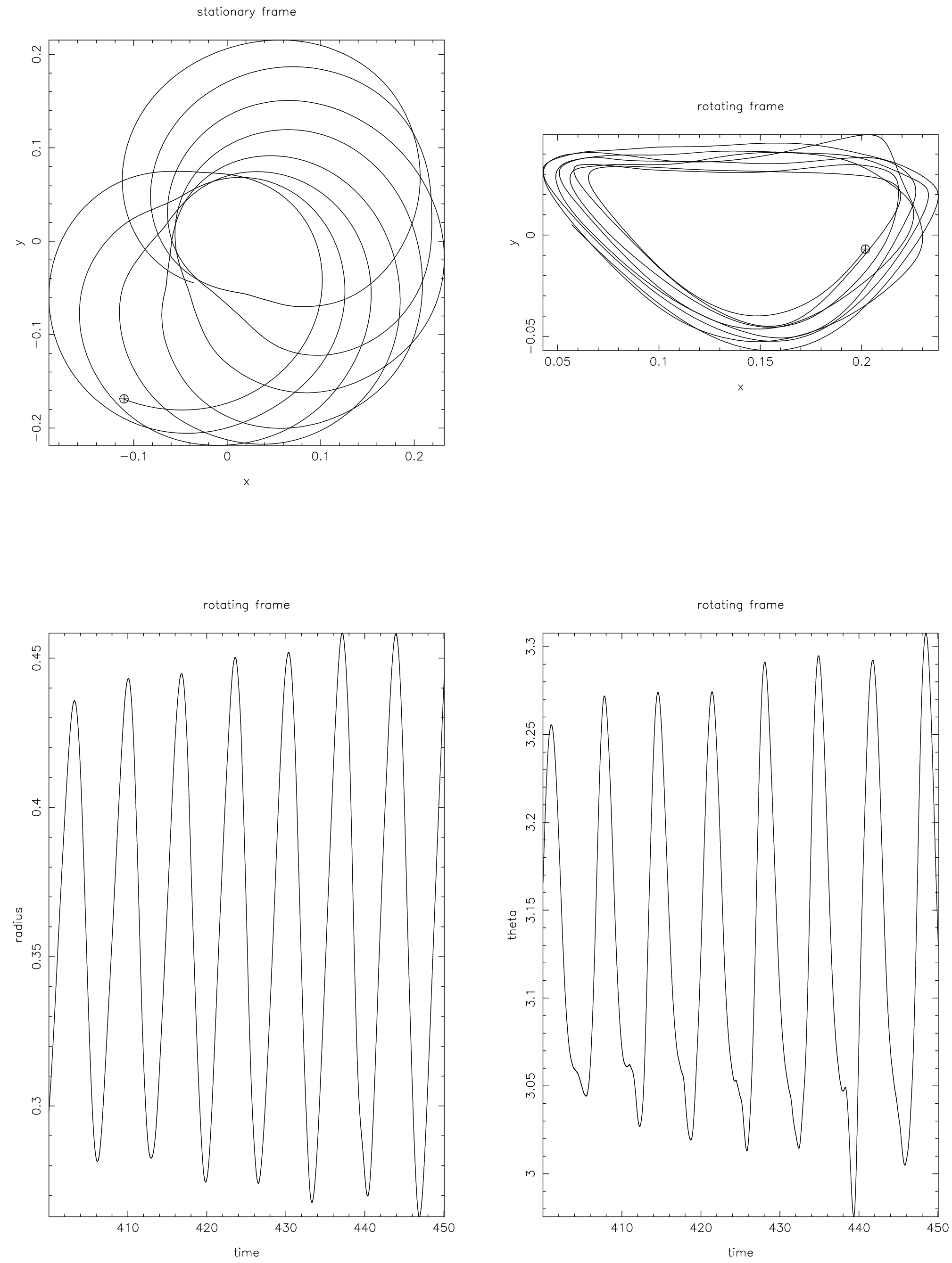

Figure 6.4.7: Plots of the motion of the centre of mass of the accretion disk for 5000 steps (50.00 scaled time units) starting from $t = 400.00$. The top two diagrams show its trajectory in the stationary and rotating frames. The lower figures show its radial and angular position with respect to the white dwarf primary as a function of time.

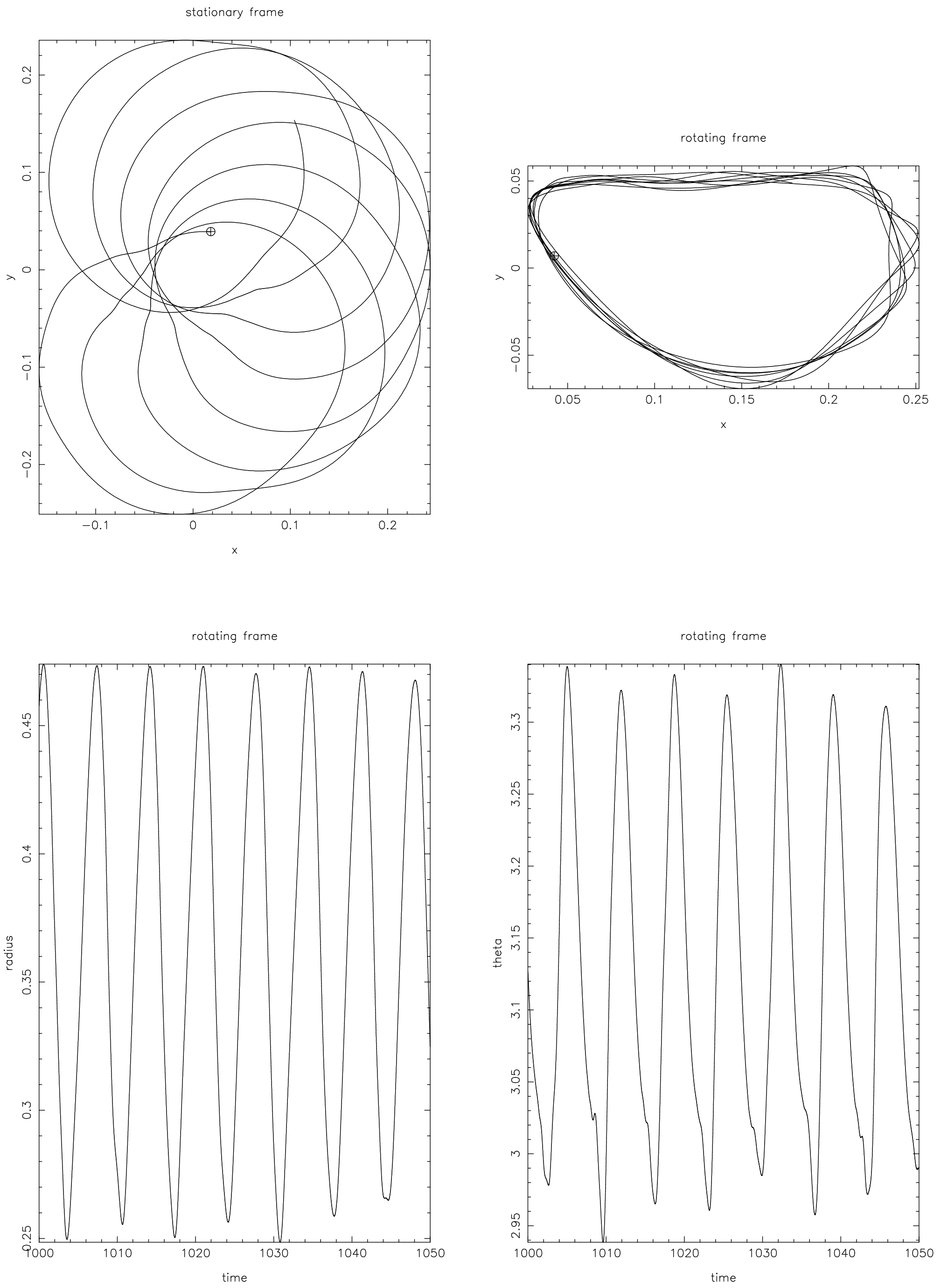

Figure 6.4.8: Plots of the motion of the centre of mass of the accretion disk for 5000 steps (50.00 scaled time units) starting from $t = 1000.00$. The top two diagrams show its trajectory in the stationary and rotating frames. The lower figures show its radial and angular position with respect to the white dwarf primary as a function of time.

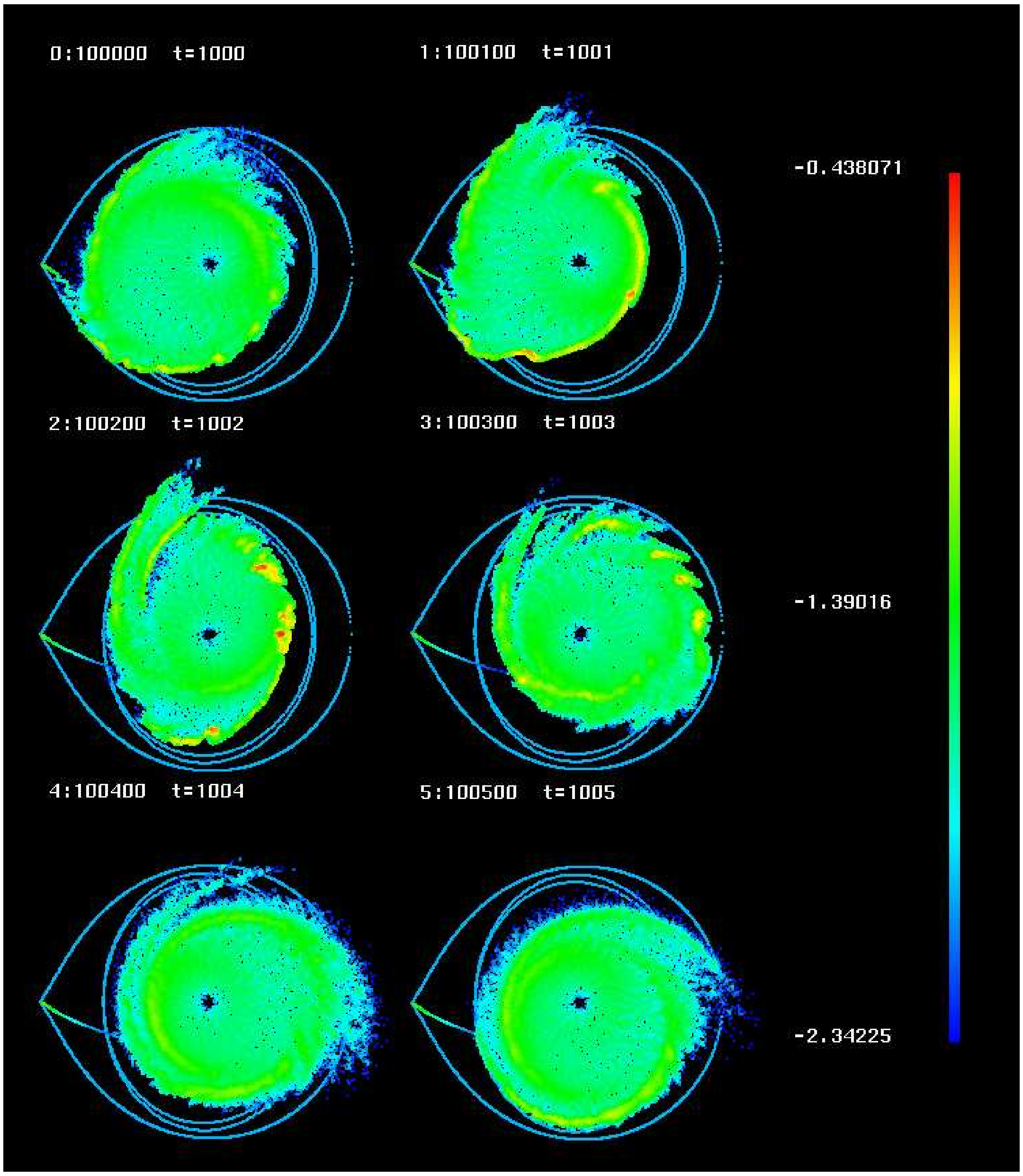

Figure 6.4.9: Particle plots for the $\mu = 0.85$ disk at the times shown. The disk is coloured according to surface density using a log scale (key to right). The six plots are spaced 1.00 scaled time units apart and roughly cover a full period of the disk precession

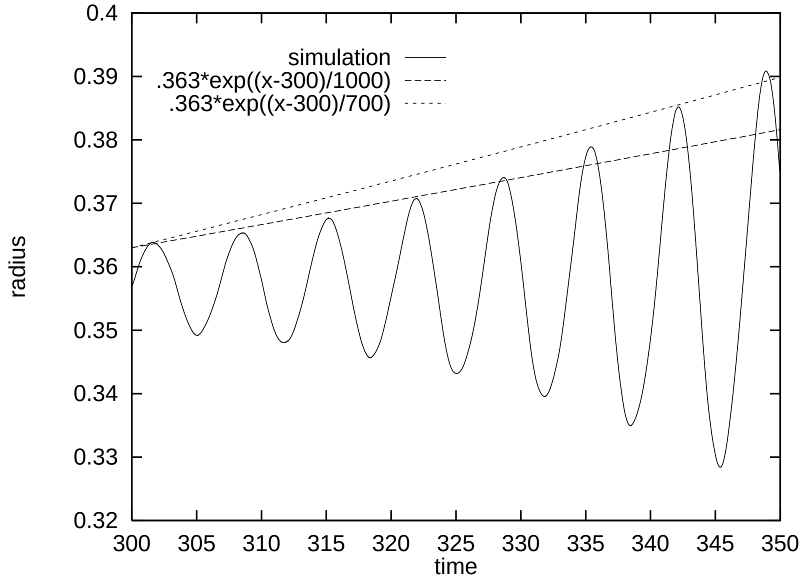

Figure 6.4.10: Radial coordinate of the centre of mass of the accretion disk (in the frame co-rotating with the binary) plotted against time with two attempts to fit the peaks to exponentials. This is just plot c of the previous figure reproduced.

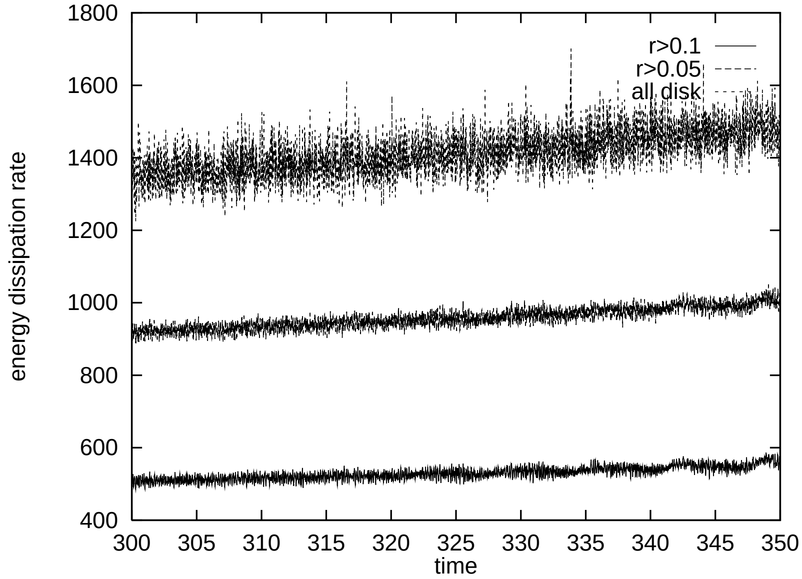

Figure 6.4.11: Energy dissipated per unit time by the disk as a function of time for 5000 time steps starting at $t = 300.00$. The top curve is for the entire disk. The middle and bottom curves give the energy dissipated in the regions of the disk more than 0.05 and 0.1 from the center of the white dwarf respectively.

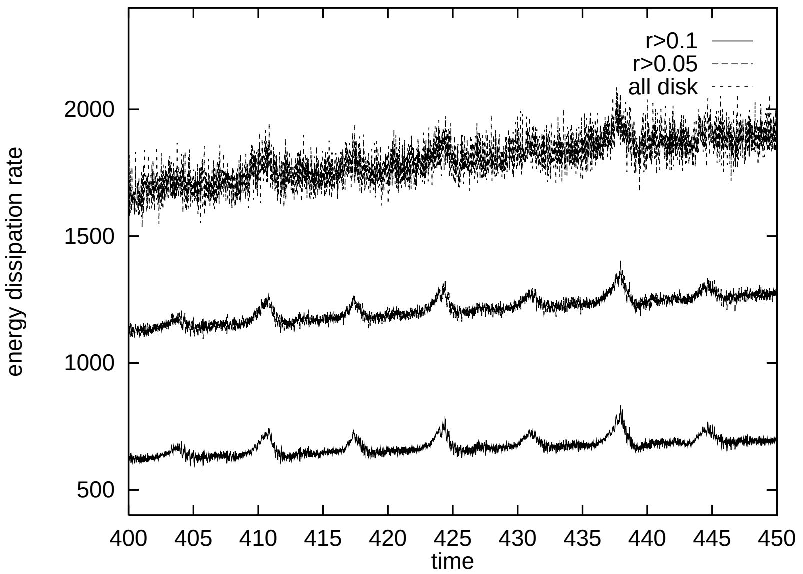

Figure 6.4.12: Energy dissipated per unit time by the disk as a function of time for 5000 time steps starting at $t = 400.00$. The top curve is for the entire disk. The middle and bottom curves give the energy dissipated in the regions of the disk more than 0.05 and 0.1 from the center of the white dwarf respectively.

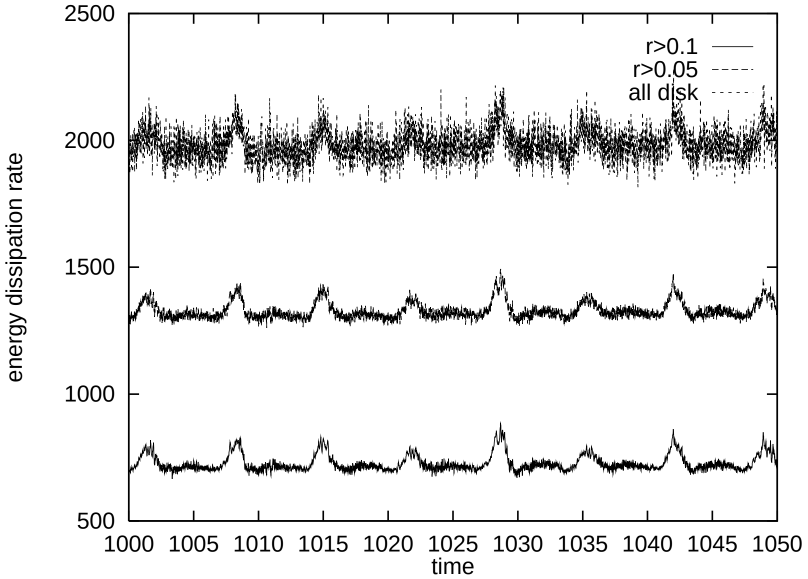

Figure 6.4.13: Energy dissipated per unit time by the disk as a function of time for 5000 time steps starting at $t = 1000.00$. The top curve is for the entire disk. The middle and bottom curves give the energy dissipated in the regions of the disk more than 0.05 and 0.1 from the center of the white dwarf respectively.

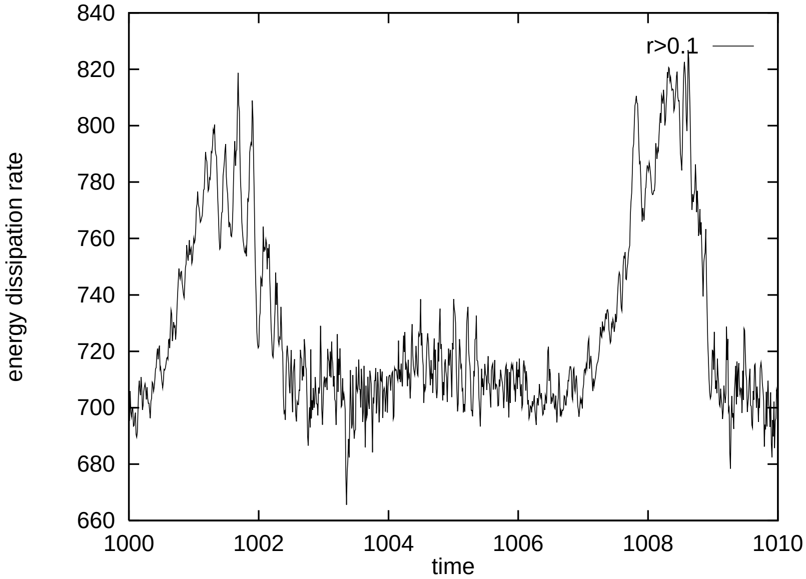

Figure 6.4.14: Energy dissipated per unit time by the disk as a function of time for 1000 time steps starting at $t = 1000.00$.

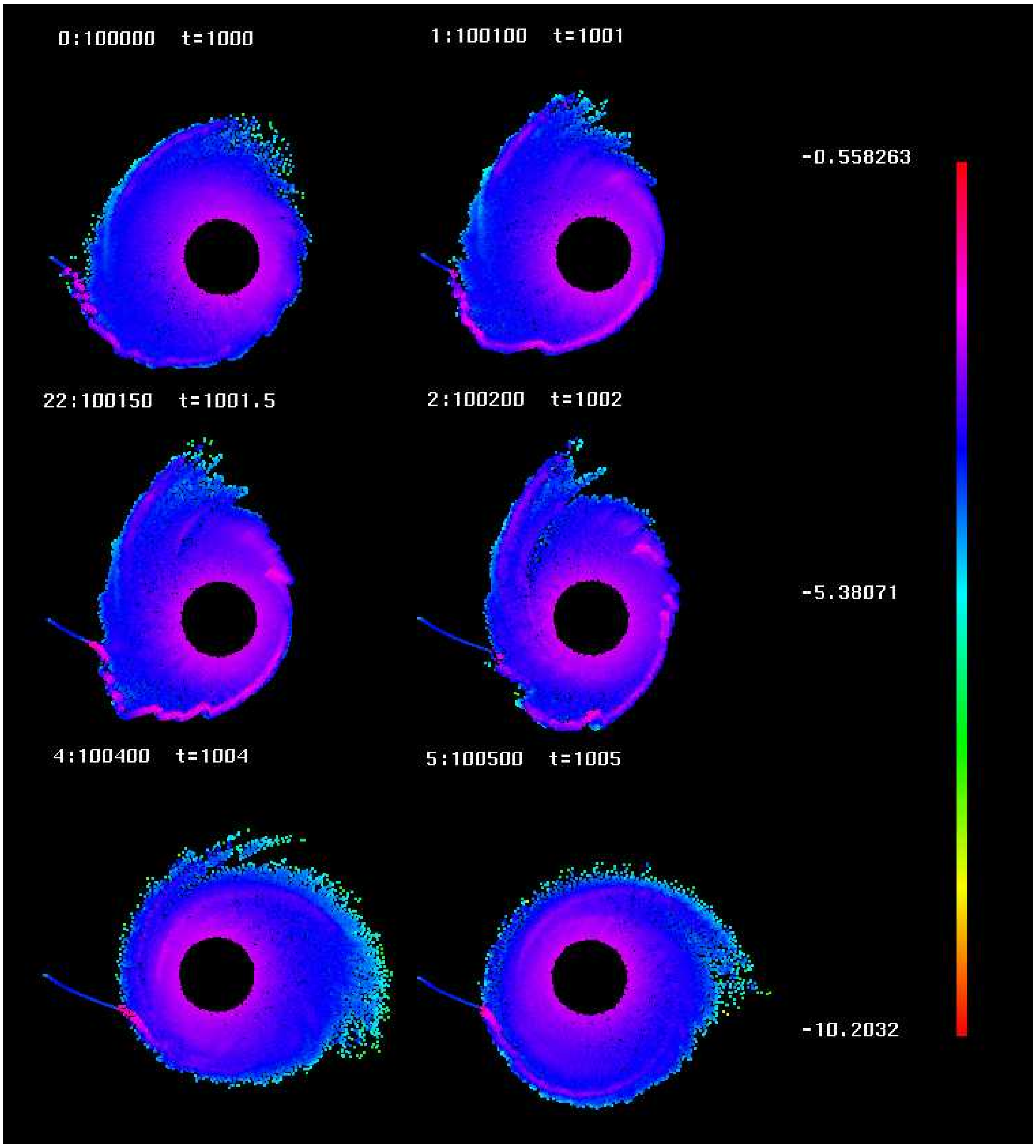

Figure 6.4.15: Particle plots for the $\mu = 0.85$ disk at the times shown. The disk is coloured according to the rate of energy dissipation **per unit area** calculated at the particle. A logarithmic scale (key to right) is used. To highlight the structure in the outer disk all particles at radii $r < 0.15$ are excluded from the plots.

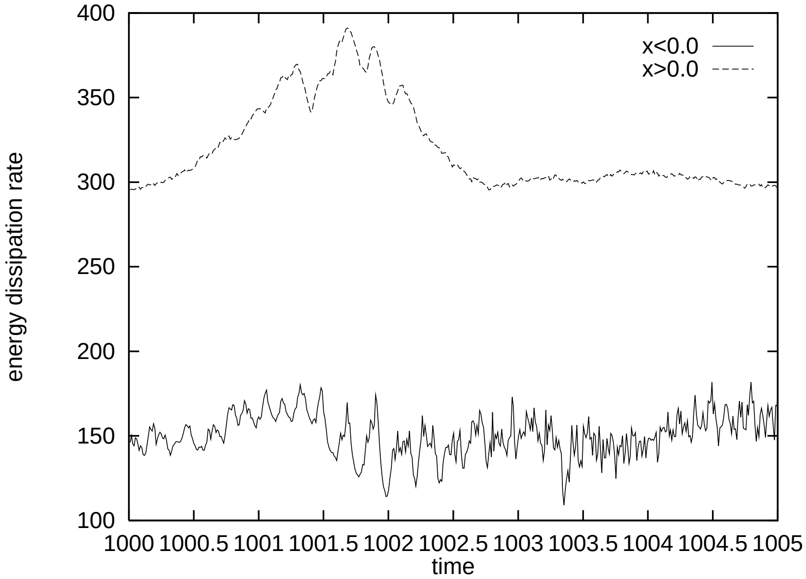

Figure 6.4.16: Energy dissipated per unit time by the outer disk as a function of time for 500 time steps starting at $t = 1000.00$. The two curves combined give the total dissipation occurring at radii > 0.15. Within that context the top curve plots the dissipation that occurs at positive x and the bottom curve shows the balance. In Fig. 6.4.15 the origin corresponds to the leftmost point of the masked out disk.

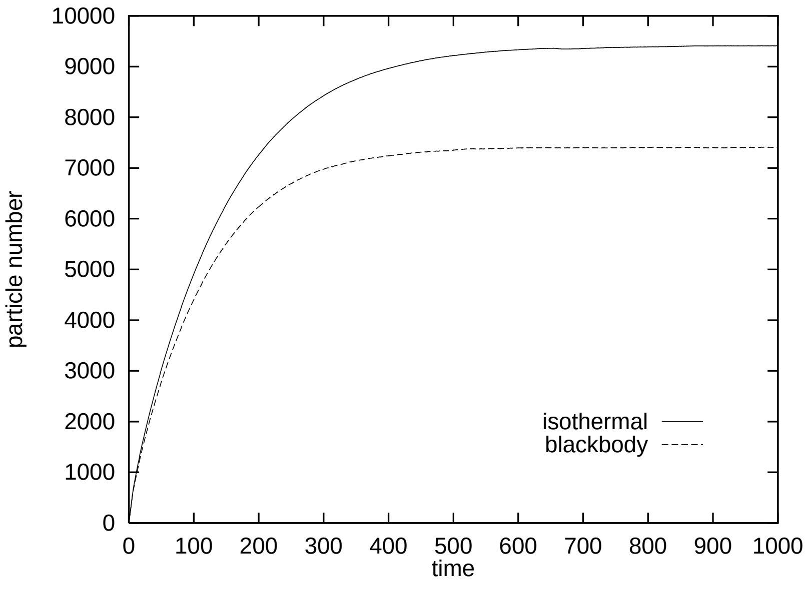

Figure 6.7.1: Plot of particle number against time for the blackbody $\mu = \frac{1}{2}$ disk.

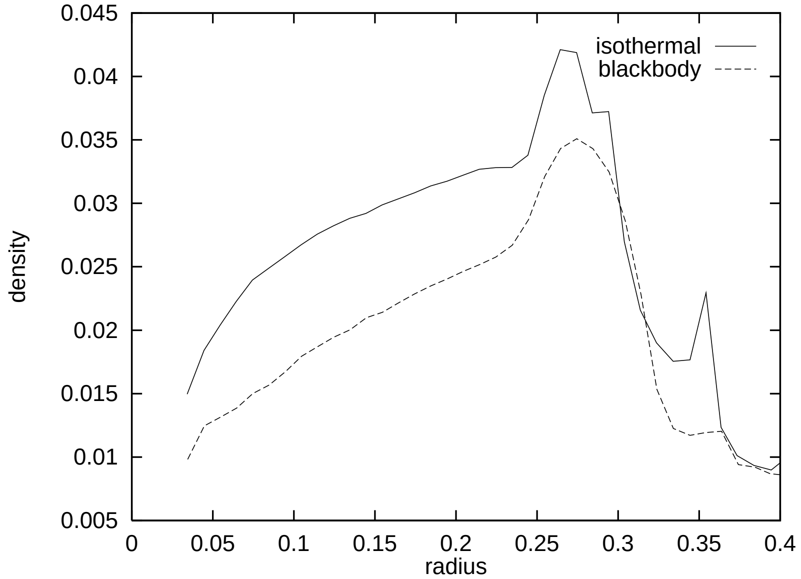

Figure 6.7.2: Comparison of steady state density profiles for the isothermal and blackbody $\mu = \frac{1}{2}$ simulations.

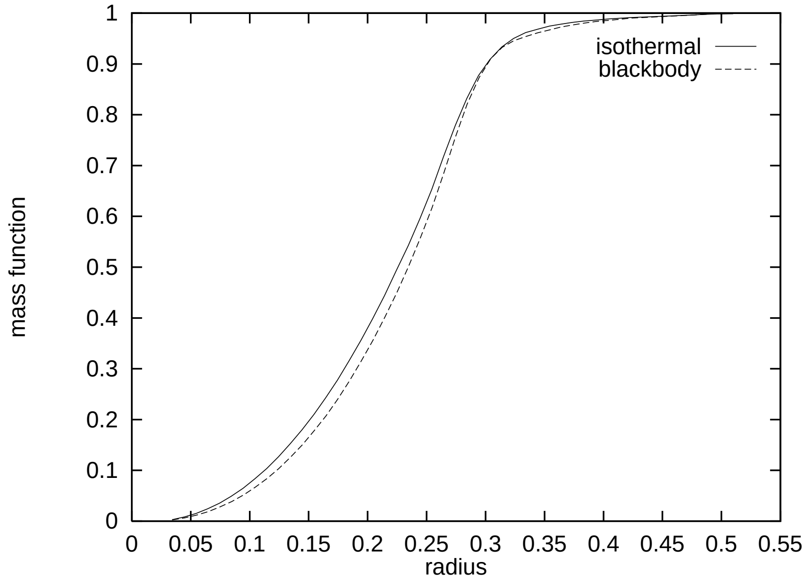

Figure 6.7.3: Comparison of steady state mass function profiles for the isothermal and blackbody $\mu = \frac{1}{2}$ simulations.

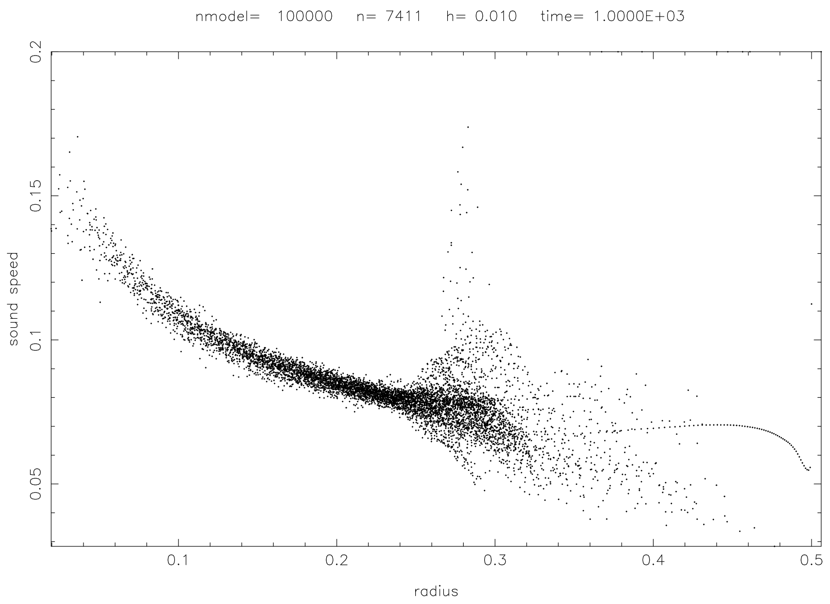

Figure 6.7.4: Plot of sound speed vs radius for the blackbody $\mu = \frac{1}{2}$ disk.

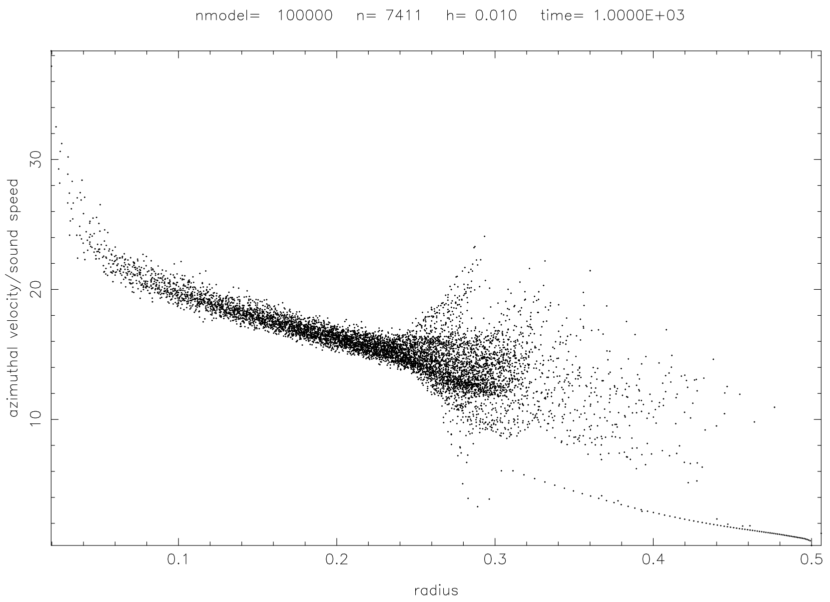

Figure 6.7.5: Plot of Mach number vs radius for each particle in the steady state blackbody $\mu = \frac{1}{2}$ disk. Note that a large Mach number implies the disk is geometrically thin there.

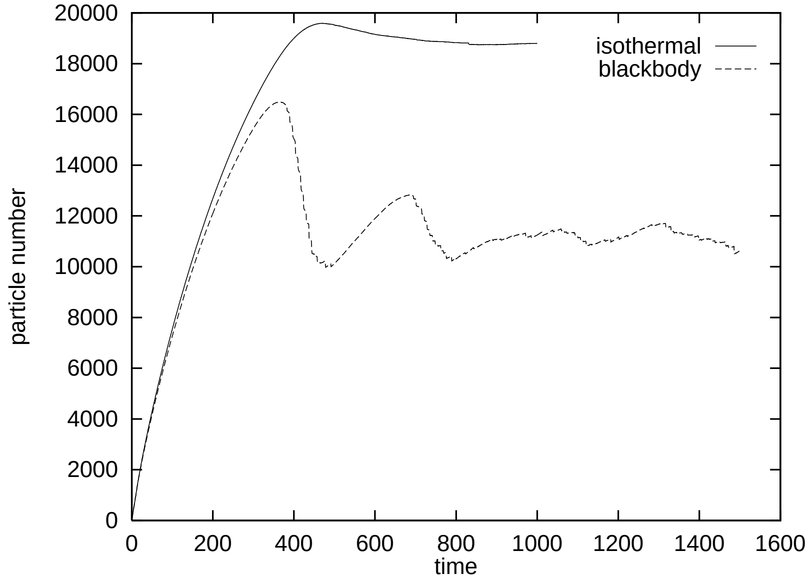

Figure 6.8.1: Plot of particle number against time for the black body and isothermal $\mu = 0.85$ disk simulations.

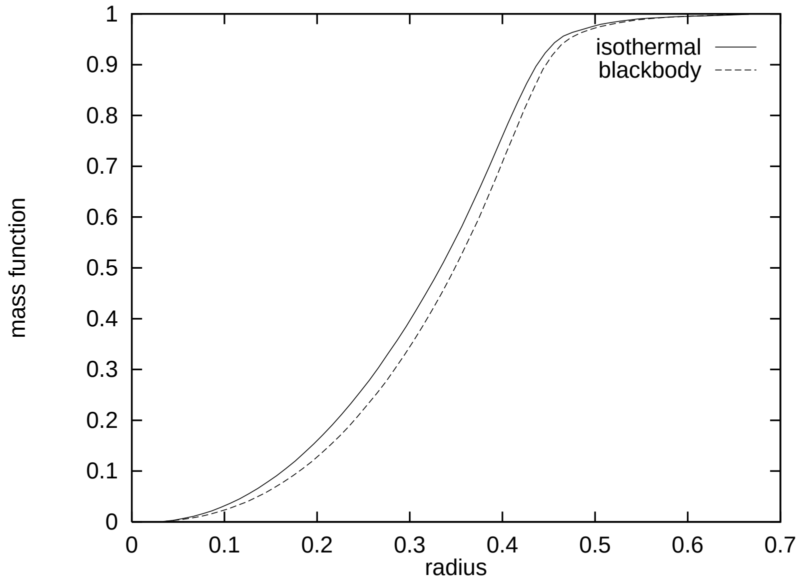

Figure 6.8.2: Comparison of mass distribution curves $M_D(r)$ for the isothermal and blackbody $\mu = 0.85$ simulations at time $t = 250.00$.

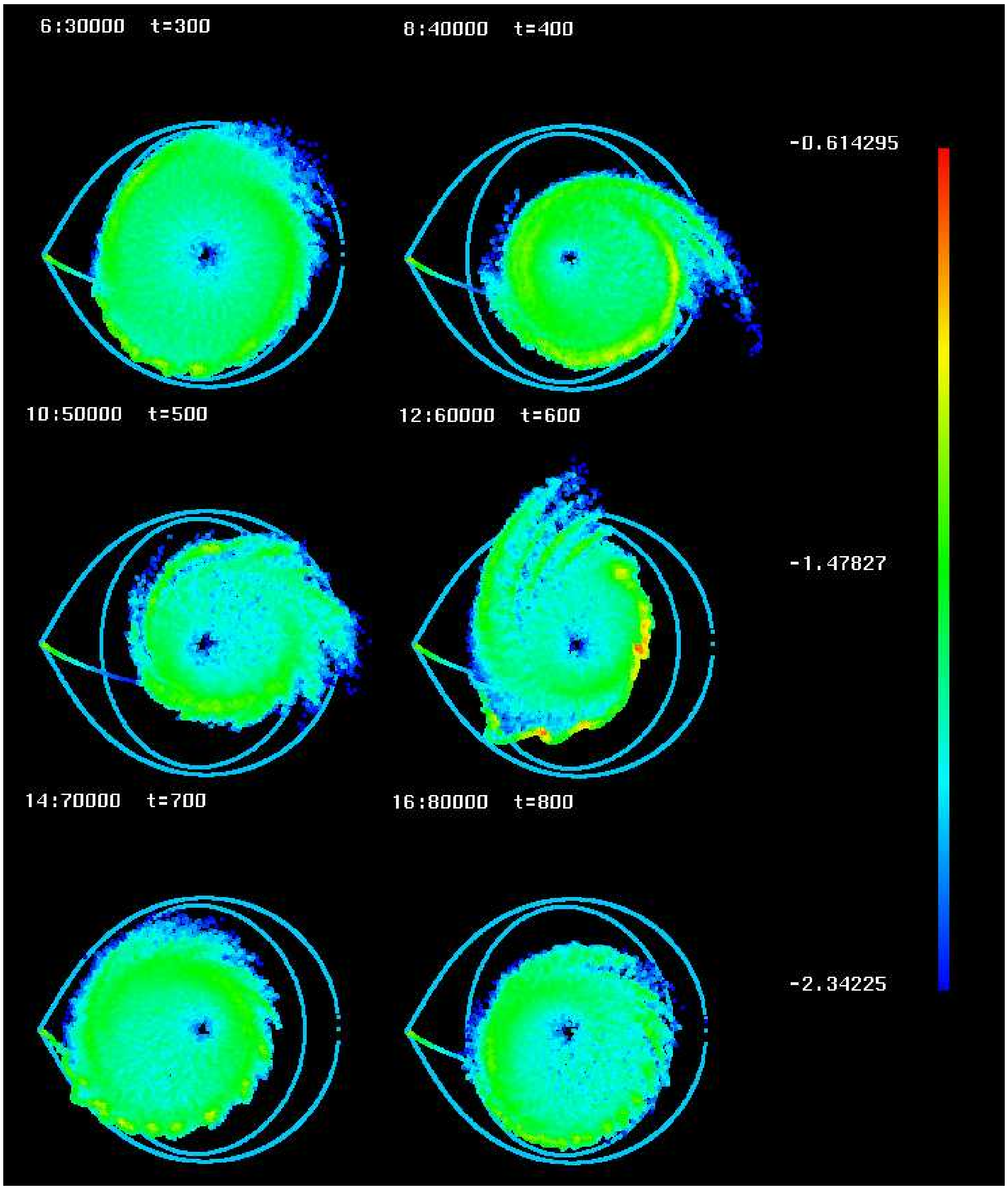

Figure 6.8.3: Snapshots of the blackbody $\mu = 0.85$ disk, coloured according to density using the logarithmic scale to right. Used in conjunction with Fig. 6.8.1 these frames give some idea of the evolution of the disk.

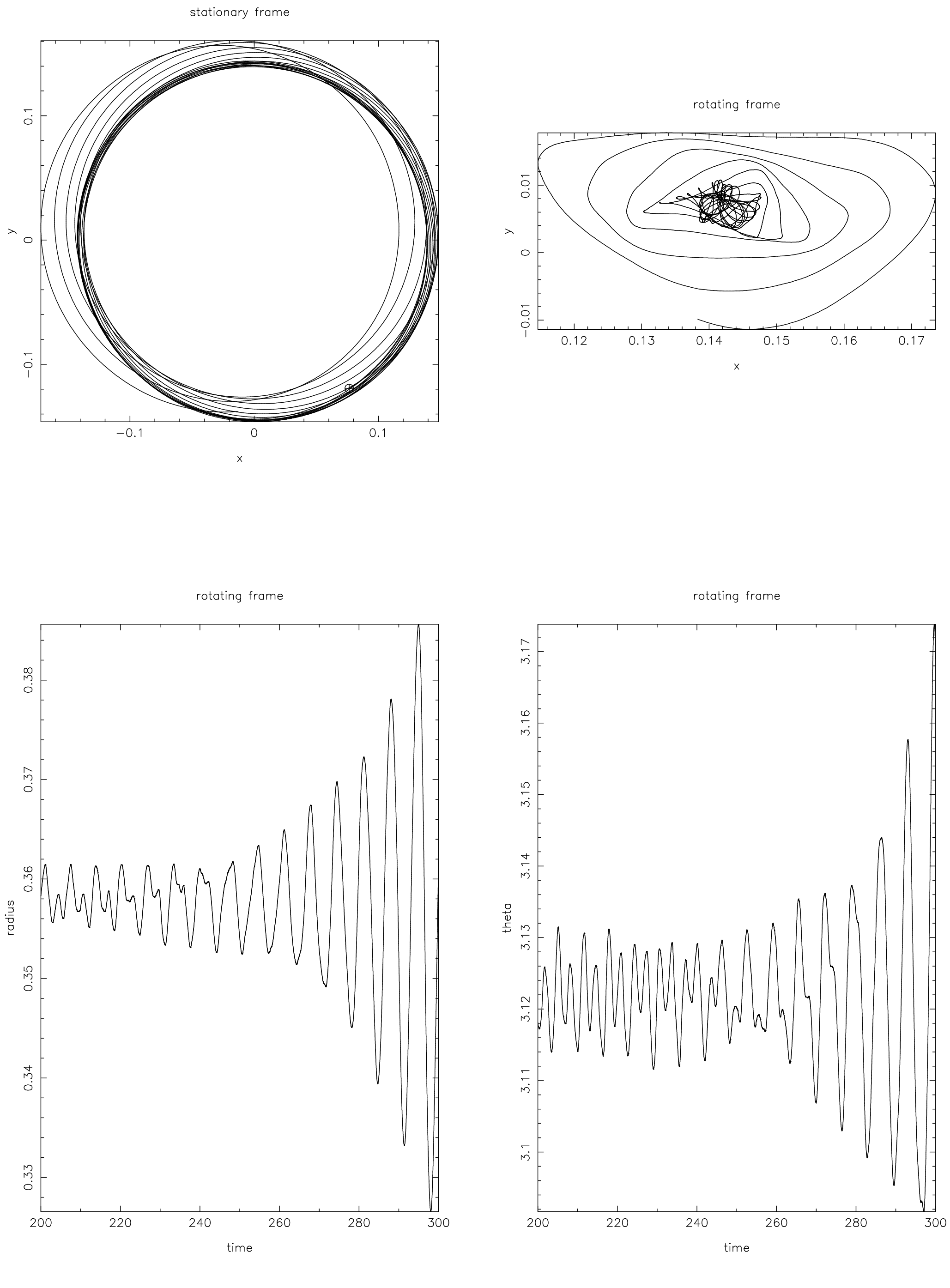

Figure 6.8.4: Plots of the motion of the centre of mass of the blackbody disk in the $\mu = 0.85$ simulation for 10000 steps (100.00 scaled time units) starting from $t = 200.00$. The top two diagrams show its trajectory in the stationary and rotating frames. The lower figures show its radial and angular position with respect to the white dwarf primary as a function of time.

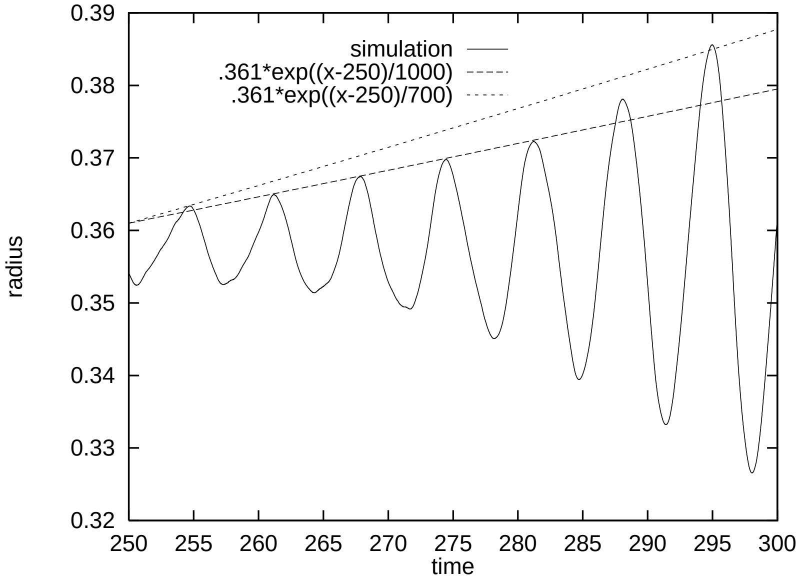

Figure 6.8.5: Radial coordinate of the centre of mass of the $\mu = 0.85$ black body disk (in the frame co-rotating with the binary) plotted against time with two attempts to fit the peaks to exponentials.

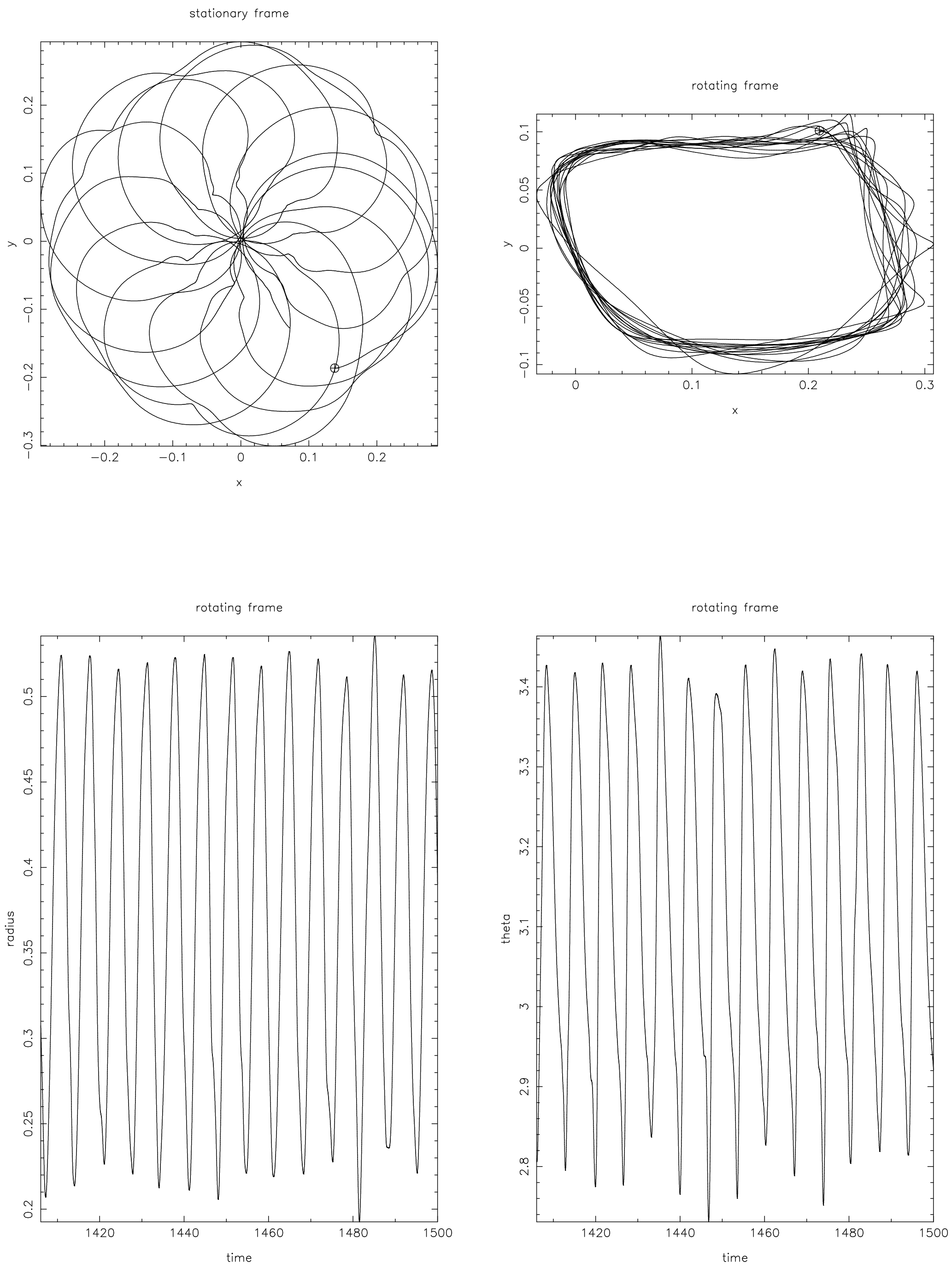

Figure 6.8.6: Plots of the motion of the centre of mass of the blackbody disk in the $\mu = 0.85$ simulation, from $t = 1406.04$ to $t = 1500.00$. The top two diagrams show its trajectory in the stationary and rotating frames. The lower figures show its radial and angular position with respect to the white dwarf primary as a function of time.

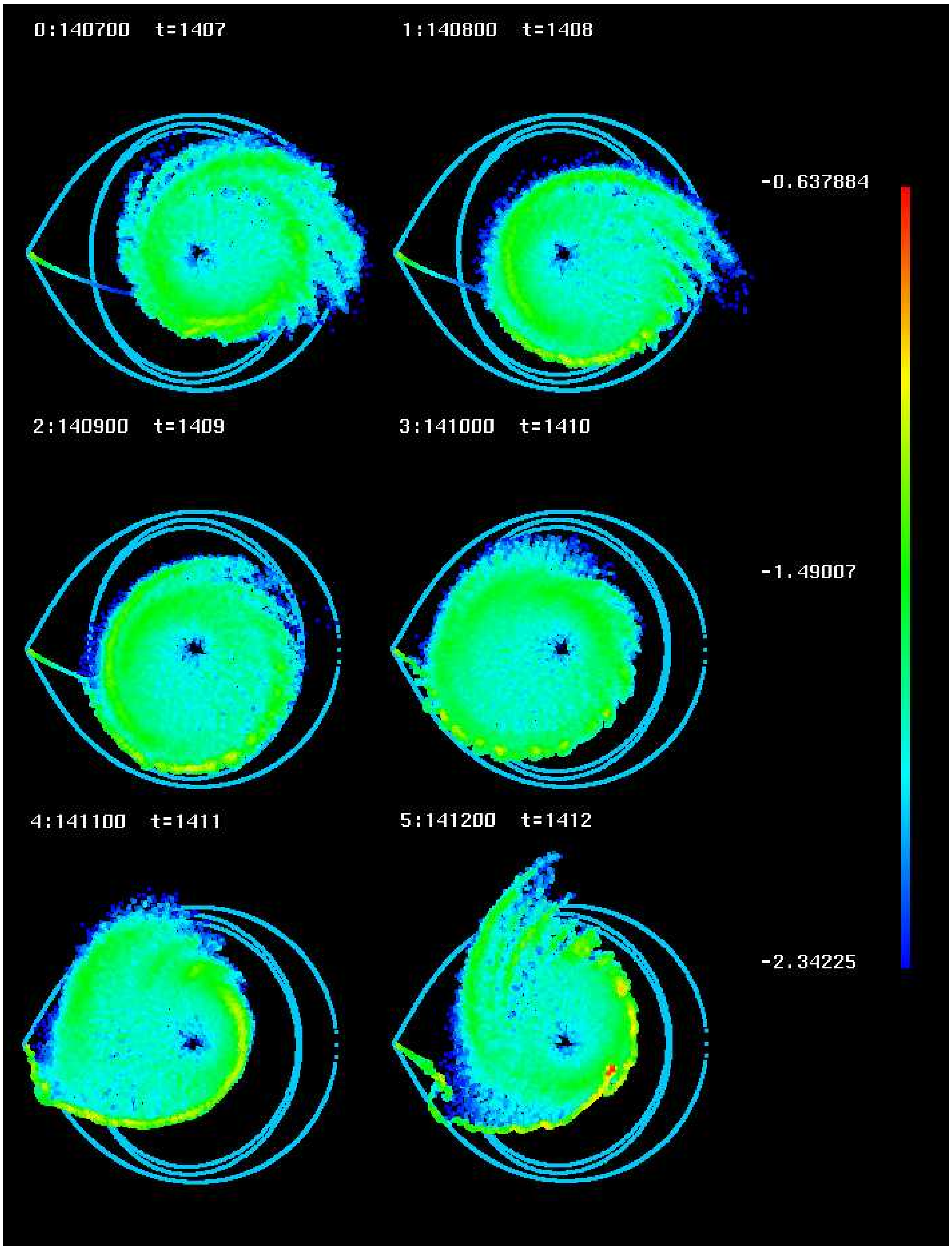

Figure 6.8.7: Snapshots of the blackbody $\mu = 0.85$ disk, coloured according to density using the logarithmic scale to right. The six frames cover a single precession period of the disk.

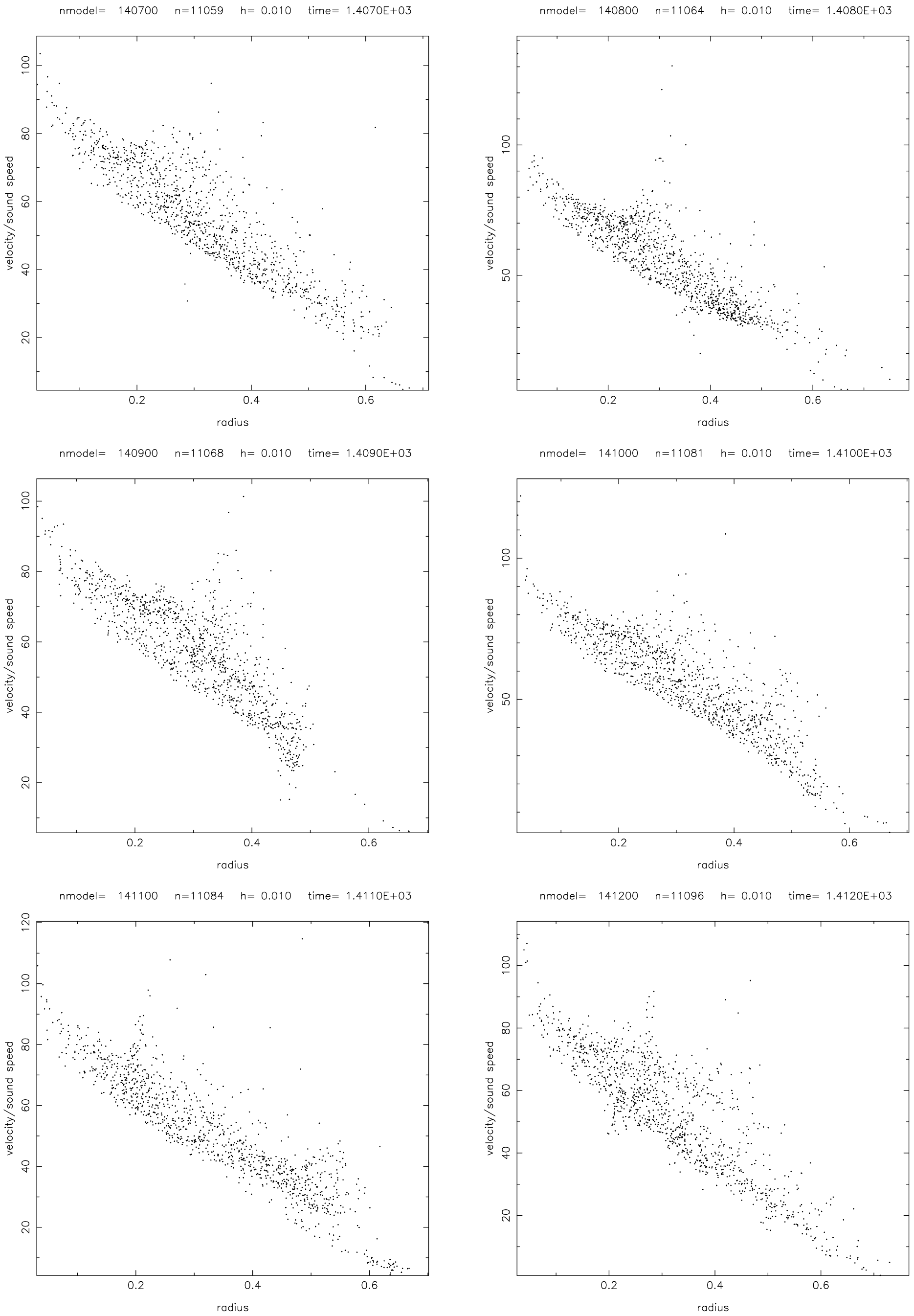

Figure 6.8.8: Mach number , M, for every tenth particle in the $\mu = 0.85$ blackbody disk. The six graphs correspond to the six frames in Fig. 6.8.7.

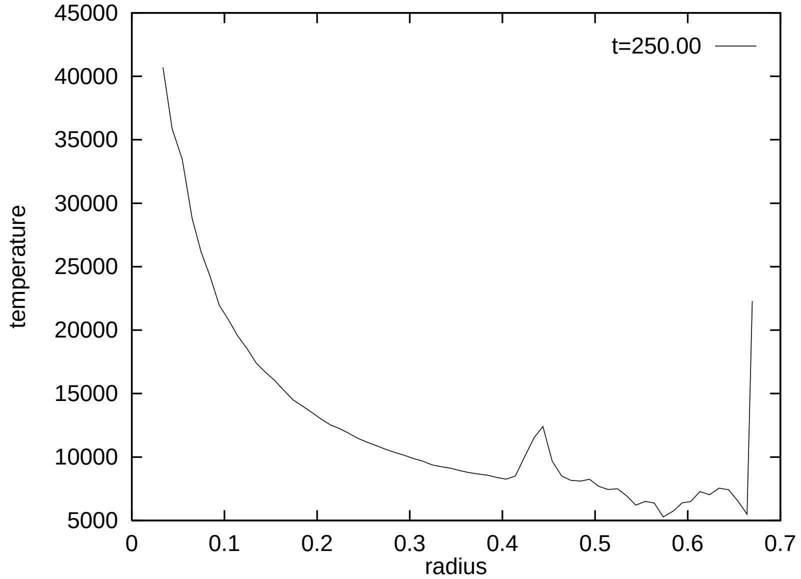

Figure 6.8.9: Azimuthally averaged temperature profile from the blackbody simulation of OY Car at $t = 250.00$.

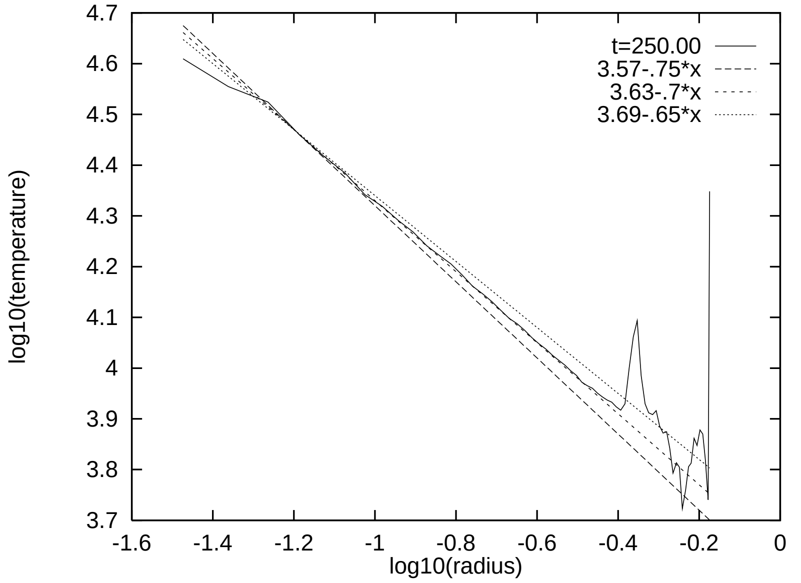

Figure 6.8.10: Azimuthally averaged temperature profile from the blackbody simulation of OY Car at $t = 250.00$ plotted on logarithmic scales. The linear fits show the temperature varies as $r^{-.70\pm.05}$.

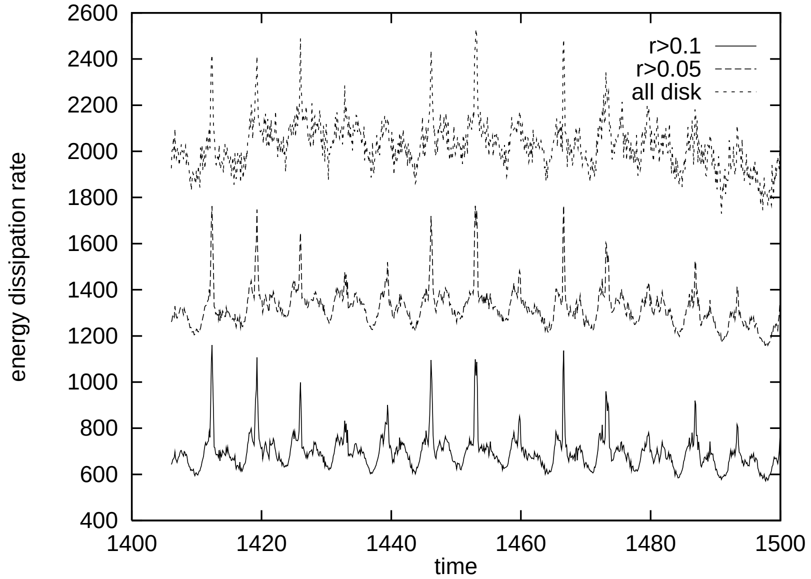

Figure 6.8.11: Energy dissipation rate (scaled units) as a function of time for the steadily precessing blackbody disk. The top curve plots the total dissipation of the disk. The middle and bottom curves give the energy dissipated at radii larger than 0.05 and 0.1 respectively. Each point on the curve represents the average value of the dissipation rate over ten timesteps.

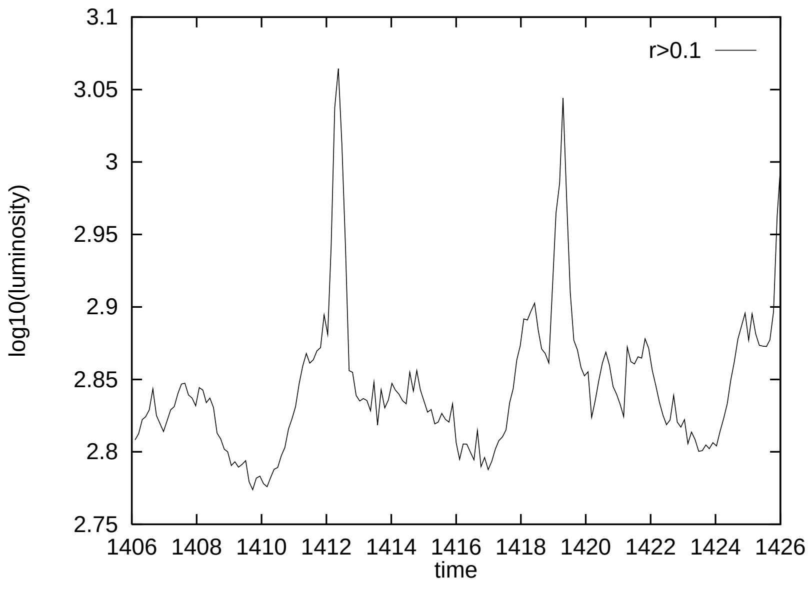

Figure 6.8.12: The logarithm of the energy dissipation rate (equated to the luminosity) as a function of time for the outer regions ($r > 0.10$) of the steadily precessing blackbody disk for twenty scaled time units. Each point on the curve represents the average value of the dissipation rate over ten timesteps.

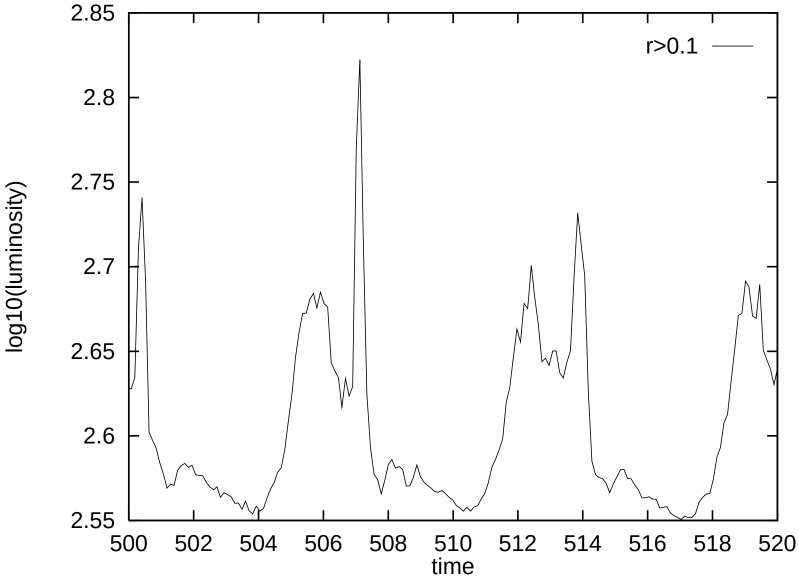

Figure 6.8.13: The logarithm of the energy dissipation rate (equated to the luminosity) as a function of time for the outer regions ($r > 0.10$) of a steadily precessing blackbody disk for twenty scaled time units. Each point on the curve represents the average value of the dissipation rate over ten timesteps. In this simulation particles were injected in a circular orbit at the circularisation radius instead of at L_1.

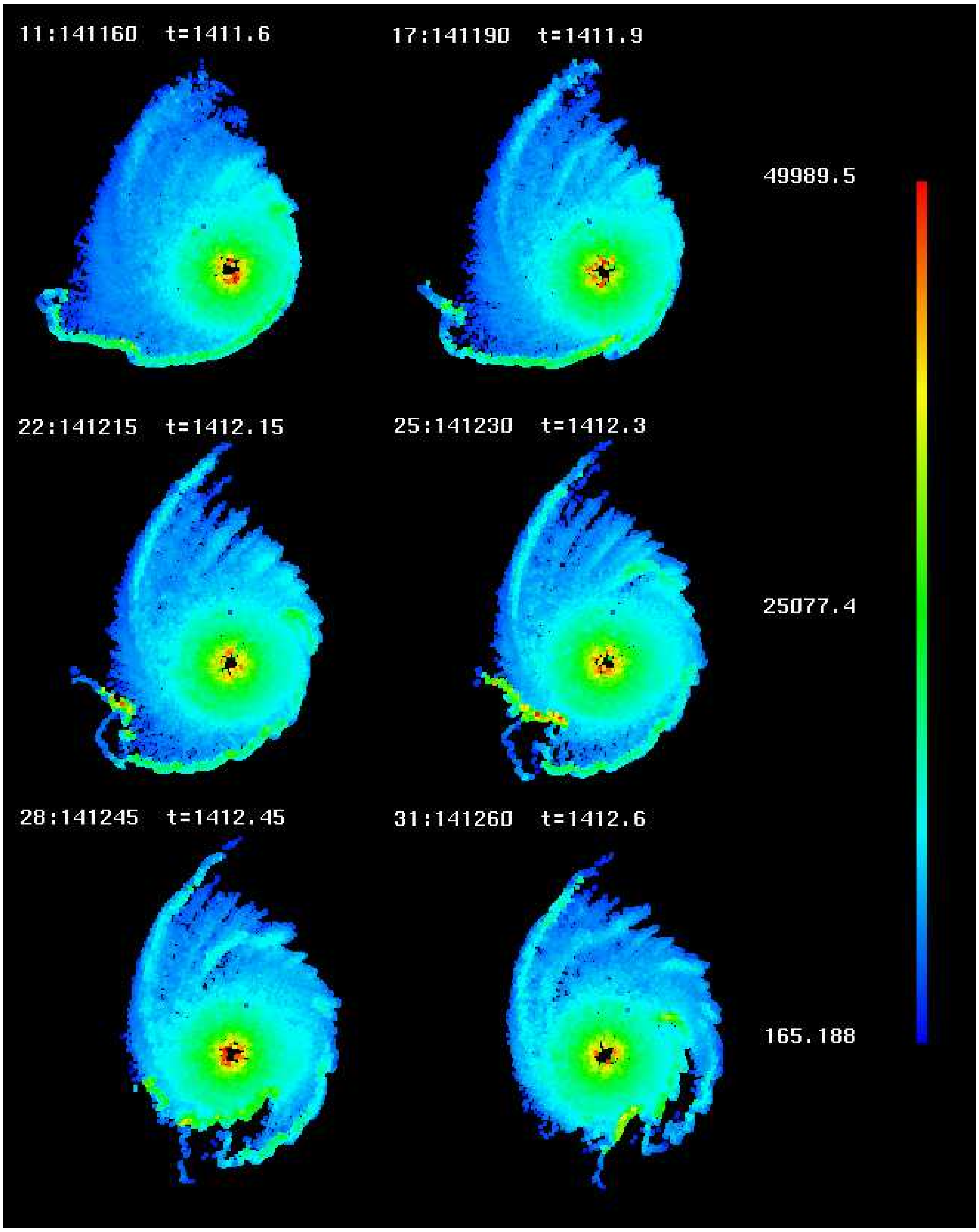

Figure 6.8.14: Snapshots of the blackbody $\mu = 0.85$ disk, coloured according to temperature using the linear scale to right. Particles with $T > 5 \times 10^4$ are not shown. The six frames (times shown) follow the development of a luminosity spike).

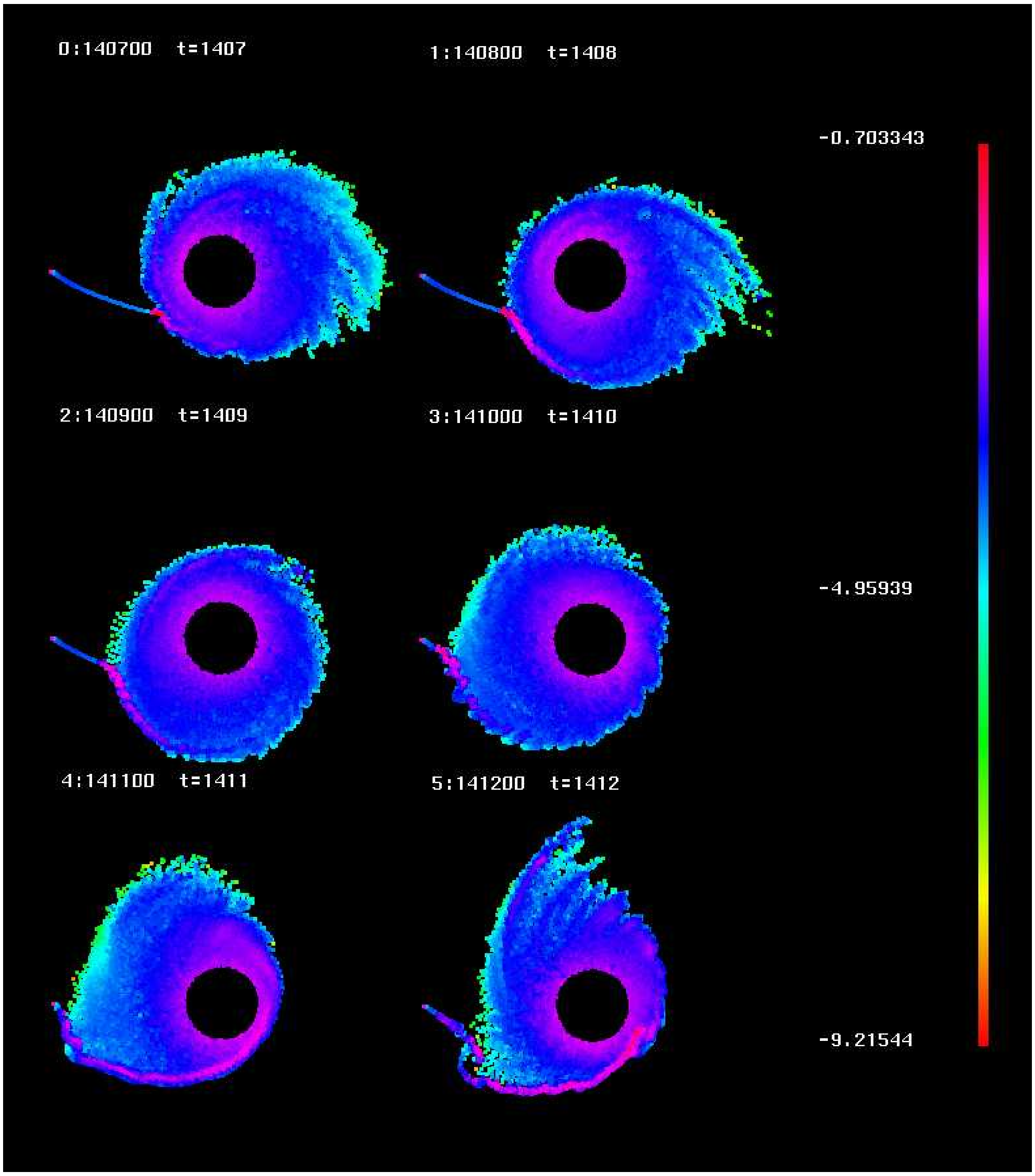

Figure 6.8.15: Snapshots of the blackbody $\mu = 0.85$ disk, coloured according to energy dissipation rate using the logarithmic scale to right. The inner region ($r < 0.10$) of the disk has been masked out. The six frames correspond to those in Fig. 6.8.7.

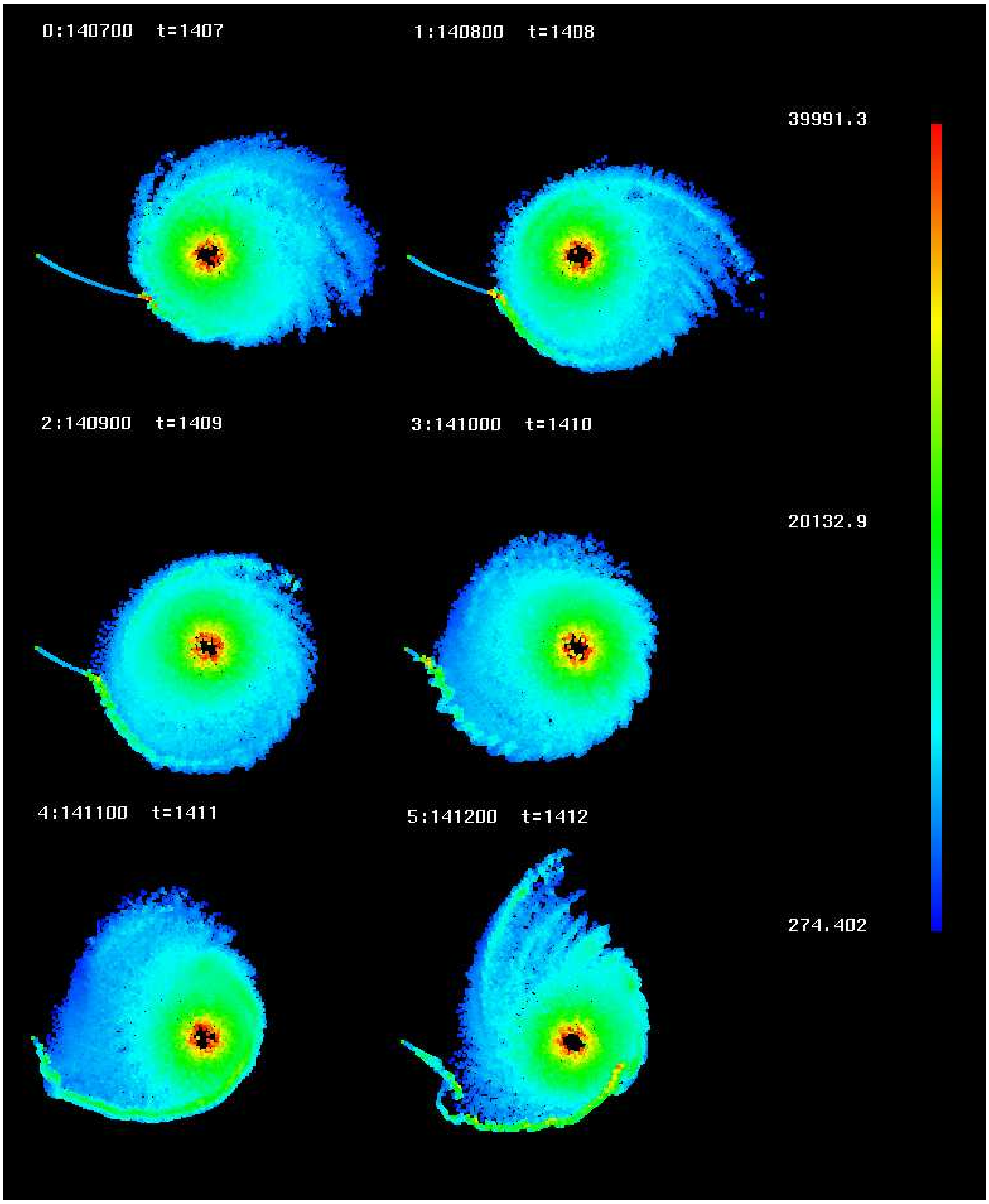

Figure 6.8.16: Snapshots of the blackbody $\mu = 0.85$ disk, coloured according to temperature using the linear scale to right. The six frames cover a single precession period of the disk.

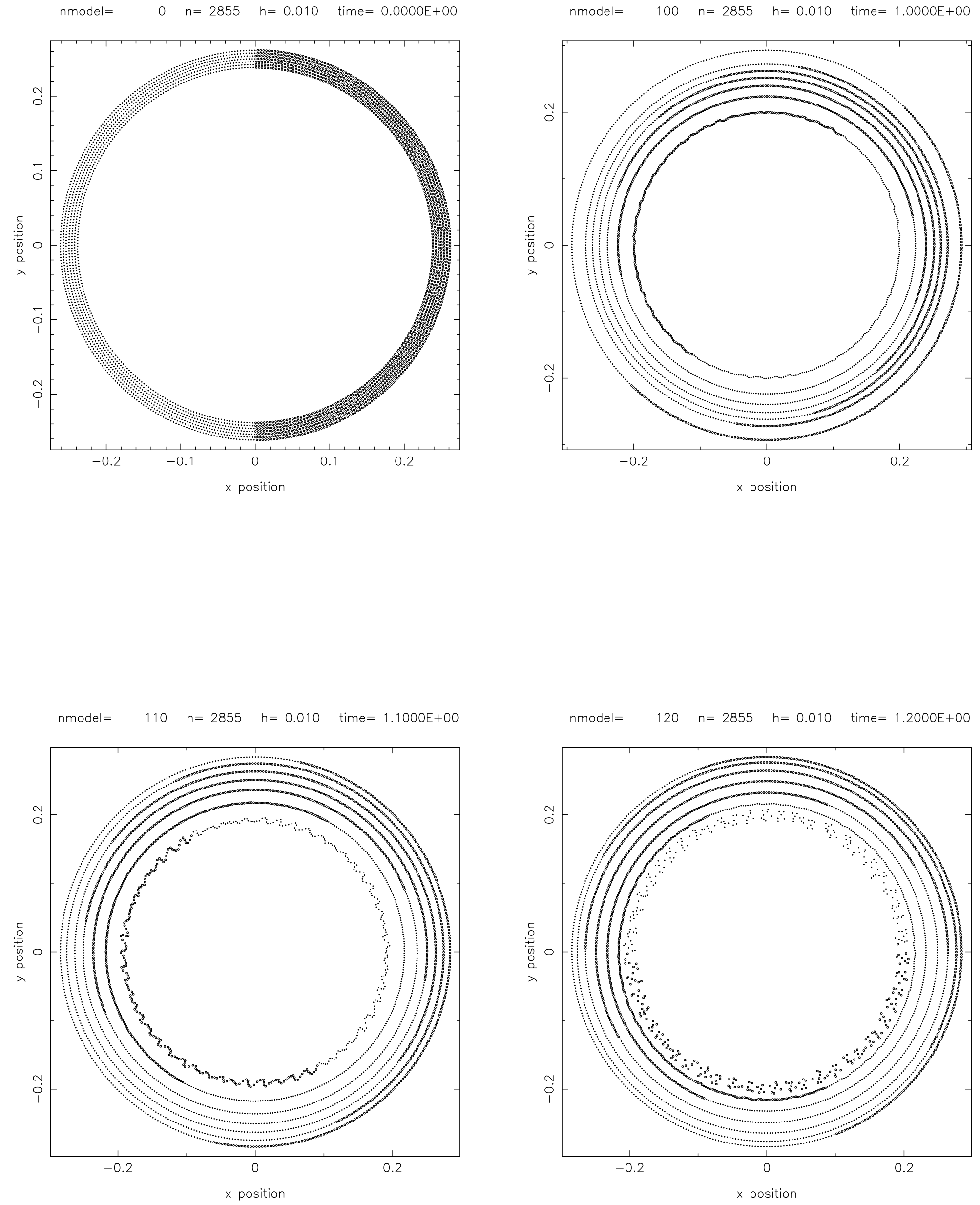

Figure 7.1: Instability growth in a 'viscous' disk. The initial annulus is composed of 7 rings with particle separation set at $\frac{5h}{13}$. The central body has unit mass. The smoothing length $h = 0.01$. The pressure has been switched off. $\bar{\alpha} = 10$ and $c = 0.02$. The only interparticle forces are SPH artificial viscosity interactions. Follow the evolution from left to right, top to bottom.

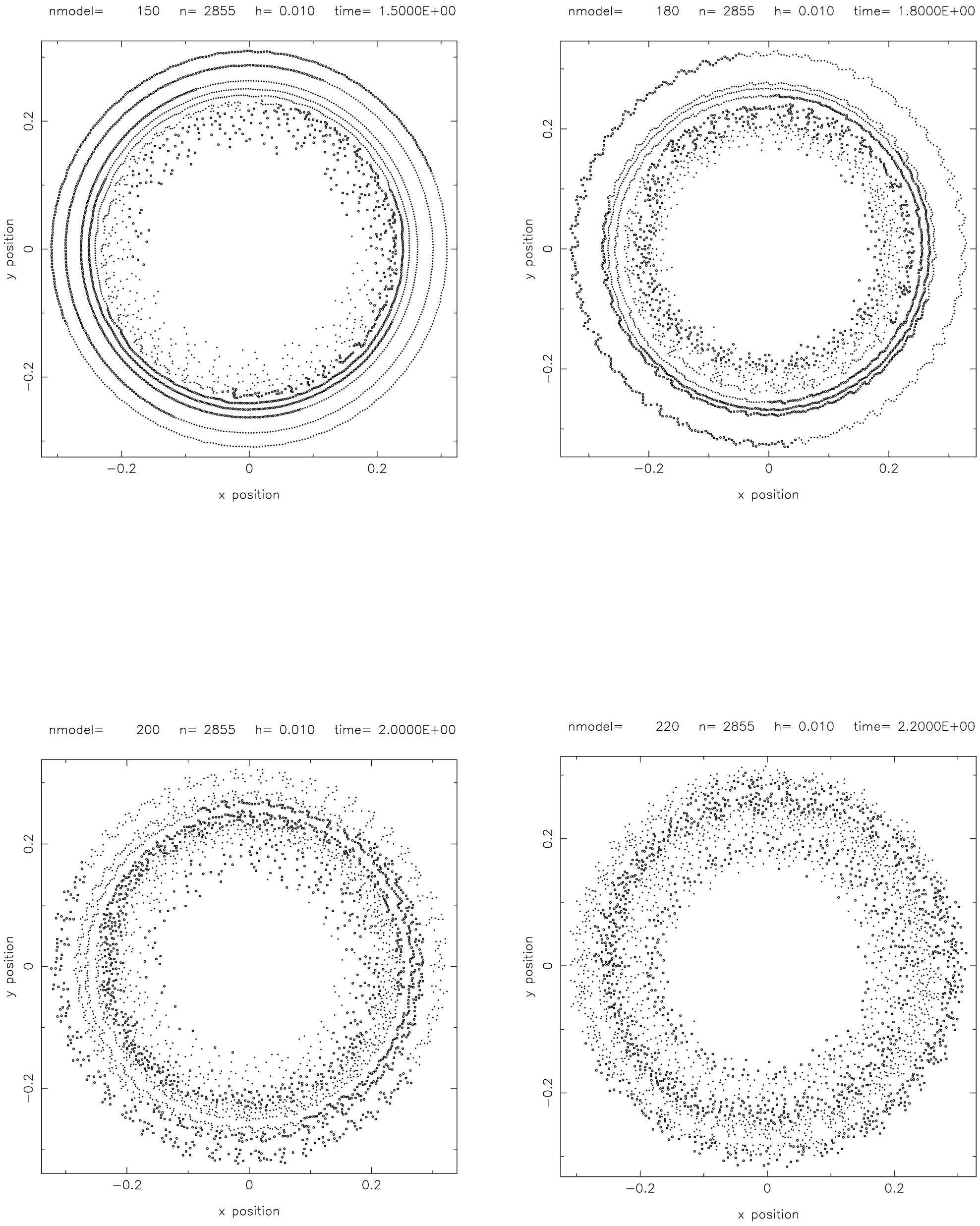

Figure 7.2: The continued evolution of the disk shown in Fig. 7.1.

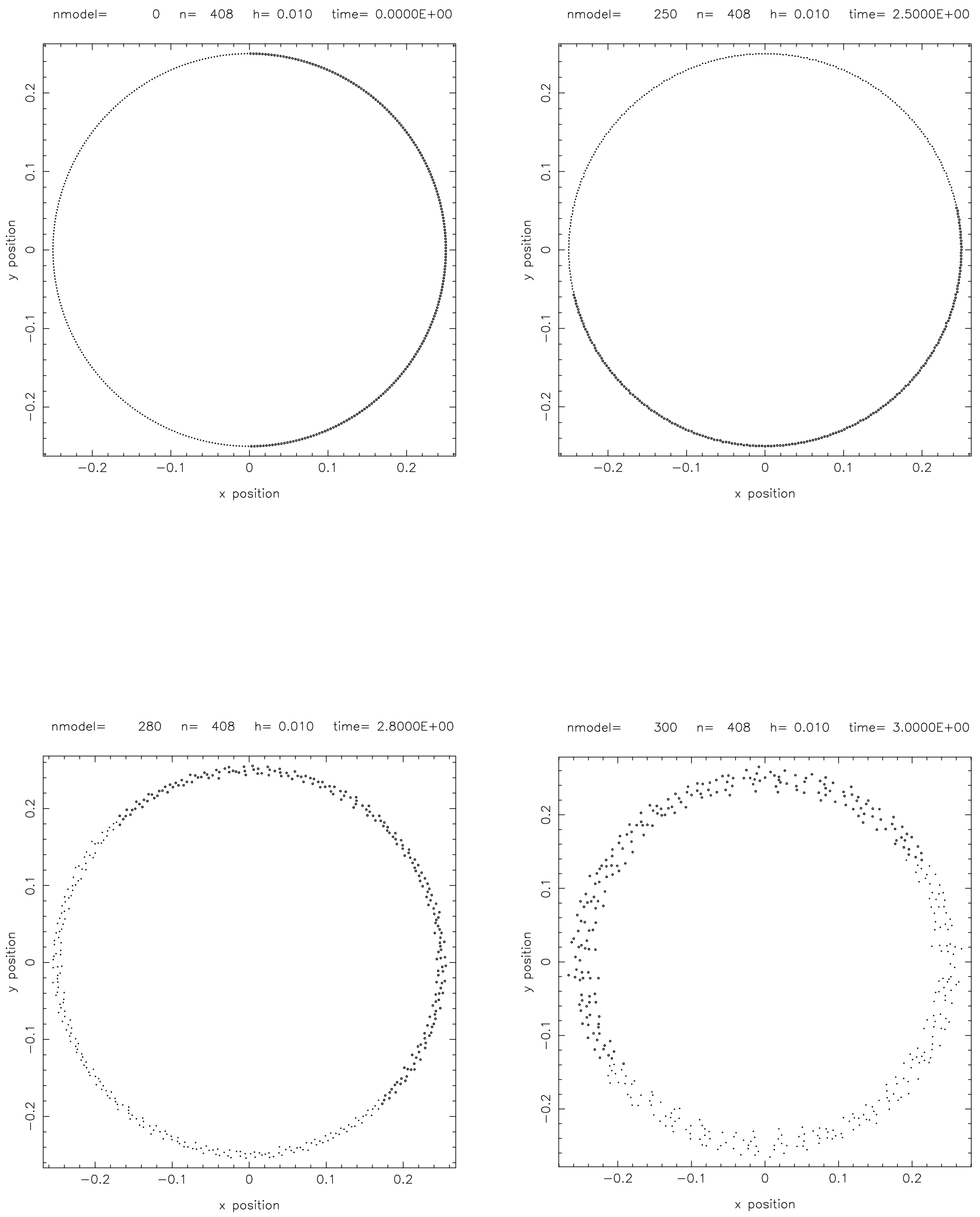

Figure 7.3: Development of disorder in a single ring of viscous particles. Parameters are as for Fig. 7.1.

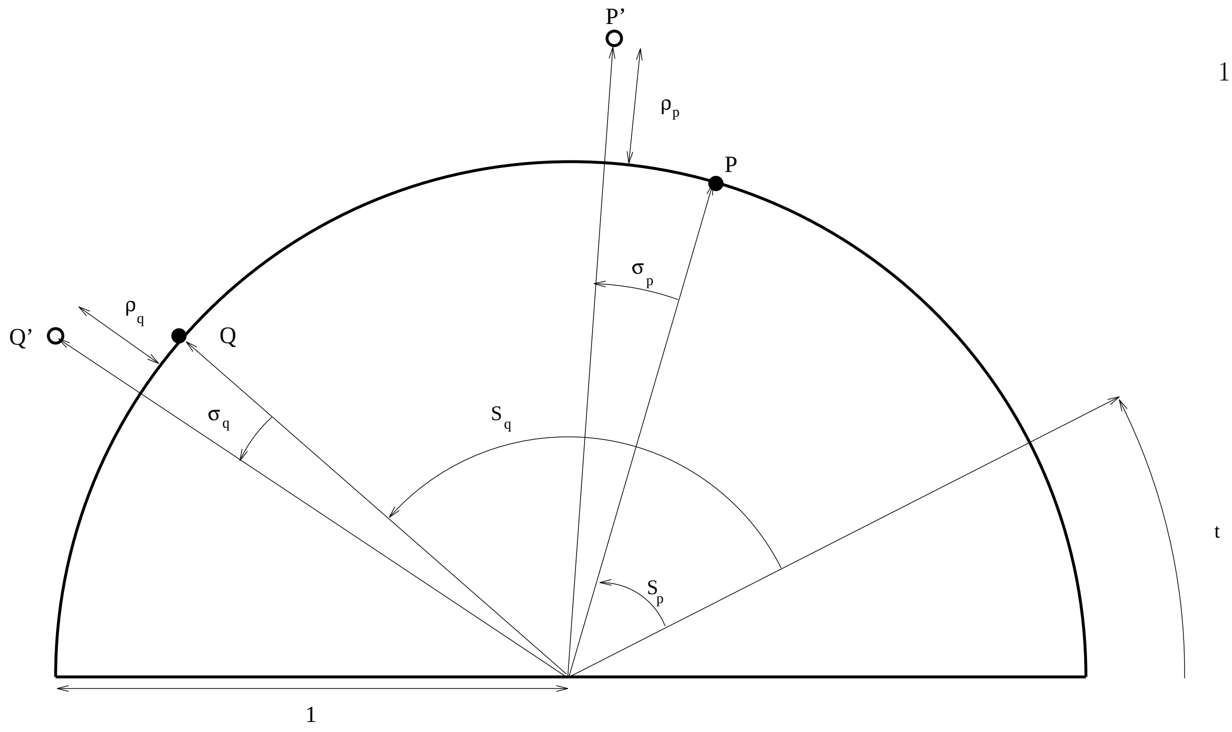

Figure 7.4: The perturbed and unperturbed positions of particles P and Q.

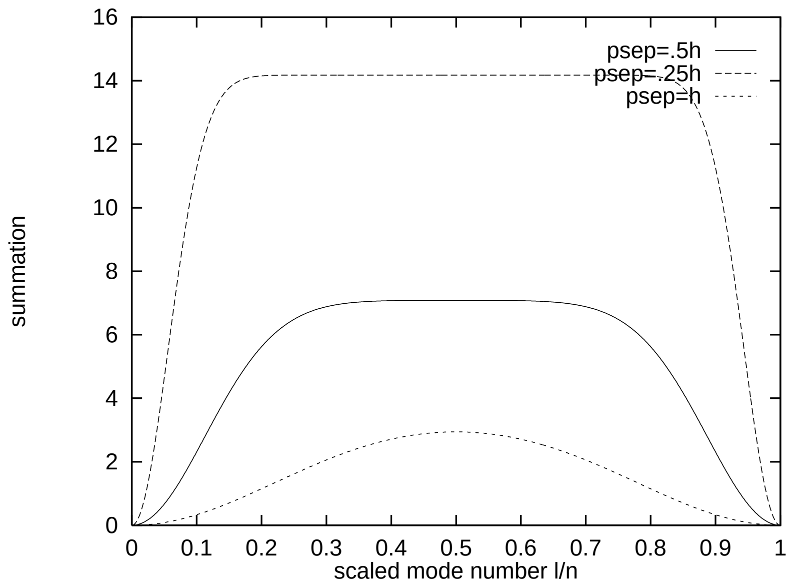

Figure 7.5: $\pi h^2 \Phi$ as a function of $\frac{l}{n}$ for three values of the ratio of the particle separation to the smoothing length h.

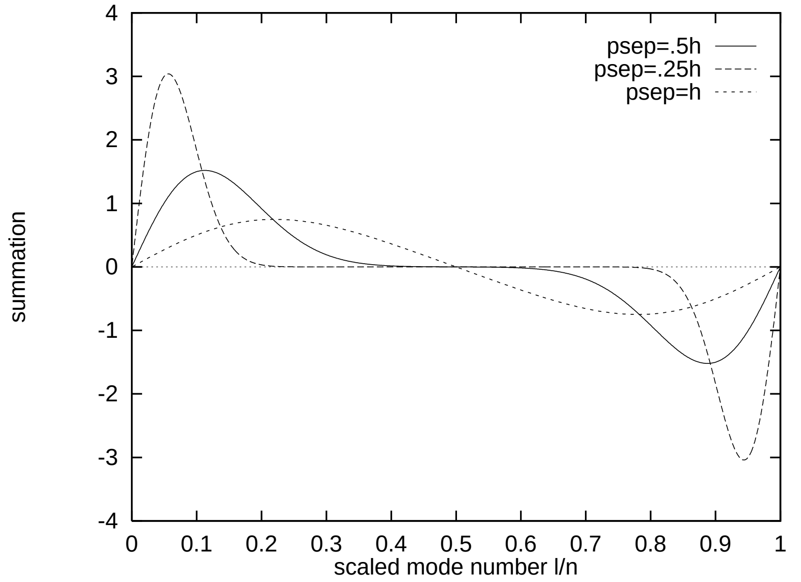

Figure 7.6: $\pi h \Psi$ as a function of $\frac{l}{n}$ for three values of the ratio of the particle separation to the smoothing length h.

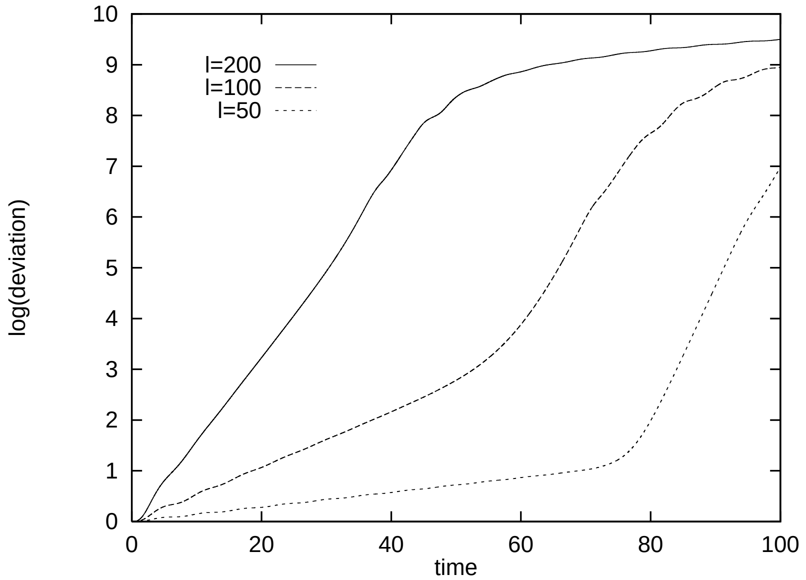

Figure 7.7: $\ln \frac{\gamma(t)}{\gamma(0)}$ plotted as a function of time for perturbations of varying l. The simulation parameters are listed in Table 1.2.1.

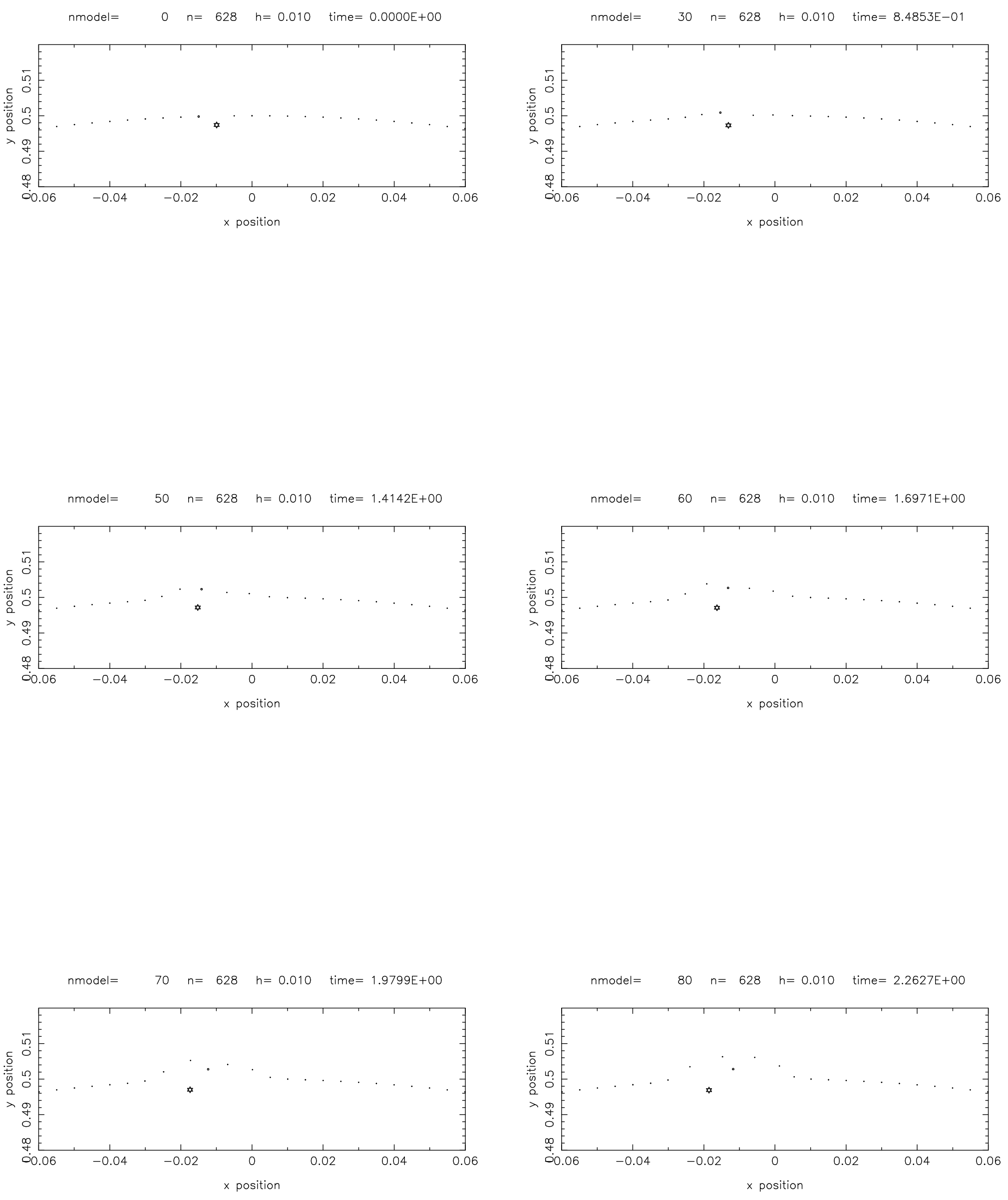

Figure 7.8: Segment of a single ring of 'viscous' particles in orbit about a point mass. The initially perturbed particle (shown as a star) has a mass one hundred times that of the other particles.

Contents